School of Earth and Planetary Science

Nanoscale Investigation of Metamorphic Processes

Tommaso Tacchetto
0000-0001-5447-7021

This thesis is presented for the Degree of
Doctor of Philosophy
of
Curtin University

April 2022

Declaration

To the best of my knowledge and belief this thesis contains no material previously published by any other person except where due acknowledgment has been made. I have obtained permission from the copyright owners to use any of my own published work in which the copyright is held by another party.

This thesis contains no material which has been accepted for the award of any other degree or diploma in any university.

Signature:
Date:

Abstract

Crustal fluids (aqueous and/or melts) are important agents of mass and heat transfer, playing an intrinsic role in the geochemical and physical evolution of the Earth's crust. The presence of fluids impacts the properties of geological materials including their melting temperature, viscosities, the density of magmas and reactivities. Fluids enhance diffusion, enable mass transfer processes, and help overcome kinetic barriers to metamorphic reactions. Deformation is responsible for the physical transformation of rocks typically leading to a reduction in grain size of the deforming material, and the associated increase in fluid permeability. The growth of new minerals by fluid-aided replacement reactions during fluid-present deformation may have drastic weakening consequences with a profound effect on the rheological behaviour of the rock. The complex interplay between fluid-rock interactions and deformation within crustal lithologies, therefore, represents a fundamental aspect of the geological processes of rock transformation.

At a fundamental level, the underlying mechanisms affecting larger-scale rock dynamics are governed by processes operating at the nanoscale within minerals and at the interfaces between them. However, until recently, the quantification of elemental and isotopic information at this scale has been difficult due to the technical difficulties in measuring compositional data from small volumes of natural materials.

This doctoral thesis presents four micro- to nanoscale investigations of metamorphic processes taking place within the Earth's lower crust through the application of a suite of cutting-edge techniques, with a particular focus to enhance our understanding of the nanoscale manifestation of fluid-rock interactions and their consequences for mass transport at depths.

The approach used in this thesis centred on the application of atom probe tomography (APT) to metamorphic applications. With the intrinsic ability to resolve in 3D the chemical and structural properties of materials at near-atomic resolutions, the use of APT opens up the opportunity to overcome size-related limitations, helping uncover fundamental rock mechanisms. The applied workflow also integrates more established microanalytical techniques such as electron backscattered diffraction (EBSD) and transmission electron microscopy (TEM), to enable the selection of specific sites for atom probe analyses and support the interpretation of the acquired APT datasets.

This analytical workflow has been applied to type localities of deep crustal fluid-melt-rock interaction and deformation: i) glassy anatectic melt inclusions found within a granulite

from the Betic Cordillera (southern Spain) and ii) the granulites, eclogites and amphibolites of the Bergen Arcs (western Norway). The four studies presented in this thesis encompass a suite of unique geological processes allowing the isolation and detailed investigation of particular aspects of the complex interplay between fluids, rocks and deformation.

The first study focuses on glassy melt inclusions trapped within peritectic garnets. ToF-SIMS microscale compositional analysis confirms that these inclusions remain a closed system at geological timescales. At the nanoscale, TEM and APT reveal compositional clustering of elements within the glass and along inclusion walls. These nano-spherical domains are interpreted as pre-nucleation clusters, indicating a "captured" stage of melt crystallization. Moreover, a comparison between the composition of melt inclusions with previously published work indicates that crystallization is dependent on the H_2O contents of the entrapped melt. By investigating a small undeformed closed system as melt inclusions, this study provided an unprecedented picture of the dynamics of crystallization and the role that water plays in enhancing trace element diffusivity during anatexis of the lower crust.

The second study, and the first of the three undertaken on the rocks from the Bergen Arcs, is focused on the geochemical and microstructural evolution of an amphibolite shear zone developed within partially metasomatized granulites. U-Pb age data obtained from zircon grains within the shear zone cluster at 883 ± 3 Ma consistent with ages derived from the granulite facies assemblage. Phase equilibria modelling constraints the condition of deformation at ~ 600 °C and ~ 11 kbar. At the microscale, EBSD orientation analysis allowed to identify a sequence of deformation microstructures progressively evolving during syn-kinematic hydration of the lower crust and dominated at the grain scale by crystal plastic mechanisms. The outcrop- to micro-scale workflow of investigation conducted in this study provided context and constraint to refine our understanding of the role that fluid infiltration plays in promoting shear localization and rheological weakening in the anhydrous rocks of the lower continental crust.

In the third study, a low-angle boundary developed by crystal plasticity within a granulite-facies garnet of a subduction zone generated pseudotachylyte is investigated. APT data shows enrichment of trace elements (Ca, Cl, Na, K, Ti, P, Cu and H) at the targeted interface. Consideration on the geological context of these samples suggests different mechanisms for trace element enrichment. Dislocation-impurity pair is responsible for the segregation of solute ions (Ca, Ti, P and Cu) during dislocation creep, whereas (Na, K, Cl and H) indicates a concomitant mechanism of intra-grain diffusion of an external fluid source along the low angle-boundary. This study provides evidence of the impact that

intracrystalline deformation has on garnet microchemistry, and thus affecting its geological applications.

The final study builds on the study of trace-element segregation in garnet to systematically investigate the relationship between trace element segregation and the degree of deformation represented in low-angle boundaries in olivine. The correlative techniques of EBSD, TEM and APT were applied to naturally-deformed olivine from exhumed spinel-lherzolites. APT analyses show enrichment of Ca, Al, Ti, P, Mn, Fe, Na, Co, Cl and H at the analysed interfaces, and the results show a correlation between trace element segregation and the dislocation density within low-angle boundaries. Olivine-derived impurities such as Ca, Al, Ti, P, Mn, Fe, Na and Co are interpreted to be segregated to the interfaces by defect-impurity pair during dislocation creep, whereas higher concentrations of Cl and H are attributed to the diffusion of fluid-derived components. The microstructural and nanoscale compositional outcome of this study indicates complexity in olivine grain boundaries that has significant implications for the deformation of olivine and mantle rheology.

The integrated outcome of this doctoral research provides new, unprecedented insights into the role that crustal fluids play in mineral replacement, strain localization, trace elements redistribution during melt crystallization and deformation at a heretofore unseen spatial resolution. The nanoscale characterization of low-angle boundaries in different fundamental rock-forming minerals revealed the presence of a ubiquitous relationship between trace element segregation and interfaces. This consequently leads to the consideration that coupled processes of trace element mobility along mineral interfaces are likely to be widespread. Moreover, the results systematically indicate that information on hydrogen distribution can be obtained by APT analyses of low-angle boundaries. This has the potential to represent an important breakthrough for the nanoscale identification of hydrogen within mantle-derived minerals allowing a better understanding of large-scale dynamics of the deep Earth. Finally, this doctoral research provides a toolbox of techniques combined into a workflow that can be integrated into future metamorphic, microstructural and geochemical studies to better understand the complex behaviour of the lithosphere when interacting with a free-fluid phase.

Acknowledgements

"Un lungo, ma meraviglioso viaggio"

"A long, but amazing journey"

This PhD has been, by far, one of the most exciting experiences I had during my academic studies. Three and a half years after having moved to the other side of the world, to the fascinating upside-down Australia, working in a world-class renowned Research University, I can confirm it really was a once-in-a-lifetime opportunity. I met so many different people from everywhere in the world, many professors, researchers, and students. I saw unutterable places and lived overwhelming emotions, but most importantly, I discovered myself. Here, I grew not only as a professional, but I also understood and embraced my real personality, drowsy by the safety feeling of my hometown. During this period, I learnt how to be alone out there, and mastered a different language allowing me to communicate with so many people of every different kind. I opened my mind and learned how to embrace and appreciate different cultures and costumes. I recognised my strengths and my limits. I faced extreme joy and horrible fears. I experienced the fear of losing a brother, deprived of his liberty for months. But I also found the deepest connection with my family and learnt what I really need and what is unnecessary. By far, surfing has been one of my biggest discoveries, the bond that you create with nature, and learning how powerful it can be.

Firstly, I thank my supervisors for giving me the opportunity to undertake this PhD, teaching me how to use my brain, and having the patience to discuss, advise, read and provide constructive comments to many manuscript drafts. In particular, Steve thanks for unravelling mysteries of structural geology, Chris for sharpening my skills of metamorphic petrology (and sharing a world-class pizza in Norway), and David for revealing me the secrets of atom probe tomography. You all contributed to making me a better geologist and I am grateful for that.

I really want to thank members of the atom probe group, Denis for always leaving the door open. Will for the support during the scary FIB sessions and for showing me what is cricket-like. Thanks to Zak for giving me the opportunity to run the TIMA lab and learn how to be

professional. Thanks to the crew of the JdL Centre: Brent, Elaine, Anusha, Payal and geo-lab, Brad for the occasional surf sessions and Andi for dealing with my inventions.

I would also like to thank my mentors Bernardo and Omar, for believing in me and pushing me to pursue an academic career. Thanks to Bruna, Omar G., Fabio and all the Padova crew, it was such a good time back there.

Thanks to all my friends I met here in Perth. Special thanks to my housemates, Garth ("the sparky") and Matty ("the chippy") for really showing me Western Australia, teaching me the slang, and for having shared together so many experiences and laughs. Thanks to the Scarborough crew Luigi, Sonia, Mo, Anna, Gary, Lars and Brooke, Joe, Emmy, Kate B., Kate M., Gav, Pao, Luna, Dome, Pep, Ago, and Lisa for making summer so much fun.

Thanks to Dan, Silvia, Vitor and Alex for being not only colleagues but good friends, and for picking me up from the hospital more than once. Thanks to my colleagues Jo and Jack, Alex W., Mike, Louisa, Andi, Taryn, Seamus and Ruby; the Germans of office 302: Kathy, Isabel, Max, Julian, Jhonas and Lucy; peps from the chatty office 301: David, Cilva, Raiza, Vickie, Jo Jo, Sean and Tony.

Riley, I want to thank you for your constant and priceless support, the coffees, Pawl's photos and so many other vital distractions you provided me during the stressful writing of this thesis. Thanks.

Finally, I want to thank my all-reunited family. Mamma Rosanna and Papà Nunzio, for their constant love and support. Luca, for being back safe and always providing a bit of spice in our lives. Eleonora, for being my big sister who I can always count on. Marta, your incredible wisdom, you always know what to do. COVID-19 has kept us separate for 2 long years, I cannot wait to see you guys.

List of publications

Peer-reviewed journal articles

Tacchetto T., Reddy S.M., Bartoli O., Rickard W. D., Fougerouse D., Saxey D., Quadir Z. and Clark C. Pre-nucleation geochemical heterogeneity within glassy anatectic inclusions and the role of water in glass preservation. *Contribution to Mineralogy and Petrology* 176 (70), 2021. https://doi.org/10.1007/s00410-021-01826-0

Tacchetto T., Reddy S. M., Saxey D. W., Fougerouse D., Rickard W. D. and Clark C. Disorientation control on trace element segregation in fluid-affected low-angle boundaries in olivine. *Contributions to Mineralogy and Petrology* 176(7), 1–16, 2021. https://doi.org/10.1007/s00410-021-01815-3

Tacchetto T., Clark C., Erickson T., Reddy S.M., Bhowany K., Hand M. Weakening the lower crust: conditions, reactions and deformation. *Lithos* 422–423, 2022. https://doi.org/10.1016/j.lithos.2022.106738

Tacchetto T., Reddy S.M., Fougerouse D., Clark C., Saxey D., Rickard W. D. Crystal plasticity enhances trace element mobility in garnet. *Geology* (2022). https://doi.org/10.1130/G50283.1

Other relevant co-authored publications

Marsden R., Danišík M., Schmitt A.K., Rankenburg K., Guillong M., Ahn U., Kirkland K., Evans N., Bachmann O., **Tacchetto T.**, McDonald B., Olierook U. SS14-28: An Age Reference Material for Zircon U-Th Disequilibrium Dating, *Geostandards and Geoanalytical Research,* (2021).

Cesare B., Parisatto M., Mancini L., Peruzzo L., Franceschi M., **Tacchetto T.**, Reddy S., Spiess R., Nestola F., Marone F. Mineral inclusions are not immutable: evidence from post-entrapment thermally-induced shape change of quartz in garnet. *Earth and Planetary Science Letters*, 2021.

Carvalho B., Bartoli O., Cesare B., **Tacchetto T.**, Gianola O., Ferri F., Aradi L., Szabó C. Primary CO2-bearing fluid inclusions in granulitic garnet usually do not survive. *Earth and Planetary Science Letters*, 2020.

Attribution Statements

Table i. Attribution statement table for chapter 2: Pre-nucleation geochemical heterogeneity within glassy inclusions and the role of water in glass presentation.

Ch.2	Conceptualization and Design	Data Acquisition and Method	Data processing and Visualization	Interpretation and discussion	Total contribution (%)
Co-author 1 Tommaso Tacchetto	75	65	80	65	60
Co-author 1 acknowledgement: I acknowledge that these represent my contribution to the above research output.			Signed:		
Co-author 2 Steven Reddy	10	-	10	10	10
Co-author 2 acknowledgement: I acknowledge that these represent my contribution to the above research output.			Signed:		
Co-author 3 Omar Bartoli	10	-	-	10	7
Co-author 3 acknowledgement: I acknowledge that these represent my contribution to the above research output.			Signed:		
Co-author 4 William Rickard	-	10	-	-	5
Co-author 4 acknowledgement: I acknowledge that these represent my contribution to the above research output.			Signed:		
Co-author 5 Denis Fougerouse	-	10	-	-	5
Co-author 5 acknowledgement: I acknowledge that these represent my contribution to the above research output.			Signed:		
Co-author 6 David Saxey	-	10	10	5	5
Co-author 6 acknowledgement: I acknowledge that these represent my contribution to the above research output.			Signed:		
Co-author 7 Zakaria Quadir	-	5	-	3	3
Co-author 7 acknowledgement: I acknowledge that these represent my contribution to the above research output.			Signed:		
Co-author 8 Chris Clark	5	-	-	7	5
Co-author 8 acknowledgement: I acknowledge that these represent my contribution to the above research output.			Signed:		
Total%	**100**	**100**	**100**	**100**	**100**	**100**

Table ii. Attribution statement table for chapter 3: Weakening the lower crust: conditions, reactions and deformation.

Ch.3	Conceptualization and Design	Data Acquisition and Method	Data processing and Visualization	Interpretation and discussion	Total contribution (%)
Co-author 1 Tommaso Tacchetto	15	40	50	65	50
Co-author 1 acknowledgement: I acknowledge that these represent my contribution to the above research output.			Signed:		
Co-author 2 Chris Clark	50	10	30	15	15
Co-author 2 acknowledgement: I acknowledge that these represent my contribution to the above research output.			Signed:		
Co-author 3 Timmons Erickson	10	45	10	10	17
Co-author 3 acknowledgement: I acknowledge that these represent my contribution to the above research output.			Signed:		
Co-author 4 Steven Reddy	20	-	10	10	10
Co-author 4 acknowledgement: I acknowledge that these represent my contribution to the above research output.			Signed:		
Co-author 5 Kamini Bhowany	-	5	-	-	5
Co-author 5 acknowledgement: I acknowledge that these represent my contribution to the above research output.			Signed:		
Co-author 6 Martin Hand	5	-	-	-	3
Co-author 6 acknowledgement: I acknowledge that these represent my contribution to the above research output.			Signed:		
Total%	**100**	**100**	**100**	**100**	**100**

Table iii. Attribution statement table for chapter 4: Crystal plasticity enhances trace element mobility in garnet.

Ch.4	Conceptualization and Design	Data Acquisition and Method	Data processing and Visualization	Interpretation and discussion	Total contribution (%)
Co-author 1 Tommaso Tacchetto	60	80	70	55	60
Co-author 1 acknowledgement: I acknowledge that these represent my contribution to the above research output.			Signed:		
Co-author 2 Steven Reddy	20	5	17	20	15
Co-author 2 acknowledgement: I acknowledge that these represent my contribution to the above research output.			Signed:		
Co-author 3 Denis Fougerouse	-	5	10	15	10
Co-author 3 acknowledgement: I acknowledge that these represent my contribution to the above research output.			Signed:		
Co-author 4 Chris Clark	20	-	-	5	7
Co-author 4 acknowledgement: I acknowledge that these represent my contribution to the above research output.			Signed:		
Co-author 5 David Saxey	-	5	-	-	3
Co-author 5 acknowledgement: I acknowledge that these represent my contribution to the above research output.			Signed:		
Co-author 6 William Rickard	5	5	3	5	5
Co-author 6 acknowledgement: I acknowledge that these represent my contribution to the above research output.			Signed:		
Total%	**100**	**100**	**100**	**100**	**100**

Table iv. Attribution statement table for chapter 5: Disorientation control on trace element segregation in fluid-affected low-angle boundaries in olivine.

Ch.5	Conceptualization and Design	Data Acquisition and Method	Data processing and Visualization	Interpretation and discussion	Total contribution (%)
Co-author 1 Tommaso Tacchetto	55	50	60	60	60
Co-author 1 acknowledgement: I acknowledge that these represent my contribution to the above research output.			Signed:		
Co-author 2 Steven Reddy	30	15	15	15	15
Co-author 2 acknowledgement: I acknowledge that these represent my contribution to the above research output.			Signed:		
Co-author 3 David Saxey	5	15	15	5	10
Co-author 3 acknowledgement: I acknowledge that these represent my contribution to the above research output.			Signed:		
Co-author 4 Denis Fougerouse	-	10	10	5	5
Co-author 4 acknowledgement: I acknowledge that these represent my contribution to the above research output.			Signed:		
Co-author 5 William Rickard	-	10	-	-	5
Co-author 5 acknowledgement: I acknowledge that these represent my contribution to the above research output.			Signed:		
Co-author 6 Chris Clark	10	-	-	15	10
Co-author 6 acknowledgement: I acknowledge that these represent my contribution to the above research output.			Signed:		
Total%	**100**	**100**	**100**	**100**	**100**	**100**

Contents

List of Figures

List of Tables

Chapter 1

Introduction

Est modus in rebus
(*Horace, S. 1.1, v. 106–107*)

Metamorphism (from the Greek "*meta morph"* or *"change of form"*) is the term used to describe the geological processes responsible for the mineralogical, chemical, textural and structural change of a pre-existing rock (protolith) at the solid state (Fettes & Desmond 2007). Generally, metamorphic processes are governed by variations from the equilibrium conditions under which a rock initially formed (Spear 1993). Changes responsible for metamorphism can include temperature (*T*), pressure (*P*), stress state and changes in fluid activity, triggered by the transport of rocks within the crust in response to large-scale geo dynamics.

On a fundamental level, geological processes are governed by the mechanisms occurring at the atomic scale within minerals and at the interfaces between them. For example, crystal nucleation is a fundamental process of rock formation from any solidifying liquid (e.g., magma). The phenomenon involves bonding of atoms at scales going from the angstrom to a few nanometres, leading to the formation of molecular aggregates that may evolve into macroscopic crystals and the development of polycrystalline materials (e.g., rocks) (Zhou *et al.* 2019). Similarly, metamorphic processes of mineral replacement reactions are driven, at a fundamental level, by exchanges of atoms at the contact plane between different atomic layers (Figure 1.1) (Putnis 2014). The development and application of nano-analytical techniques such as APT to the geosciences have permitted to expand our observations beyond the micrometre scale, allowing to a better understanding of such mechanisms previously challenged by the very small scale of these investigations.

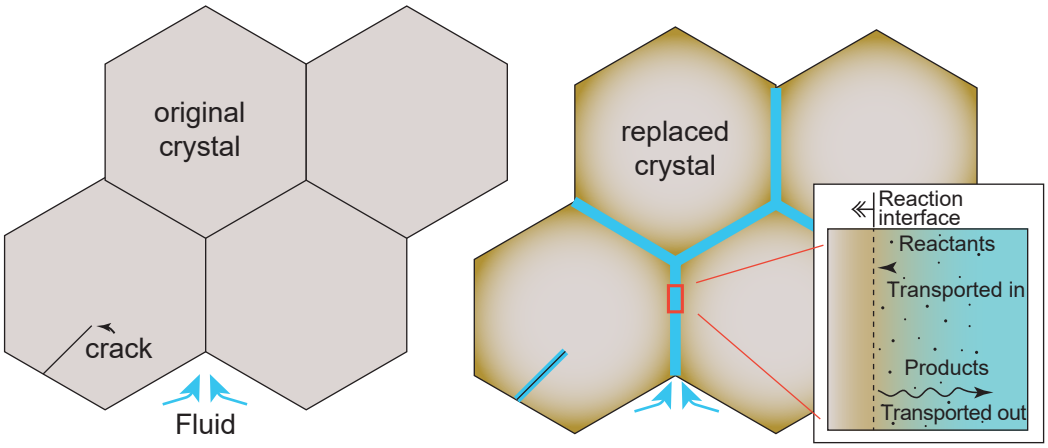

Figure 1.1. Sketch illustrating the mechanism of coupled dissolution-precipitation initiated by the infiltration of a fluid phase along initially dry grain boundaries. The reaction interface propagates from the grain boundary towards the inside of the crystal progressively replacing the parental mineral. Modified after Ague (2014).

Atom probe tomography is an advanced technique rapidly finding applications in geosciences (see Reddy *et al.* 2020 for a review). Thanks to its sub-nanometre spatial resolution combined with part-per-million elemental sensitivity (Figure 1.2) (Miller 2000), the technique has the intrinsic ability to characterize the chemistry and the structure of nanoscale features in three dimensions. Hence, APT represents a unique tool to uncover intricate information on nanoscale trace element distributions within minerals. The incorporation of APT into conventional analytical workflows has allowed new insights into processes of intracrystalline element mobility within accessory minerals (Valley *et al.* 2014; Fougerouse *et al.* 2016, 2018, 2019, 2020; Peterman *et al.* 2016, 2019, 2021; Verberne *et al.* 2019), mechanisms of element mobility during deformation (Dubosq *et al.* 2019; Fougerouse *et al.* 2021a,b; Montalvo *et al.* 2019; Piazolo *et al.* 2016; Reddy *et al.* 2016; Tacchetto *et al.* 2021a), identifying nanoscale structural features (Weber *et al.* 2016; Cao *et al.* 2019; Dubosq *et al.* 2019; Tacchetto *et al.* 2021b), and crystallographic associations of economically significant elements (Fougerouse *et al.* 2021a).

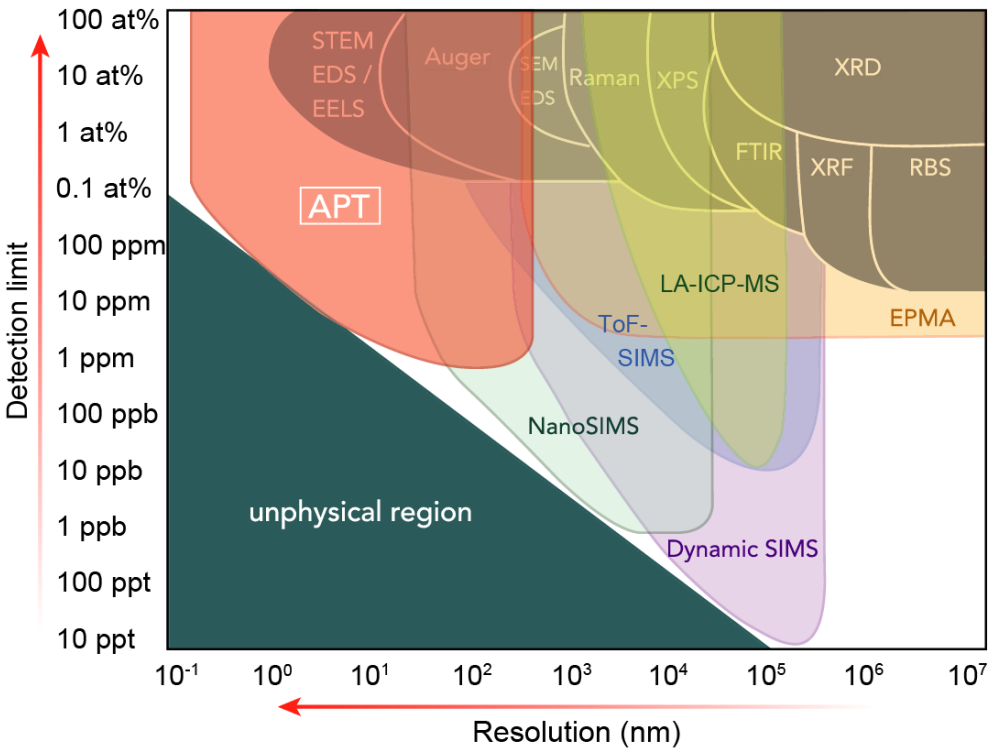

Figure 1.2 Schematic representation of the analytical sensitivity and volumetric resolution of the most common micro-analytical techniques applied in geochemistry and petrochronology. APT = Atom Probe Tomography. Modified after Reddy *et al.* (2020).

This doctoral thesis presents four micro- to nanoscale investigations of metamorphic processes taking place within lower crustal rocks affected by deformation and interactions with metamorphic fluids. The main goal of this research is to enhance our understanding of the range of processes affecting these rocks at the nanoscale through a detailed structural and geochemical analysis of rock microstructures, with a particular focus on mineral interfaces. However, to achieve this, the thesis will outline new developments in the application of atom probe tomography to minerals.

In this introduction, the concept of crustal fluids and their importance for large-scale geological dynamics will be examined first. This is followed by an overview of the composition of the lower crust and the rationale behind the selection of granulitic rocks as proxies for the study of fluid-rock interactions. As one of the two case studies, fluid inclusions in minerals are introduced, highlighting their importance as valuable tools to trace the geochemical reworking of the lithosphere. Thereafter, the role of deformation during metamorphism is discussed, followed by a geological overview aimed at setting the context for the second case study where the interplay between metamorphism, fluid and deformation is studied. To conclude, the focus of the introduction moves to the importance of mineral interfaces as a tool to unveil larger-scale geological processes.

1.1 Metamorphism and the role of crustal fluids

In addition to mass-independent variables, such as pressure and temperature, significant disequilibrium conditions can be promoted in a rock by the infiltration of externally derived fluids. Here, the term fluid is used in *sensu lato* to avoid specifying its nature or composition. Direct evidence for the presence of fluids as a free phase at depth mostly derives from studies of fluid inclusions that are found trapped within the metamorphic minerals of rocks exhumed from deep environments (Roedder 1984; Crawford & Hollister 1986; Touret 2001; Cesare *et al.* 2009; Ague 2014; Yardley & Bodnar 2014; Frezzotti & Touret 2014; Frezzotti & Ferrando 2015; Tacchetto *et al.* 2019; Carvalho *et al.* 2020). Other more indirect proofs derive from petrological observations of substantial changes in rock compositions that require the participation of fluids during their metamorphism (i.e., metasomatism) (Austrheim 1987, 2013; Carter *et al.* 1990; Klaper 1990; Rubie 1990; Ingles *et al.* 1999; Yardley 2009; Putnis & Austrheim 2010; Jamtveit *et al.* 2018a,b; Hawemann *et al.* 2019; Menegon *et al.* 2021; Putnis *et al.* 2021), geophysical data (e.g., Wannamaker 2002; Bedrosian *et al.* 2004) and theoretical models (Yardley & Valley 1997; Goncalves *et al.* 2012; Connolly & Podladchikov 2013; Manning 2013).

Crustal fluids (aqueous and/or melts) are important agents of mass and heat transfer, deeply affecting the continuous geochemical and physical reworking of the lithosphere (Brown & Rushmer 2008; Yardley 2009; Brown 2013; Yardley & Bodnar 2014; Weinberg & Hasalová 2015). Moreover, metamorphic fluids are of social relevance as they are responsible for many ore deposits formation (e.g., Kesler 2005; Yardley & Bodnar 2014). Fluids dramatically influence a variety of physical and chemical properties of geological materials such as melting temperatures, viscosities, and the density of magmas. For example, the solidus temperature of a rock might be lowered by the presence of water-rich fluids. Therefore, melting can take place at lower temperatures or metamorphic grades, with the potential to produce large volumes of melt (e.g., Yardley & Barber 1991; Winter 2014; Weinberg & Hasalová 2015). In subduction environments, aqueous fluids generated by the dehydrating oceanic crust migrate upwards metasomatizing the mantle wedge (Kerrick & Connolly 2001). The presence of fluid triggers partial melting and promotes the consequent extraction, and migration of magma towards shallower crustal levels. The interaction of these melts with the surrounding rocks promote crustal reworking and the chemical differentiation of the lithosphere (Figure 1.3) (Sawyer *et al.* 2011; Brown 2013; Klemd 2013).

The introduction of water-rich fluids into rocks strongly modifies the nature and the extent of mass transfer processes. For example, by entering anhydrous lithologies a fluid phase will enhance rates of intergranular diffusion allowing the transport of chemical species in solution for considerable length scales, driven by chemical potentials along grain boundaries (Etheridge *et al.* 1983; Carter *et al.* 1990; Bickle *et al.* 1997; Ague 2014). Moreover, fluids act as an extremely effective catalyst by helping overcome kinetics barriers promoting the activation of metamorphic reactions such as coupled dissolution – precipitation reactions (Figure 1.1) (e.g., Rubie 1986; Putnis 2002; John & Schenk 2006; Milke *et al.* 2013; Winter 2014). When a disequilibrium fluid interacts with a crystal surface, this interaction may induce chemical reactions involving the dissolution of the parent surface and the replacement with a phase that is more thermodynamically stable (e.g., Putnis & Putnis 2007). These replacement reactions can have implications for equilibria modelling and correct estimates of pressure, temperature, and fluid compositions of the geological record (e.g., Putnis & John 2010).

In addition, it is well known that the presence of fluids greatly weakens rocks. The presence of even small traces of hydrogen within nominally anhydrous minerals drastically reduces minerals yield strength for plastic deformation (Griggs & Blacic 1965; Raleigh & Paterson 1965; Griggs 1974; Kirby & Kronenberg 1984; Tullis & Yund 1989; Kronenberg *et al.* 1990; Tullis *et al.* 1996; Post & Tullis 1998; Xu et al. 2013; Stünitz *et al.* 2017; Wang *et al.* 2020 and references therein). For instance, the rheological transition of quartz from brittle to plastic deformation is strongly depended by the activity of H_2O with strong impact for the mechanical behaviour of the lower crust (e.g., Menegon *et al.* 2011). Similarly, water controls the stability of deep continental root zones by inducing the transformation of granulites to eclogites with a dramatic loss in strength of the aggregate (Jackson *et al.* 2004; Putnis 2021). Consequently, the interaction of fluids with rocks plays a fundamental role in determining if, and how, a rock deforms thereby affecting large scale rheological behaviour as well as mechanical and physical parameters on a grain scale.

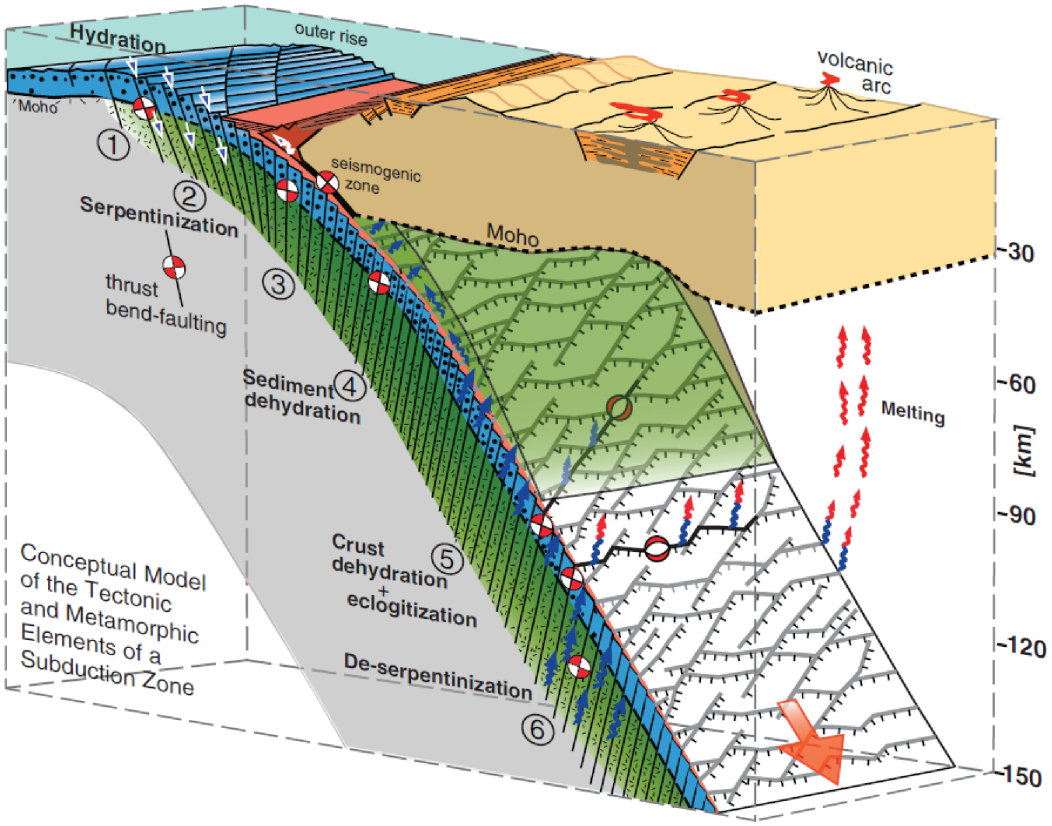

Figure 1.3 Simplified representation of the structure and metamorphism of an evolving subducting lithosphere. The liberation of fluids from the subducting slab promotes partial melting of the mantle wedge. Modified after Bebout *et al.* (2018).

1.2 Granulites as proxies for deep crustal processes

The modern lower continental crust is mainly composed of lithologically-heterogenous granulite facies metamorphic rocks, occurring on a regional scale in many continental shields (Figure 1.4) (Rudnick & Fountain 1995; Touret *et al.* 2016). Predominantly composed of anhydrous mineral assemblage such as quartz, pyroxenes, K-feldspar and quartz, the origin of granulite facies terranes is debated, but in a simplified vision, three mechanisms have been proposed. Granulites can be the final product or "residuum" of the differentiation occurring following the partial melting (anatexis) of pelitic protoliths driven by high-temperature metamorphism and migmatites formation (Phillips 1981; Clemens 1990; Vielzeuf *et al.* 1990; Cesare & Maineri 1999; Perchuk *et al.* 2000; Brown 2006; Brown 2007; Sawyer *et al.* 2011). Once the melt is formed, the H_2O content of the rock tends to be partitioned into the melt phase (i.e., leucosome) (Touret & Dietvorst 1983; Shen & Kepplert 1997). The subsequent melt extraction results in the formation of a water-undersaturated

rock composition at subsolidus conditions. Secondly, during crustal thickening, the burial of pre-existing water-poor magmatic bodies might lead to the formation of rocks of granulitic composition (Lamb & Valley 1984). Lastly, dehydration reactions can be activated due to the influx of CO_2 or NaCl-rich fluids from external sources into an igneous precursor (Newton 1980; Aranovich & Newton 1997; Newton *et al.* 1998, 2014; Touret & Huizenga 2011; Harlov 2012; Safonov & Aranovich 2014). Consequently, the investigation of mineral assemblages and reaction textures in granulitic rocks are extensively used as tools to delineate *P–T* paths of deep-buried rocks (Spear 1993), tracers for crustal fluids compositions (Yardley 2009), investigate dynamics of melt crystallization and deep crust-mantle interaction processes (Sawyer *et al.* 2011).

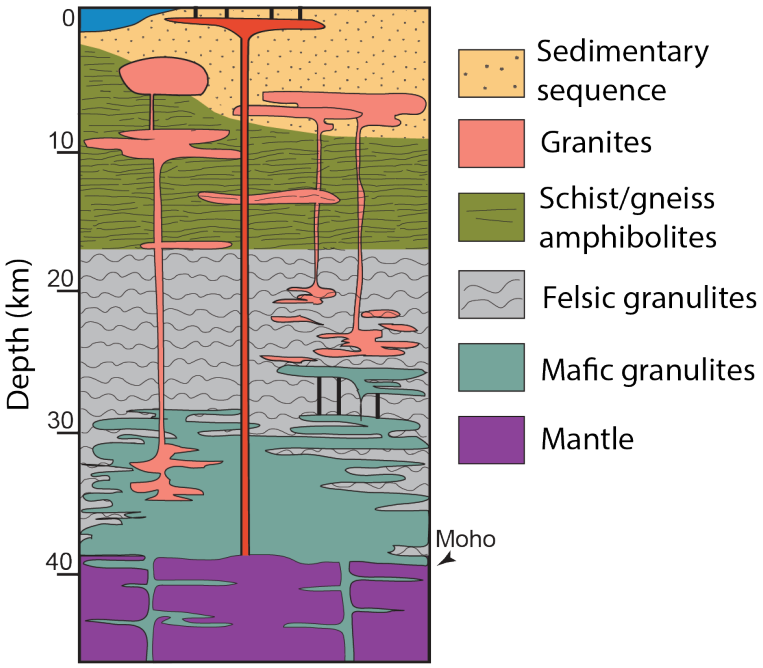

Figure 1.4 Schematic illustration approximating the chemical stratification of the modern lithosphere and the vertical differentiation generated by melt upwelling towards shallower crustal levels. Modified after Hawkesworth *et al.* (2016).

On the other hand, an important consideration is that, in the absence of infiltration by an external fluid, the granulite mineral assemblage will be preserved with no significant retrogression during its residence at lower crustal levels and return to the near-surface at conditions beyond its thermodynamic stability field, and in effect, becoming metastable (White & Powell 2002; Austrheim 2013; Jamtveit *et al.* 2016; Putnis *et al.* 2021). However, if a hydrous fluid is added, the transformation from granulite to eclogite (or amphibolite) is

kinetically favourable and takes place rapidly with a significant impact on the strength of the rock (Jackson *et al.* 2004; Jamtveit & Austrheim 2010; Jamtveit *et al.* 2016).

In light of these observations, granulite-facies rocks represent a window into the Earth's deep mechanisms as they can store evidence of their complex history of transformation and metasomatism. Therefore, granulite rocks are an excellent proxy for the study of fluid-interaction processes and crustal evolution. Unfortunately, independently of the geodynamic context of their formation, granulite rocks can spend a long period of geological time at deep crustal levels. Before being exhumed on the surface, effects, and underlying mechanisms of fluid-rock interactions, as well as their rates, are commonly erased by slow cooling and recrystallization during the later stages of metamorphism or exhumation. However, valuable examples of pristine or partially preserved examples of such manifestations reported in the literature comprise both fluid/melt inclusions trapped within peritectic minerals of granulites, and exposed root zones preserving deep metasomatic reactions. In the following sections, each of these case studies is discussed in more detail.

1.3 Melt inclusions as a record of deep crustal chemical evolution

Anatexis is the main process responsible for the formation of crustal-derived magmas (Brown 2007). During extraction and migration of melts from deeper levels, there is a continuous process of fractionation until the evolved melt completely crystallizes. Although the geochemical signature of crustal reworking is well known from studies of exposed leucosomes (Sawyer 1987; Solar & Brown 2001), obtaining information about the primary melt composition is crucial to determining how crustal differentiation occurs. Moreover, conditions and dynamics of melting are strongly controlled by fluid regimes, and much debate is ongoing on the role that fluids play during crustal melting processes (Stevens & Clemens 1993; Weinberg & Hasalová 2015). In this scenario, fluid and melt inclusions trapped in minerals have been shown to represent an important petrological tool to extrapolate information on the evolution of their host (Roedder 1984; Bodnar 2003; Goldstein 2003; Webster *et al.* 2006).

In recent years, there has been a focus on the investigation of anatectic fluid (mainly CO_2) and melt inclusions (glassy or nanogranitoids; Cesare *et al.* 2009, 2015) in metamorphic lower crustal rocks (Figure 1.5) (Acosta-Vigil *et al.* 2010; Bartoli *et al.* 2013, 2016; Cesare *et al.* 2015; Ferrero *et al.* 2016; Tacchetto *et al.* 2019; Gianola *et al.* 2020; Carvalho *et al.* 2020). As

it will be discussed in more detail in *Chapter* 2 these inclusions are important not only because they contain preserved droplets of anatectic melt or fluids that coexisted during the formation of the host rock (Cesare *et al.* 2015), but also because they permit direct compositional analyses of deep continental fluids otherwise lost or modified during later metamorphism (Ferrero *et al.* 2012, 2016, 2018; Bartoli *et al.* 2013; Ferrero & Angel 2018; Tacchetto *et al.* 2019; Bartoli 2020; Gianola *et al.* 2020; Carvalho *et al.* 2020; Bartoli & Cesare 2020; Nicoli & Ferrero 2021; Nicoli *et al.* 2022). However, some aspects remain unexplored, such as: (1) what drives the crystallization of anatectic glass inclusions in a closed melt-host system? (2) what is the role of the post-entrapment nanoscale distribution of elements in enhancing crystallization? (3) to what extent does the trapped fluid interact with the surrounding host and, in turn, how valuable is the compositional signature of these inclusions in geological timescales?

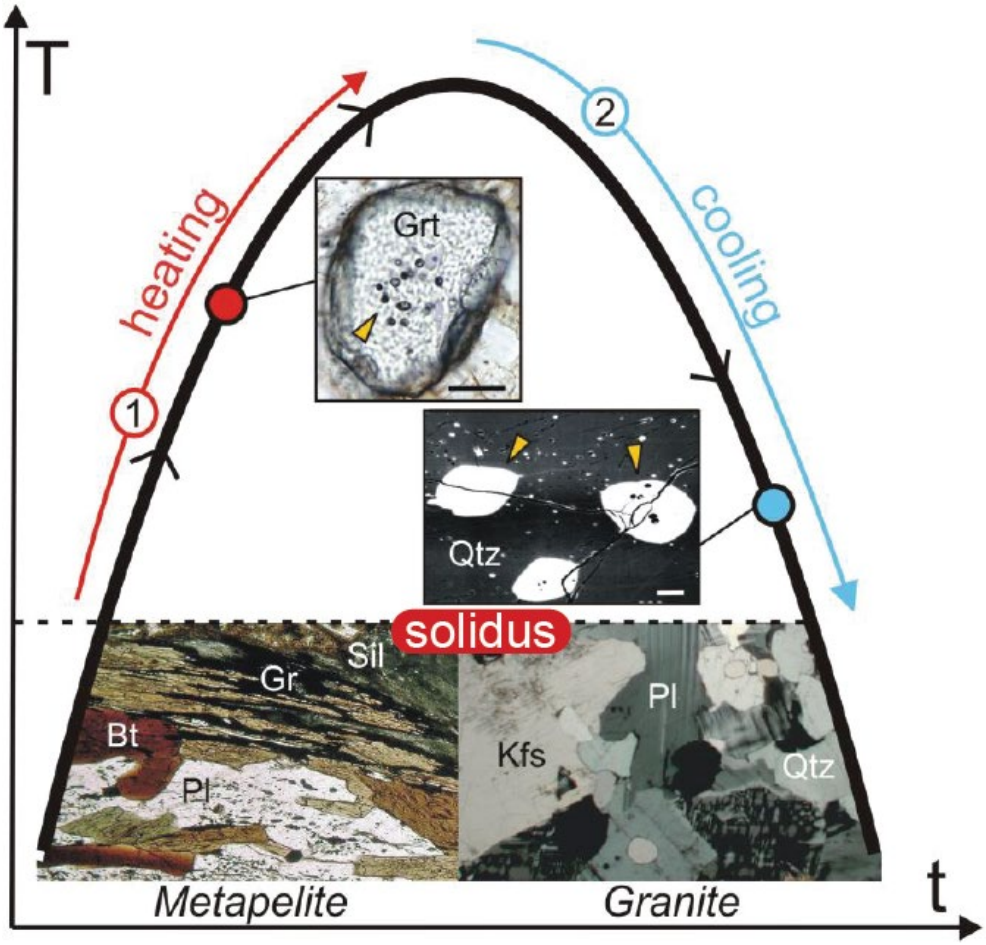

Figure 1.5 Schematic P-t diagram showing the differences between melt inclusions trapped upon heating following incongruent reactions (1) and during magma crystallization (2). Modified after Bartoli (2020).

Generally, the lack of data to address these questions derives from the challenge in analysing these inclusions. Fluid inclusions are commonly small (< 50 μm), and the phases

that crystallized within them, if present, may be only a few microns. This range of dimensions is therefore below analytical volume for most conventional analytical instruments (Figure 1.1). *Chapter 2* demonstrates how the application of modern, high-resolution techniques like transmission electron microscopy and atom probe tomography, allow derivation of previously unidentified mechanisms of melt-rock interactions and dynamics of crystallization.

1.4 The influence of deformation in enhancing fluid-rock interactions

Within the Earth's interior, rocks are continually subject to stress fields, commonly generated by large scale geological dynamics. These stresses drive deformation, and deformation promotes structural and metamorphic transformations of rocks (e.g., Rubie 1983; Brodie & Rutter 1985; Rutter & Brodie 1995; Hobbs *et al.* 2010). For example, deformation is the main responsible for the decrease of grain size of rocks at the solid state. Grain size reduction is a particular characteristic of the deformation mechanisms of shearing and mylonitization which can occur on a wide range of metamorphic regimes and rock compositions in response to stress perturbations (e.g., Poirier 1980; Rutter & Brodie 1988; Bestmann & Prior 2003; Passchier & Trouw 2005; Fitz Gerald *et al.* 2006; Warren & Hirth 2006). The reduction in grain size has major implications for the rheological behaviour of rocks as it effectively decreases diffusive pathlengths between grains. This, in turn, can lead to a decrease in the importance of grain size-insensitive processes (e.g., dislocation creep) promoting deformation by grain size-sensitive accommodated deformation (e.g., Bestmann & Prior 2003). On the other hand, extreme localization of strain associated with seismic faulting can promote melting (i.e., frictional melting) and pseudotachylyte formation (Wallace *et al.* 2019). The presence of melted material may contribute to dynamic weakening facilitating sliding along the fault core (i.e., frictional melting lubrification; Di Toro *et al.* 2011; Toro *et al.* 2021).

Rock rheology varies as a function of a number of constitutive factors, such as mineralogy and grain size, and from environmental controls such as pressure, temperature, differential stress and availability of fluids (Passchier & Trouw 2005). Brittle processes of faulting and cataclasis are expected to control rock strength at low pressure and temperature conditions found in the shallower layers of the crust, particularly at high strain rates (Brace & Kohlstedt 1980; Kirby 1980; Jackson *et al.* 2008). Nevertheless, examples of brittle failure

associated with deep crustal earthquakes are not uncommon in the literature (e.g., Austrheim & Boundy 1994; Austrheim *et al.* 1996, 2017; Prieto *et al.* 2013; Scambelluri *et al.* 2017; Jamtveit *et al.* 2019; Hawemann *et al.* 2019; Papa *et al.* 2020 and references therein). With the increase of the metamorphic grade, generally coincident with greater depths, increased temperature promotes strain accommodation in the ductile regime by deformation mechanisms such as diffusion and dislocation creep (Passchier & Trouw 2005). In detail, diffusion creep is characterized by the diffusion of vacancies throughout the crystal lattice (Nabarro-Herring creep; Herring 1950) or by the diffusion along grain boundaries (Coble creep; Coble 1963) (Figure 1.6). Vacancy diffusion occurs by mechanisms of vacancy-atom exchange where crystal boundaries serve as sink and source of vacancies in response to the applied stress (Figure 1.6) (Mesarovic 2017). During dislocation creep, the migration of dislocations across the crystal lattice is involved, accommodated by glide and climb mechanisms (Figure 1.6) (Weertman 1970). In the lithosphere, the natural expression of strain accommodated by ductile mechanisms is given by shear zones (Mukherjee & Mulchrone 2015; Fossen & Cavalcante 2017).

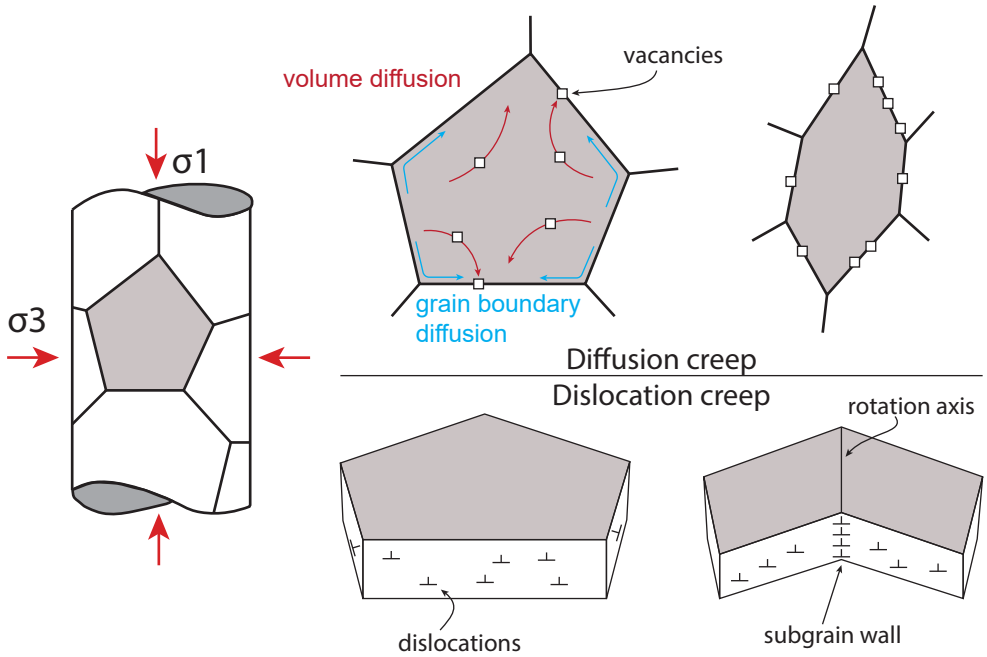

Figure 1.6 Schematic model showing the theoretical mechanisms of diffusion and dislocation creep. Nabarro-Herring creep is characterized by movement of vacancies throughout the crystal lattice (red). Coble-creep involves the diffusion of vacancies along the grain boundaries (blue). During dislocation creep the migration of dislocations into subgrain walls leads to a gradual bending around a specific rotation axis. With increasing strain, the nature of the boundary wall changes with increasing input of dislocations.

On the other hand, deformation enhances the permeability of the rock and in turn promotes the influx of fluids (e.g., Carter *et al.* 1990; Stewart *et al.* 2000; Mancktelow &

Pennacchioni 2004, 2005; Getsinger *et al.* 2013; Austrheim 2013; Menegon *et al.* 2015). As discussed in section *1.1*, the involvement of a fluid phase during metamorphism has significant implications for crustal environments. Similarly, the presence of fluids during deformation and metamorphism can have drastic weakening consequences. For example, "water" facilitates the activation of creep mechanism with impacts on fabric development (Figure 1.7) (Jung & Karato 2001; Rybacki & Dresen 2004; Jung *et al.* 2006; Bürgmann & Dresen 2008). Similarly, changes in the strengths of slip systems can be affected by water fugacity, with implications for the dominant slip system accommodating stress (Jung *et al.* 2006, 2013; Wallis *et al.* 2019; Wang *et al.* 2020).

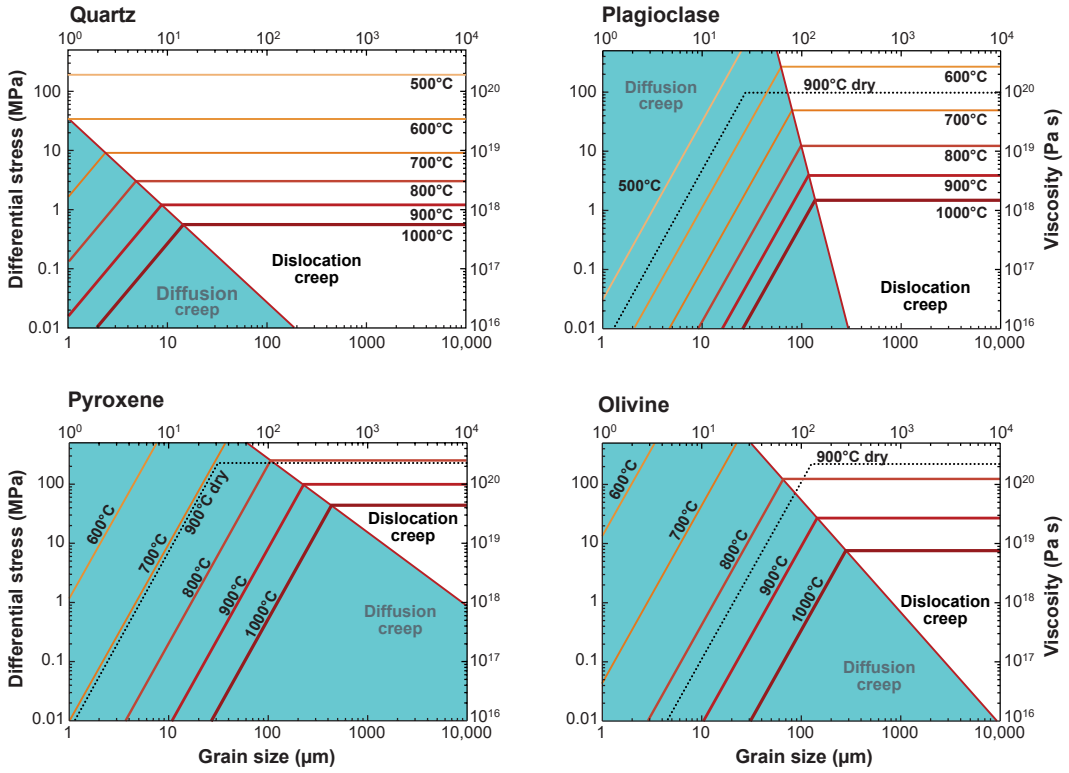

Figure 1.7 Deformation mechanisms maps for water wet rheologies of quartz, plagioclase, pyroxene, and olivine. Except for quartz, diffusion-controlled creep dominates in rocks with grain size smaller than ~ 200 μm at temperature between 500 and 900 °C. Modified after Bürgmann & Dresen (2008).

The intimate interplay between metamorphism, deformation and fluid-infiltration is expressed in shear zones of nominally anhydrous rock, such as granulites. The replacement of strong anhydrous mineral assemblages, with typically weaker OH-bearing minerals following the infiltration of externally-derived fluid, initiates reaction softening mechanisms leading to strain localization, deformation and shear zone development (White & Knipe 1978; Carter *et al.* 1990; Klaper 1990; Rubie 1990; Ingles *et al.* 1999; Stünitz & Tullis 2001;

Gueydan *et al.* 2003; Oliot *et al.* 2010; Hawemann *et al.* 2019). Metasomatic shear zones are therefore natural expressions where the complex interaction between deformation and metamorphism during syn-deformational fluid infiltration may be investigated for a better understanding of their effects on the rheological behaviour and material transport within the Earth's crust.

1.5 Deep, preserved reactions of the Bergen Arcs (SW Norway)

The Bergen Arcs is a series of arcuate Caledonian thrust sheets, which include the Lindås Nappe (SW Norway) (Figure 1.8). The Lindås Nappe outcrops over 200 km^2 of Neoproterozoic granulitic basement, comprising a minor proportion of gabbroic components, mangerites, charnockites and ultramafic lenses (Griffin 1972; Austrheim & Griffin 1985; Austrheim 2013). During the Caledonian orogeny, vast parts of the Lindås Nappe were affected by a process of deformation coupled by fluid-infiltration along fractures and shear zones which lead to the transformation of the granulites to eclogite and amphibolite (Figure 1.8) (Austrheim & Griffin 1985; Austrheim 1987; Jamtveit *et al.* 1990; Boundy *et al.* 1992; Camacho *et al.* 2005). This interpretation is founded in both the appearance of a hydrous high-pressure mineral assemblage (garnet + omphacite + kyanite + zoisite + phengite) and the presence of pseudotachylytes that were recrystallized at eclogitic conditions (Figure 1.8) (ca. 60 km depth; Austrheim & Boundy 1994; Bhowany *et al.* 2018; Jamtveit *et al.* 2019). These brittle structures acted as preferential channels for fluid infiltration (Austrheim & Boundy 1994). Importantly, not all of the granulite-facies rocks have been transformed, indicating that reaction progress was potentially limited to the availability of hydrous fluids coming from an external source (Bhowany *et al.* 2018). Therefore, the Lindås Nappe represents an outstanding, well-studied example of exposed lower continental crust.

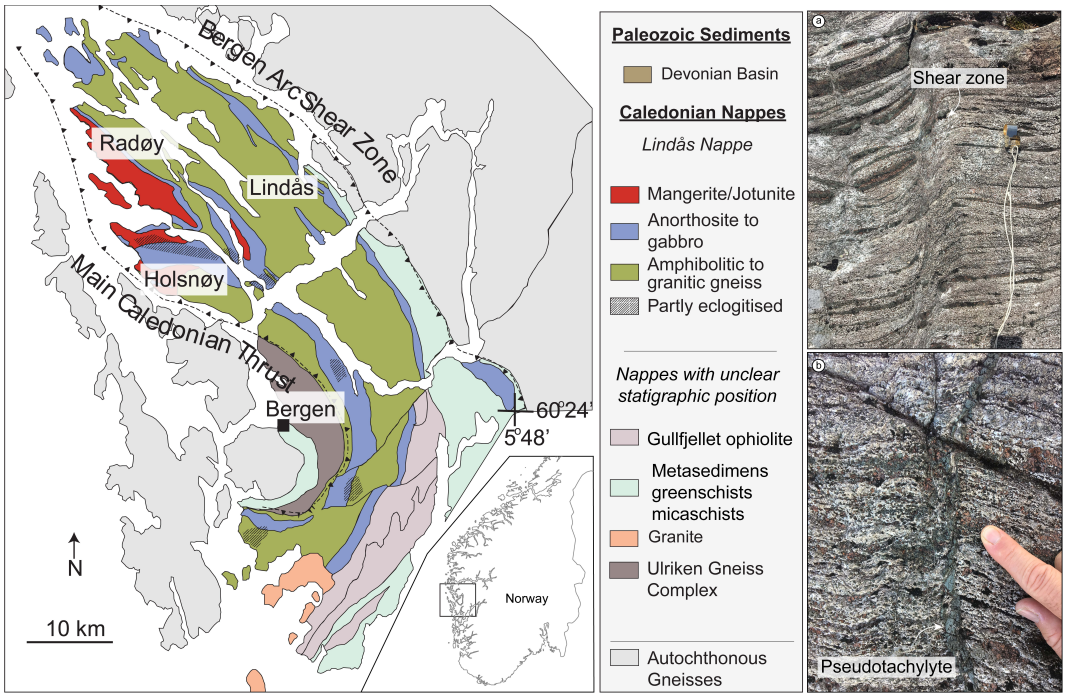

Figure 1.8 Geological map of the Bergen Arcs showing the main lithologies and structures. Modified after Mukai *et al.* (2014). Outcrop photographs displaying the occurrence of a amphibolite-eclogite ductile shear zone (a) and pseudotachylyte (b) within partially retrogressed granulites.

Numerous studies have been conducted in the Lindås Nappe, to assess the complex metasomatic history of these rocks (e.g., Austrheim & Griffin 1985; Austrheim 1987, 2013; Klaper 1990; Jamtveit *et al.* 2000, 2018a,b, 2019, 2021; Mukai *et al.* 2014; Austrheim *et al.* 2017; Putnis *et al.* 2017, 2021; Bhowany *et al.* 2018; Moore *et al.* 2019; Putnis 2021 and references therein). To date, the discussion has primarily focused on the petrological conditions and rheological implications of the transformation of these rocks as well as the consequences that these processes have on broader-scale geodynamic processes, such as deep seismicity (Jackson *et al.* 2004; Austrheim 2013; Putnis *et al.* 2017; Jamtveit *et al.* 2018a, 2019). However, little attention has been given to the analysis of deformation microstructures in revealing the progressive evolution of shear zones exposed in the area. The discussion of *Chapter 3* deals with the importance of extending the observation to important mechanisms operating during metasomatic transformations.

1.6 The importance of resolving mineral interfaces

Fundamentally, metamorphic and metasomatic processes are dominated by reactions that are associated with mechanisms occurring at the nanoscale between grains of the rock (e.g., Figure 1.1). Rocks are polycrystalline aggregates in which individual grains are separated one each other by planar interfaces (Figure 1.9). These interfaces may comprise phase boundaries, which separate two different phases, and grain boundaries, where the interface separates two grains of the same mineral phase. Here, the term grain boundary is used in *sensu lato* without specifying the nature of the interface. Although only a few nanometres wide, these interfaces affect a large number of physical, mechanical and rheological properties of rocks. For example, diffusion rates along grain boundaries can be up to four orders of magnitude faster than volume diffusion (Joesten 1991; Dohmen & Milke 2010). During deformation, the density and composition of grain boundaries strongly influence the rheology of the rocks by favouring the activation of different mechanisms of accommodating strain (e.g., Watanabe 1985; Aust *et al.* 1994). For example, during deformation, grain boundaries can act as a preferential environment for the segregation of incompatible elements promoted by intracrystalline mechanisms of re-equilibration (Figure 1.9) (Watanabe 1985; Wirth 1996; Priester 2013; Marquardt *et al.* 2015; Piazolo *et al.* 2016; Marquardt & Faul 2018; Fougerouse *et al.* 2019, 2021a; Tacchetto *et al.* 2021a; Verberne *et al.* 2022 and references therein). Variation of the interface chemistry affects the energy of the interface which in turn controls the grain size, with strong implications for the rheological behaviour of the aggregate (Watanabe 1985; Hiraga *et al.* 2007; Priester 2013). Mechanisms of trace element segregation to mineral interfaces will be discussed in more detail in *Chapters 4* and *5*.

Importantly for this research, grain boundaries represent the very first point of entry for fluids into dry rocks (e.g., Putnis & John 2010; Kruhl *et al.* 2013; Etschmann *et al.* 2014; Kirkland *et al.* 2018; Fougerouse *et al.* 2019; Tacchetto *et al.* 2021a). The distribution of fluids at grain boundaries has the potential to decrease the strengths in dislocation and diffusion creep regimens (Mei & Kohlstedt 2000), as well as enhance diffusion processes favouring elemental transport. Moreover, in the presence of a fluid phase, ductile deformation can be accommodated by stress-driven mass transfer creep such as pressure-solution. This process may lead to important compositional variations of the mineral assemblage with implications for the strength of the rock (Elliott 1973; Rutter 1983; Wintsch & Yi 2002; Menegon *et al.* 2008; Putnis & John 2010; Gratier *et al.* 2013; Wassmann & Stöckhert 2013; Mukai *et al.* 2014; Giuntoli *et al.* 2018; Moore *et al.* 2021)

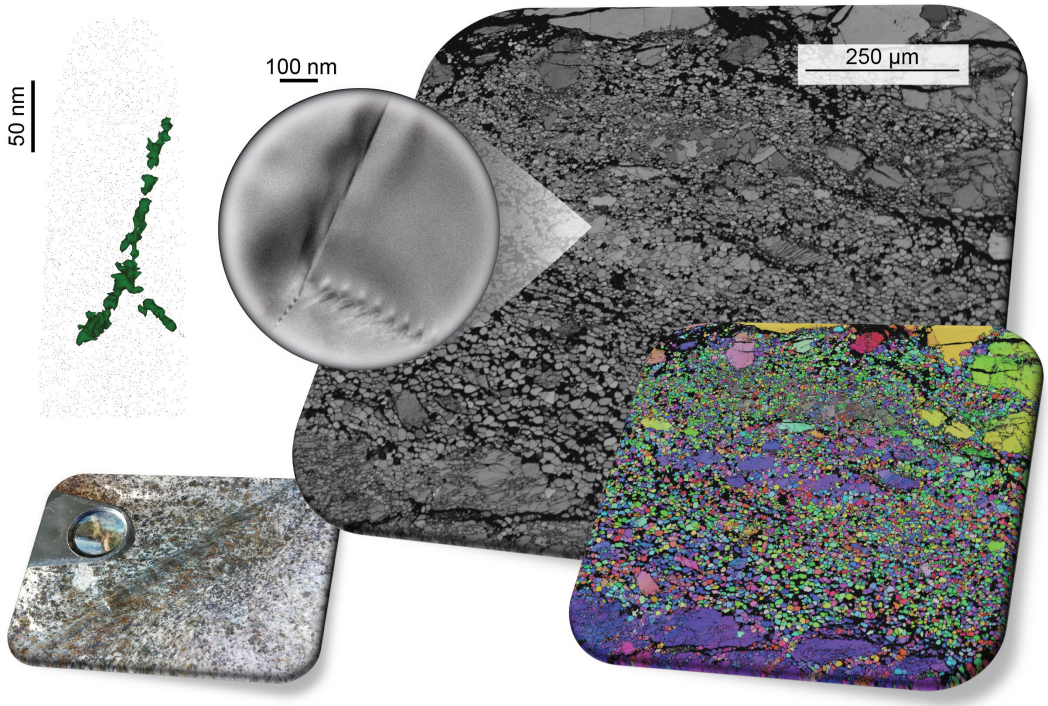

Figure 1.9 Multiscale close-up illustrating the importance of resolving mineral interfaces. From left bottom corner outcrop photograph of a shear zone. EBSD orientation contrast map and IPF-x plot of the shear zone observed in thin section. TEM image showing a grain boundary interface. APT reconstructed dataset revealing the presence of trace elements segregated at the interface indicated in the TEM image. The green isosurface highlights the planar region of the APT specimen where the enrichment of trace elements is localised.

Large-scale geological dynamics are therefore fundamentally affected by interfaces properties, and ultimately by nanoscale mechanisms and elemental distribution at the mineral-(fluid)-mineral interface (e.g., Putnis 2014). Grain-scale microstructures formed during deformation processes are widely used to reconstruct the history of metamorphic rocks (Passchier & Trouw 2005; Winter 2014). However, how these processes are manifested at the nanoscale remains substantially unexplored. As discussed in the introductory section, thanks to advances in micro-analytical techniques, it is now accessible to resolve these questions. In *Chapters 4* and *5*, deformation-induced microstructures developed in different rheological regimes and minerals are investigated. The aim of these two studies is to evaluate the impact of deformation on the nanoscale mobility of trace elements and their link to larger-scale geological implications.

1.7 Analytical workflow

In this thesis, the characterization of mineral interfaces is undertaken by a multiscale analytical approach involving a range of scales from metre-scale petrographic evaluation down to sub-nanometre observations. The workflow comprises a systematic combination of both conventional microanalytical techniques correlated to the application of site-specific analyses by atom probe tomography.

Preliminary petrographic and microstructural characterizations of samples textures are undertaken by optical and scanning electron microscopy (SEM) observations. Imaging of the microstructures is then followed by compositional analyses carried out by energy-dispersive X-ray (EDS), time-of-flight secondary ion mass spectrometer (ToF-SIMS), Tescan Integrated Mineral Analyzer (TIMA) and Laser Ablation ICPMS to obtain major and trace elements compositional information. Electron backscatter diffraction (EBSD) mapping and transmission electron microscopy (TEM) are used to obtain micro- to nano-structural analysis of the samples, also allowing the evaluation of orientation relationships within grains of the sample. These data represent a key step to identifying regions of interest for site-specific targeting by atom probe tomography. Samples for TEM and APT investigations are prepared by using focused-ion-beam (FIB)-SEM technique. Additional details of the methodology and specifics on the acquisition conditions utilized to address different aspects of this project are extensively indicated in their respective chapters.

1.8 Introducing Atom Probe Tomography

The technological progress in microanalyses has permitted a better understanding of processes and agents of metasomatism in the Earth's deep crust and upper mantle (Coltorti & Grégoire 2008). Above all, atom probe tomography permits the investigation and quantification of compositional variations in specifically-targeted specimens with sub-nanometre resolution (Larson *et al.* 2013). APT is a point-projection microscope that combines spatial information obtained from position-sensitive detection of field-evaporated ions with time-of-flight mass spectrometry to provide 3D chemical and isotopic information of the studied specimen (Figure 1.10). In this case, the analytical material is represented by a needle-shaped sample, with a tip radius generally smaller than 50nm. This particular shape, combined with the very small dimensions of the specimen, is key to promote field

evaporation of atoms under the application of a strong electrical field. The introduction of laser-assisted atom probe helped overcome the problematics of field evaporation of non-conductive materials and doing so, opened the possibility to study geological materials at the sub-manometer size scale (Kelly & Miller 2007; Larson *et al.* 2013; Reddy *et al.* 2020). By means of a local electrode, a high-electrical field is generated at the tip of the specimen, and a laser pulse is used to initiate and control thermally-assisted field-evaporation of ions. Field evaporated ions and charged molecular species are accelerated towards a position-sensitive detector and the time between laser pulse and ion detection can be used to identify the mass-to-charge ratio of the evaporated ion. The coordinates of where the ion hits the detector, coupled with the order of evaporation, are used to reconstruct the position of the ion within the sample (Figure 1.10). APT is the only technique that combines sub-nanometre spatial resolution, high chemical sensitivity, and isotopic resolution. It is therefore highly suited to the study of trace element distribution around defects in minerals, such as dislocations and low-angle boundaries. Details of the APT technique can be found in a number of publications (Kelly & Miller 2007; Gault *et al.* 2012, 2021; Larson *et al.* 2013; Miller & Forbes 2014; Kelly 2017; Reddy *et al.* 2020) and the advantages and recommendations on the use of APT will be further discussed in *Chapter 6*.

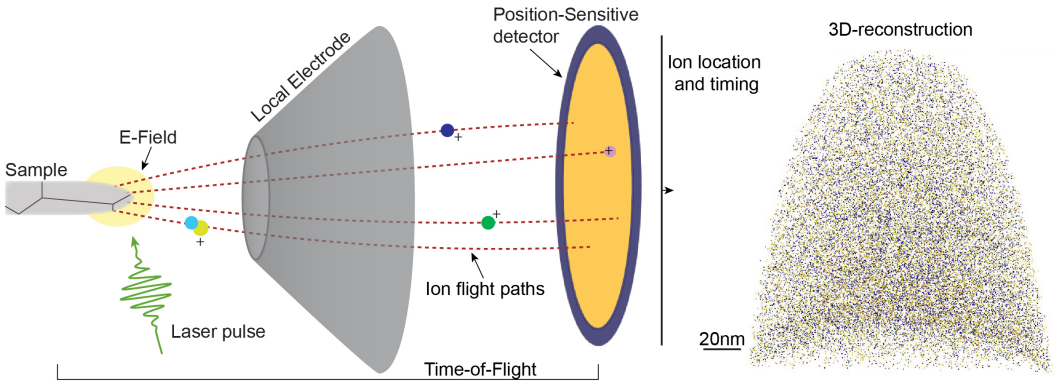

Figure 1.10 Schematic diagram of APT. The spatial coordinates obtained from the sensitive detector are combined with timing information to reconstruct the original atomic structure of the analysed sample in three-dimensions. The image is not in scale.

1.9 Research Objectives

Processes and mechanisms occurring at the nanoscale within rocks are fundamental aspects of metamorphism. However, because of the very small scale of investigation required, a variety of these manifestations remains largely unexplored. APT offers the

opportunity to investigate the nanoscale manifestation and expand our understanding of the fundamentals of rocks transformation. The primary goal of this research is to develop a detailed geochemical and structural understanding of deep crustal metamorphic prosses and their relationships with continental fluids at the nanoscale, by the application of a suite of cutting-edge analytical techniques, including EBSD, TEM and APT. With the acquired data, this research aims to:

a) Establish the dynamics of crystallization and trace element mobility within anatectic melt inclusions trapped in peritectic minerals and thereby determine their validity as a tool for crustal anatexis studies;
b) Characterise the impact of fluid infiltration to grain scale mechanisms which can promote the rheological weakening of a dry and robust lower crust;
c) Evaluate the impact of deformation on trace element mobility in fundamental minerals of the lower crustal and upper mantle thereby contributing to a better understanding of larger-scale mass transfer processes.

By doing so, this research ultimately aims to enhance the understanding of the metasomatic processes taking place within Earth's lower crust and deliver new workflows of investigation for the Earth science community.

1.10 Thesis structure

This thesis is presented as a series of published papers to peer-reviewed journals. The structure reflects the research topics outlined in the introduction and each chapter addresses specific aspects of fluid-rock interaction arranged on a basis of the increasing complexity of the investigations. Due to the compositive nature of this thesis, there are some inevitable repetitions, mostly regarding the applied methodology and the geological setting. Supplementary information for each chapter is provided in the appendix at the end of the thesis. In detail:

Chapter 2. **Pre-nucleation geochemical heterogeneity within glassy anatectic inclusions and the role of water in glass preservation**.

The focus of this chapter is the analysis of glassy melt inclusions found in peritectic garnets of a migmatite from the Spanish Betic Cordillera (southern Spain). This chapter

provides an evaluation of the distribution of trace elements within a trapped melt and at the interface with its host by a combined application of time-of-flight secondary ion mass spectrometry, transmission electron microscopy and atom probe tomography. By focusing on a simpler undeformed and closed system, the aim of this study is to determine whether the application of nanoscale investigations can reveal unobserved fluid-rock interaction mechanisms. The geochemical information obtained offer a more comprehensive understanding of the dynamics of crystallization, post-entrapment evolution of melt inclusions and the role of water in enhancing melt crystallization. Moreover, this study contributed to evaluating the ability of APT in resolving complex phase boundaries in geological material and the identifications of 3D-reconstruction artefacts.

Chapter 3. **Weakening the lower crust: conditions, reactions and deformation**.

With this chapter, deformation, and its relationship with fluid-rock interactions is introduced. The study uses a multiscale structural, geochemical, and thermobaric analysis across a shear zone/wall-rock interface exposed on the island of Radøy in the Bergen Arcs (western Norway). The aim of the study is to assess the impact of fluid infiltration on the deformation mechanisms that facilitated the formation of the lower-crustal ductile shear zone. Here, a systematic stepwise application of EBSD provides a detailed map of the evolution of the deformation microstructures for multiple minerals at increasing interaction with a fluid phase. Results of this study highlight the key role of fluid infiltration and metamorphic reactions on strain localization processes contributing to a better understanding of rheological weakening mechanisms of the lower crust. Importantly, this study helped to identify an efficient workflow for the identification of significant deformation microstructures to be analysed at the APT in the following *Chapters 4 and 5* of this thesis.

Chapter 4. **Crystal plasticity enhances trace element mobility in garnet.**

This study introduces the application of APT to the investigation of fluid-induced deformation microstructures. The research integrates a detailed microstructural analysis by EBSD with interfacial compositional analysis by APT to investigate mechanisms associated

with low-angle boundary formation within a granulitic-facies garnet of the Lindås Nappe (western Norway). The objective of this chapter is to evaluate the distribution and mobility of trace elements in garnet, a key mineral of most lower crustal lithologies (e.g., granulites, eclogites and mantle peridotites). Understanding the mobility of trace elements in garnet during deformations is crucial for its use in petro-chronological applications. In correlation with EBSD data, APT results allowed to determine the role of intracrystalline deformation in promoting both the segregation of lattice impurities and in-grain diffusion of externally derived trace elements to low-angle boundaries. The outcome of this study highlights the influence of crystal plasticity in increasing the extent of element exchange between rock-forming minerals thereby questioning the robustness of garnet geochemistry.

Chapter 5. **Disorientation control on trace element segregation in fluid-affected low-angle boundaries in olivine.**

In this study the microstructures developed within an olivine crystal of a spinel-lherzolite from the Lindås Nappe (western Norway) are investigated using EBSD and APT. This research aims to determine the relationship between low-angle boundary misorientation and trace element segregation. To do so, EBSD was used to systematically select a set of low-angle boundaries with increasing disorientation, but formed by the same slip system, for APT analyses. The distribution of trace elements at the analysed interfaces is found to increase at higher disorientation degrees, as well as the structure of the boundary evolves from intersecting to arrays of spatially distributed parallel dislocations. In addition, APT data permitted to identify fluid-derived elements infiltrated along the interfaces during deformation. These results have implications both for the rheology of the upper mantle and the mobility of trace elements along interfaces in the deep Earth.

Chapter 6. **Synthesis and thesis conclusions.**

In this conclusive chapter of the thesis, observations and key findings of each case study are brought together to evaluate and discuss the larger picture outcome of this doctoral research.

1.11 References

Acosta-Vigil, A., Buick I., Hermann J., Cesare B., Rubatto D., London D., & Morgan GB VI. 2010. Mechanisms of crustal anatexis: a geochemical study of partially melted metapelitic enclaves and host dacite, SE Spain. *Journal of Petrology 51,* 785–821.

Ague, J.J. 2014. Fluid Flow in the Deep Crust. In: *Treatise on Geochemistry*. Elsevier, 203–247. DOI 10.1016/B978-0-08-095975-7.00306-5

Aranovich L. Y. & Newton R.C. 1997. H2O activity in concentrated KCl and KCl–NaCl solutions at high temperatures and pressures measured by the brucite–periclase equilibrium. *Contributions to Mineralogy and Petrology 127,* 261–271.

Aust, K.T., Erb, U. & Palumbo, G. 1994. Interface control for resistance to intergranular cracking. *Materials Science and Engineering: A 176(1–2),* 329–334. DOI 10.1016/0921-5093(94)90995-4

Austrheim, H. & Griffin, W.L. 1985. Shear deformation and eclogite formation within granulite-facies anorthosites of the Bergen Arcs, western Norway. *Chemical Geology 50(1–3),* 267–281.

Austrheim, H., Erambert, M. & Boundy, T.M. 1996. Garnets recording deep crustal earthquakes. *Earth and Planetary Science Letters 139(1–2),* 223–238.

Austrheim, H. 1987. Eclogitization of lower crustal granulites by fluid migration through shear zones. *Earth and Planetary Science Letters 81(2–3),* 221–232. DOI 10.1016/0012-821X(87)90158-0

Austrheim, H. 2013. Fluid and deformation induced metamorphic processes around Moho beneath continent collision zones: Examples from the exposed root zone of the Caledonian mountain belt, W-Norway. *Tectonophysics 609,* 620–635. DOI 10.1016/j.tecto.2013.08.030

Austrheim, H. & Boundy, T.M. 1994. Pseudotachylytes generated during seismic faulting and eclogitization of the deep crust. *Science 265(5168),* 82–83.

Austrheim, H., Dunkel, K.G., Plümper, O., Ildefonse, B., Liu, Y. & Jamtveit, B. 2017. Fragmentation of wall rock garnets during deep crustal earthquakes. *Science Advances 3(2),* e1602067. DOI 10.1126/sciadv.1602067

Bartoli, O. 2020. Characterizing fluid and melt in high-grade metamorphic rocks. In: Lecumberri-Sanchez P, Steele-McInnis M (eds) Fluid inclusions, , Short Course Ser. *Mineral Association of Canada,* 36.

Bartoli, O. & Cesare, B. 2020. Nanorocks: a 10-year-old story. *Rendiconti Lincei. Scienze Fisiche e Naturali 31(2),* 249–257. DOI 10.1007/s12210-020-00898-7

Bartoli, O., Cesare B., Poli S., Bodnar R.J., Acosta-Vigil A., Frezzotti M.L., & Meli S. 2013. Recovering the composition of melt and the fluid regime at the onset of crustal anatexis and S-type granite formation. *Geology 41,* 115–118.

Bartoli, O., Acosta-Vigil, A., Ferrero, S. & Cesare, B. 2016. Granitoid magmas preserved as melt inclusions in high-grade metamorphic rock. *American Mineralogist 101(7),* 1543–1559. DOI 10.2138/am-2016-5541CCBYNCND

Bebout, G.E., Scholl, D.W., Stern, R.J., Wallace, L.M. & Agard, P. 2018. Twenty Years of Subduction Zone Science: Subduction Top to Bottom 2 (ST2B-2). *GSA Today,* 4–10. DOI 10.1130/GSATG354A.1

Bedrosian, P.A., Unsworth, M.J., Egbert, G.D. & Thurber, C.H. 2004. Geophysical images of the creeping segment of the San Andreas fault: implications for the role of crustal fluids in the earthquake process. *Tectonophysics 385(1–4),* 137–158. DOI 10.1016/j.tecto.2004.02.010

Bestmann, M. & Prior, D.J. 2003. Intragranular dynamic recrystallization in naturally deformed calcite marble: diffusion accommodated grain boundary sliding as a result of subgrain rotation recrystallization. *Journal of Structural Geology 25(10),* 1597–1613. DOI 10.1016/S0191-8141(03)00006-3

Bhowany, K., Hand, M., Clark, C., Kelsey, D.E., Reddy, S.M., Pearce, M.A., Tucker, N.M. & Morrissey, L.J. 2018. Phase equilibria modelling constraints on *P-T* conditions during fluid catalysed conversion of granulite to eclogite in the Bergen Arcs, Norway. *Journal of Metamorphic Geology 36(3),* 315–342. DOI 10.1111/jmg.12294

Bickle, M.J., Chapman, H.J., Ferry, J.M., Iii, D.R. & Fallick, A.E. 1997. Fluid Flow and Diffusion in the Waterville Limestone, South–Central Maine: Constraints from Strontium, Oxygen and Carbon Isotope Profiles. *Journal of Petrology 38(11),* 24.

Bodnar, R.J. 2003. Fluid inclusions: Analysis and interpretation. *Mineral Association of Canada 32,* 1–8.

Boundy, T.M., Fountain, D.M. & Austrheim, H. 1992. Structural development and petrofabrics of eclogite facies shear zones, Bergen Arcs, western Norway: implications for deep crustal deformational processes. *Journal of Metamorphic Geology 10(2),* 127–146.

Brace, W.F. & Kohlstedt, D.L. 1980. Limits on lithospheric stress imposed by laboratory experiments. *Journal of Geophysical Research: Solid Earth 85(B11),* 6248–6252. DOI 10.1029/JB085iB11p06248

Brodie, K.H. & Rutter, E.H. 1985. On the Relationship between Deformation and Metamorphism, with Special Reference to the Behavior of Basic Rocks. In: Thompson, A.B., Rubie, D.C. (eds) Metamorphic Reactions. vol 4. *Springer*, New York, NY. https://doi.org/10.1007/978-1-4612-5066-1_6.

Brown M. 2006. Melt extraction from the lower continental crust of orogens: The fi eld evidence, in Brown, M., and Rushmer, T., eds., Evolution and Differentiation of the Continental Crust: Cambridge, UK, p. 332–384. *Cambridge University Press.*

Brown, M. 2007. Crustal melting and melt extraction, ascent and emplacement in orogens: mechanisms and consequences. *Journal of the Geological Society 164(4),* 709–730.

Brown, M. 2013. Granite: From genesis to emplacement. *Geological Society of America Bulletin 125(7–8),* 1079–1113.

Brown M. & Rushmer T. 2008. Evolution and Differentiation of the Continental Crust. *Cambridge University Press.*

Bürgmann, R. & Dresen, G. 2008. Rheology of the Lower Crust and Upper Mantle: Evidence from Rock Mechanics, Geodesy, and Field Observations. *Annual Review of Earth and Planetary Sciences 36(1),* 531–567. DOI 10.1146/annurev.earth.36.031207.124326

Camacho, A., Lee, J.K.W., Hensen, B.J. & Braun, J. 2005. Short-lived orogenic cycles and the eclogitization of cold crust by spasmodic hot fluids. *Nature 435(7046),* 1191–1196. DOI 10.1038/nature03643

Cao, M., Evans, N.J., Reddy, S.M., Fougerouse, D., Hollings, P., Saxey, D.W., McInnes, B.I.A., Cooke, D.R., McDonald, B.J. & Qin, K. 2019. Micro- and nano-scale textural and compositional zonation in plagioclase at the Black Mountain porphyry Cu deposit: Implications for magmatic processes. *American Mineralogist 104(3),* 391–402. DOI 10.2138/am-2019-6609

Carter, N.L., Kronenberg, A.K., Ross, J.V. & Wiltschko, D.V. 1990. Control of fluids on deformation of rocks. *Geological Society, London, Special Publications 54(1),* 1–13. DOI 10.1144/GSL.SP.1990.054.01.01

Carvalho, B.B., Bartoli, O., Cesare, B., Tacchetto, T., Gianola, O., Ferri, F., Aradi, L.E. & Szabó, C. 2020. Primary CO2-bearing fluid inclusions in granulitic garnet usually do not survive. *Earth and Planetary Science Letters 536,* 116170. DOI 10.1016/j.epsl.2020.116170

Cesare, B. & Maineri, C. 1999. Fluid-present anatexis of metapelites at El Joyazo (SE Spain): constraints from Raman spectroscopy of graphite. *Contributions to Mineralogy and Petrology 135(1),* 41–52.

Cesare, B., Ferrero, S., Salvioli-Mariani, E., Pedron, D. & Cavallo, A. 2009. "Nanogranite" and glassy inclusions: The anatectic melt in migmatites and granulites. *Geology 37(7),* 627–630.

Cesare, B., Acosta-Vigil, A., Bartoli, O. & Ferrero, S. 2015. What can we learn from melt inclusions in migmatites and granulites? *Lithos 239,* 186–216. DOI 10.1016/j.lithos.2015.09.028

Clemens, J.D. 1990. The Granulite — Granite Connexion. In: Vielzeuf, D., Vidal, P. (eds) Granulites and Crustal Evolution. NATO ASI Series, vol 311. *Springer*, Dordrecht. https://doi.org/10.1007/978-94-009-2055-2_3.

Coble, R.L. 1963. A Model for Boundary Diffusion Controlled Creep in Polycrystalline Materials. *Journal of Applied Physics 34(6),* 1679–1682. DOI 10.1063/1.1702656

Coltorti, M. & Grégoire, M. 2008. Metasomatism in oceanic and continental lithospheric mantle: introduction. *Geological Society, London, Special Publications 293(1),* 1–9. DOI 10.1144/SP293.1

Connolly, J.A.D. & Podladchikov, Y.Y. 2013. A Hydromechanical Model for Lower Crustal Fluid Flow. In: *Metasomatism and the Chemical Transformation of Rock*. Springer Berlin Heidelberg, Berlin, Heidelberg, Lecture Notes in Earth System Sciences, 599–658. DOI 10.1007/978-3-642-28394-9_14

Crawford, M.L. & Hollister, L.S. 1986. Metamorphic Fluids: The Evidence from Fluid Inclusions. In: Walther, J.V. & Wood, B.J. (eds) *Fluid—Rock Interactions during Metamorphism*. Springer New York, New York, NY, 1–35. DOI 10.1007/978-1-4612-4896-5_1

Di Toro, G., Han, R., Hirose, T., De Paola, N., Nielsen, S., Mizoguchi, K., Ferri, F., Cocco, M. & Shimamoto, T. 2011. Fault lubrication during earthquakes. *Nature 471(7339),* 494–498. DOI 10.1038/nature09838

Dohmen, R. & Milke, R. 2010. Diffusion in Polycrystalline Materials: Grain Boundaries, Mathematical Models, and Experimental Data. *Reviews in Mineralogy and Geochemistry 72(1),* 921–970. DOI 10.2138/rmg.2010.72.21

Dubosq, R., Rogowitz, A., Schweinar, K., Gault, B. & Schneider, D.A. 2019. A 2D and 3D nanostructural study of naturally deformed pyrite: assessing the links between trace element mobility and defect structures. *Contributions to Mineralogy and Petrology 174(9),* 72. DOI 10.1007/s00410-019-1611-5

Elliott, D. 1973. Diffusion Flow Laws in Metamorphic Rocks. *GSA Bulletin* 1973;; 84 (8): 2645–2664.

Etheridge, M.A., Wall, V.J. & Vernon, R.H. 1983. The role of the fluid phase during regional metamorphism and deformation. *Journal of Metamorphic Geology 1(3),* 205–226. DOI 10.1111/j.1525-1314.1983.tb00272.x

Etschmann, B., Brugger, J., Pearce, M.A., Ta, C., Brautigan, D., Jung, M. & Pring, A. 2014. Grain boundaries as microreactors during reactive fluid flow: experimental dolomitization of a calcite marble. *Contributions to Mineralogy and Petrology 168(2),* 1045. DOI 10.1007/s00410-014-1045-z

Ferrero, S. & Angel, R.J. 2018. Micropetrology: Are Inclusions Grains of Truth? *Journal of Petrology*. DOI 10.1093/petrology/egy075

Ferrero, S., Bartoli, O., Cesare, B., Salvioli-Mariani, E., Acosta-Vigil, A., Cavallo, A., Groppo, C. & Battiston, S. 2012. Microstructures of melt inclusions in anatectic metasedimentary rocks: anatectic melt inclusions in migmatites. *Journal of Metamorphic Geology 30(3),* 303–322. DOI 10.1111/j.1525-1314.2011.00968.x

Ferrero, S., Ziemann, M.A., Angel, R.J., O'Brien, P.J. & Wunder, B. 2016. Kumdykolite, kokchetavite, and cristobalite crystallized in nanogranites from felsic granulites, Orlica-Snieznik Dome (Bohemian Massif): not evidence for ultrahigh-pressure conditions. *Contributions to Mineralogy and Petrology 171(1)*. DOI 10.1007/s00410-015-1220-x

Ferrero, S., O'Brien, P.J., Borghini, A., Wunder, B., Wälle, M., Günter, C. & Ziemann, M.A. 2018. A treasure chest full of nanogranitoids: an archive to investigate crustal melting in the Bohemian Massif. *Geological Society, London, Special Publications 478(1),* 13–38. DOI 10.1144/SP478.19

Fettes, D. & Desmond, J. 2007. Metamorphic Rocks: A Classification and Glossary of Terms. Recommendations of the International Union of Geological Sciences Subcommission on the Systematics of Metamorphic Rocks, p. 256. *Cambridge University Press*. Cambridge.

Fitz Gerald, J.D., Parsons I. & Cayzer N. 2006. Nanotunnels and pull-aparts: Defects of exsolution lamellae in alkali feldspars. *American Mineralogist 91(5–6),* 772–783. DOI 10.2138/am.2006.2029

Fossen, H. & Cavalcante, G.C.G. 2017. Shear zones – A review. *Earth-Science Reviews 171,* 434–455. DOI 10.1016/j.earscirev.2017.05.002

Fougerouse, D., Reddy, S.M., Saxey, D.W., Rickard, W.D.A., van Riessen, A. & Micklethwaite, S. 2016. Nanoscale gold clusters in arsenopyrite controlled by growth rate not concentration: Evidence from atom probe microscopy. *American Mineralogist 101(8),* 1916–1919. DOI 10.2138/am-2016-5781CCBYNCND

Fougerouse, D., Reddy, S.M., Saxey, D.W., Erickson, T.M., Kirkland, C.L., Rickard, W.D.A., Seydoux-Guillaume, A.-M., Clark, C. & Buick, I.S. 2018. Nanoscale distribution of Pb in monazite revealed by atom probe microscopy. *Chemical Geology 479,* 251–258. DOI 10.1016/j.chemgeo.2018.01.020

Fougerouse, D., Reddy, S.M., Kirkland, C.L., Saxey, D.W., Rickard, W.D. & Hough, R.M. 2019. Time-resolved, defect-hosted, trace element mobility in deformed Witwatersrand pyrite. *Geoscience Frontiers 10(1),* 55–63. DOI 10.1016/j.gsf.2018.03.010

Fougerouse, D., Kirkland, C.L., Saxey, D.W., Seydoux-Guillaume, A., Rowles, M.R., Rickard, W.D.A. & Reddy, S.M. 2020. Nanoscale Isotopic Dating of Monazite. *Geostandards and Geoanalytical Research 44(4),* 637–652. DOI 10.1111/ggr.12340

Fougerouse, D., Reddy, S.M., Aylmore, M., Yang, L., Guagliardo, P., Saxey, D.W., Rickard, W.D.A. & Timms, N. 2021a. A new kind of invisible gold in pyrite hosted in deformation-related dislocations. *Geology 49(10),* 1225–1229. DOI 10.1130/G49028.1

Fougerouse, D., Reddy, S.M., Seydoux-Guillaume, A.-M., Kirkland, C.L., Erickson, T.M., Saxey, D.W., Rickard, W.D.A., Jacob, D., Leroux, H. & Clark, C. 2021b. Mechanical twinning of monazite expels radiogenic lead. *Geology 49(4),* 417–421. DOI 10.1130/G48400.1

Frezzotti, M.L. & Ferrando, S. 2015. The chemical behavior of fluids released during deep subduction based on fluid inclusions. *American Mineralogist 100(2–3),* 352–377. DOI 10.2138/am-2015-4933

Frezzotti, M.-L. & Touret, J.L.R. 2014. CO2, carbonate-rich melts, and brines in the mantle. *Geoscience Frontiers 5(5),* 697–710. DOI 10.1016/j.gsf.2014.03.014

Gault, B., Moody, M.P., Cairney, J.M. & Ringer, S.P. 2012. Atom probe crystallography. *Materials Today 15(9),* 378–386. DOI 10.1016/S1369-7021(12)70164-5

Gault, B., Chiaramonti, A., Cojocaru-Mirédin, O., Stender, P., Dubosq, R., Freysoldt, C., Makineni, S.K., Li, T., Moody, M. & Cairney, J.M. 2021. Atom probe tomography. *Nature Reviews Methods Primers 1(1),* 51. DOI 10.1038/s43586-021-00047-w

Getsinger, A.J., Hirth, G., Stünitz, H. & Goergen, E.T. 2013. Influence of water on rheology and strain localization in the lower continental crust: Water, Rheology, and Strain Localization. *Geochemistry, Geophysics, Geosystems 14(7),* 2247–2264. DOI 10.1002/ggge.20148

Gianola, O., Bartoli, O., Ferri, F., Galli, A., Ferrero, S., Capizzi, L.S., Liebske, C., Remusat, L., Poli, S. & Cesare, B. 2020. Anatectic melt inclusions in ultra high temperature granulites. *Journal of Metamorphic Geology 39(3),* 321–342. DOI 10.1111/jmg.12567

Giuntoli, F., Menegon, L. & Warren, C.J. 2018. Replacement reactions and deformation by dissolution and precipitation processes in amphibolites Brown, M. (ed.). *Journal of Metamorphic Geology 36(9),* 1263–1286. DOI 10.1111/jmg.12445

Goldstein, R.H. 2003. Petrographic analysis of fluid inclusions. Fluid Inclusions: Analysis and Interpretation *32,* 9–53.

Goncalves, P., Oliot, E., Marquer, D. & Connolly, J.A.D. 2012. Role of chemical processes on shear zone formation: an example from the Grimsel metagranodiorite (Aar massif, Central Alps): SHEAR ZONE FORMATION. *Journal of Metamorphic Geology 30(7),* 703–722. DOI 10.1111/j.1525-1314.2012.00991.x

Gratier, J.-P., Dysthe, D.K. & Renard, F. 2013. The Role of Pressure Solution Creep in the Ductility of the Earth's Upper Crust. In: *Advances in Geophysics*. Elsevier, 47–179. DOI 10.1016/B978-0-12-380940-7.00002-0

Griffin W. L. 1972. Formation of eclogites and the coronas in anorthosites, Bergen Arcs, Norway. *Geol Soc Am Mem* 135: 37-63.

Griggs, D. 1974. A model of hydrolytic weakening in quartz. *Journal of Geophysical Research 79(11),* 1653–1661. DOI 10.1029/JB079i011p01653

Griggs, D.T. & Blacic, J.D. 1965. Quartz: Anomalous Weakness of Synthetic Crystals. *Science 147(3655),* 292–295. DOI 10.1126/science.147.3655.292

Gueydan, F., Leroy, Y.M., Jolivet, L. & Agard, P. 2003. Analysis of continental midcrustal strain localization induced by microfracturing and reaction-softening: continental midcrustal strain localization. *Journal of Geophysical Research: Solid Earth 108(B2)*. DOI 10.1029/2001JB000611

Harlov, D.E. 2012. The potential role of fluids during regional granulite-facies dehydration in the lower crust. *Geoscience Frontiers 3(6),* 813–827. DOI 10.1016/j.gsf.2012.03.007

Hawemann, F., Mancktelow, N., Wex, S., Pennacchioni, G. & Camacho, A. 2019. Fracturing and crystal plastic behaviour of garnet under seismic stress in the dry lower continental crust (Musgrave Ranges, Central Australia). *Solid Earth 10(5),* 1635–1649. DOI 10.5194/se-10-1635-2019

Hawkesworth, C.J., Cawood, P.A. & Dhuime, B. 2016. Tectonics and crustal evolution. *GSA Today 26(09),* 4–11. DOI 10.1130/GSATG272A.1

Herring, C. 1950. Diffusional Viscosity of a Polycrystalline Solid. *Journal of Applied Physics 21(5),* 437–445. DOI 10.1063/1.1699681

Hiraga, T., Hirschmann, M.M. & Kohlstedt, D.L. 2007. Equilibrium interface segregation in the diopside–forsterite system II: Applications of interface enrichment to mantle geochemistry. *Geochimica et Cosmochimica Acta 71(5),* 1281–1289. DOI 10.1016/j.gca.2006.11.020

Hobbs, B.E., Ord, A., Spalla, M.I., Gosso, G. & Zucali, M. 2010. The interaction of deformation and metamorphic reactions. *Geological Society, London, Special Publications 332(1),* 189–223. DOI 10.1144/SP332.12

Ingles, J., Lamouroux, C., Soula, J.-C., Guerrero, N. & Debat, P. 1999. Nucleation of ductile shear zones in a granodiorite under greenschist facies conditions, NeÂ ouvielle massif, Pyrenees, France. *Journal of Structural Geology,* 22.

Jackson, J., McKENZIE, D., Priestley, K. & Emmerson, B. 2008. New views on the structure and rheology of the lithosphere. *Journal of the Geological Society 165(2),* 453–465. DOI 10.1144/0016-76492007-109

Jackson, J.A., Austrheim, H., McKenzie, D. & Priestley, K. 2004. Metastability, mechanical strength, and the support of mountain belts. *Geology 32(7),* 625–628.

Jamtveit, B. & Austrheim, H. 2010. Metamorphism: The Role of Fluids. *Elements 6(3),* 153–158. DOI 10.2113/gselements.6.3.153

Jamtveit, B., Bucher-Nurminen, K. & Austrheim, H. akon. 1990. Fluid controlled eclogitization of granulites in deep crustal shear zones, Bergen arcs, Western Norway. *Contributions to Mineralogy and Petrology 104(2),* 184–193.

Jamtveit, B., Austrheim, H. akon & Malthe-Sørenssen, A. 2000. Accelerated hydration of the Earth's deep crust induced by stress perturbations. *Nature 408(6808),* 75.

Jamtveit, B., Austrheim, H. & Putnis, A. 2016. Disequilibrium metamorphism of stressed lithosphere. *Earth-Science Reviews 154,* 1–13. DOI 10.1016/j.earscirev.2015.12.002

Jamtveit, B., Ben-Zion, Y., Renard, F. & Austrheim, H. 2018a. Earthquake-induced transformation of the lower crust. *Nature 556(7702),* 487–491. DOI 10.1038/s41586-018-0045-y

Jamtveit, B., Moulas, E., Andersen, T.B., Austrheim, H., Corfu, F., Petley-Ragan, A. & Schmalholz, S.M. 2018b. High Pressure Metamorphism Caused by Fluid Induced Weakening of Deep Continental Crust. *Scientific Reports 8(1).* DOI 10.1038/s41598-018-35200-1

Jamtveit, B., Petley-Ragan, A., Incel, S., Dunkel, K.G., Aupart, C., Austrheim, H., Corfu, F., Menegon, L. & Renard, F. 2019. The Effects of Earthquakes and Fluids on the Metamorphism of the Lower Continental Crust. *Journal of Geophysical Research: Solid Earth 124(8),* 7725–7755. DOI 10.1029/2018JB016461

Jamtveit, B., Dunkel, K.G., Petley-Ragan, A., Austrheim, H., Corfu, F. & Schmid, D.W. 2021. Rapid fluid-driven transformation of lower continental crust associated with thrust-induced shear heating. *Lithos 396–397,* 106216. DOI 10.1016/j.lithos.2021.106216

Joesten, R. 1991. Grain-Boundary Diffusion Kinetics in Silicate and Oxide Minerals. In: Ganguly, J. (ed.) Diffusion, Atomic Ordering, and Mass Transport. Springer US, New York, NY, *Advances in Physical Geochemistry*, 345–395. DOI 10.1007/978-1-4613-9019-0_11

John, T. & Schenk, V. 2006. Interrelations between intermediate-depth earthquakes and fluid flow within subducting oceanic plates: Constraints from eclogite facies pseudotachylytes. *,* 4.

Jung, H. & Karato, S.-I. 2001. Effects of water on dynamically recrystallized grain-size of olivine. *Journal of Structural Geology 23(9),* 1337–1344.

Jung, H., Katayama, I., Jiang, Z., Hiraga, T. & Karato, S. 2006. Effect of water and stress on the lattice-preferred orientation of olivine. *Tectonophysics 421(1–2),* 1–22. DOI 10.1016/j.tecto.2006.02.011

Jung, H., Lee, J., Ko, B., Jung, S., Park, M., Cao, Y. & Song, S. 2013. Natural type-C olivine fabrics in garnet peridotites in North Qaidam UHP collision belt, NW China. *Tectonophysics 594,* 91–102. DOI 10.1016/j.tecto.2013.03.025

Kelly, T.F. 2017. Atomic-Scale Analytical Tomography. *Microscopy and Microanalysis 23(1),* 34–45. DOI 10.1017/S1431927617000125

Kelly, T.F. & Miller, M.K. 2007. Atom probe tomography. *Review of Scientific Instruments 78(3),* 031101. DOI 10.1063/1.2709758

Kerrick, D.M. & Connolly, J.A.D. 2001. Metamorphic devolatilization of subducted marine sediments and the transport of volatiles into the Earth's mantle. *Nature 411(6835),* 293–296. DOI 10.1038/35077056

Kesler, S.E. 2005.
Ore-Forming Fluids. *Elements 1(1),* 13–18. DOI 10.2113/gselements.1.1.13

Kirby, S.H. 1980. Tectonic stresses in the lithosphere: Constraints provided by the experimental deformation of rocks. *Journal of Geophysical Research: Solid Earth 85(B11),* 6353–6363. DOI 10.1029/JB085iB11p06353

Kirby, S.H. & Kronenberg, A.K. 1984. Deformation of clinopyroxenite: Evidence for a transition in flow mechanisms and semibrittle behavior. *Journal of Geophysical Research: Solid Earth 89(B5),* 3177–3192. DOI 10.1029/JB089iB05p03177

Kirkland, C.L., Fougerouse, D., Reddy, S.M., Hollis, J. & Saxey, D.W. 2018. Assessing the mechanisms of common Pb incorporation into titanite. *Chemical Geology 483,* 558–566. DOI 10.1016/j.chemgeo.2018.03.026

Klaper, E.M. 1990. Reaction-enhanced formation of eclogite-facies shear zones in granulite-facies anorthosites. *Geological Society,* London, Special Publications 54(1), 167–173. DOI 10.1144/GSL.SP.1990.054.01.16

Klemd, R. 2013. Metasomatism During High-Pressure Metamorphism: Eclogites and Blueschist-Facies Rocks. In: *Metasomatism and the Chemical Transformation of Rock*. Springer Berlin Heidelberg, Berlin, Heidelberg, Lecture Notes in Earth System Sciences, 351–413. DOI 10.1007/978-3-642-28394-9_10

Kronenberg, A. K., Segall, P. & Wolf, G. H. 1990. *Hydrolytic Weakening and Penetrative Deformation within a Natural Shear Zone. The Brittle-ductile Transition in Rocks, 56, 21-36.*

Kruhl, J.H., Wirth, R. & Morales, L.F.G. 2013. Quartz grain boundaries as fluid pathways in metamorphic rocks: QUARTZ GRAIN BOUNDARIES. *Journal of Geophysical Research: Solid Earth 118(5),* 1957–1967. DOI 10.1002/jgrb.50099

Lamb, W.M. & Valley, J.W. 1984. Metamorphism of reduced granulites in low-CO2 vapor free environment. *Nature* 321, 56–58.

Larson, D.J., Prosa, T.J., Ulfig, R.M., Geiser, B.P. & Kelly, T.F. 2013. *Local Electrode Atom Probe Tomography*. Springer New York, New York, NY. DOI 10.1007/978-1-4614-8721-0

Mancktelow, N.S. & Pennacchioni, G. 2004. The influence of grain boundary fluids on the microstructure of quartz-feldspar mylonites. *Journal of Structural Geology 26(1),* 47–69. DOI 10.1016/S0191-8141(03)00081-6

Mancktelow, N.S. & Pennacchioni, G. 2005. The control of precursor brittle fracture and fluid–rock interaction on the development of single and paired ductile shear zones. *Journal of Structural Geology 27(4),* 645–661. DOI 10.1016/j.jsg.2004.12.001

Manning, C.E. 2013. Thermodynamic Modeling of Fluid-Rock Interaction at Mid-Crustal to Upper-Mantle Conditions. *Reviews in Mineralogy and Geochemistry 76(1),* 135–164. DOI 10.2138/rmg.2013.76.5

Marquardt, K. & Faul, U.H. 2018. The structure and composition of olivine grain boundaries: 40 years of studies, status and current developments. *Physics and Chemistry of Minerals 45(2),* 139–172. DOI 10.1007/s00269-017-0935-9

Marquardt, K., Rohrer, G.S., Morales, L., Rybacki, E., Marquardt, H. & Lin, B. 2015. The most frequent interfaces in olivine aggregates: the GBCD and its importance for grain boundary related processes. *Contributions to Mineralogy and Petrology 170(4).* DOI 10.1007/s00410-015-1193-9

Mei, S. & Kohlstedt, D.L. 2000. Influence of water on plastic deformation of olivine aggregates 2. Dislocation creep regime. *J Geophys Res* 105(B9):21471–21481.

Menegon, L., Pennacchioni, G. & Spiess, R. 2008. Dissolution-precipitation creep of K-feldspar in mid-crustal granite mylonites. *Journal of Structural Geology 30(5),* 565–579. DOI 10.1016/j.jsg.2008.02.001

Menegon, L., Nasipuri, P., Stünitz, H., Behrens, H. & Ravna, E. 2011. Dry and strong quartz during deformation of the lower crust in the presence of melt. *Journal of Geophysical Research 116(B10),* B10410. DOI 10.1029/2011JB008371

Menegon, L., Fusseis, F., Stünitz, H. & Xiao, X. 2015. Creep cavitation bands control porosity and fluid flow in lower crustal shear zones. *Geology 43(3),* 227–230. DOI 10.1130/G36307.1

Menegon, L., Campbell, L., Mancktelow, N., Camacho, A., Wex, S., Papa, S., Toffol, G. & Pennacchioni, G. 2021. The earthquake cycle in the dry lower continental crust: insights from two deeply exhumed terranes (Musgrave Ranges, Australia and Lofoten, Norway). *Philosophical Transactions of the Royal Society A: Mathematical, Physical and Engineering Sciences 379(2193),* 20190416. DOI 10.1098/rsta.2019.0416

Mesarovic, S.Dj. 2017. Dislocation Creep: Climb and Glide in the Lattice Continuum. *Crystals 7(8),* 243. DOI 10.3390/cryst7080243

Milke, R., Neusser, G., Kolzer, K. & Wunder, B. 2013. Very little water is necessary to make a dry solid silicate system wet. *Geology 41(2),* 247–250. DOI 10.1130/G33674.1

Miller, M.K. 2000. *Atom Probe Tomography*. Springer US, Boston, MA. DOI 10.1007/978-1-4615-4281-0

Miller, M.K. & Forbes, R.G. 2014. The Local Electrode Atom Probe. In: *Atom-Probe Tomography*. Springer US, Boston, MA, 229–258. DOI 10.1007/978-1-4899-7430-3_5

Montalvo, S.D., Reddy, S.M., Saxey, D.W., Rickard, W.D.A., Fougerouse, D., Quadir, Z. & Johnson, T.E. 2019. Nanoscale constraints on the shock-induced transformation of zircon to reidite. *Chemical Geology 507,* 85–95. DOI 10.1016/j.chemgeo.2018.12.039

Moore, J., Beinlich, A., Porter, J.K., Talavera, C., Berndt, J., Piazolo, S., Austrheim, H. & Putnis, A. 2019. Microstructurally controlled trace element (Zr, U–Pb) concentrations in metamorphic rutile: An example from the amphibolites of the Bergen Arcs. *Journal of Metamorphic Geology 38(1),* 103–127. DOI 10.1111/jmg.12514

Moore, J., Beinlich, A., Piazolo, S., Austrheim, H. & Putnis, A. 2021. Metamorphic Differentiation via Enhanced Dissolution along High Permeability Zones. *Journal of Petrology 61(10),* egaa096. DOI 10.1093/petrology/egaa096

Mukai, H., Austrheim, H., Putnis, C.V. & Putnis, A. 2014. Textural Evolution of Plagioclase Feldspar across a Shear Zone: Implications for Deformation Mechanism and Rock Strength. *Journal of Petrology 55(8),* 1457–1477. DOI 10.1093/petrology/egu030

Mukherjee, S. & Mulchrone, K.F. (eds). 2015. *Ductile Shear Zones: From Micro- to Macro-Scales*. 1 pp. Wiley Blackwell, Chichester, UK ; Hoboken, NJ.

Newton R.C. 1980. Carbonic metamorphism, granulites and crustal growth. *Nature* 288, 45–50.

Newton R.C., Aranovich L. Y., Hansen E. C., & Vandenheuvel B. A. 1998. Hypersaline fluids in Precambrian deep-crustal metamorphism. *Precambrian Research* 91, 41–63.

Newton R.C., Touret J. L. R., & Aranovich L. Y. 2014. Fluids and H2O activity at the onset of granulite facies metamorphism. *Precambrian Research* 253, 17–25.

Nicoli, G. & Ferrero, S. 2021. Nanorocks, volatiles and plate tectonics. *Geoscience Frontiers 12(5),* 101188. DOI 10.1016/j.gsf.2021.101188

Nicoli, G., Gresky, K. & Ferrero, S. 2022. Mesoarchean melt and fluid inclusions in garnet from the Kangerlussuaq basement, Southeast Greenland. *Mineralogia 53(1),* 1–9. DOI 10.2478/mipo-2022-0001

Oliot, E., Goncalves, P. & Marquer, D. 2010. Role of plagioclase and reaction softening in a metagranite shear zone at mid-crustal conditions (Gotthard Massif, Swiss Central Alps): Strain localization in granitic rocks. *Journal of Metamorphic Geology 28(8),* 849–871. DOI 10.1111/j.1525-1314.2010.00897.x

Papa, S., Pennacchioni, G., Menegon, L. & Thielmann, M. 2020. High-stress creep preceding coseismic rupturing in amphibolite-facies ultramylonites. *Earth and Planetary Science Letters 541,* 116260. DOI 10.1016/j.epsl.2020.116260

Passchier, C.W. & Trouw, R.A.J. 2005. *Microtectonics*. 2nd, rev.enl. ed ed. 366 pp. Springer, Berlin ; New York.

Perchuk, L.L., Safonov, O.G., Gerya, T.V., Fu, B. & Harlov, D.E. 2000. Mobility of components in metasomatic transformation and partial melting of gneisses: an example from Sri Lanka. *Contributions to Mineralogy and Petrology 140(2),* 212–232.

Peterman, E.M., Reddy, S.M., Saxey, D.W., Snoeyenbos, D.R., Rickard, W.D.A., Fougerouse, D. & Kylander-Clark, A.R.C. 2016. Nanogeochronology of discordant zircon measured by atom probe microscopy of Pb-enriched dislocation loops. *Science Advances 2(9),* e1601318. DOI 10.1126/sciadv.1601318

Peterman, E.M., Reddy, S.M., Saxey, D.W., Fougerouse, D., Snoeyenbos, D.R. & Rickard, W.D.A. 2019. Nanoscale processes of trace element mobility in metamorphosed zircon. *Contributions to Mineralogy and Petrology 174(11)*. DOI 10.1007/s00410-019-1631-1

Peterman, E.M., Reddy, S.M., Saxey, D.W., Fougerouse, D., Quadir, M.Z. & Jercinovic, M.J. 2021. Trace-element segregation to dislocation loops in experimentally heated zircon. *American Mineralogist 106(12),* 1971–1979. DOI 10.2138/am-2021-7654

Phillips, G.N. 1981. Water activity changes across an amphibolite-granulite facies transition, Broken Hill, Australia. *Contributions to Mineralogy and Petrology 75(4),* 377–386. DOI 10.1007/BF00374721

Piazolo, S., La Fontaine, A., Trimby, P., Harley, S., Yang, L., Armstrong, R. & Cairney, J.M. 2016. Deformation-induced trace element redistribution in zircon revealed using atom probe tomography. *Nature Communications 7(1)*. DOI 10.1038/ncomms10490

Poirier, J.P. 1980. Shear localization and shear instability in materials in the ductile field. *Journal of Structural Geology 2(1–2),* 135–142. DOI 10.1016/0191-8141(80)90043-7

Post, A. & Tullis, J. 1998. The rate of water penetration in experimentally deformed quartzite: implications for hydrolytic weakening. *Tectonophysics 295(1–2),* 117–137. DOI 10.1016/S0040-1951(98)00145-0

Priester, L. 2013. *Grain Boundaries*. Springer Netherlands, Dordrecht, Springer Series in Materials Science. DOI 10.1007/978-94-007-4969-6

Prieto, G.A., Florez, M., Barrett, S.A., Beroza, G.C., Pedraza, P., Blanco, J.F. & Poveda, E. 2013. Seismic evidence for thermal runaway during intermediate-depth earthquake rupture: seismic evidence for thermal runaway. *Geophysical Research Letters 40(23),* 6064–6068. DOI 10.1002/2013GL058109

Putnis, A. 2002. Mineral replacement reactions: from macroscopic observations to microscopic mechanisms. *Mineralogical Magazine 66(5),* 689–708. DOI 10.1180/0026461026650056

Putnis, A. 2014. Why Mineral Interfaces Matter. *Science 343(6178),* 1441–1442. DOI 10.1126/science.1250884

Putnis, A. 2021. Fluid–Mineral Interactions: Controlling Coupled Mechanisms of Reaction, Mass Transfer and Deformation. *Journal of Petrology 62(12),* egab092. DOI 10.1093/petrology/egab092

Putnis, A. & Austrheim, H. 2010. Fluid-induced processes: metasomatism and metamorphism. *Geofluids*. DOI 10.1111/j.1468-8123.2010.00285.x

Putnis, A. & John, T. 2010. Replacement Processes in the Earth's Crust. *Elements 6(3),* 159–164. DOI 10.2113/gselements.6.3.159

Putnis, A. & Putnis, C.V. 2007. The mechanism of reequilibration of solids in the presence of a fluid phase. *Journal of Solid State Chemistry 180(5),* 1783–1786. DOI 10.1016/j.jssc.2007.03.023

Putnis, A., Jamtveit, B. & Austrheim, H. 2017. Metamorphic Processes and Seismicity: the Bergen Arcs as a Natural Laboratory. *Journal of Petrology 58(10),* 1871–1898. DOI 10.1093/petrology/egx076

Putnis, A., Moore, J., Prent, A.M., Beinlich, A. & Austrheim, H. 2021. Preservation of granulite in a partially eclogitized terrane: Metastable phenomena or local pressure variations? *Lithos 400–401,* 106413. DOI 10.1016/j.lithos.2021.106413

Raleigh, C.B. & Paterson, M.S. 1965. Experimental deformation of serpentinite and its tectonic implications. *Journal of Geophysical Research 70(16),* 3965–3985. DOI 10.1029/JZ070i016p03965

Reddy, S.M., van Riessen, A., Saxey, D.W., Johnson, T.E., Rickard, W.D.A., Fougerouse, D., Fischer, S., Prosa, T.J., Rice, K.P., Reinhard, D.A., Chen, Y. & Olson, D. 2016. Mechanisms of deformation-induced trace element migration in zircon resolved by atom probe and correlative microscopy. *Geochimica et Cosmochimica Acta 195,* 158–170. DOI 10.1016/j.gca.2016.09.019

Reddy, S.M., Saxey, D.W., Rickard, W.D.A., Fougerouse, D., Montalvo, S.D., Verberne, R. & Riessen, A. 2020. Atom Probe Tomography: Development and Application to the Geosciences. *Geostandards and Geoanalytical Research 44(1),* 5–50. DOI 10.1111/ggr.12313

Roedder, E. 1984. Fluid Inclusions. *Mineralogical Society of America*, Reviews in Mineralogy.

Rubie, C. 1983. Reaction-enhanced ductility: the role of solid-solid univariant reactions in deformation of the crust and mantle. *Tectonophysics,* 22.

Rubie, D.C. 1986. The catalysis of mineral reactions by water and restrictions on the presence of aqueous fluid during metamorphism. *Mineralogical Magazine 50(357),* 399–415. DOI 10.1180/minmag.1986.050.357.05

Rubie, D.C. 1990. Mechanisms of reaction-enhanced deformability in minerals and rocks. In: *Deformation Processes in Minerals, Ceramics and Rocks*. Springer Netherlands, Dordrecht, 262–295. DOI 10.1007/978-94-011-6827-4_11

Rudnick, R.L. & Fountain, D.M. 1995. Nature and composition of the continental crust: A lower crustal perspective. *Reviews of Geophysics 33(3),* 267. DOI 10.1029/95RG01302

Rutter, E. 1983. Pressure solution in nature, theory and experiment. *Journal of the Geological Society*, 140(5), 725-740. http://doi.org/10.1144/gsjgs.140.5.0725.

Rutter, E.H. & Brodie, K.H. 1988. The role of tectonic grain size reduction in the rheological stratification of the lithosphere. *Geologische Rundschau 77(1),* 295–307. DOI 10.1007/BF01848691

Rutter, E.H. & Brodie, K.H. 1995. Mechanistic interactions between deformation and metamorphism. *Geological Journal 30(3–4),* 227–240. DOI 10.1002/gj.3350300304

Rybacki, E. & Dresen, G. 2004. Deformation mechanism maps for feldspar rocks. *Tectonophysics 382(3–4),* 173–187. DOI 10.1016/j.tecto.2004.01.006

Safonov O. G. & Aranovich L. Y. 2014. Alkali control of high-grade metamorphism and granitization. Geoscience Frontiers 5, 711–727.

Sawyer, E.W. 1987. The Role of Partial Melting and Fractional Crystallization in Determining Discordant Migmatite Leucosome Compositions. *Journal of Petrology 28(3),* 445–473. DOI 10.1093/petrology/28.3.445

Sawyer, E.W., Cesare, B. & Brown, M. 2011. When the Continental Crust Melts. *Elements 7(4),* 229–234. DOI 10.2113/gselements.7.4.229

Scambelluri, M., Pennacchioni, G., Gilio, M., Bestmann, M., Plümper, O. & Nestola, F. 2017. Fossil intermediate-depth earthquakes in subducting slabs linked to differential stress release. *Nature Geoscience 10(12),* 960–966. DOI 10.1038/s41561-017-0010-7

Shen, A.H. & Kepplert, H. 1997. Direct observation of complete miscibility in the albite-H_2 0 system. *Letters to Nature,* 3.

Solar, G.S. & Brown, M. 2001. Petrogenesis of Migmatites in Maine, USA: Possible Source of Peraluminous Leucogranite in Plutons? *Journal of Petrology 42(4),* 789–823. DOI 10.1093/petrology/42.4.789

Spear, F.S. 1993. *Metamorphic Phase Equilibria and Pressure-Temperature-Time Paths, Mineralogical Society of America.*

Stevens, G. & Clemens, J.D. 1993. Fluid-absent melting and the roles of fluids in the lithosphere: a slanted summary? *Chemical Geology 108(1–4),* 1–17. DOI 10.1016/0009-2541(93)90314-9

Stewart, M., Holdsworth, R.E. & Strachan, R.A. 2000. Deformation processes and weakening mechanisms within the frictional–viscous transition zone of major crustal-scale faults: insights from the Great Glen Fault Zone, Scotland. *Journal of Structural Geology 22(5),* 543–560. DOI 10.1016/S0191-8141(99)00164-9

Stünitz, H. & Tullis, J. 2001. Weakening and strain localization produced by syn-deformational reaction of plagioclase. *International Journal of Earth Sciences 90(1),* 136–148. DOI 10.1007/s005310000148

Stünitz, H., Thust, A., Heilbronner, R., Behrens, H., Kilian, R., Tarantola, A. & Fitz Gerald, J.D. 2017. Water redistribution in experimentally deformed natural milky quartz single crystals-Implications for H $_2$ O-weakening processes: water in experimentally deformed quartz. *Journal of Geophysical Research: Solid Earth 122(2),* 866–894. DOI 10.1002/2016JB013533

Tacchetto, T., Bartoli, O., Cesare, B., Berkesi, M., Aradi, L.E., Dumond, G. & Szabó, C. 2019. Multiphase inclusions in peritectic garnet from granulites of the Athabasca granulite terrane (Canada): Evidence of carbon recycling during Neoarchean crustal melting. *Chemical Geology 508,* 197–209. DOI 10.1016/j.chemgeo.2018.05.043

Tacchetto, T., Reddy, S.M., Saxey, D.W., Fougerouse, D., Rickard, W.D.A. & Clark, C. 2021a. Disorientation control on trace element segregation in fluid-affected low-angle boundaries in olivine. *Contributions to Mineralogy and Petrology 176(7),* 59. DOI 10.1007/s00410-021-01815-3

Tacchetto, T., Reddy, S.M., Bartoli, O., Rickard, W.D.A., Fougerouse, D., Saxey, D.W., Quadir, Z. & Clark, C. 2021b. Pre-nucleation geochemical heterogeneity within glassy anatectic inclusions and the role of water in glass preservation. *Contributions to Mineralogy and Petrology 176(9),* 70. DOI 10.1007/s00410-021-01826-0

Toro, G.D., Aretusini, S., Cornelio, C., Nielsen, S., Spagnuolo, E., Núñez-Cascajero, A., Tapetado, A. & Vázquez, C. 2021. Friction during earthquakes: 25 years of experimental studies. *IOP Conference Series: Earth and Environmental Science 861(5),* 052032. DOI 10.1088/1755-1315/861/5/052032

Touret, J. & Dietvorst, P. 1983. Fluid inclusions in high-grade anatectic metamorphites. *Journal of the Geological Society 140(4),* 635–649.

Touret, J.L.R. 2001. Fluids in metamorphic rocks. *Lithos 55(1–4),* 1–25. DOI 10.1016/S0024-4937(00)00036-0

Touret, J.L.R. & Huizenga, J.-M. 2011. Fluids in granulites. In: *Geological Society of America Memoirs*. Geological Society of America, 25–37. DOI 10.1130/2011.1207(03)

Touret, J.L.R., Santosh, M. & Huizenga, J.M. 2016. High-temperature granulites and supercontinents. *Geoscience Frontiers 7(1),* 101–113. DOI 10.1016/j.gsf.2015.09.001

Tullis, J. & Yund, R.A. 1989. Hydrolytic weakening of quartz aggregates: The effects of water and pressure on recovery. *Geophysical Research Letters 16(11),* 1343–1346. DOI 10.1029/GL016i011p01343

Tullis, J., Yund, R. & Farver, J. 1996. Deformation-enhanced fluid distribution in feldspar aggregates and implications for ductile shear zones. *Geology,* 4.

Valley, J.W., Cavosie, A.J., Ushikubo, T., Reinhard, D.A., Lawrence, D.F., Larson, D.J., Clifton, P.H., Kelly, T.F., Wilde, S.A., Moser, D.E. & Spicuzza, M.J. 2014. Hadean age for a post-magma-ocean zircon confirmed by atom-probe tomography. *Nature Geoscience 7(3),* 219–223. DOI 10.1038/ngeo2075

Verberne R., Saxey D., Reddy S., Rickard W., Fougerouse D., & Clark C. 2019. Analysis of Natural Rutile (TiO2) by Laser-assisted Atom Probe Tomography. *Microscopy and Microanalysis*, 1-8. doi:10.1017/S1431927618015477.

Verberne, R., Reddy, S.M., Saxey, D.W., Fougerouse, D., Rickard, W.D.A., Quadir, Z., Evans, N.J. & Clark, C. 2022. Dislocations in minerals: Fast-diffusion pathways or trace-element traps? *Earth and Planetary Science Letters 584,* 117517. DOI 10.1016/j.epsl.2022.117517

Vielzeuf, D., Clemens, J.D., Pin, C. & Moinet, E. 1990. Granites, Granulites, and Crustal Differentiation. In: Vielzeuf, D., Vidal, P. (eds) Granulites and Crustal Evolution. NATO ASI Series, vol 311. Springer, Dordrecht. https://doi.org/10.1007/978-94-009-2055-2_5.

Wallace, P.A., De Angelis, S.H., Hornby, A.J., Kendrick, J.E., Clesham, S., von Aulock, F.W., Hughes, A., Utley, J.E.P., Hirose, T., Dingwell, D.B. & Lavallée, Y. 2019. Frictional melt homogenisation during fault slip: Geochemical, textural and rheological fingerprints. *Geochimica et Cosmochimica Acta 255,* 265–288. DOI 10.1016/j.gca.2019.04.010

Wallis, D., Hansen, L.N., Tasaka, M., Kumamoto, K.M., Parsons, A.J., Lloyd, G.E., Kohlstedt, D.L. & Wilkinson, A.J. 2019. The impact of water on slip system activity in olivine and the formation of bimodal crystallographic preferred orientations. *Earth and Planetary Science Letters 508,* 51–61. DOI 10.1016/j.epsl.2018.12.007

Wang, Z., Shi, F. & Zhang, J. 2020. Effects of Water on the Rheology of Dominant Minerals and Rocks in the Continental Lower Crust: A Review. *Journal of Earth Science 31(6),* 1170–1182. DOI 10.1007/s12583-020-1307-9

Wannamaker, P.E. 2002. Fluid generation and pathways beneath an active compressional orogen, the New Zealand Southern Alps, inferred from magnetotelluric data. *Journal of Geophysical Research 107(B6),* 2117. DOI 10.1029/2001JB000186

Warren, J.M. & Hirth, G. 2006. Grain size sensitive deformation mechanisms in naturally deformed peridotites. *Earth and Planetary Science Letters 248(1–2),* 438–450. DOI 10.1016/j.epsl.2006.06.006

Wassmann, S. & Stöckhert, B. 2013. Rheology of the plate interface — Dissolution precipitation creep in high pressure metamorphic rocks. *Tectonophysics 608,* 1–29. DOI 10.1016/j.tecto.2013.09.030

Watanabe, T. 1985. Structural effects on grain boundary segregation, hardening and fracture. *Le Journal de Physique Colloques 46(C4),* C4-555-C4-566. DOI 10.1051/jphyscol:1985462

Weber, J., Barthel, J., Brandt, F., Klinkenberg, M., Breuer, U., Kruth, M. & Bosbach, D. 2016. Nano-structural features of barite crystals observed by electron microscopy and atom probe tomography. *Chemical Geology 424,* 51–59. DOI 10.1016/j.chemgeo.2016.01.018

Webster, J.D., Geological Association of Canada & Mineralogical Association of Canada (eds). 2006. *Melt Inclusions in Plutonic Rocks: Short Course Delivered in Association with the Annual Meeting of the Geological Association of Canada and the Mineralogical Association of Canada, Montreal, Quebec, 13 - 14 May, 2006*. 237 pp. Mineralogical Association of Canada, Montreal, Short course series / Mineralogical Association of Canada, 36.

Weertman, J. 1970. The creep strength of the Earth's mantle. *Reviews of Geophysics 8(1),* 145. DOI 10.1029/RG008i001p00145

Weinberg, R.F. & Hasalová, P. 2015. Water-fluxed melting of the continental crust: A review. *Lithos 212–215,* 158–188. DOI 10.1016/j.lithos.2014.08.021

White, R.W. & Powell, R. 2002. Melt loss and the preservation of granulite facies mineral assemblages. *Journal of Metamorphic Geology*, Volume 20, Number 7.

White, S.H. & Knipe, R.J. 1978. Transformation- and reaction-enhanced ductility in rocks. *Journal of the Geological Society of London.* 135, 513-516. *,* 4.

Winter, J.D. 2014. Principles of Igneous and Metamorphic Petrology. 2. ed., Pearson new internat. ed. 740 pp. Pearson Education, Harlow.

Wintsch, R.P. & Yi, K. 2002. Dissolution and replacement creep: a significant deformation mechanism in mid-crustal rocks. *Journal of Structural Geology,* 15.

Wirth, R. 1996. Thin amorphous films (1-2 nm) at olivine grain boundaries in mantle xenoliths from San Carlos, Arizona. *Contributions to Mineralogy and Petrology 124(1),* 44–54. DOI 10.1007/s004100050172

Xu, L., Mei, S., Dixon, N., Jin, Z., Suzuki, A.M. & Kohlstedt, D.L. 2013. Effect of water on rheological properties of garnet at high temperatures and pressures. *Earth and Planetary Science Letters 379,* 158–165. DOI 10.1016/j.epsl.2013.08.002

Yardley, B.W.D. 2009. The role of water in the evolution of the continental crust. *Journal of the Geological Society 166(4),* 585–600. DOI 10.1144/0016-76492008-101

Yardley, B.W.D. & Barber, J.P. 1991. Melting reactions in the Connemara Schists: the role of water infiltration in the formation of amphibolite facies migmatites. *American Mineralogist* 76, 848–856.

Yardley, B.W.D. & Bodnar, R.J. 2014. Fluids in the Continental Crust. *Geochemical Perspectives 3(1),* 1–127. DOI 10.7185/geochempersp.3.1

Yardley, B.W.D. & Valley, J.W. 1997. The petrologic case for a dry lower crust. *Journal of Geophysical Research: Solid Earth 102(B6),* 12173–12185. DOI 10.1029/97JB00508

Zhou, J., Yang, Yongsoo, Yang, Yao, Kim, D.S., Yuan, A., Tian, X., Ophus, C., Sun, F., Schmid, A.K., Nathanson, M., Heinz, H., An, Q., Zeng, H., Ercius, P. & Miao, J. 2019. Observing crystal nucleation in four dimensions using atomic electron tomography. *Nature 570(7762),* 500–503. DOI 10.1038/s41586-019-1317-x

Chapter 2

Pre-nucleation geochemical heterogeneity within glassy anatectic inclusions and the role of water in glass preservation

This chapter is published as:

Tacchetto T., Reddy S.M., Bartoli O., Rickard W. D., Fougerouse D., Saxey D., Quadir Z. and Clark C. Pre-nucleation geochemical heterogeneity within glassy anatectic inclusions and the role of water in glass preservation. *Contribution to Mineralogy and Petrology*, 176 (70), 2021. https://doi.org/10.1007/s00410-021-01826-0

Abstract

Glassy melt inclusions are unique geological repositories that preserve evidence of the formation and evolution of mantle- and crustal-derived magmas. However, the mechanisms responsible for their preservation in slowly-cooled crustal rocks remain contentious, in some part due to their small size (commonly <10 μm) and the technical difficulty in quantifying composition and microstructures. In this work, time-of-flight secondary ion mass spectrometry, transmission electron microscopy and atom probe tomography are used to characterize glassy melt inclusions found in peritectic garnets of a migmatite from the Spanish Betic Cordillera. The glassy melt inclusions coexist in a close spatial relationship with partially- to totally-crystallized melt inclusions (nanogranitoids). Analyses of the glassy inclusions show a heterogeneous, patchy distribution of Na and K within the glass and along inclusion walls. Nanoscale spherical domains of Al, Fe, K, Na, Cl and Li are also found systematically distributed at inclusion edges and are interpreted to represent pre-nucleation clusters. The location and compositional similarity of these clusters with micas and feldspars in nanogranitoids indicates that the glassy inclusions represent former nanogranitoids "captured" at an earlier stage of crystallization, suggesting a likely common origin for both the glassy inclusions and nanogranitoids. A comparison between the composition of melt inclusions with previously published data reveals that preserved glassy inclusions contain significant less H_2O (av. 2.72 wt.%) than nanogranitoids (average of 6.91 wt.%). This suggests the low-H_2O contents representing a further impediment to crystallization, along with the very small volume of these cavities, favouring the coexistence of glassy inclusions and nanogranitoids. In contrast, crystal nucleation is enhanced in more hydrous melts, where H_2O reduces melt viscosity and promotes diffusion.

2.1 Introduction

Melt inclusions *s.l.* in minerals are small (generally <50 μm) droplets of melt trapped during the growth of the host mineral in a fluid-mineral system (Sorby 1858; Roedder 1984). Though small, they provide a unique record of primary melt compositions within rocks, many of which have undergone a prolonged and complex geological history. Hence, the study of melt inclusions in volcanic rocks is a mature science, in particular melt inclusions in olivine, where they are used to constrain the origin and chemical evolution of magmatic systems (Frezzotti 2001; Bodnar & Student 2006; Webster & Thomas 2006; Thomas & Davidson 2012; Audetat & Lowenstern 2014). In this scenario, solid phases trap droplets of melt from which they are crystallizing (Faure & Schiano 2005).

Over the past decade, it has been shown that primary melt inclusions can also be formed during the early stages of crustal anatexis, and are trapped within peritectic minerals in granulites and migmatites (Cesare *et al.* 2009, 2015; Bartoli *et al.* 2016a; Bartoli 2020; Bartoli & Cesare 2020). In this case, the host mineral is, with melt, a prograde product of incongruent melting reactions consuming hydrous minerals, for example melt inclusions in peritectic garnet are formed by melting reactions that consume biotite (Cesare *et al.* 2015). Thus, these melt inclusions are a direct record of the most primitive anatectic melt composition in the host metamorphic rocks (Cesare *et al.* 2015; Bartoli 2020).

Once trapped, the melt inclusions may partially to totally crystallize forming a polycrystalline aggregate or they may solidify as a single-phase glassy inclusion. The latter scenario is considered typical of settings characterized by fast cooling rates (e.g., volcanic systems; Audetat & Lowenstern 2014). In more slowly-cooled melt inclusions, inclusion walls may become the sites of nucleation of shrinkage bubbles and crystallization of daughter minerals (Steele-Macinnis *et al.* 2011). Cooling over even longer periods, for example in plutonic or regional metamorphic rocks, may lead to the complete crystallization of the trapped melt inclusion and the growth of multiple daughter minerals (Webster *et al.* 2006; Cesare B. *et al.* 2009). These inclusions typically comprise (sub)micrometric crystals often showing hypidiomorphic texture and have been referred to as nanogranitoids (Cesare *et al.* 2015).

Despite the broad relationships between the melt inclusions characteristics and geological settings outlined above, some melt inclusions preserve evidence for a more complex behaviour. For example, granulites that experienced extremely slow cooling rates (~ 3–6 °C/Ma; Cenki *et al.* 2004) may preserve glassy melt inclusions (Cesare *et al.* 2009).

Coexisting nanogranitoids and glassy inclusions have also been found in several high-grade metamorphic terranes (Ferrero *et al.* 2012; Bartoli *et al.* 2013, 2016a; Borghini *et al.* 2018; Gianola *et al.* 2020; Borghini *et al.* 2020). Their coexistence has been attributed to the inhibition of mineral nucleation due to small pore volumes (Cesare *et al.* 2009), infiltration of externally-derived hydrous-siliceous fluids (Clemens 2009) or to variations in H_2O contents, which control the viscosity of the melt and thereby the diffusivity of elements (Bartoli *et al.* 2015; Bartoli 2020). However, despite the observation that ~15 % of melt inclusions in metamorphic rocks are glassy, there is no clear understanding of the mechanisms responsible for their formation and preservation.

To date, the microstructural and compositional characterization of anatectic melt inclusions and the interface with their host minerals have used conventional beam-based techniques, such as scanning electron microscopy (e.g., Acosta-Vigil A. *et al.* 2012; Ferrero *et al.* 2012; Carvalho *et al.* 2020), although these approaches are often challenged by the intrinsic small nature of these features. To advance our understanding of the mechanisms of melt inclusions solidification and crystallization, and the processes that may subsequently affect them, a state-of-the-art nanoscale analytical workflow has been used to characterize the nanoscale textural and compositional heterogeneity within naturally preserved glass inclusions.

The investigated melt inclusions are found within migmatites from the Spanish Betic Cordillera which have been extensively studied (Tubía *et al.* 1997; Bartoli *et al.* 2013, 2015, 2016b; Acosta-Vigil *et al.* 2014 and references therein). Moreover, melt inclusions occurring within host garnets have been previously studied using conventional techniques, and these data provide context for our nanoscale analysis (Bartoli *et al.* 2015, 2016a). The new data presented here allow the genetic relationships between different melt inclusion types to be addressed and demonstrate that the formation and evolution of the different types of melt inclusions is critically dependent on the H_2O content of the melt.

2.2 Analytical techniques

Glassy melt inclusions analysed in this study were previously characterized in detail by (Bartoli *et al.* 2016b) using a multi-technique approach comprising backscattered electron (BSE) imaging, energy dispersive spectroscopy (EDS), electron microprobe (EMP) and Raman spectroscopy. In this follow up study, characterization by scanning electron microscope (SEM) used both a Tescan Mira3 FESEM, a Tescan Vega3 SEM and a TESCAN

Integrated Mineral Analyzer (TIMA) housed at the John de Laeter Centre at Curtin University. These systems were used to characterize the mineralogy of the rock and to identify glassy inclusions that were suitable for further analyses by time-of-flight secondary ion mass spectrometry (ToF-SIMS), transmission electron microscopy (TEM) and atom probe tomography (APT).

ToF-SIMS investigations were conducted using a Ga^+ Tescan Lyra3 Focused Ion Beam Scanning Electron Microscope (FIB-SEM) equipped with a Tofwerk ToF-SIMS system housed at the John de Laeter Centre at Curtin University. High spatial resolution maps were acquired for two glassy inclusions exposed on the polished surface of the host garnet using the primary Ga^+ ion beam operating at 50 pA and 20kV. Maps were acquired in positive ion mode with a resolution of 1024x1024 pixels over a 10x10 μm region of interest for each inclusion and a total number of 50 frames (< 2 μm in depth). During acquisition, charging of the sample surface were compensated using the electron beam operating in scanning mode at low acceleration voltage (2kV). Post-processing of the acquired data was performed using the ToF-SIMS Explorer version 1.4.3 software provided by Tofwerk.

An electron-transparent thin foil for TEM observation and needle-shaped atom probe tomography specimens were prepared using a Tescan Lyra3 FIB-SEM. For the TEM study, the foil was obtained in cross-section from an unexposed inclusion located at ~ 3 μm below the polished thin section surface of the host garnet. The milling of the region of interest was performed using a 30kV Ga^+ ion beam. Before lift-out, the inclusion was exposed by acquiring high-resolution ToF-SIMS maps, even though meaningful data were challenged by the high level of background generated by the in-depth surface of acquisition. After extraction, the ~ 0.5 μm thick foil was mounted into a copper grid then thinned to <100 nm in a smaller area dedicated to TEM observations. A final stage of low-voltage polishing was performed at 5 kV to reduce Ga^+ implantation and the damaged layer generated by the initial high-beam energy. Bright field (BF) scanning transmission electron microscopy (STEM), high-angle annular dark-field (HAADF) and high-resolution bright field (HR-TEM) images were acquired at 200 kV using a FEI Talos FS200X Field Emission Gun (FEG) Transmission Electron Microscope (TEM) housed at the John de Laeter Centre at Curtin University.

For the APT study, preliminary specimens were obtained from both the garnet and the silica glass in order to obtain optimal working conditions for both phases (Supplementary Table 2.A.1). Since the silica glass requires a higher electrical field for ion evaporation than garnet, the atom probe specimens were manufactured so that garnet lies above the glass in

the APT needle-shaped specimen. This targeting of the host-inclusion interface was performed from above the edges of semi-exposed glassy inclusions using the electron-beam deposited Pt markers (Rickard *et al.* 2020). The analyses of 14 specimens were carried out on a Cameca LEAP 4000X HR at the Geoscience Atom Probe Facility, Curtin University. The acquisitions were performed in laser-assisted mode with a base temperature of 60 K. The ultraviolet laser (λ= 355nm) pulse energy ranged between 300 and 500 pJ using a frequency of 200 kHz. A detection rate between 0.3 and 0.6 % was used based on the response of the individual specimens to the applied electric field. The presented dataset comprises a specimen representative of the silica glass (Gl-1) and of the interface boundary (PB1, PB2). PB2 specimen comprises two reconstructions, PB2a and PB2b, where PB2b represents a subsequent analysis following an instrumental failure of the automatic tip-focus tracking during acquisition, likely related to a minor fracture of the specimen during evaporation.

Collected mass spectra were processed and reconstructed in 3D using Cameca's IVAS 3.8.2 software. The identified peaks of each mass spectrum were compared with the local background and those with peak intensities that were twice above the background were ranged. In order to limit graphical artefacts, the reconstruction mode was chosen between voltage, tip profile and shank angle based on the linearity of the electrical field during each run. The accuracy of the 3D reconstructions will be discussed in this paper. Details of the acquisition and reconstruction parameters are summarized in the Supplementary Table 2.A.1 following Blum *et al.* (2018). 2D chemical profiles were also plotted to observe the spatial distribution of major and trace elements within the atom probe specimens and along the captured phase boundaries.

2.3 Geological setting and sample description

The investigated rock is a quartzo-feldspathic mylonitic diatexite from the Ojén unit, Betic Cordillera (southern Spain) (Figure 2.1a). The Ojén unit represents a polymetamorphic crustal sequence mainly composed of metasedimentary mylonites and migmatites, with minor schists and marbles (Figure 2.1a). Structurally, the unit represents the footwall of the Ronda peridotites, the largest exposure of lithospheric mantle worldwide (Obata 1980; Tubía *et al.* 1997).

The quartzo-feldspatic mylonite occurs at the contact with the peridotitic slab and displays the highest metamorphic grade of the crustal sequence, recording granulite-facies

peak conditions of ~ 820 °C and < 8 kbar (Tubía *et al.* 1997; Bartoli *et al.* 2016a) (Figure 2.1b). A progressive downgrading associated with a decrease in melt proportions is observed towards the bottom of the unit where the underlying migmatitic sequence is characterized by metasedimentary diatexites on top of banded metatexites, the latter recording peak conditions of ~ 5 kbar and ~ 700°C (Bartoli *et al.* 2013). The high-temperature metamorphism, anatexis of the crustal rocks and formation of the migmatitic sequence are associated with the crustal emplacement of the Ronda peridotites (Tubía *et al.* 1997; Platt *et al.* 2003; Esteban *et al.* 2008; Mazzoli *et al.* 2013; Bartoli *et al.* 2013, 2016b; Acosta-Vigil *et al.* 2014, 2016). The timing of the high-temperature melting event remains controversial, being ascribed to either the Alpine and/or Varisican orogenies (Sánchez-Rodríguez & Gebauer 2000; Esteban *et al.* 2011; Acosta-Vigil *et al.* 2014).

In thin section, the matrix of the rock is defined by leucocratic bands mainly composed of medium- to coarse- grained K-feldspar, plagioclase and quartz alternating with fine- grained mesocratic layers comprising garnet porphyroblasts, quartz, K-feldspar, plagioclase and sillimanite with minor biotite and ilmenite (Figures 2.1c, d). The reader is also referred to Bartoli *et al.* (2016b) for a more detailed petrographic description of the rock.

The inclusions investigated in this contribution are crystal-free melt inclusions (*glassy inclusions* hereafter) occurring in clusters within garnets (Figure 2.2). The garnet host is almandine-rich in composition ($Alm_{72-75}Prp_{20-23}Sps_{02–03}Grs_{02–03}$; X_{Mg} = 0.21–0.24) recording a slight increase of spessartine towards the rim of the grains when locally in contact with biotite (Bartoli *et al.* 2016b). Glassy inclusions are small (≤ 15 μm, mostly 5-10 μm in diameter), optically isotropic and often characterized by a visible empty shrinkage bubble (Figure 2.2b). Raman spectroscopic analysis of these bubbles did not show any evidence of H_2O and CO_2. They generally exhibit rounded (isometric) to negative crystal shape (Figures 2.2b, c). In places, glassy inclusions may contain crystals of apatite occurring as trapped phase. The glassy inclusions are often found coexisting with partially and totally crystallized polycrystalline inclusions comprising micrometric aggregates of quartz, K-feldspar, biotite, muscovite, and plagioclase (nanogranitoids) **(**Figures 2.2c; 2.3).

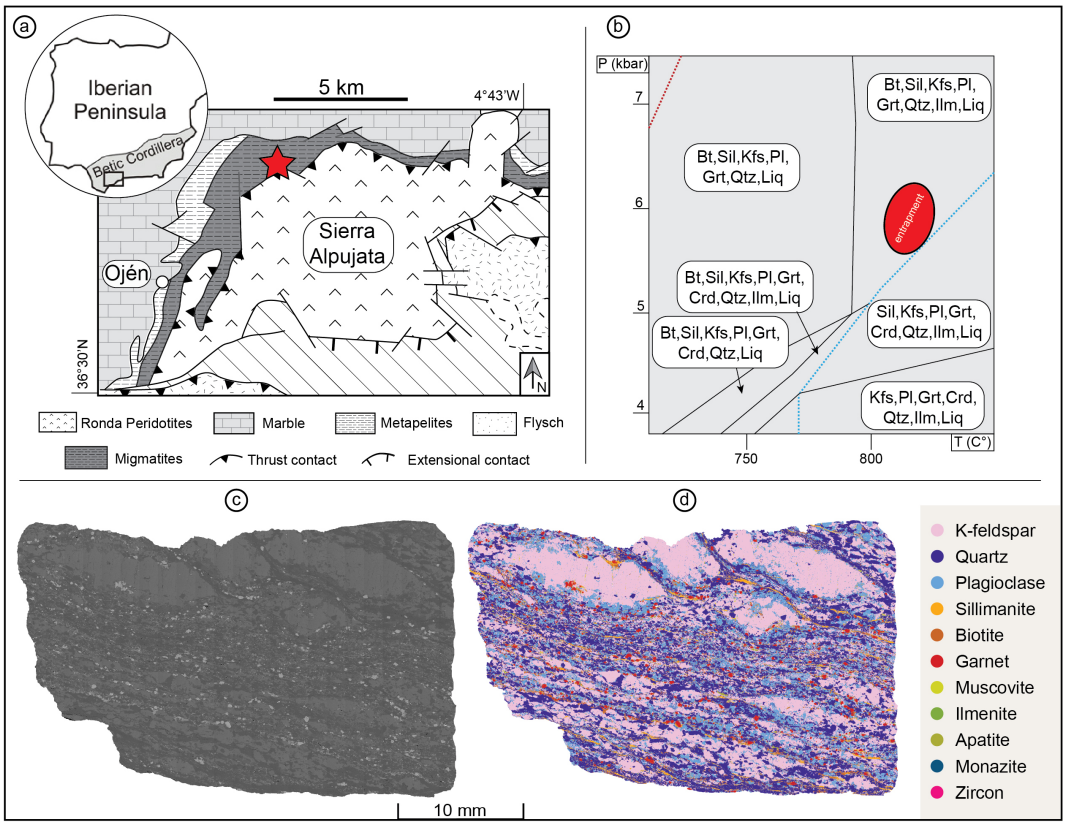

Figure 2.1 Geological map of the Sierra Alpujata massif (modified after Esteban *et al.* 2011). Red star indicates the location of the studied sample investigated by Bartoli *et al.* (2016b). b) P-T section calculated in the C-free system MnNCaKFMASHT for the investigated rock sample showing the estimated P-T conditions of entrapment of the glassy inclusions (modified after Bartoli *et al.* 2016b). Blue and red dashed lines represent Bt- and Ms-out curves respectively. c-d) TIMA SEM-BSE and mineral phase map panorama images of the investigated quartzo-feldspatic mylonitic diatexite (sample ALP-13 in Bartoli *et al.* 2016b). The main foliation is defined by elongated K-feldspar grains, the alignment of sillimanite crystals and ribbons of quartz. Garnet porphyroblasts generally occur as small grains within the leucocranitic domains.

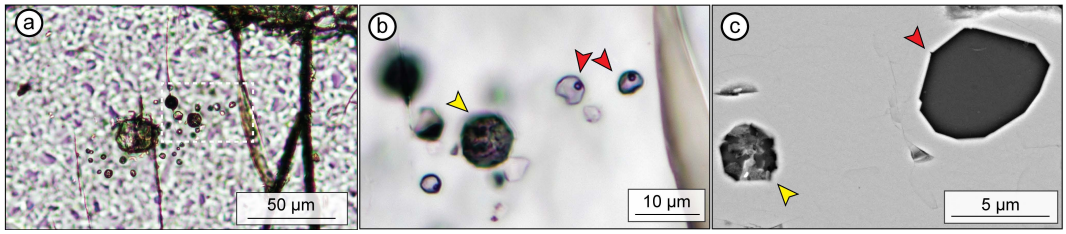

Figure 2.2 (a) Photomicrograph of MI clusters in zonal arrangement within the host garnet. (b) Close-up photomicrograph of the white dashed region showed in (a) showing glassy melt inclusions (red arrows) highlighted by visible shrinkage bubbles coexisting with nanogranitoid type inclusion (yellow arrow). (c) SEM-BSE image of coexisting nanogranitoid and glassy inclusion with the latter being larger in size (modified after Bartoli *et al.* 2015).

Glassy inclusions are leucogranitic (SiO_2 ~ 76 wt%, FeO + MgO + MnO + TiO_2 < 2 wt%) and peraluminous [ASI =1.05–1.38; ASI = mol. Al_2O_3 /(CaO + Na_2O + K_2O)] in composition, with average H_2O content raging between 0 and 4–6.7 wt% (average 2.7 wt%), estimated by difference from EMP analyses (Bartoli *et al.* 2016b). Detailed microstructural and compositional data, along with phase equilibria modelling, has led to the interpretation that the glassy inclusions represent anatectic melt trapped during the growth of peritectic garnet produced by incongruent reactions at ~ 820 °C and ~ 6 kbar (Bartoli *et al.* 2016b) (Figure 1.1b).

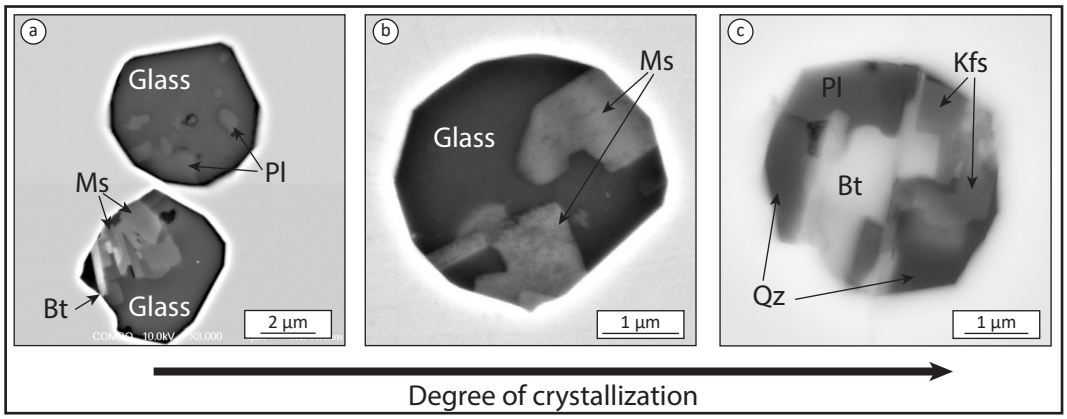

Figure 2.3 SEM-BSE images of partially crystallized (a,b) and totally crystallized (c, nanogranitoid) in garnet from the Ojén unit metatexite (a) and diatexite (b,c) (see also Bartoli *et al.* 2013; 2016b). (a) modified after Cesare *et al.* (2011). (b) modified after Bartoli *et al.* (2015).

2.4 Results

2.4.1 Transmission Electron Microscopy

TEM imaging of a cross-section prepared from a representative unexposed glassy inclusion (GI4) is presented in Figure 2.4. In BF mode the surrounding garnet is characterized by the presence of darker curved linear features, mostly projecting from inclusion edges towards the host (Figure 2.4a). These features are interpreted to represent local bending or structural defects of the crystal lattice, likely developed in the garnet host to accommodate the strain generated by the entrapped inclusion.

Within the glassy inclusion, localized features can be distinguished close to the inclusion margin (white arrows on Figure 2.4a). These features are better resolved in

HAADF, appearing as clusters of circular geometries (< 30 nm in diameter) heterogeneously distributed within slightly lighter domains (Figure 2.4b). These lighter domains are distinguishable from the surrounding darker silica glass matrix which appear homogeneous moving towards the inner side of the inclusion. In HAADF mode, higher grey-scale intensities (i.e., whiter) are indicative of particles with higher atomic number (Reimer & Kohl 2008). This therefore indicates that both the circular features and the lighter domains have a compositional contrast compared to the surrounding darker glass matrix. High-resolution TEM imaging in BF mode of the interfacial domain between the garnet host and the glass displays a significant microstructural discontinuity, characterized by a sharp boundary separating the ordered crystal lattice of the host from the amorphous silica glass (Figure 2.4c).

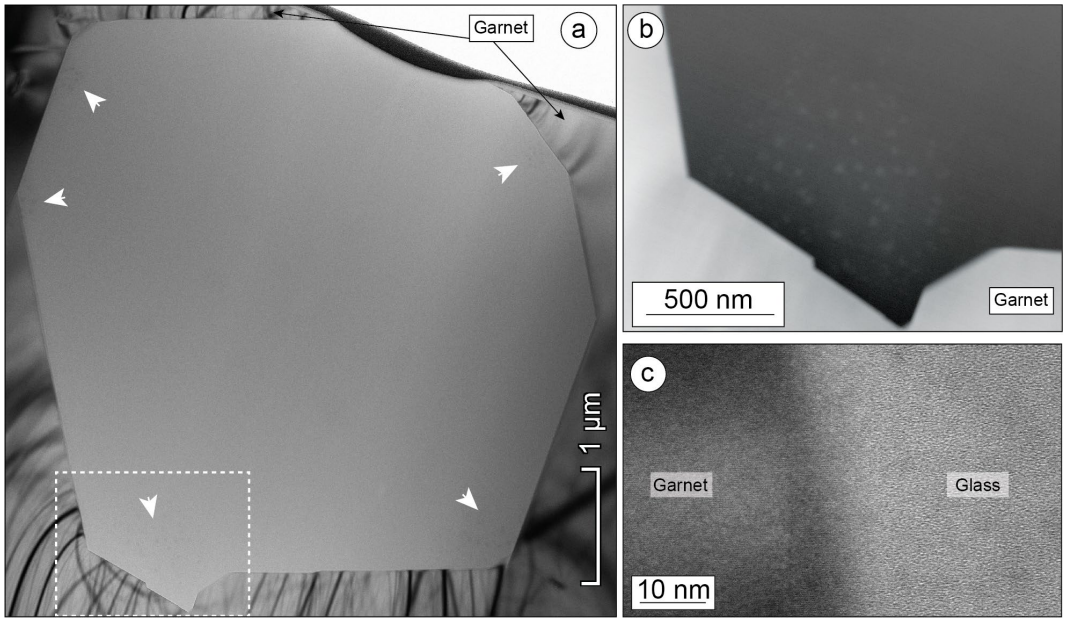

Figure 2.4 TEM analysis of cross-section foil extracted from representative glassy inclusion (GI4). a) BF-STEM image showing the whole inclusion hosted by the host garnet showing a characteristic negative crystal shape. White arrows indicate regions of heterogeneity localized at the inclusion edges. b) HAADF STEM close-up image of the lower portion of the inclusion. Clusters of heterogeneous circular features are visible localized at the inclusion edges. c) Bright Field high-resolution TEM image of the phase boundary showing a sharp interface separation between a crystalline domain of the host garnet (*left*) and the amorphous glass (*right*).

2.4.2 Time-of-Flight Secondary Ion Mass Spectrometry

The ToF-SIMS data from two exposed glassy inclusions (GI5, GI6) show that the glassy inclusions have lower concentrations of $^{24}Mg^{+}$, $^{40}Ca^{+}$, $^{56}Fe^{+}$ and $^{27}Al^{+}$, and higher

concentrations of $^{28}Si^{+}$, $^{39}K^{+}$ and $^{23}Na^{+}$ (Figure 2.5), compared to the host garnet. This is in agreement with the leucogranitic composition of these inclusions (Bartoli *et al.* 2015). In 2D, the concentration of $^{24}Mg^{+}$, $^{40}Ca^{+}$, $^{56}Fe^{+}$ and $^{27}Al^{+}$ is homogenous throughout the whole inclusion. In contrast, $^{39}K^{+}$ and $^{23}Na^{+}$ display regions of localised enrichment restricted to irregular portions within the inclusion (GI6) or localized along the boundary walls (GI5) (Figure 2.5).

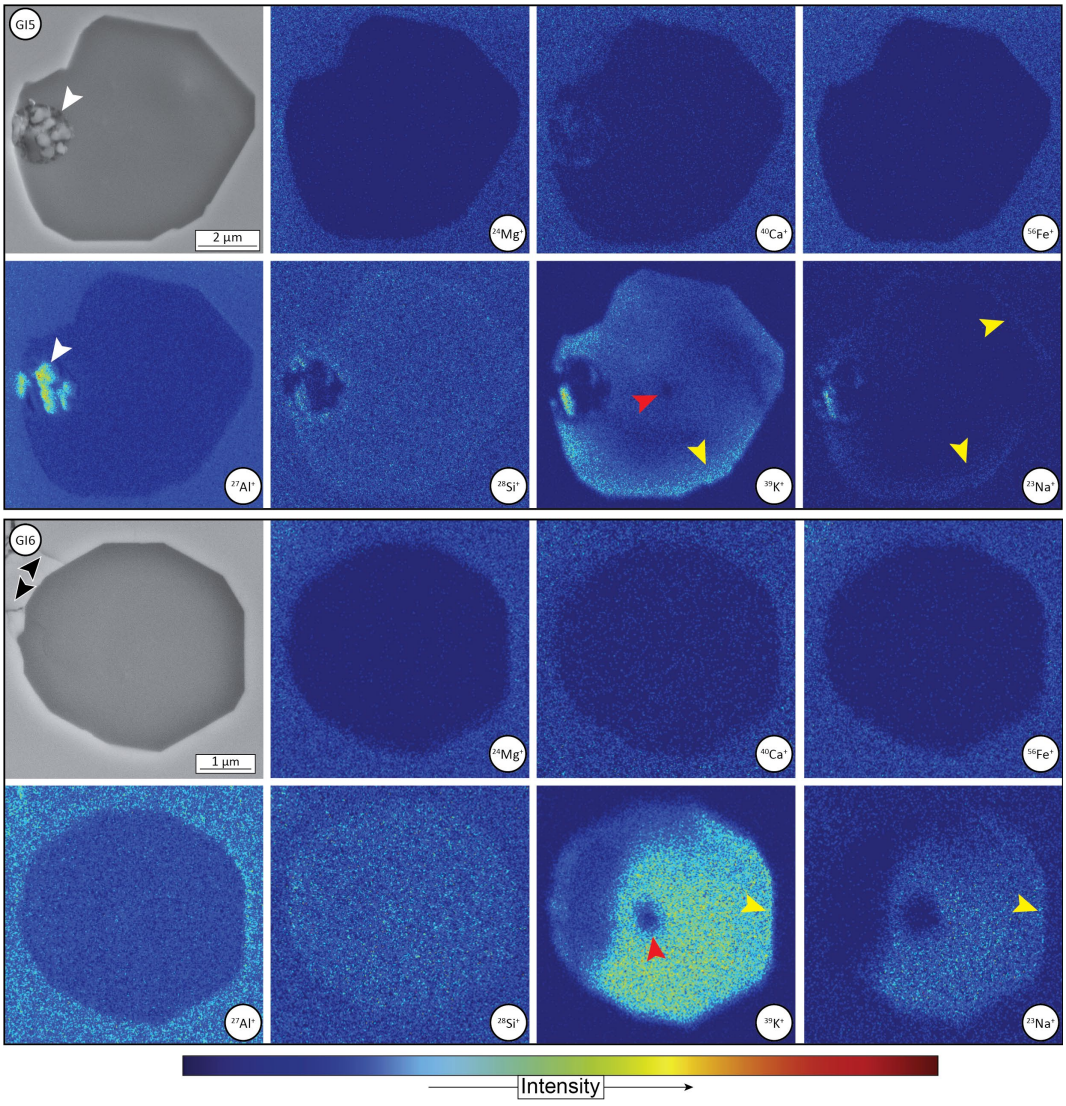

Figure 2.5 SE-SEM images and ToF-SIMS isotopic maps showing spatial distributions of major elements within two representative glassy inclusions (GI5-GI6). *Yellow* arrows indicate visible local enrichment of Na and K at the inclusion walls. *White* arrow indicates a shrinkage bubble cavity filled with polishing material. *Red* arrows indicate damage created by SEM-EDS spot analyses. *Black* arrows indicate fractures generated by mechanical polishing of the sample surface.

2.4.3 Atom Probe Tomography

From 14 APT prepared specimens, 7 yielded sufficient APT data for further analysis and interpretation. The remaining 7 specimens fractured during the early stages of data acquisition. These fractured specimens are not considered further. The mass-to-charge ratio spectra obtained from APT analyses comprise single elements and molecular species at a variety of charge states (Supplementary Figure 2.A.1).

The specimen representative of the silicate glass (Gl-1) was obtained a few nanometres away from the edge of the inclusion. The bulk glass composition resulting from the APT analyses is consistent with a leucogranitic melt (Bartoli *et al.* 2015), with few identified trace elements forming minor peaks (Supplementary Figure 2.A.1; Supplementary Table 2.A.2). 3D reconstructions and 2D concentration profiles of the APT data reveal the presence of discrete compositional heterogeneities, most noticeable for Al and Fe, within a more homogeneous Si-rich matrix (Figure 2.6). These features define sub-spherical domains with a ~10 nm radius (Figure 2.6).

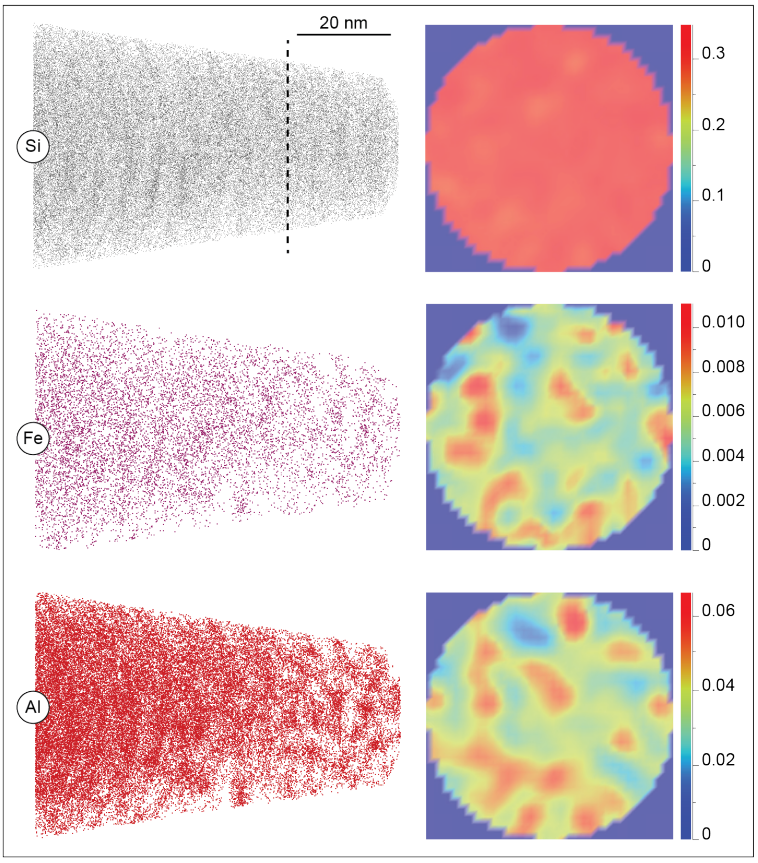

Figure 2.6 (left) 3D reconstruction of atom probe specimen Gl-1 (glass) for Si, Fe, and Al. Each dot represents a detected atom. (right) 2D compositional profile of the planar surface indicated by the back dashed line. The compositional heterogeneities of Fe and Al are highlighted by peaks of atomic concentrations whereas Si displays a more homogeneous distribution. In the 2D profiles, concentrations are expressed in at% (right y scale).

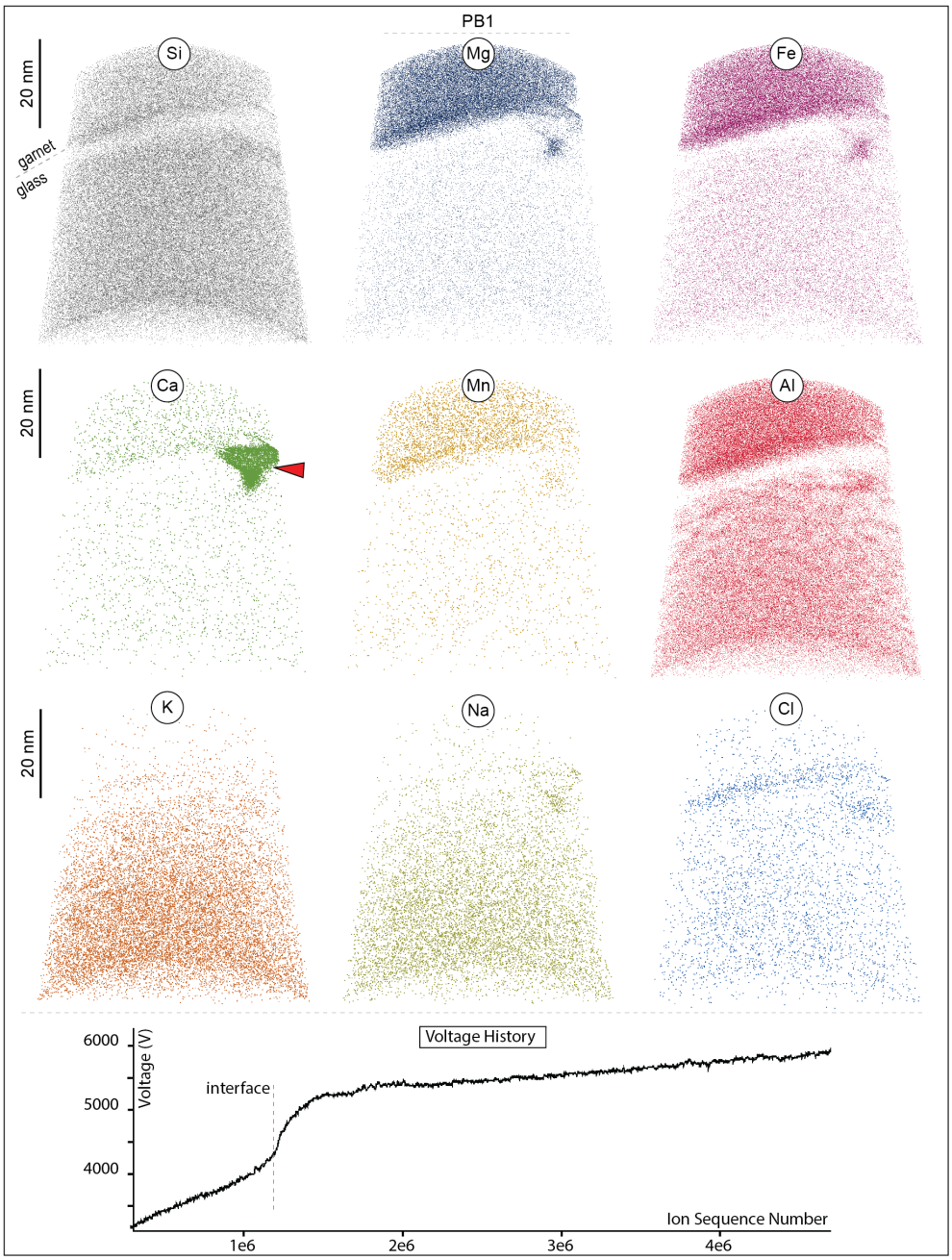

Figure 2.7 3D reconstruction of PB1 atom probe specimen and voltage history during acquisition. Each dot represents one detected atom. Not all detected atoms are displayed for clarity. Homogeneous distribution of garnet major elements (Fe, Mg, Al, and Si) is observed within the garnet portion whereas heterogeneities are observed for Al in the glass domain. Red arrow: apatite inclusion highlighted by high atomic concentrations of Ca. A dramatic increase in voltage is observed at the interface with the glass concomitant with the evaporation of the apatite inclusion.

The 3D reconstructions of specimen PB1 and PB2 show that the interface between garnet and glass is captured in the specimen (Figures 2.7, 2.8). The maps show a distinct compositional variation between the garnet and the silica glass separated by a sharp planar boundary. The major elements of garnet (Si, Mg, Fe, Mn and Al) are homogeneously distributed across the entire garnet analysis and display an abrupt decrease in concentration

at the interface with the glass (Figures 2.7, 2.8). In specimen PB1, a region of higher Ca and P highlights a nano-inclusion of apatite captured along the interface and extending into the glass (Figures 2.7). A few tens of nanometres away from the interface, a patchy clustering of Al is visible in the glassy matrix of both dataset (Figures 2.7, 2.8) and is similar to that observed within specimen Gl-1. In PB2 this clustering is also recorded by K and Na. Also in PB2, the interfacial domain is highlighted by a layered structure, only a few nanometres wide, that is defined by the local enrichment of K, Na, Li and Cl within the garnet as defined by major element variations (Figure 2.8). A weaker clustering of Cl and Li is visible from 2D profiles across this interface (Figure 2.9). In the PB2b reconstruction, an elongated feature is noticeable at the interface projecting towards the host garnet and mostly enriched in Al, K, Cl and Li (Figure 2.8).

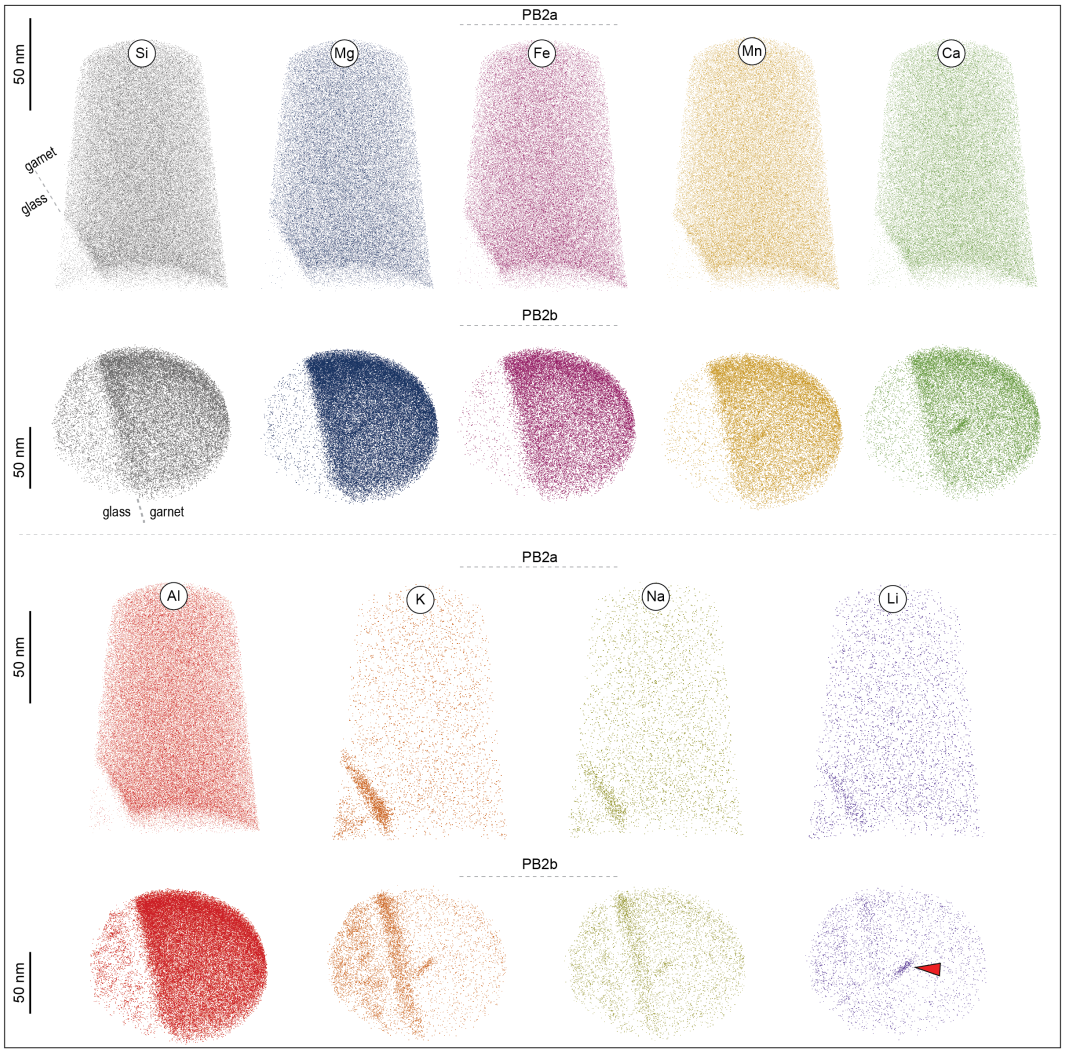

Figure 2.8 3D reconstruction of PB2(a/b) atom probe specimen. Each dot represents one detected atom. Not all detected atoms are displayed for clarity. The maps show a clear enrichment of K, Na, Li atoms at the targeted phase boundary. Homogeneous distribution of major elements is observed within the garnet portion whereas heterogeneities are observed for Al, K, and Na in the glass domain. Red arrow: signal "hot-spot artefact" generated by local magnification effect.

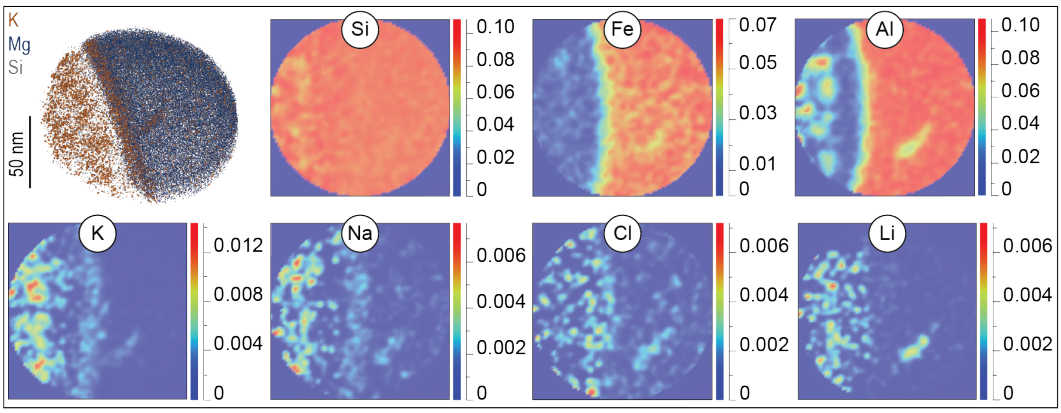

Figure 2.9 (top left) 3D reconstruction of PB2-b portion displaying the atomic distribution of K, Mg and Si. 2D compositional profiles of the projected planar cross-section displaying atomic concentrations for Si, Fe, Al, K, Na, Cl and Li. The interface boundary domain is highlighted by K, Na, Cl and Li local enrichment. Al, K, Na, Cl and Li peaks of concentration are visible within the glassy matrix a few nanometers away from the interface.

2.5 Discussion

2.5.1 Are nanoscale features analytical artefacts?

The damaging of an amorphous glassy material by an electron beam is a well-known effect in the Material Sciences and it has been demonstrated that TEM observations have the potential to induce the chemical decomposition or the formation of nanostructures within glassy materials (Meldrum *et al.* 1997; Humphreys *et al.* 2006). To avoid electron-induced artefacts in this study, care was taken during TEM imaging to avoid focus adjustments directly on the regions of interest and not overexpose the sample surface during observation. Moreover, the first acquired low-magnification image revealed the presence of sub-spherical features strictly localized at inclusions edges whereas the overall matrix appears homogeneous (Figure 2.4). In addition, bright field HR-TEM observations acquired after low-magnification imaging do not show evidence of induced crystallinity at the observed interfaces (Figure 2.4c). APT utilizes a combination of an electric field and thermal energy from laser pulses to sequentially evaporate atoms from the specimen surface (Larson *et al.* 2013). The similar results by both approaches on different selected inclusions further indicate that the effects of electron-beam irradiation during TEM analyses are negligible.

The 3D reconstruction of APT data assumes that evaporation takes place from a tip that has a hemispherical shape and that ion flight paths follow field lines associated with a

simple electric field at the specimen tip. In situations where APT specimens have two phases with different evaporation fields, the volume reconstruction and compositional information can be affected by analytical artefacts, such as local magnification effects (Miller & Hetherington 1991; Vurpillot *et al.* 2000; De Geuser *et al.* 2007; Reddy *et al.* 2020). Such artefacts arise because preferential evaporation of one phase gives rise to topography on the specimen surface and this leads to regions of lower radius of curvature that become the focus of subsequent evaporation events (Reddy *et al.* 2020) (Figure 2.10), and these will be dependent upon the geometry of the interface within the specimen tip. The localized distortion of the phase boundary interface may also lead to the aberration of ions trajectories (Fougerouse *et al.* 2016). The application of correction methods, which operate to homogenise the volume according to a gradient of atomic density (e.g., De Geuser *et al.* 2007), serve to effectively improve the reliability of the three-dimensional reconstructions. However, when interpreting datasets obtained from such heterogenous materials, the possible presence of remaining artefacts is difficult to exclude.

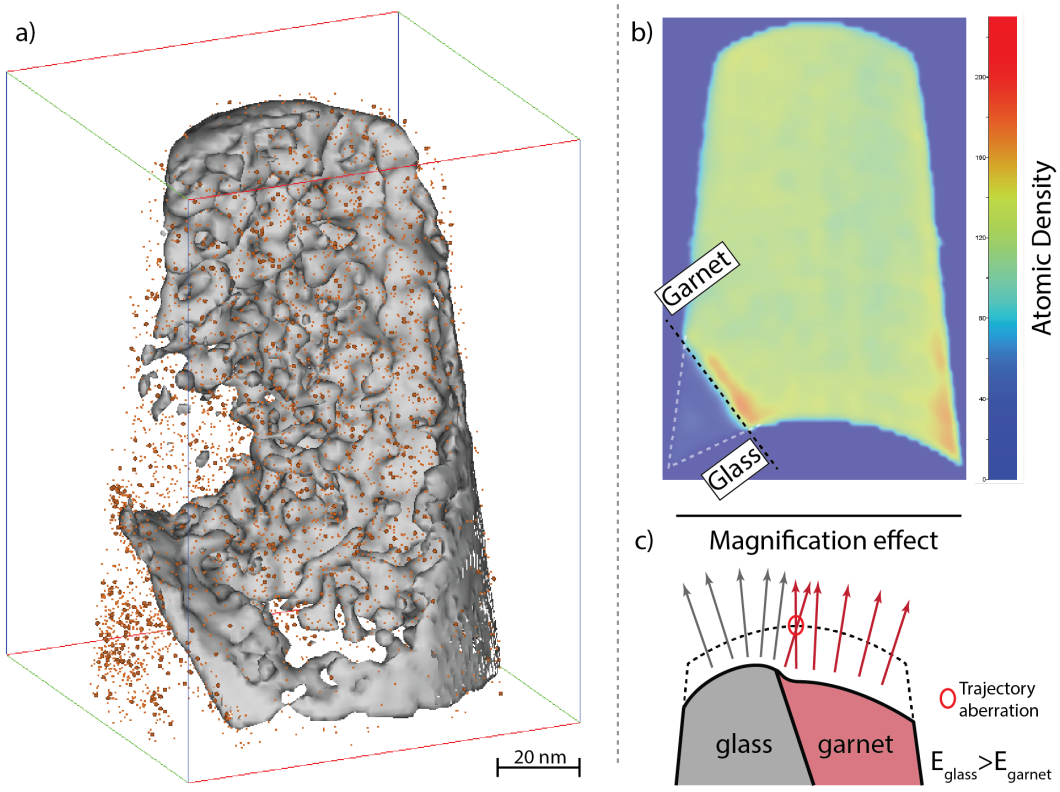

Figure 2.10 (a) 3D density isosurface reconstruction for all the elements within the atom probe specimen PB2a. (b) 2D plot displaying the density distribution of all the elements in the specimen. A higher level of atomic density can be observed at the phase boundary likely being generated by the local magnification effect. (c) Sketch illustrating the local magnification effect associated with the difference in the electrical field of adjacent materials (modified after Reddy *et al.* 2020).

In this study, the 3D reconstruction of specimen PB2 is characterized by a restricted compositional zonation (a few nm wide) in K, Na and Li within the garnet host immediately adjacent to the glass interface and a zone of decreased K, Na and Li in the glass adjacent to the interface (Figure 2.8). To assess if this represents a reconstruction artefact, an atomic density isosurface was generated from all of the elements present in the specimen (Figure 2.10a). The 2D and 3D density distribution show a higher ion density in the garnet immediately adjacent to the interface (Figures 2.10a, b) that directly corresponds to the region of higher K, Na and Li concentration seen in the garnet (Figure 2.8). This pattern of K, Na and Li distribution adjacent to the glass-garnet interface is consistent with trajectory aberrations associated with field evaporation differences between the garnet and glass and is therefore interpreted as a local reconstruction artefact in the proximity of the interface (Figure 2.10c). Such an interpretation is consistent with the known incompatibility of K, Na and Li in garnet. Similarly, comparing the mass spectra extracted from a Li atomic concentration isosurface obtained from the elongated feature observed in PB2b, the local background shows higher intensities than the majority of the enriched ions present in the dataset (Supplementary Figure 2.A.2). Therefore, the localized enrichment of Al, K, Cl and Li visible in the reconstruction likely represents a similar artefact generated by a localised topographic irregularity of the phase boundary surface.

2.5.2 Prenucleation clusters as snapshots of incipient crystallization

The TEM analysis of a glassy inclusion revealed the presence of heterogeneously localized sub-spherical features systematically distributed at the rim of the inclusion (Figure 2.4). In addition, site-specific APT analyses also revealed the presence of compositionally distinct clusters in the amorphous material both in the matrix of the glassy specimen (Gl-1) and close to the boundaries with the host garnet (Figures 2.6–2.9). These features show geometrical similarities to those observed in TEM studies of glass crystallization in synthetic glasses which are interpreted as crystal prenucleation sites (Höche 2010; Gebauer *et al.* 2014; Karpukhina *et al.* 2014; Schreiber *et al.* 2017). Recently, TEM observations have documented the presence of nano-crystals, termed nanolites (30 nm to 1 μm in width) and ultrananolites (<30 nm), in an increasing number of geological samples and in quenched glasses from volcanic samples (Barone *et al.* 2016; Mujin *et al.* 2017; Di Genova *et al.* 2018, 2020). These nanoscale features resemble those found in the investigated glassy inclusions (Figure 2.4).

Even though the latter do not show high levels of crystallinity such as nanolites, they clearly represent a more ordered structure when compared to the surrounding amorphous glassy matrix (Figure 2.4b).

In fluid/melt inclusions the crystallization of new phases (daughter minerals) is generally observed initiating from the walls of the cavities as the pre-existing phase boundary represents a favourable site of lower nucleation energy (Roedder 1984; Malaspina *et al.* 2015). In the specific case of nanogranitoids, the euhedral shape of biotite and/or muscovite microcrystals, and their sharp and planar contacts with the walls of the inclusions, have been used to infer that micas are the first mineral to crystallize from the entrapped melt (Ferrero *et al.* 2012, 2015; Barich *et al.* 2014; Bartoli *et al.* 2016b; Carvalho *et al.* 2018; Tacchetto *et al.* 2019). This is consistent with their occurrence as only crystallized phases within glass in partially crystallized inclusions (Figures 2. 3a, b; see also Ferrero *et al.* 2012; Bartoli *et al.* 2013, 2015). In some cases, "patchy" plagioclase has sometimes been observed as the only daughter phase within partially crystallized inclusions (Figure 2.3a). Moreover, Ferrero *et al.* (2016) and Carvalho *et al.* (2018) also documented the finding of K-feldspar crystals and kokchetavite (its high-P polymorph) having euhedral shape and planar contacts with inclusion walls.

High-resolution compositional analyses revealed that the distribution of elements (in terms of atomic concentrations) is not homogeneous within the preserved glassy inclusions. In particular, ToF-SIMS maps show a developed chemical zonation for Na and K within (e.g., GI6) and along the walls of the inclusions (e.g., GI5). In addition, clusters of Fe, Al, Na, K, Cl and Li atoms are visible in the glassy matrix in the APT reconstructions (Figures 2.6-2.9). With the exception of inclusion GI6, the observed circular nanostructures observed on the TEM images (Figures 2.4b) appear in close spatial relationship with the distribution of the Na + K enriched rim in the ToF-SIMS data (Figure 2.5). Hence, considering: (i) the coexistence of glassy inclusions with partially and totally crystallized inclusions within the same clusters; (ii) the systematic localization of the nanostructures observed along inclusions edges (potential sites of daughter mineral crystallization) as well as their similarities with nano-structures reported in the literature; (iii) the compatibility in micas and feldspars of the elements enriched towards the inclusions rims (first mineral phases that crystallize from the entrapped melt), with the available dataset we interpret the observed compositional variations as representative of self-organised pre-nucleation clusters (i.e., the sites of subsequent crystal nucleation; Gebauer *et al.* 2014). Our results therefore suggest the presence of a "captured" primitive stage of daughter mineral formation within the

amorphous material investigated in this study and the existence of a systematic relationship between glassy and nanogranitoid inclusions.

2.5.3 Evolution of anatectic melt inclusions

The nucleation of crystals from a liquid phase (e.g., silicate melt) at any sub-liquidus temperature represents a complex mechanism, which requires the overcoming of a critical radius of pre-nucleation clusters (Gebauer *et al.* 2014) in order for the mineral components to segregate from the melt to nucleate (Baronnet 1993; Xiao *et al.* 2018). In fluid or melt inclusions, the formation of new phases within the cavities is generally induced by the supersaturation of the trapped fluid phase with respect to particular crystalline phases generated by the decreasing temperature and pressure of the host rock upon cooling (Roedder 1984).

The formation of the observed enriched layer of Na and K at inclusion walls requires the presence of a short-range gradient of diffusion within the inclusions. The formation of a gradient of concentration has been previously observed around melt inclusions in olivine (Newcombe *et al.* 2014), and particularly effective for volatile elements in response to compositional differences between melt inclusions and the host-rock system (Le Voyer *et al.* 2014). Similarly, element-rich rims developed in glassy inclusions have also been observed in plagioclase and pyroxene from basalt (Marques *et al.* 2010, 2012). In this study, the ToF-SIMS data show no zonation of major compatible elements within the garnet in the proximity of the inclusions. This observation is not consistent with diffusional exchange of compatible cations as the responsible mechanism for the development of a chemical gradient at the inclusion margin.

Solid-state transformation of the original rounded shape of inclusions after entrapment (i.e., shape maturation) is a common phenomenon observed occurring in anatectic melt and mineral inclusions in granulite terranes (Ferrero *et al.* 2012; Cesare *et al.* 2021). This process is manifested by the development of negative crystal geometries in response to the minimization of the surface free-energy generated by the inclusion-host phase boundaries (Roedder 1984; Lowenstern 1995; Cesare *et al.* 2021). However, while these post-entrapment readjustments result in a variation of the inclusion shape, the total volume and the bulk chemical composition of the entrapped fluid are not significantly modified (Audétat & Günther 1999; Frezzotti 2001; Lambrecht & Diamond 2014). Microstructurally,

the inclusions analysed in this study are faceted displaying a clear development of planar surface and shape edges suggesting that the shape of the inclusions evolved after their entrapment at peak metamorphic conditions.

The observation of pre-nucleation clusters at inclusions rims (Figure 2.4) may reflect the process of shape maturation that promotes the nucleation through the development of planar phase boundaries and edges. The short-range segregation of highly diffusive elements, such as Na and K, throughout the glass towards the rim of the inclusions could therefore represent the direct consequence of the reorganization of the melt volume in response to the variation in shape of the inclusion cavity (Figure 2.11). In this microstructural scenario, the localized enrichment of particular elements (Al, Fe, K, and Na), combined with the peraluminous character of the entrapped melt has the potential to initiate the crystallization of phases such as micas and/or feldspars that can be observed in partially crystallized and nanogranitoid inclusions (Figures 2.3, 2.11).

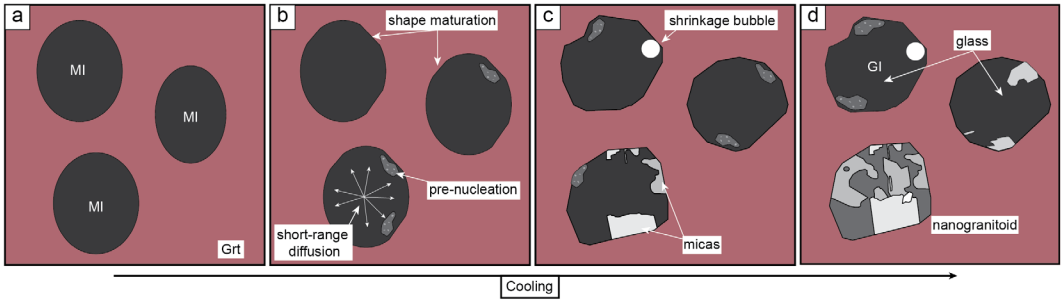

Figure 2.11 Schematic representation of the proposed model for the chemical and microstructural evolution of the melt inclusion upon cooling. (a) Entrapment of melt inclusions in peritectic garnet. (b) Developing of energetically favorable negative crystal shape and pre-nucleation development. Partitioning of more diffusive elements (K, Na, Cl, and Li) towards sites of prenucleation and inclusions walls. (c) Crystallization of microcrystal of micas and feldspars. (d) Fully-developed negative crystal shape. Coexistence of totally and partially crystallized inclusions with glassy inclusions.

2.5.4 Reliability of glassy melt inclusions in migmatites and granulites

The occurrence of MI in migmatites, granulites and anatectic enclaves allows the pristine compositional information of crustal melts to be obtained directly from the source rock (Cesare *et al.* 2015). The coexistence of nanogranitoids and glassy inclusions in the same host and cluster has been used to argue for a common origin of these inclusions and therefore compositionally representative of the same anatectic melt (Cesare *et al.* 2009). By contrast, Clemens (2009) proposed an alternative hypothesis based on the observation that a

supercritical aqueous fluid can dissolve a substantial silicate component at high-pressure (Shen & Kepplert 1997). In this case, the occurrence of glassy inclusions could represent subsequent infiltration of externally-derived aqueous-siliceous fluids, rather than the melt composition represented by nanogranitoid inclusions. It is clear that these two hypotheses have strongly different petrological implications.

The nanoscale investigation performed in this study reveals the presence of pre-crystallization compositional clusters within the amorphous material. The location and compositional trend of these clusters are consistent with the distribution and composition of minerals in the coexisting nanogranitoids and both of these are typical of formation from a peraluminous leucogranitic melt. Therefore, the results represent evidence that both nanogranitoids and glassy inclusions are representative of the same anatectic melt trapped during the formation of the peritectic host, with glassy inclusions representing an earlier stage of the pre-nucleation process. As such, we interpret the composition of preserved glassy inclusions in migmatites and granulites to be representative of the anatectic melt present during the partial melting event.

When analysing the composition of melt inclusions, the possible post-entrapment processes that may have altered their pristine character need to be considered (Roedder 1984). Many of these processes are driven by temperature and pressure variations of the rock-host system, and/or the geochemical nature of the host-fluid system. Diffusional exchange between garnet and the content of inclusions was proposed by Clemens (2009). However, ToF-SIMS maps acquired in this investigation do not show noticeable enrichments of Mg, Al, Fe and Ca in the glass close to the garnet-inclusion interface (Figure 2.5). Minor bright rims of Al and Si are strictly localized at inclusions edges within the garnet host and likely being the results of an "edge effect" generated by the topography of the inclusion under the Ga^{+}-beam (Figure 2.5). Nanoscale reconstructions of element distributions obtained by APT on different selected inclusions also display an abrupt decrease in concentration of Mg, Al, Fe and Ca at the phase boundary interfaces (Figures 2.7, 2.8). These observations are consistent with those of Acosta-Vigil *et al.* (2012) who have previously reported the lack of compositional gradients between glassy inclusions of anatectic melt and their host by using beam-based compositional profiles obtained across the phase boundary. The higher-spatial resolution compositional data obtained in this study are a further indication that diffusional exchange between melt and garnet did not occur after inclusion formation. The previously measured compositions of MI from the Ojén unit are therefore representative of the bulk melt composition (Bartoli *et al.* 2016b).

2.5.5 Glass preservation in slowly-cooled metamorphic rocks

The occurrence of preserved glassy inclusions and/or residual glass within migmatites and granulites has been widely documented (Bartoli 2020 for a review). However, in contrast to glassy melt inclusions associated with the rapid cooling of igneous rocks, the slow cooling rates of metamorphic terranes are expected to preclude the possibility of forming glass.

Statistical analysis of melt inclusions size in populations of nanogranitoids (average diameter ~12.5 μm) and glassy (average diameter ~8.2 μm) inclusions from khondalites of southern India has been used to infer that mineral nucleation in glass is inhibited because the volume of material in the melt inclusion does not enable the nucleation of critical nuclei (Cesare *et al.* 2009). Similarly, further analyses of glassy inclusions (2-5 μm) coexisting with nanogranitoids (5-20 μm) have reported similar size relationships (Borghini *et al.* 2018, 2020). However, this dimensional relationship, referred to as the pore-size effect (Putnis *et al.* 1995; Holness & Sawyer 2008), is unable to entirely explain the presence of glassy inclusions at Ronda, where their size can be equal or even larger than that of nanogranitoids (Fig. 2c and Fig. 7 in Bartoli *et al.* 2015).

A detailed microstructural and compositional analysis of melt inclusions found in the rocks of the Ojén unit has shown a systematic variation in the degree of melt inclusions crystallization within the migmatitic sequence (Bartoli *et al.* 2015). In details, the rare occurrence of preserved glassy inclusions in the metatexite is dominated by totally or partially crystallized melt inclusions (Figure 2.3). Conversely, the occurrence of preserved glassy inclusions exponentially increases within the overlying diatexites (Bartoli *et al.* 2015, 2016b; this study). Since the composition of melt inclusions from the two host-rocks mainly differ in H_2O contents (2.7 vs. 6.5 wt% on average), the greater H_2O content may be responsible for the partial or total crystallization of the entrapped melt at Ronda (Bartoli *et al.* 2015).

To assess this inference based on a single terrane, we interrogated the current database on melt inclusions in metamorphic rocks. Preserved glassy inclusions show a mean value of 2.72 wt.% and about 90% of the data lie within the 0–5 wt.% H_2O range (Figure 2.12). Moreover, even though the detection of H_2O can sometimes be challenged by its occurrence as thin liquid films at the bubble-glass interface (e.g., Esposito *et al.* 2016), Raman spectroscopy excluded the presence of H_2O within shrinkage bubbles of glassy inclusions, which range from completely empty (Bartoli *et al.* 2016b; Borghini *et al.* 2020) to containing carbonic species (Gianola *et al.* 2020), therefore allowing to interpret the measured H_2O

concentration to reflect that of the trapped melt. By contrast, nanogranitoids generally have higher H_2O contents, with about 70% of the data plotting between 4 and 11 wt.% H_2O (average value of 6.91 wt.%) (Figure 2.12b). One could argue that such high H_2O contents cannot be accommodated solely by crystallization of micas within inclusions. However, Raman mapping has shown the presence of liquid H_2O hosted in micro-pores or of H_2O-rich residual glass among crystallized phases within nanogranitoids (Bartoli *et al.* 2013; Ferrero *et al.* 2015).

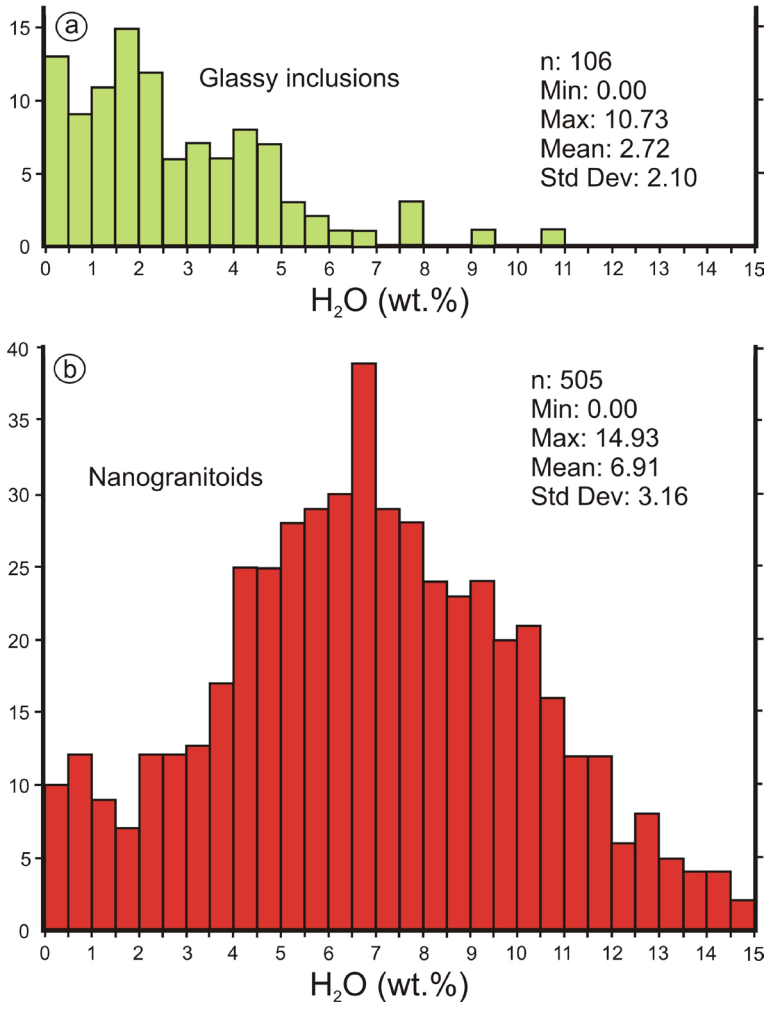

Figure 2.12 Histogram showing the H_2O content (wt%) of glassy inclusions (a) and nanogranitoids (b) from high-grade metamorphic rocks (data from: Acosta-Vigil *et al.* 2016; Carvalho *et al.* 2019; Gianola *et al.* 2020; Bartoli *et al.* 2013, 2014, 2016; Bartoli 2019; Borghini *et al.* 2018, 2020; Ferrero *et al.* 2012, 2014, 2015, 2016, 2018; Tacchetto *et al.* 2019; Ferri *et al.* 2020; Nicoli & Ferrero 2021). H_2O concentrations were estimated by Raman spectroscopy, NanoSIMS, and by difference (100-EMP totals).

The ability to form glass is strongly dependent on the amount of dissolved H_2O, as a significant amount of H_2O will decrease the glass transition temperature (Gavrilenko *et al.* 2019). At the same time, melt viscosity decreases as H_2O content increases (Giordano *et al.* 2008), favouring diffusivity, which influences the nucleation process (Di Genova *et al.* 2020). The viscosity of a melt containing 3 wt.% H_2O (~10^6 Pa s at 800 °C) is two orders of magnitude greater than the viscosity calculated for 7 wt.% H_2O (~10^4 Pa s) at the same temperature (Scaillet *et al.* 1996). By contrast, less hydrous melts are more viscous, and more viscous melts are more easily quenched, because diffusivity and in turn nucleation are hampered.

The full dataset, therefore, seems to support the view of Bartoli *et al.* (2015) regarding the H_2O control on "quenchability" of anatectic melts, where this term refers to the ability of a silicate to be transformed to a glass upon cooling (see Gavrilenko *et al.* 2019). However, previous case studies have shown the possible coexistence of both glassy inclusions and nanogranitoids that display similar H_2O concentrations (e.g., Cesare *et al.* 2009; Ferrero *et al.* 2012; Bartoli *et al.* 2015). Despite some overlap between the two populations, the plotted compositions statistically reveal major differences in terms of H_2O content (Figure 2.12). Therefore, considering the available dataset, we propose that the geological oddity of glass preservation in slowly cooled rocks is likely related to a statistical probability of nucleation, which appears to be lower when the entrapped melt is characterised by low H_2O content (this study), and/or the volume of the inclusions cavities is very small (pore-size effect; Cesare *et al.* 2009).

2.5.6 New insights on the quench control on H_2O estimates

From the analysis of Figure 2.12**,** a H_2O content ≥ 5–6 wt.% seems to favour the formation of partially to totally crystallized melt inclusions, whereas the fate of dryer melts is uncertain (some crystallize, others quench). It is therefore clear that analysing only preserved glassy melt inclusions may lead to underestimating the maximum H_2O content (see also Gianola *et al.* 2020) and that the study of their crystallized counterparts (nanogranitoids) is crucial for obtaining a complete record of the wettest anatectic melts.

A similar sampling bias has been recently proposed for glassy inclusions of mafic melt at volcanic arcs (Gavrilenko *et al.* 2019). These authors have experimentally shown that mafic magmas containing > 9 wt% H_2O cannot be quenched, despite cooling rates

approaching those for eruptions. Instead, aggregates of crystallites, bubbles, and devitrified glass form. At H_2O contents up to 6 wt%, hydrous melts consistently quench to form glass, whereas melts containing 6–9 wt% H_2O are partially quenched. Because mafic glasses preserved in melt inclusions in olivine are thought to preserve the pre-eruptive H_2O contents of mantle-derived magmas and because these melts have H_2O contents rarely exceeding ≈6 wt%, Gavrilenko *et al.* (2019) proposed a quench control of H_2O estimates, hampering the common view of a restricted range of H_2O contents in arc magmas (see also Steele-MacInnis 2019).

The results obtained in our study suggest that the quench control of H_2O estimates of melt inclusions can be present also in settings characterized by very slow cooling rates. Considering the available data set of anatectic melts, the limit of quenchability inferred by Gavrilenko *et al.* (2019) for mafic melts (9 wt% of dissolved H_2O) may also be applied to felsic systems, as well as the transition between "easy to quench" and "hard to quench" melts at 5–6 wt% H_2O (Figure 2.12; cf. Gavrilenko et al. 2019, Fig. 1). Incidentally, preserved glassy inclusions from felsic plutons show < 8 wt% H_2O contents, which are much lower (up to 3 times) than those of coexisting crystallized melt inclusions (Webster & Thomas 2006).

2.6 Conclusions

The characterization of the nanoscale features and chemistry of glassy melt inclusions obtained in this study provides evidence of pre-nucleation clusters within the preserved amorphous material. The process of elemental reorganization within the entrapped melt involves a combination of clustering concomitant with the mechanism of shape maturation of the inclusions after their entrapment from peak metamorphic conditions. The nanoscale results obtained in this study provide a robust indication of the anatectic origin of the glassy melt inclusions and their close relationship with nanogranitoids. Integration of our results with previously published work on melt inclusions suggests that the impediment to crystallization might not only be facilitated by the small volume of these cavities, but also from the H_2O contents of the entrapped melt. Our results confirm that the study of partially to totally crystallized melt inclusions is crucial for obtaining a complete record of the wettest melts present in each setting, included volcanic arcs.

2.7 Acknowledgments

This work was supported by the Science and Industry Endowment Fund (SIEF RI13-01) and Australian Research Council support (DP160104637). The authors gratefully acknowledge use of the Microscopy and Microanalysis Facility and Geoscience Atom Probe Facility at the John de Laeter Centre (Curtin University). Tim Johnson is thanked for constructive comments on an earlier version of this manuscript and M. Gavrilenko and an anonymous reviewer are thanked for constructive reviews that helped improve the quality of the manuscript. We thank H. Keppler for the editorial handling.

2.8 References

Acosta-Vigil A., London D., & Morgan GB VI. 2012. Chemical diffusion of major and minor components in granitic liquids: implications for the rates of homogenization of crustal melts. *Lithos,* 153:308–323.

Acosta-Vigil, A., Rubatto, D., Bartoli, O., Cesare, B., Meli, S., Pedrera, A., Azor, A. & Tajčmanová, L. 2014. Age of anatexis in the crustal footwall of the Ronda peridotites, S Spain. *Lithos 210–211,* 147–167. DOI 10.1016/j.lithos.2014.08.018

Acosta-Vigil, A., Barich, A., Bartoli, O., Garrido, C.J., Cesare, B., Remusat, L., Poli, S. & Raepsaet, C. 2016. The composition of nanogranitoids in migmatites overlying the Ronda peridotites (Betic Cordillera, S Spain): the anatectic history of a polymetamorphic basement. *Contributions to Mineralogy and Petrology 171(3)*. DOI 10.1007/s00410-016-1230-3

Audétat A. & Günther D. 1999. Mobility and H2O-loss from fluid inclusions in natural quartz crystals. *Contributions to Mineralogy and Petrology*, 137, 1–14.

Audetat A. & Lowenstern J.B. 2014. Melt inclusions. In: Holland, H.D., Turekian, K.K. (Eds.), Treatise on Geochemistry, Second edition Elsevier, Oxford, pp. 143–173.

Barich, A., Acosta-Vigil, A., Garrido, C.J., Cesare, B., Tajčmanová, L. & Bartoli, O. 2014. Microstructures and petrology of melt inclusions in the anatectic sequence of Jubrique

(Betic Cordillera, S Spain): Implications for crustal anatexis. *Lithos 206–207,* 303–320. DOI 10.1016/j.lithos.2014.08.003

Barone, G., Mazzoleni, P., Corsaro, R.A., Costagliola, P., Di Benedetto, F., Ciliberto, E., Gimeno, D., Bongiorno, C. & Spinella, C. 2016. Nanoscale surface modification of Mt. Etna volcanic ashes. *Geochimica et Cosmochimica Acta 174,* 70–84. DOI 10.1016/j.gca.2015.11.011

Baronnet, A. 1993. Natural crystallization and relevant crystal growth experiments. *Progress in Crystal Growth and Characterization of Materials 26,* 1–24. DOI 10.1016/0960-8974(93)90007-Q

Bartoli, O. 2020. Characterizing fluid and melt in high-grade metamorphic rocks. In: Lecumberri-Sanchez P, Steele-McInnis M (eds) Fluid inclusions, , Short Course Ser. *Mineral Association of Canada,* 36.

Bartoli, O. & Cesare, B. 2020. Nanorocks: a 10-year-old story. *Rendiconti Lincei. Scienze Fisiche e Naturali 31(2),* 249–257. DOI 10.1007/s12210-020-00898-7

Bartoli, O., Tajčmanová, L., Cesare, B. & Acosta-Vigil, A. 2013. Phase equilibria constraints on melting of stromatic migmatites from Ronda (S. Spain): insights on the formation of peritectic garnet. *Journal of Metamorphic Geology 31(7),* 775–789. DOI 10.1111/jmg.12044

Bartoli, O., Acosta-Vigil, A. & Cesare, B. 2015. High-temperature metamorphism and crustal melting: working with melt inclusions. *Periodico di Mineralogia 84,* 591–614.

Bartoli, O., Acosta-Vigil, A., Ferrero, S. & Cesare, B. 2016a. Granitoid magmas preserved as melt inclusions in high-grade metamorphic rock. *American Mineralogist 101(7),* 1543–1559. DOI 10.2138/am-2016-5541CCBYNCND

Bartoli, O., Acosta-Vigil, A., Tajčmanová, L., Cesare, B. & Bodnar, R.J. 2016b. Using nanogranitoids and phase equilibria modeling to unravel anatexis in the crustal footwall of the Ronda peridotites (Betic Cordillera, S Spain). *Lithos 256–257,* 282–299. DOI 10.1016/j.lithos.2016.03.016

Bartoli, O. 2019. Reintegrating nanogranitoid inclusion composition to reconstruct the prograde history of melt-depleted rocks. *Geoscience Frontiers* 10(2), 517–525. DOI 10.1016/j.gsf.2018.02.002

Blum, T.B., Darling, J.R., Kelly, T.F., Larson, D.J., Moser, D.E., Perez-Huerta, A., Prosa, T.J., Reddy, S.M., Reinhard, D.A., Saxey, D.W., Ulfig, R.M. & Valley, J.W. 2018. Best Practices for Reporting Atom Probe Analysis of Geological Materials. In: Moser, D.E., Corfu, F., Darling, J.R., Reddy, S.M. & Tait, K. (eds) *Geophysical Monograph Series*. John Wiley & Sons, Inc., Hoboken, NJ, USA, 369–373. DOI 10.1002/9781119227250.ch18

Bodnar R.J. & Student. 2006. Melt inclusions in plutonic rocks: petrography and microthermometry. In: Webster, J.D. (ed.): Melt inclusions in plutonic rocks. Mineralogical Association of Canada, Short Course 36, 1-26.

Borghini, A., Ferrero, S., Wunder, B., Laurent, O., O'Brien, P.J. & Ziemann, M.A. 2018. Granitoid melt inclusions in orogenic peridotite and the origin of garnet clinopyroxenite. *Geology*. DOI 10.1130/G45316.1

Borghini, A., Ferrero, S., O'Brien, P.J., Laurent, O., Günter, C. & Ziemann, M.A. 2020. Cryptic metasomatic agent measured in situ in Variscan mantle rocks: Melt inclusions in garnet of eclogite, Granulitgebirge, Germany. *Journal of Metamorphic Geology 38(3),* 207–234. DOI 10.1111/jmg.12519

Carvalho B. B, Bartoli O., Ferri F., Cesare B., Ferrero S., Laurent R., Capizzi S. L., & Poli S. 2018. Anatexis and fluid regime of the deep continental crust: New clues from melt and fluid inclusions in metapelitic migmatites from Ivrea Zone (NW Italy). Journal of Metamorphic Geology. DOI https://doi.org/10.1111/jmg.12463

Carvalho, B.B., Bartoli, O., Cesare, B., Tacchetto, T., Gianola, O., Ferri, F., Aradi, L.E. & Szabó, C. 2020. Primary CO2-bearing fluid inclusions in granulitic garnet usually do not survive. *Earth and Planetary Science Letters 536,* 116170. DOI 10.1016/j.epsl.2020.116170

Cenki, B., Braun, I. & Bröcker, M. 2004. Evolution of the continental crust in the Kerala Khondalite Belt, southernmost India: evidence from Nd isotope mapping, U–Pb and Rb–

Sr geochronology. *Precambrian Research 134(3–4),* 275–292. DOI 10.1016/j.precamres.2004.06.002

Cesare, B., Ferrero, S., Salvioli-Mariani, E., Pedron, D. & Cavallo, A. 2009. "Nanogranite" and glassy inclusions: The anatectic melt in migmatites and granulites. *Geology 37(7),* 627–630.

Cesare B., Ferrero S., Salvioli-Mariani E., Pedron D., & Cavallo A. 2009. Nanogranite and glassy inclusions: the anatectic melt in migmatites and granulites. Geology 37: 627-630.

Cesare, B., Acosta-Vigil, A., Bartoli, O. & Ferrero, S. 2015. What can we learn from melt inclusions in migmatites and granulites? *Lithos 239,* 186–216. DOI 10.1016/j.lithos.2015.09.028

Cesare, B., Parisatto, M., Mancini, L., Peruzzo, L., Franceschi, M., Tacchetto, T., Reddy, S., Spiess, R., Nestola, F. & Marone, F. 2021. Mineral inclusions are not immutable: Evidence of post-entrapment thermally-induced shape change of quartz in garnet. *Earth and Planetary Science Letters 555,* 116708. DOI 10.1016/j.epsl.2020.116708

Clemens, J.D. 2009. The message in the bottle: "Melt" inclusions in migmatitic garnets. *Geology 37(7),* 671–672. DOI 10.1130/focus072009.1

De Geuser, F., Lefebvre, W., Danoix, F., Vurpillot, F., Forbord, B. & Blavette, D. 2007. An improved reconstruction procedure for the correction of local magnification effects in three-dimensional atom-probe. *Surface and Interface Analysis 39(2–3),* 268–272. DOI 10.1002/sia.2489

Di Genova, D., Caracciolo, A. & Kolzenburg, S. 2018. Measuring the degree of "nanotilization" of volcanic glasses: Understanding syn-eruptive processes recorded in melt inclusions. *Lithos 318–319,* 209–218. DOI 10.1016/j.lithos.2018.08.011

Di Genova, D., Brooker, R.A., Mader, H.M., Drewitt, J.W.E., Longo, A., Deubener, J., Neuville, D.R., Fanara, S., Shebanova, O., Anzellini, S., Arzilli, F., Bamber, E.C., Hennet, L., La Spina, G. & Miyajima, N. 2020. In situ observation of nanolite growth in volcanic melt: A driving force for explosive eruptions. *Science Advances 6(39),* eabb0413. DOI 10.1126/sciadv.abb0413

Esposito, R., Lamadrid, H.M., Redi, D., Steele-MacInnis, M., Bodnar, R.J., Manning, C.E., De Vivo, B., Cannatelli, C. & Lima, A. 2016. Detection of liquid H_2O in vapor bubbles in reheated melt inclusions: Implications for magmatic fluid composition and volatile budgets of magmas? *American Mineralogist 101(7),* 1691–1695. DOI 10.2138/am-2016-5689

Esteban, J.J., Cuevas, J., Vegas, N. & Tubía, J.M. 2008. Deformation and kinematics in a melt-bearing shear zone from the Western Betic Cordilleras (Southern Spain). *Journal of Structural Geology 30(3),* 380–393. DOI 10.1016/j.jsg.2007.11.010

Esteban, J.J., Tubía, J.M., Cuevas, J., Vegas, N., Sergeev, S. & Larionov, A. 2011. Peri-Gondwanan provenance of pre-Triassic metamorphic sequences in the western Alpujarride nappes (Betic Cordillera, southern Spain). *Gondwana Research 20(2–3),* 443–449. DOI 10.1016/j.gr.2010.11.006

Faure, F. & Schiano, P. 2005. Experimental investigation of equilibration conditions during forsterite growth and melt inclusion formation. *Earth and Planetary Science Letters 236(3–4),* 882–898. DOI 10.1016/j.epsl.2005.04.050

Ferrero, S., Bartoli, O., Cesare, B., Salvioli-Mariani, E., Acosta-Vigil, A., Cavallo, A., Groppo, C. & Battiston, S. 2012. Microstructures of melt inclusions in anatectic metasedimentary rocks: anatectic melt inclusions in migmatites. *Journal of Metamorphic Geology 30(3),* 303–322. DOI 10.1111/j.1525-1314.2011.00968.x

Ferrero, S., Wunder, B., Walczak, K., O'Brien, P.J. & Ziemann, M.A. 2015. Preserved near ultrahigh-pressure melt from continental crust subducted to mantle depths. *Geology 43(5),* 447–450. DOI 10.1130/G36534.1

Ferrero, S., Ziemann, M.A., Angel, R.J., O'Brien, P.J. & Wunder, B. 2016. Kumdykolite, kokchetavite, and cristobalite crystallized in nanogranites from felsic granulites, Orlica-Snieznik Dome (Bohemian Massif): not evidence for ultrahigh-pressure conditions. *Contributions to Mineralogy and Petrology 171(1).* DOI 10.1007/s00410-015-1220-x

Ferri, F., Cesare, B., Bartoli, O., Ferrero, S., Palmeri, R., Remusat, L. & Poli, S. 2020. Melt inclusions at MT. Edixon (Antarctica): Chemistry, petrology and implications for the

evolution of the Lanterman range. *Lithos* 374–375, 105685. DOI 10.1016/j.lithos.2020.105685

Fougerouse, D., Reddy, S.M., Saxey, D.W., Rickard, W.D.A., van Riessen, A. & Micklethwaite, S. 2016. Nanoscale gold clusters in arsenopyrite controlled by growth rate not concentration: Evidence from atom probe microscopy. *American Mineralogist 101(8),* 1916–1919. DOI 10.2138/am-2016-5781CCBYNCND

Frezzotti, M.-L. 2001. Silicate-melt inclusions in magmatic rocks: applications to petrology. *Lithos 55(1–4),* 273–299. DOI 10.1016/S0024-4937(00)00048-7

Gavrilenko, M., Krawczynski, M., Ruprecht, P., Li, W. & Catalano, J.G. 2019. The quench control of water estimates in convergent margin magmas. *American Mineralogist 104(7),* 936–948. DOI 10.2138/am-2019-6735

Gebauer, D., Kellermeier, M., Gale, J.D., Bergström, L. & Cölfen, H. 2014. Pre-nucleation clusters as solute precursors in crystallisation. *Chem. Soc. Rev. 43(7),* 2348–2371. DOI 10.1039/C3CS60451A

Gianola, O., Bartoli, O., Ferri, F., Galli, A., Ferrero, S., Capizzi, L.S., Liebske, C., Remusat, L., Poli, S. & Cesare, B. 2020. Anatectic melt inclusions in ultra high temperature granulites. *Journal of Metamorphic Geology 39(3),* 321–342. DOI 10.1111/jmg.12567

Giordano, D., Russell, J.K. & Dingwell, D.B. 2008. Viscosity of magmatic liquids: A model. *Earth and Planetary Science Letters 271(1–4),* 123–134. DOI 10.1016/j.epsl.2008.03.038

Höche, T. 2010. Crystallization in glass: elucidating a realm of diversity by transmission electron microscopy. *Journal of Materials Science 45(14),* 3683–3696. DOI 10.1007/s10853-010-4541-1

Holness, M.B. & Sawyer, E.W. 2008. On the Pseudomorphing of Melt-filled Pores During the Crystallization of Migmatites. *Journal of Petrology 49(7),* 1343–1363. DOI 10.1093/petrology/egn028

Humphreys, M.C.S., Kearns, S.L. & Blundy, J.D. 2006. SIMS investigation of electron-beam damage to hydrous, rhyolitic glasses: Implications for melt inclusion analysis. *American Mineralogist 91(4),* 667–679. DOI 10.2138/am.2006.1936

Karpukhina, N., Hill, R.G. & Law, R.V. 2014. Crystallisation in oxide glasses – a tutorial review. *Chem. Soc. Rev. 43(7),* 2174–2186. DOI 10.1039/C3CS60305A

Lambrecht, G. & Diamond, L.W. 2014. Morphological ripening of fluid inclusions and coupled zone-refining in quartz crystals revealed by cathodoluminescence imaging: Implications for CL-petrography, fluid inclusion analysis and trace-element geothermometry. *Geochimica et Cosmochimica Acta 141,* 381–406. DOI 10.1016/j.gca.2014.06.036

Larson, D.J., Prosa, T.J., Ulfig, R.M., Geiser, B.P. & Kelly, T.F. 2013. *Local Electrode Atom Probe Tomography*. Springer New York, New York, NY. DOI 10.1007/978-1-4614-8721-0

Le Voyer, M., Asimow, P.D., Mosenfelder, J.L., Guan, Y., Wallace, P.J., Schiano, P., Stolper, E.M. & Eiler, J.M. 2014. Zonation of H2O and F Concentrations around Melt Inclusions in Olivines. *Journal of Petrology 55(4),* 685–707. DOI 10.1093/petrology/egu003

Lowenstern J. 1995. Applications of silicate-melt inclusions to the study of magmatic volatiles. In: Magmas, Fluids and Ore Deposits (ed. Thompson, J.F.H.), pp. 71–99. Mineralogical Association of Canada, Victoria, Short Course, 23.

Malaspina, N., Alvaro, M., Campione, M., Wilhelm, H. & Nestola, F. 2015. Dynamics of mineral crystallization from precipitated slab-derived fluid phase: first in situ synchrotron X-ray measurements. *Contributions to Mineralogy and Petrology 169(3),* 26. DOI 10.1007/s00410-015-1121-z

Marques, A.F.A., Scott, S.D. & Sodhi, R.N.S. 2010. Determining major and trace element compositions of exposed melt inclusions in minerals using ToF-SIMS. *Surface and Interface Analysis 43(1–2),* 436–442. DOI 10.1002/sia.3594

Marques, A.F.A., Scott, S.D. & Sodhi, R.N.S. 2012. Time-Of-Flight SIMS (TOF-SIMS) analyses of melt inclusions. *The Canadian Mineralogist 50(5),* 1305–1320. DOI 10.3749/canmin.50.5.1305

Mazzoli, S., Martín-Algarra, A., Reddy, S.M., Sánchez-Vizcaíno, V.L., Fedele, L. & Noviello, A. 2013. The evolution of the footwall to the Ronda subcontinental mantle peridotites: insights from the Nieves Unit (western Betic Cordillera). *Journal of the Geological Society 170(3),* 385–402. DOI 10.1144/jgs2012-105

Meldrum, A., Boatner, L.A. & Ewing, R.C. 1997. Electron-irradiation-induced nucleation and growth in amorphous $LaPO_4$, $ScPO_4$, and zircon. *Journal of Materials Research 12(7),* 1816–1827. DOI 10.1557/JMR.1997.0250

Miller, M.K. & Hetherington M.G. 1991. Local magnification effects in the atom probe. Surface Science, 246, 442–449.

Mujin, M., Nakamura, M. & Miyake, A. 2017. Eruption style and crystal size distributions: Crystallization of groundmass nanolites in the 2011 Shinmoedake eruption. *American Mineralogist 102(12),* 2367–2380. DOI 10.2138/am-2017-6052CCBYNCND

Newcombe, M.E., Fabbrizio, A., Zhang, Y., Ma, C., Le Voyer, M., Guan, Y., Eiler, J.M., Saal, A.E. & Stolper, E.M. 2014. Chemical zonation in olivine-hosted melt inclusions. *Contributions to Mineralogy and Petrology 168(1),* 1030. DOI 10.1007/s00410-014-1030-6

Nicoli, G. & Ferrero, S. 2021. Nanorocks, volatiles and plate tectonics. *Geoscience Frontiers* 12(5), 101188. DOI 10.1016/j.gsf.2021.101188

Obata, M. 1980. The Ronda Peridotite: Garnet-, Spinel-, and Plagioclase-Lherzolite Facies and the P—T Trajectories of a High-Temperature Mantle Intrusion. *Journal of Petrology,* 40.

Platt, J.P., Argles, T.W., Carter, A., Kelley, S.P., Whitehouse, M.J. & Lonergan, L. 2003. Exhumation of the Ronda peridotite and its crustal envelope: constraints from thermal modelling of a *P – T* –time array. *Journal of the Geological Society 160(5),* 655–676. DOI 10.1144/0016-764902-108

Putnis, A., Prieto, M. & Fernandez-Diaz, L. 1995. Fluid supersaturation and crystallization in porous media. *Geological Magazine 132(1),* 1–13. DOI 10.1017/S0016756800011389

Reddy, S.M., Saxey, D.W., Rickard, W.D.A., Fougerouse, D., Montalvo, S.D., Verberne, R. & Riessen, A. 2020. Atom Probe Tomography: Development and Application to the Geosciences. *Geostandards and Geoanalytical Research 44(1),* 5–50. DOI 10.1111/ggr.12313

Reimer, L. & Kohl, H. 2008. *Transmission Electron Microscopy: Physics of Image Formation*. 5. ed. 587 pp. Springer, New York, NY, Springer series in optical sciences, 36.

Rickard, W.D.A., Reddy, S.M., Saxey, D.W., Fougerouse, D., Timms, N.E., Daly, L., Peterman, E., Cavosie, A.J. & Jourdan, F. 2020. Novel Applications of FIB-SEM-Based ToF-SIMS in Atom Probe Tomography Workflows. *Microscopy and Microanalysis,* 1–8. DOI 10.1017/S1431927620000136

Roedder, E. 1984. *Fluid Inclusions*. Mineralogical Society of America, Reviews in Mineralogy.

Sánchez-Rodríguez, L. & Gebauer, D. 2000. Mesozoic formation of pyroxenites and gabbros in the Ronda area (southern Spain), followed by Early Miocene subduction metamorphism and emplacement into the middle crust: U–Pb sensitive high-resolution ion microprobe dating of zircon. *Tectonophysics 316(1–2),* 19–44. DOI 10.1016/S0040-1951(99)00256-5

Scaillet, B., Holtz, F., Pichavant, M. & Schmidt, M. 1996. Viscosity of Himalayan leucogranites: Implications for mechanisms of granitic magma ascent. *Journal of Geophysical Research: Solid Earth 101(B12),* 27691–27699. DOI 10.1029/96JB01631

Schreiber, R.E., Houben, L., Wolf, S.G., Leitus, G., Lang, Z.-L., Carbó, J.J., Poblet, J.M. & Neumann, R. 2017. Real-time molecular scale observation of crystal formation. *Nature Chemistry 9(4),* 369–373. DOI 10.1038/nchem.2675

Shen, A.H. & Kepplert, H. 1997. Direct observation of complete miscibility in the albite-H_2 0 system. *Letters to Nature ,* 3.

Sorby H.C. 1858. On the microscopical structure of crystals, indicating the origin of minerals and rocks, *Quarterly Journal of the Geological Society of London.* 14, 453-500.

Steele-MacInnis, M. 2019. Seeking the most hydrous, primitive arc melts: The glass is half full. *American Mineralogist 104(9),* 1217–1218. DOI 10.2138/am-2019-7124

Steele-Macinnis, M., Esposito, R. & Bodnar, R.J. 2011. Thermodynamic Model for the Effect of Post-entrapment Crystallization on the H2O-CO2 Systematics of Vapor-saturated, Silicate Melt Inclusions. *Journal of Petrology 52(12),* 2461–2482. DOI 10.1093/petrology/egr052

Tacchetto, T., Bartoli, O., Cesare, B., Berkesi, M., Aradi, L.E., Dumond, G. & Szabó, C. 2019. Multiphase inclusions in peritectic garnet from granulites of the Athabasca granulite terrane (Canada): Evidence of carbon recycling during Neoarchean crustal melting. *Chemical Geology 508,* 197–209. DOI 10.1016/j.chemgeo.2018.05.043

Thomas, R. & Davidson, P. 2012. Water in granite and pegmatite-forming melts. *Ore Geology Reviews 46,* 32–46. DOI 10.1016/j.oregeorev.2012.02.006

Tubía J.M., Cuevas J. & Gil-Ibarguchi J.I. 1997. Sequential development of the metamorphic aureole beneath the Ronda peridotites and its bearing on the tectonic evolution of the Betic Cordillera. *Tectonophysics*, 279, 227–252.

Vurpillot, F., Bostel, A. & Blavette, D. 2000. Trajectory overlaps and local magnification in three-dimensional atom probe. *Applied Physics Letters 76(21),* 3127–3129. DOI 10.1063/1.126545

Webster, J.D. & Thomas, R. 2006. Silicate melt inclusions in felsic plutons: a synthesis and review. In: Webster JD (ed) Melt inclusions in Plutonic Rocks. *Mineral Association Canada*, Short Course Ser, vol 36, pp 165–188. *,* 25.

Webster, J.D., Geological Association of Canada & Mineralogical Association of Canada (eds). 2006. Melt Inclusions in Plutonic Rocks: Short Course Delivered in Association with the Annual Meeting of the Geological Association of Canada and the Mineralogical Association of Canada, Montreal, Quebec, 13 - 14 May, 2006. 237 pp. M*ineralogical Association of Canada*, Montreal, Short course series 36.

Xiao, Y., Lei, H., Yang, B., Wang, G., Wang, Q. & Jin, W. 2018. Nucleation and growth for magnesia inclusion in Fe–O–Mg melt. *RSC Advances 8(67),* 38336–38345. DOI 10.1039/C8RA07728B

Chapter 3

Weakening the lower crust: conditions, reactions and deformation

This chapter is published as:

Tacchetto T., Clark C., Erickson T., Reddy S.M., Bhowany K and Hand M. Weakening the lower crust: conditions, reactions and deformation. *Lithos*, 422–423, 2022. https://doi.org/10.1016/j.lithos.2022.106738

Abstract

The impact of fluid infiltration on the deformation mechanisms that facilitate the development of lower-crustal ductile shear zones is evaluated through a multiscale structural, geochemical, and thermobaric analysis undertaken across a shear zone/wall-rock interface exposed on the island of Radøy in the Bergen Arcs (western Norway). At the outcrop scale, the shear zone is characterized by a strain gradient reflected in the progressive evolution from weakly-deformed coronitic gabbroic anorthosite to finer-grained foliated amphibolite characterised by a distinct mineral lineation, shear bands, and σ-type porphyroblasts. Electron backscattered diffraction (EBSD) crystallographic orientation data from the coronitic gabbroic anorthosite define an initial stage of shear localization whereby most of the deformation is accommodated by crystal plasticity within plagioclase accompanied by grain size reduction through subgrain rotation recrystallization. As deformation proceeds, complementary to increasing fluid-rock interaction, the replacement of the anhydrous mineral assemblage results in strain partitioning and the development of a heterogeneous ductile shear zone. At the grain scale, the distinct crystallographic preferred orientation (CPO) of amphibole, epidote and kyanite suggests deformation being dominated by crystal plastic mechanisms. U-Pb age data obtained from zircon grains within the Caledonian shear zone cluster at 883 ± 3 Ma consistent with ages derived from the granulite facies assemblage. Phase equilibria modelling indicates conditions of deformation within the shear zone at ~ 600 °C and ~11kbar, consistent with mid-crustal levels at amphibolite facies conditions. Conversely, geochemical data from garnet of the shear zone characterized by the absence of Eu anomaly, point to mineralogical reactions having initially occurred at higher pressure conditions. This study highlights the key role of fluid infiltration and metamorphic reactions on strain localization processes which can facilitate the ductile deformation of the original assemblage and ultimately contribute to the rheological weakening of an anhydrous and refractory lower crust.

3.1 Introduction

The interaction between rocks and fluids during metamorphism and associated deformation plays a key role in modifying the large-scale rheological behaviour of Earth's lithosphere (Walther & Wood 1986; Austrheim 1987; Jackson *et al.* 2004). There is broad consensus that the composition of the lower continental crust is dominated by nominally-dry granulite facies rocks at high temperature and pressure conditions (Yardley & Valley 1997).

Over several decades, the idea that the stability of the lower continental crust can be controlled by the spatial and temporal availability of fluids, has been considered a critical aspect, strongly affecting the mechanisms of deformation and the dynamics of the lithosphere (Austrheim & Boundy 1994; Jackson 2002; Jackson *et al.* 2004, 2008; Scambelluri *et al.* 2017; Jamtveit *et al.* 2018b, 2019; Menegon *et al.* 2021). When rocks are anhydrous, strain-accumulation by plastic deformation mechanisms such as dislocation creep (Tullis & Yund 1989), as well as fluid-assisted diffusion (Vernon 2004), is slowed by the absence of wet intergranular interfaces (i.e., grain boundaries). On the contrary, given the high temperatures, diffusive mass transfer mechanisms (e.g., Nabarro-Herring creep; Herring 1950) can become significant. It follows that under fluid-absent conditions, the lower continental crust will behave as a mechanically "stronger" body in response to stress perturbations (Jackson *et al.* 2004).

The introduction of fluids substantially influences a wide range of mechanical properties of the rock upon deformation (Carter *et al.* 1990). For example, the presence of a free-fluid phase has the potential to generate an environment for mineral alteration and hydration reactions with the associated activation of softening mechanisms by the growth of new phases that are more susceptible to deformation (i.e., reaction softening) (White & Knipe 1978; Carter *et al.* 1990; Rubie 1990; Klaper 1990; Ingles *et al.* 1999; Stünitz & Tullis 2001; Gueydan *et al.* 2003; Oliot *et al.* 2010; Hawemann *et al.* 2019). In addition, diffusion along wet grain boundaries is faster than along dry boundaries and can enhance mechanisms such as pressure solution which has the potential to generate a significant strength reduction in a deforming rock (e.g., Elliott 1973; Rutter 1983; Wintsch & Yi 2002; Menegon *et al.* 2008; Putnis & John 2010; Wassmann & Stöckhert 2013; Mukai *et al.* 2014; Giuntoli *et al.* 2018). Consequently, the investigation of how the introduction of fluids into dry, metastable, mechanically strong crustal lithologies influences the mechanisms that lead to weakening, strain localization, and shear zone nucleation is critical to a better understanding of

lithosphere dynamics (Boundy *et al.* 1992; Ingles *et al.* 1999; Stünitz & Tullis 2001; Mancktelow & Pennacchioni 2004; White 2004; Jamtveit *et al.* 2019 and references therein). However, the imprint of these processes, and underlying mechanisms, can be easily erased by recrystallization and/or overprinting of the rocks during later stages of retrograde metamorphism and exhumation from deep crustal levels.

The Lindås Nappe of the Bergen Arcs is one of the best localities where the interplay between hydrous fluids and locally-deformed anhydrous lower crustal rocks has been preserved. The granulite facies orthogneisses of the Lindås Nappe preserve a near-complete record of the transformation from a dry granulitic lower crustal protolith into their hydrated amphibolite to eclogite facies counterparts at km–μm scales. In many places, the transition from early-stage brittle deformation and pseudotachylyte formation followed by eclogite-facies shear zone formation and retrograde hydrous amphibolite facies shear zone development can be observed within the same outcrop (e.g., Austrheim & Griffin 1985; Austrheim 2013; Bhowany *et al.* 2018; Jamtveit *et al.* 1990, 2018b). As such, the region has been the focus of numerous studies exploring the effects of hydrous fluid infiltration in dry granulitic protoliths, particularly in relation to the development of brittle and ductile structural networks that are ubiquitous throughout the region (Austrheim & Griffin 1985; Austrheim 1987; Jamtveit *et al.* 1990; Klaper 1990; Austrheim 2013; Mukai *et al.* 2014; Austrheim *et al.* 2017; Putnis *et al.* 2017; Bhowany *et al.* 2018; Jamtveit *et al.* 2018a,b, 2019; Moore *et al.* 2019; Jamtveit *et al.* 2021 and references therein). To date, work in the Lindås Nappe has primarily focused on the petrological conditions and rheological implications of the transformation of these rocks as well as the consequences that these processes have on broader-scale geodynamic processes, such as deep seismicity (Jackson *et al.* 2004; Austrheim 2013; Putnis *et al.* 2017; Jamtveit *et al.* 2018b, 2019). However, a systematic evaluation of the progressive development of the deformation microstructures and the role that fluid-enhanced metamorphic reactions play on a broad range of minerals preserved in these ductile shear zones has yet to be fully realised (e.g., Mukai *et al.* 2014).

In this study we apply a microstructural, geochemical, and petrological workflow, to investigate the transition from granulite-facies orthogneiss to a well-developed amphibolitic-facies shear zone at Isdal on the island of Radøy (western Norway). The workflow involves the application of both single mineral thermometry coupled with phase equilibrium thermobarometry and trace element geochemistry to assess the *P*–*T* (pressure–temperature) conditions of rock deformation and mineral growth. The data generated in this study enable

a systematic documentation of the progressive evolution of deformation, and the role that progressive fluid infiltration plays in enhancing mineral transitions.

3.2 Geological setting and sample petrography

The samples investigated in this study belong to the Lindås Nappe of the Bergen Arcs, a suite of dominantly Meso-Neoproterozoic orthogneisses recrystallized at granulite-facies conditions (~ 800-900 °C and < 10 kbar) during the Sveconorwegian orogeny at ~ 930 Ma ± 50 Ma (Bingen *et al.* 2001) (Figure 3.1). Rocks of the Lindås Nappe were subsequently reworked during the ~ 430-410 Ma Caledonian orogeny. Caledonian deformation was spatially limited to shear zones, occurred at amphibolite-eclogite facies conditions, and has been inferred to be accompanied by fluid infiltration (Austrheim & Griffin 1985; Bingen *et al.* 2001; Putnis *et al.* 2017; Bhowany *et al.* 2018; Jamtveit *et al.* 2018b).

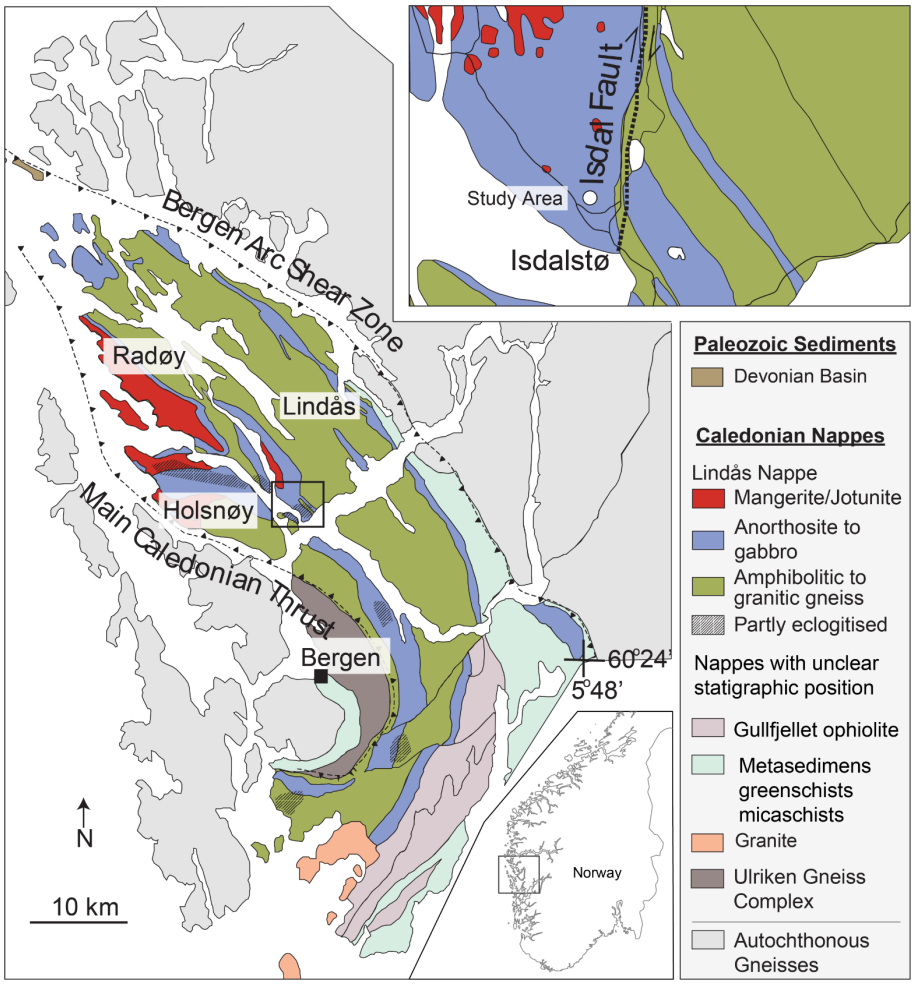

Figure 3.1 Geological map of the Bergen Arcs showing the main lithologies and structures (modified after Mukai *et al.* 2014). The location of the sampled outcrop is indicated by a white dot in the inset.

The specific focus of this study is a set of samples collected from adjacent to and within a shear zone that overprints a coronitic gabbroic anorthosite exposed along route 565 near Isdal on the island of Radøy (Figures 3.2a, b).

The gabbroic anorthosite shares a transitional contact with the high-strain domain and it preserves, in the most distal parts, the original macroscopic textural features of the main gabbroic anorthosite ('undeformed metagabbro', Figure 3.2b). The rock is coarse-grained and comprises centimetre-sized clinopyroxene, garnet, and plagioclase. Garnet forms coronae that surround the clinopyroxene separating it from the plagioclase. Within the outcrop, the foliation of the rock is defined by weakly aligned clinopyroxene grains and can be traced continuously in the shear zone where it becomes subparallel to the shear zone margin. This reorientation of the foliation is accompanied by a corresponding mineralogical change manifested by the replacement of the coronitic garnet and clinopyroxene by aligned amphiboles (Figure 3.2b).

The shear zone is characterized by a decrease in grain size compared to the adjacent granulite. The steeply north-east dipping planar foliation of the shear zone (75°/018°; dip/dip direction) is well-developed and defined by melanocratic layers of elongated amphibole that alternate with feldspar-dominated leucocratic bands of variable width (Figure 3.2c). Centimetre-size porphyroblasts of amphibole aggregates are present within the foliation, and these represent the replacement of the coronitic clinopyroxene and garnet observed in the wall rock of the shear zone (Figure 3.2c). The amphiboles define a well-developed stretching lineation (75°/340°; plunge/trend) on foliation surfaces (Figure 3.2d). In places, the foliation within the shear zone is offset along shear bands mostly composed of plagioclase and finer-grained amphibole (Figure 3.2e).

Thermodynamic modelling and U-Pb ages on similar amphibolite-facies lithologies found in the Lindås Nappe have constrained the thermobarometric conditions associated with the Caledonian overprint of the regional orthogneisses to temperatures of ~ 590-730 °C and 10-14 kbar at ~ 450-430 Ma (Boundy *et al.* 1996; Glodny *et al.* 2008; Jamtveit *et al.* 2018b).

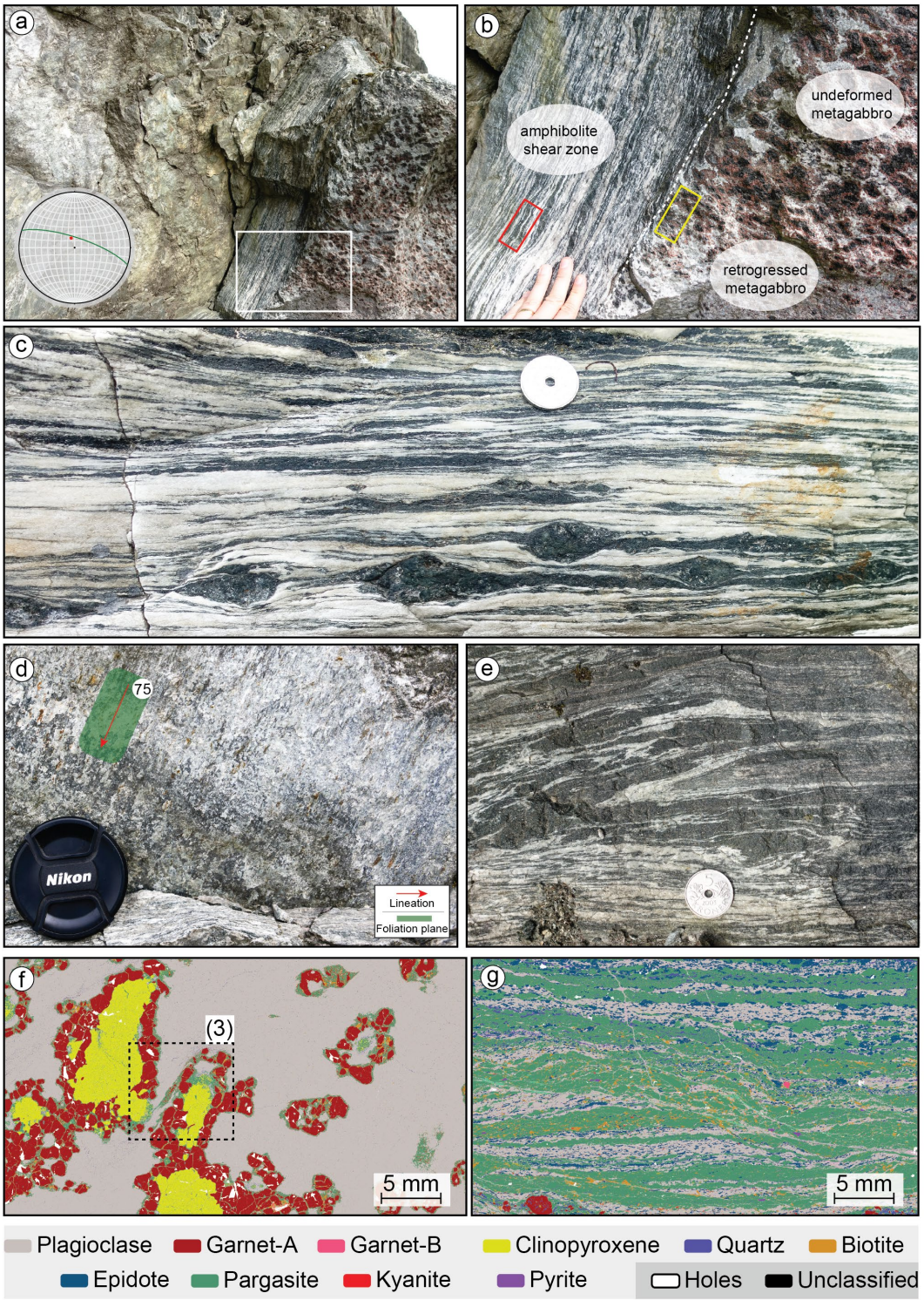

Figure 3.2 (a) Outcrop photograph and stereographic diagram (equal-area and lower hemisphere projection) displaying the orientation of amphibolitic foliation and lineation direction. (b) Close-up of the shear zone area indicated by the white box in (a) showing the relationship between the different lithologies. Sample locations are indicated by red and yellow boxes. (c) Close-up of the amphibolitic foliation defined by the alternation of mafic and leucocratic layers in which coarse-grained relict clinopyroxene and garnet porphyroclasts occur as an aggregate of amphibole. (d) Field evidence of mineral lineation visible on the foliation plane defined by elongated amphiboles and epidote. (e) Isoclinal shear bands in the amphibolite domain indicative of pre-existing foliation reworking. (f, g) TIMA phase maps of the investigated gabbro anorthosite and shear zone respectively. Black dashed box [(3)] in (f) indicates the area showed in Figure 3.3.

3.3 Analytical techniques

3.3.1 Scanning Electron Microscopy

Backscattered electron (BSE) imaging, electron backscattered diffraction (EBSD) and Energy Dispersive Spectrometry (EDS) qualitative analyses were acquired using Tescan Mira3 and Tescan Clara field emission scanning electron microscopes (FESEM) housed at the John de Laeter Centre at Curtin University. Microstructural EBSD analyses were performed using 20 kV, 3-5 nA and orientation data acquired with both high sensitivity HKL NordlysNano and Symmetry Oxford detectors and indexed using AZtec software. The step size used in the orientation maps ranged between 0.7 and 6 μm for large area maps (LAM) and from 0.25 to 0.5 μm for the zircon grains. EBSD orientation data were post-processed using Aztec Crystal 1.1. software after applying a standard noise reduction procedure involving the removal of misindexed "wild spikes" and a 6 nearest neighbour zero solution algorithm. The M-index is insensitive to the number of measured grains (Skemer *et al.* 2005) and is used to estimate the fabric strength of weaker mineral crystallographic preferred orientations (CPO). Orientation analyses and CPO of minerals present within the shear zone were studied in an oriented thin section prepared in the x-z plane of finite strain, where x represents the direction parallel to lineation and z is the direction normal to foliation. Cathodoluminescence (CL) imaging of zircon grains was undertaken using an accelerating voltage of 10 kV and ca. 18 mm working distance on the Tescan MIRA3 FESEM. Phase maps and mineral mass percentages of the whole investigated samples were obtained by using a Tescan Integrated Mineral Analyser (TIMA) operated in dot-map mode at 3μm pixel size operating at 25 kV and 5nA.

3.3.2 Laser Ablation Inductively coupled mass spectrometry

3.3.2.1 Zircon

Zircon grains were imaged prior to in situ thin section analysis. Collection of LA–ICP–MS data was performed at the GeoHistory Facility in the John de Laeter Centre, Curtin University, Perth, Australia. Individual zircon grains were ablated using an ASI RESOlution

M-50A-LR, incorporating a Compex 193nm Ar-F excimer laser attached in Split Stream (LASS) mode (Kylander-Clark *et al.* 2013) to a Nu Instruments Nu-Plasma2 HR multi-collector ICP-MS and Agilent 7700 quadrupole ICP-MS. The Nu-Plasma2 was set up to collect U and Th on faraday cups whilst all Pb and Hg peaks were measured using high sensitivity ion counters. The Agilent quadrupole was set up to collect the following trace elements, each of which was monitored for 0.03 s: ^{29}Si, ^{31}P, ^{49}Ti, ^{89}Y, ^{90}Zr, ^{93}Nb, ^{147}Sm, ^{151}Eu, ^{157}Gd, ^{159}Tb, ^{163}Dy, ^{165}Ho, ^{166}Er, ^{168}Tm, ^{172}Yb, ^{175}Lu, ^{178}Hf, ^{204}Pb, ^{232}Th, ^{238}U. Analyses were performed at a laser repetition rate of 6 Hz and a 23 μm spot diameter at 26% attenuation, resulting in a power output of ~2 J/cm^2 at the sample surface. A single analysis involved 2 cleaning pulses, a long initial background collection of 40 s, followed by 25 s of ablation, and 15 s of washout time. A long background collection on the highly sensitive ion counters is essential for the use of the "step forward" baseline collection on the Iolite software. Laser gas flows of 320 ml/min He and 1.2 ml/min N were used, with matched mass spec argon gas flows of ~1 l/min on the Nu Plasma2 and ~1 l/min on the Agilent.

The time-resolved mass spectra were reduced using the U_Pb_Geochronology4 data reduction scheme in Iolite (Paton *et al.* 2011). The primary reference material used in this study was 91500 (1062.4 ± 0.4 Ma; Wiedenbeck *et al.* 1995) with Plesovice (337.1±0.4 Ma; Sláma *et al.* 2008), GJ1 (601.9 ± 0.7 Ma; Jackson et al., 2004) and Curtin University internal standard KLDF (553.3 ± 0.3 Ma) used as secondary age standards. Calculation of the ^{206}Pb/^{238}U ages for the secondary zircon age standards was used to calculate an additional uncertainty required for a single analytical population in these materials. This additional uncertainty of ~1% was incorporated into the calculation of the ^{206}Pb/^{238}U age of the unknowns. For the calculation of other weighted means and the plotting of concordia diagrams an additional 0.5% uncertainty was added to the analytical uncertainties for the ^{207}Pb/^{235}U and ^{207}Pb/^{206}Pb ratios. Internal standardization for trace elements used a Zr concentration of 43.14 % in zircon standard GJ-1 (Jackson *et al.* 2004). Data is provided in the Supplementary Table 3.B.5 and 3.B.6.

3.3.2.2 Garnet

Rare earth and other trace element compositions of garnet were measured by LA–ICP–MS using an ASI RESOlution M-50A-LR, incorporating a Compex 193nm Ar-F excimer laser with an Agilent 7700 mass spectrometer at Curtin University. Garnet grains were analysed in a polished thin section using a 75 μm spot size and an ablation period of 40

seconds with a repetition rate of 7 Hz. NIST glasses (610, 612, 614) (Pearce *et al.* 1997) were used as reference materials, with NIST 610 as the primary standard. Calibration of trace elements in garnet assumed stoichiometric Si (18 wt%). Time-resolved data were processed following each session using the Iolite software (Paton *et al.* 2011), which permits the detection of data affected by the analysis of mineral inclusions. Data is provided in the Supplementary Table 3.B.9 and Table 3.B.10.

3.3.2.3 Rutile

Rutile trace element analyses were measured by LA-ICP-MS using an ASI RESOlution M-50A-LR, incorporating a Compex 193nm Ar-F excimer laser with an Agilent 8900 triple quadrupole ICP. The Agilent 8900 quadrupole was set up to monitor trace elements for 0.03 s; ^{24}Mg, ^{27}Al, ^{28}Si, ^{44}Ca, ^{45}Sc, ^{49}Ti, ^{51}V, ^{52}Cr, ^{57}Fe, ^{60}Ni, ^{63}Cu, ^{66}Zn, ^{89}Y, ^{90}Zr, ^{93}Nb, ^{95}Mo, ^{118}Sn, ^{121}Sb, ^{178}Hf, ^{181}Ta, ^{182}W, ^{204}Pb, ^{206}Pb, ^{207}Pb, ^{208}Pb, ^{232}Th, ^{238}U. The laser employed a repetition rate of 4 Hz at a 50 μm spot size, and at a 26% beam attenuation leading to a fluence of ~2 J/cm^2. Each analysis consisted of two cleaning pulses, a background of 40 s, followed by 35 s of ablation and 15 s of washout time. Laser gas flow of 320 ml/min He, and 1.2 ml/min N were mixed with an argon gas flow of ~1 l/min. Trace element calibration was conducted using ^{47}Ti as the internal standard, assuming 59.94 wt%, and BHVO (^{24}Mg, ^{27}Al, ^{28}Si, ^{44}Ca, ^{45}Sc, ^{52}Cr, ^{57}Fe, ^{60}Ni, ^{63}Cu, ^{66}Zn, ^{89}Y, ^{118}Sn, ^{232}Th) and R10 (^{49}Ti, ^{51}V, ^{90}Zr, ^{93}Nb, ^{95}Mo, ^{121}Sb, ^{178}Hf, ^{181}Ta, ^{182}W, ^{204}Pb, ^{206}Pb, ^{207}Pb, ^{208}Pb, ^{238}U) were used as the primary RMs using the TraceElements data reduction scheme within Iolite4. Data is provided in the Supplementary Table 3.B.8.

3.3.3 Mineral equilibria forward modelling and Zr-in-rutile thermometry

Whole-rock chemical analyses used as the basis for the calculation of metamorphic phase equilibria were measured by XRF at Franklin and Marshall College, Pennsylvania. Major element oxides were analysed by fusing 0.4 g of the powdered sample with lithium tetraborate (Boyd & Mertzman 1987). Obtained values are provided in the Supplementary Table 3.B.4.

Phase equilibria modelling was performed using THERMOCALC v.3.333 in the Na_2O–CaO–FeO–MgO–Al_2O_3–SiO_2–H_2O–TiO_2–O (NCFMASHTO; where 'O' is a proxy

for Fe_2O_3) chemical system using the 'ds5' thermodynamic dataset (Holland & Powell 1998). The activity–composition (*a–x*) models used were as follows: amphibole (Diener *et al.* 2007; Diener & Powell 2012); clinopyroxenes (Green *et al.* 2007; Diener & Powell 2012); chlorite, talc and epidote–clinozoisite (Holland & Powell 1998); garnet and biotite (White *et al.* 2007); plagioclase and K-feldspar (Holland & Powell 2003); ilmenite and chloritoid (White *et al.* 2000). Based on the abundance of hydrous minerals in the rock sample (e.g., clinozoisite and biotite), the measured LOI was used as a proxy for H_2O content during modelling.

Zr-in-rutile thermometry was applied to multiple grains using the calibration of Tomkins *et al.* (2007). Rather than simply taking the highest temperature determined from each dataset, we follow the proposal by Tomkins *et al.* (2007) and use a conservative estimate of temperature as given by the upper quartile (the top of the box) of a box-and-whisker plot. These authors suggested the uncertainty associated with this value be approximated as ± 30°C or half the interquartile range if this is larger, based on the rationale that the real uncertainty relates to the scatter in the data rather than to analytical uncertainties combined with calibration uncertainties, which are likely to be much smaller than ± 30°C. Calculated temperatures are provided in the Supplementary Table 3.B.2.

3.4 Results

3.4.1 Petrological observation and microstructures

In thin section, the coronitic gabbroic anorthosite is coarse-grained comprising a mineral assemblage of plagioclase (~ 60 wt%), garnet (~ 18 wt%), and clinopyroxene (~ 11 wt%) (Figure 3.2f). The matrix of the rock is mostly composed of medium- to fine-grained plagioclase in which millimetre-sized crystals of clinopyroxene occur surrounded by garnet coronae (Figure 3.3). Elongated crystals of pargasitic amphibole (~ 8 wt%) variably replace clinopyroxene and form thin rinds around garnet grains (Figure 3.3). Minor phases comprise kyanite, quartz, epidote and biotite (Supplementary Table 3.B.3). Locally, plagioclase and amphibole grains are elongated along small, SW-NE trending microshear zones that are localized between larger grains of clinopyroxene and garnet and characterized by deformation microstructures that are absent in the host-rock away from the shear zone margin (Figures 3.3b, c). A dramatic decrease in the grain size of plagioclase is observed

towards the centre of the microshear domain where the pre-existing coarser grains of the wall rock are gradually replaced by a fine-grained (10-20 μm) aggregates of recrystallized plagioclase (Figure 3.3). Along the microshear domain, deformation microstructures of coarser-grained plagioclase include patchy and undulose extinction under crossed polarized light (Figure 3.3c). Bundles of elongated pargasite amphibole (< 100 μm) are observed enveloping garnet porphyroblasts with their long axis parallel to the maximum principal strain direction. Within these plagioclase-rich domains, bundles of clinozoisite are formed at the expense of the former plagioclase of the rock (Figure 3.3c). Locally, kyanite, clinozoisite, and quartz are mostly found aligned along grain boundaries.

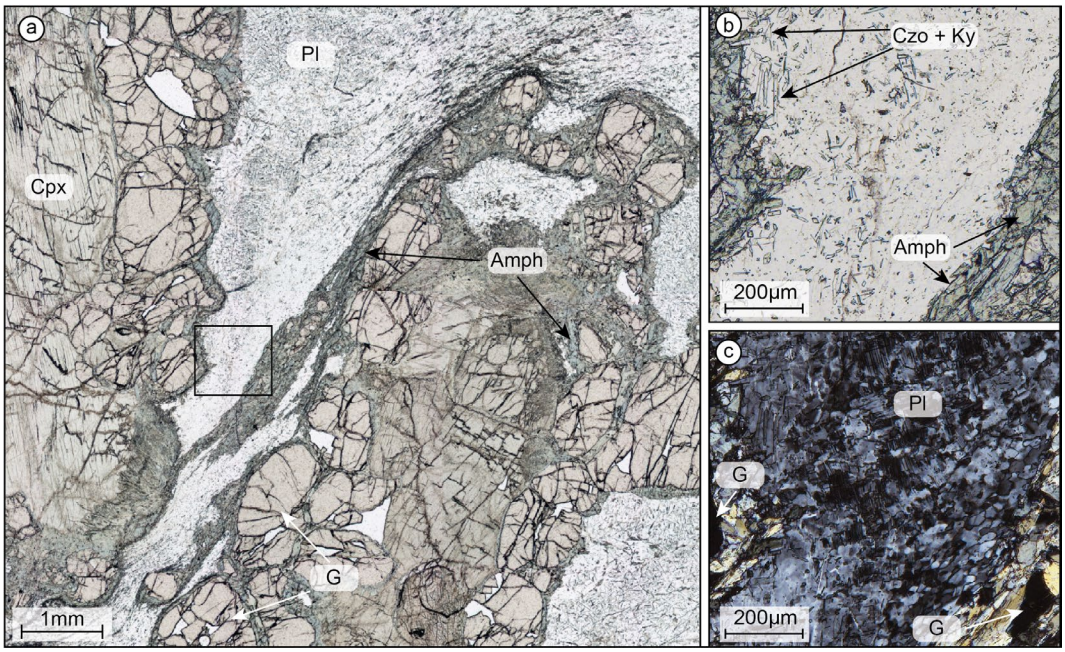

Figure 3.3 (a) Optical plane-polarized photomicrographs of the investigated portion of the gabbro anorthosite. (b) Optical plane and crossed-polarized (c) photomicrographs of the area of the microshear zone domain indicated by the black box in (a). (a), (b) and (c) represent the areas of the sample investigated by EBSD orientation analysis.

The shear zone is characterized by the dominance of a mineral assemblage composed of coarse-grained pargasitic amphibole (~ 54 wt%), plagioclase (~ 23 wt%), clinozoisite (~ 11 wt%), quartz (~ 4 wt%), and garnet (~ 0.6 wt%), with minor kyanite, clinopyroxene, and biotite (Figure 3.2g; Supplementary Table 3.B.3). At the outcrop to thin section scale, the foliation of the rock is defined by an interlayering of melanocratic amphibole-rich and leucocratic plagioclase-rich domains (Figure 3.4). Elongated lens-shaped crystals of greenish amphibole dominate the mafic domain, with the larger grains exhibiting mineral fish-like geometries with the upper and lower margins of the grains oriented sub-parallel to the

lineation and transected by a set of subparallel shear bands which define a distinguishable S-C fabric, where C-planes are aligned parallel to shear zones boundaries (Figure 3.4). The leucocratic domains are composed of quartz and polygonal grains of plagioclase in which poikilitic garnet porphyroblasts (G-A) occur in minor amounts and are enclosed by aggregates of amphibole and clinozoisite of the rock foliation (Figures 3.2g, 3.4c). Within the garnet porphyroblasts, quartz and rutile represent the most common mineral inclusions. A second generation of garnet (G-B) is also visible within the matrix of the sheared rock. Petrographically, they are characterized by smaller grain size and the absence of inclusions (Figures 3.2g, 3.4c). X-ray EDS data indicate that garnets of the shear zone are not chemically zoned (Supplementary Figure 3.B.1). However, G-A displays higher concentrations of Ca, Fe and Mg compared to G-B (Supplementary Figures 3.B.1, 3.B.2; Supplementary Table 3.B.1). Biotite in the rock is restricted to narrow domains associated with shear bands.

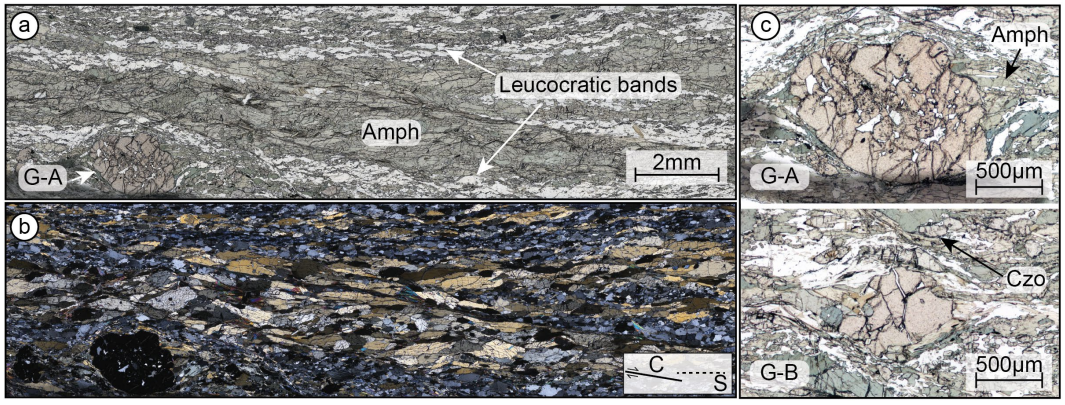

Figure 3.4 (a,b) Optical plane-polarized and crossed-polarized photomicrographs of the investigated portion of the shear zone within the amphibolite sample. (a) and (b) represent the area of EBSD orientation analyses. (c) Plane polarized light images of type A and B garnets.

Zircon grains are generally < 100 μm in length (with most of the grains ranging between 10 to 50 μm) and are associated with the amphibole-rich domains where the long axes of the larger crystals tend to be aligned with the main foliation. CL imaging shows that crystals are characterized by irregular or patchy zoning (Figure 3.5).

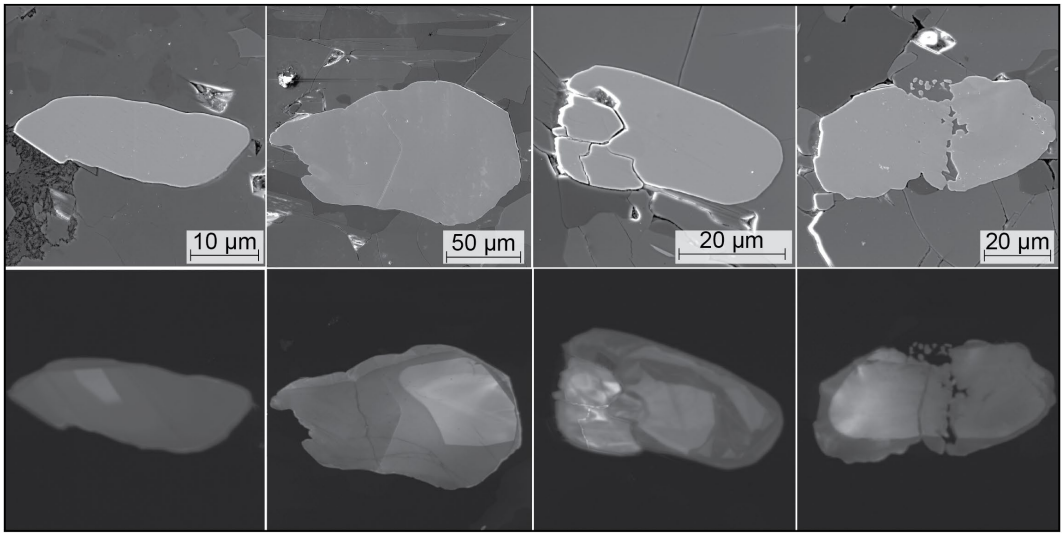

Figure 3.5 BSE-SEM (top) and cathodoluminescence (bottom) images of analysed zircon from the shear zone. In the images the longer axes of the grains are subparallel to the rock lineation.

In the oriented thin section, kinematic markers are represented by σ-type porphyroblasts of garnet in which strain shadows are composed of a finer polycrystalline aggregate of amphibole and plagioclase. These microstructures together with the shape of the mica-fish-like amphibole grains are consistent with a dextral direction of shear with respect to the thin section orientation (Figure 3.4).

3.4.2 Trace element geochemistry and geochronology

3.4.2.1 Garnet

Rare earth element (REE) abundances of the investigated samples were determined for 57 garnet grains selected from both the shear zone and the host granulite. Representative trace element concentrations are compiled in the Supplementary Table 3.B.1 and plotted on chondrite normalised REE plots in Figure 3.6a. The full dataset is provided in the Supplementary Tables 3.B.9 and Table 3.B.10.

The majority of garnets from the host granulite are characterized by a distinctive positive Eu anomaly (Eu/Eu* = 5.9 average) in the chondrite-normalized patterns and low-LREE abundances. A general flat to slightly negative slope is defined by the HREE (Figure 3.6a; Supplementary Table 3.B.1).

The REE patterns obtained from both G-A and G-B within the shear zone are characterized by a strong enrichment in HREE (Lu_N/Sm_N = 0.2–4.5) (Figure 3.6a) relative to the wall-rock garnet. There is a progressive increase in concentration from light to intermediate lanthanides with a pronounced Sm maximum (up to ~ 5 ppm). G-A generally shows higher Ca concentrations compared to G-B (Supplementary Figure 3.B.2; Supplementary Table 3.B.1). Contrarily, the latter shows higher values of Y (~ 100 ppm average) and Sm (~ 4 ppm average) compared to G-A (Supplementary Table 3.B.1). When compared with the anorthositic gabbro, garnets from the shear zone generally display the highest concentrations of Y as well as middle- to heavy-REE.

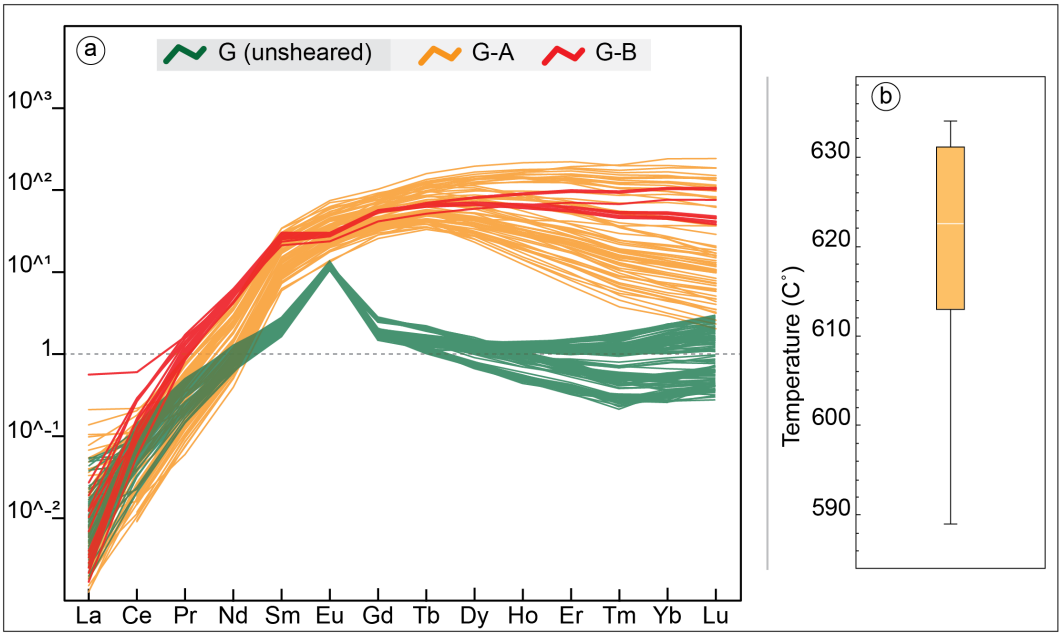

Figure 3.6 (a) Comparison between granulite and amphibolite-facies garnet trace element REE patters. (b) Box and Whiskers plot displaying Zr-in-rutile temperature estimates for the amphibolite lithology.

3.4.2.2 Rutile

Zr concentrations were determined from grains found in the amphibolite sample to determine the syn-deformational temperature conditions**.** Zirconium concentrations in the analysed rutile grains range between 130 and 240 ppm. The results of the calculations yielded an average crystallization temperature of 619 ± 26 °C (Figure 3.6b; Supplementary Table 3.B.2). The full dataset is provided in the Supplementary Table 3.B.8.

3.4.2.3 Zircon

Forty-eight U-Pb analyses from 21 zircon grains from the shear zone produced a weighted mean $^{206}Pb/^{238}U$ age of 883 ± 3 Ma (MSWD = 2.3; Figures 3.7a, b). No age difference was detected between the different domains of zircon grains. For the age calculations, only the grains that overlapped concordia with 2σ uncertainties were used. The chondrite normalised REE patterns yield flat middle to heavy REE (M–HREE) slope, slight enrichment in HREE (Lu_N/Sm_N = 4–42, av. 23), and a general positive Ce anomaly (Figure 3.7c). Europium anomaly (Eu/Eu*) varies from weakly negative (0.7–0.9) to positive (up to 3.4, av. 1.4) (Supplementary Table 3.B.1). The full dataset is provided in the Supplementary Tables 3.B.5, 3.B.6 and 3.B.7.

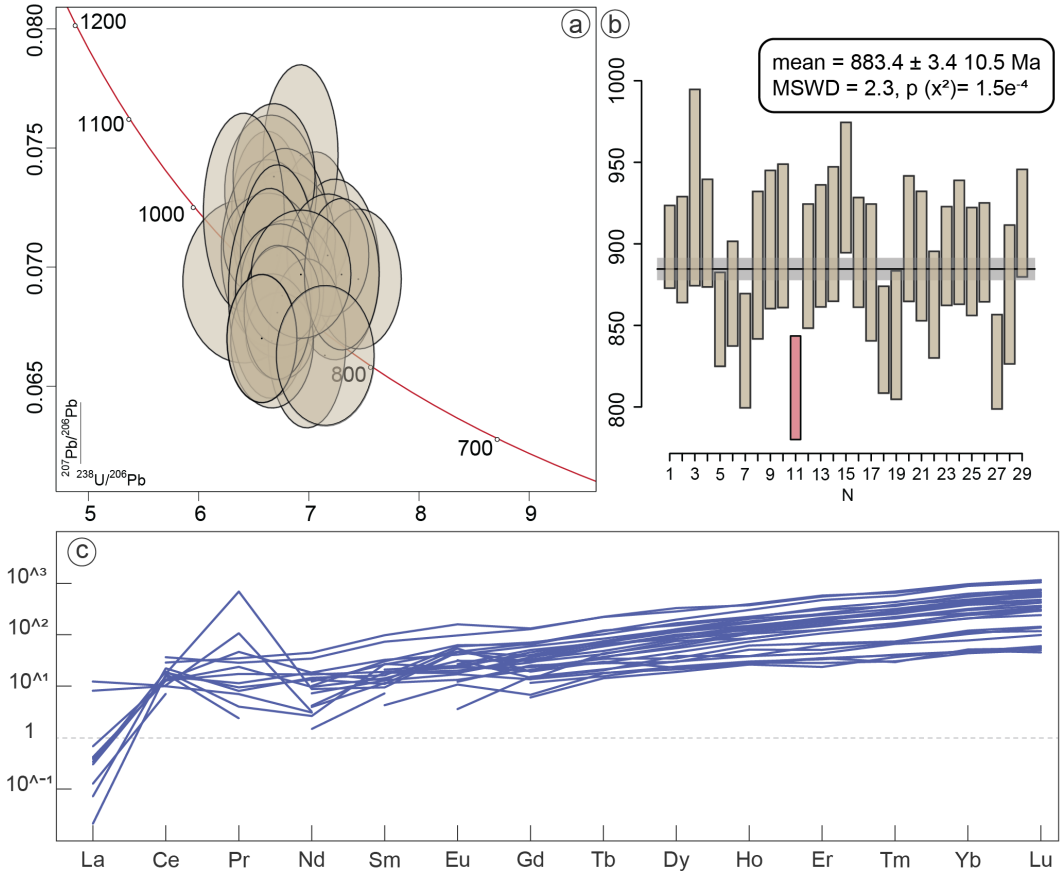

Figure 3.7 U-Pb and REE concentration data for phorphyroclastic zircons in the shear zone obtained via LA-ICP-MS analysis. (a) U-Pb concordia diagram where ellipses are representing 2σ uncertainty. (b) Weighted mean age of individual analysis. Red box indicates age outliner. (c) Trace elements REE patterns of the analysed zircons.

3.4.3 EBSD orientation analysis

3.4.3.1 Coronitic gabbroic anorthosite

The microstructures of the microshear domains observed within the overprinted granulite sample were investigated by EBSD orientation mapping and representative results are shown in Figures 3.8, 3.9 and 3.10.

In the LAM of the granulite from outside the shear zone, amphibole crystals appear distributed as ~ 75 μm rims at garnet-plagioclase phase boundaries and as ~ 600 μm thick layer separating coarser clinopyroxene and plagioclase grains. Acicular aggregates of amphibole surround garnet porphyroclasts (Figure 3.9). The variation of the amphibole orientations decreases within the high-strain domain. Here, aggregates of amphibole grains surrounding relict grains of garnet, display a general alignment of the longer axes along the principal SW-NE stretching direction of the shearing domain (Figures 3.9c, Supplementary Figure 3.B.3). The pole figures for the grains within the microshear zone show a CPO with maxima of orientation scattered along the [100] and [001] crystallographic directions (Supplementary Figure 3.B.3).

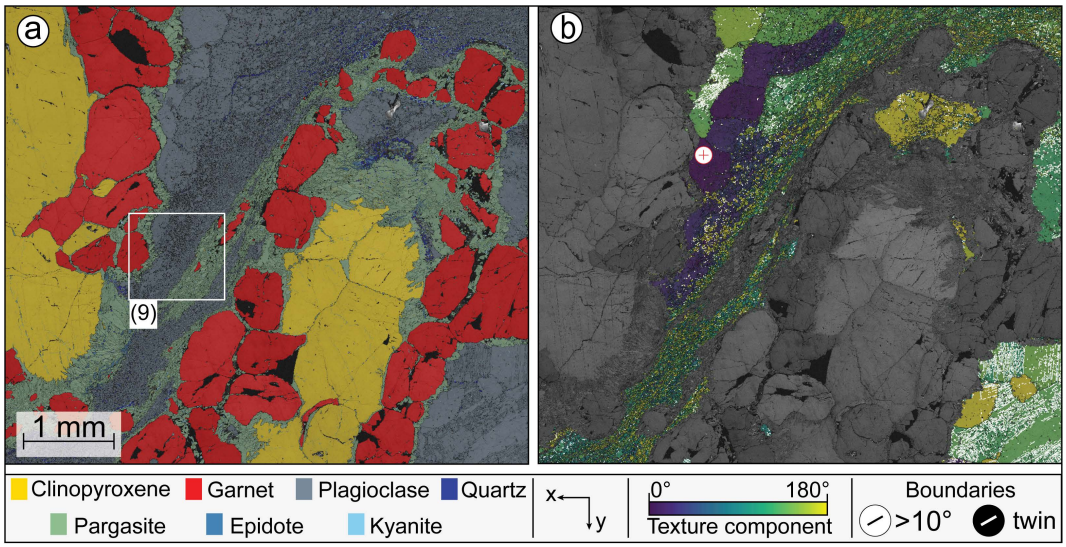

Figure 3.8 Microstructure analysis of the gabbro anorthosite microshear domain. (a) Phase map obtained by automated EBSD mapping at 6 μm spacing. White box [(9)] indicates the area of detailed EBSD analysis performed at a smaller step size. (b) Plagioclase grain reference orientation deviation map obtained by EBSD mapping. Each pixel is colour coded based on the deviation angle relative to the reference point indicated by a red cross in the map. High-angle boundaries (>10 °) are plotted in black, and twin boundaries (<010>180°) are plotted in white.

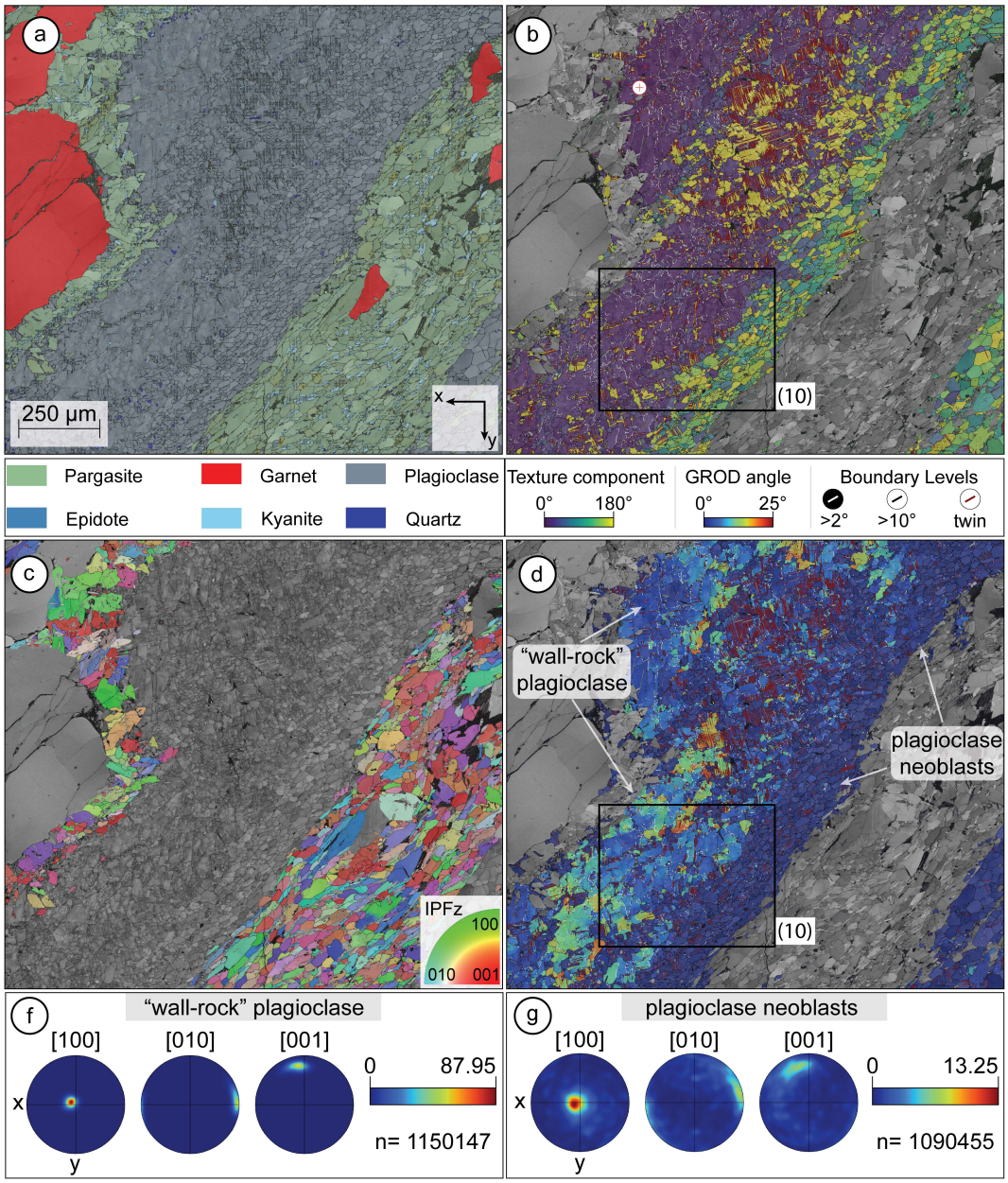

Figure 3.9 Microstructure analysis of area (9) obtained by EBSD data. (a) Phase map of the investigated area obtained by automatic mapping at 0.7 µm spacing. (b) Plagioclase grain reference orientation deviation map (texture component) relative to the reference point indicated by a red cross in the map. Low-angle boundaries (2-10°) are plotted in white, high-angle boundaries (> 10°) are plotted in black. Twin boundaries (<010>180°) are plotted in red. Black box [(10)] indicated the area showed in Figure 10. (c) Inverse Pole Figure (IPFz) EBSD map for amphibole. (d) GROD-angle orientation map of plagioclase in the micro-shear domain. Black box [(10)] indicated the area showed in Figure 3.10. (f, g) The orientation of both plagioclase wall-rock and neoblast grains are presented as contoured pole figures (equal area and lower hemisphere). The colour coding indicates the density of data points. "n" represents the number of grains.

The plagioclase is characterized by grain size variations from coarse-grained (< 500 µm; "wall-rock" grains) to very fine-grained (< 20 µm) towards the inner side of the microshear domain (Figures 3.8b, Supplementary Figure 3.B.4). An EBSD orientation map acquired within the microshear domain reveals that the wall-rock grains are characterized by

the preservation of polysynthetic twins, the development of subgrain boundaries, and lattice distortion (Figures 3.9b, d; 3.10). Pole figures of the wall-rock plagioclase show a strong CPO (Figure 3.9f). Toward the inner side of the microshear zone, the larger deformed plagioclase grains pass into an interconnected aggregate of individual fine-grained strain-free neoblasts (Figures 3.9b, d). These new grains are characterized by a foam texture with straight to curved boundaries exhibiting 120° triple junctions (Figures 3.10a, b). These finer grains show a weak shape preferred orientation (SPO) with a slight elongation along the SW-NE direction of the microshear domain. In places, tapered deformation twin boundaries are visible at the contact between grains (Figure 3.10). The orientation maps show a progressive scattering of crystallographic orientation of the plagioclase neoblasts away from the orientation of the wall-rock grains, also appreciable in the pole figures (Figure 3.9g).

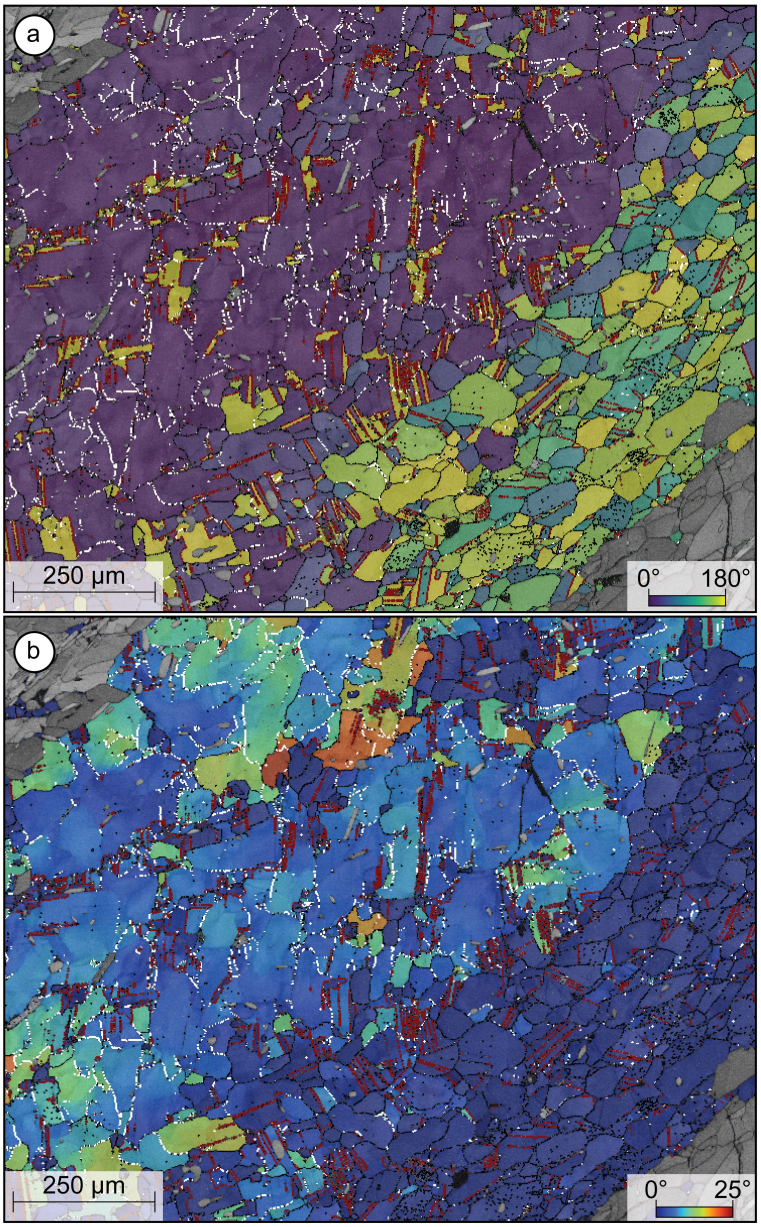

Figure 3.10 Microstructure analysis of area (10) obtained by EBSD data. (a) Plagioclase grain reference orientation deviation map (texture component) relative to the reference point indicated by a red cross in Figure 3.9. (b) GROD-angle orientation map of plagioclase of area (10). Low-angle boundaries (2-10°) are plotted in white, high-angle boundaries (> 10°) are plotted in black. Twin boundaries (<010>180°) are plotted in red.

3.4.3.2 Shear zone domain

In the LAM, the shear zone is dominated by bands of coarse-grained (> 500 μm) elongated crystals of amphibole displaying a shape preferred orientation (SPO) characterized by their long axes oriented subparallel to the rock lineation (Figures 3.11a, b). These amphibole-rich layers are locally separated by leucocratic domains of finer-grained plagioclase. Internally, larger grains are characterized by lattice distortion (up to 10°) and sub-grains. Intracrystalline deformation increases towards the edges of shear bands (Figures 3.11c).

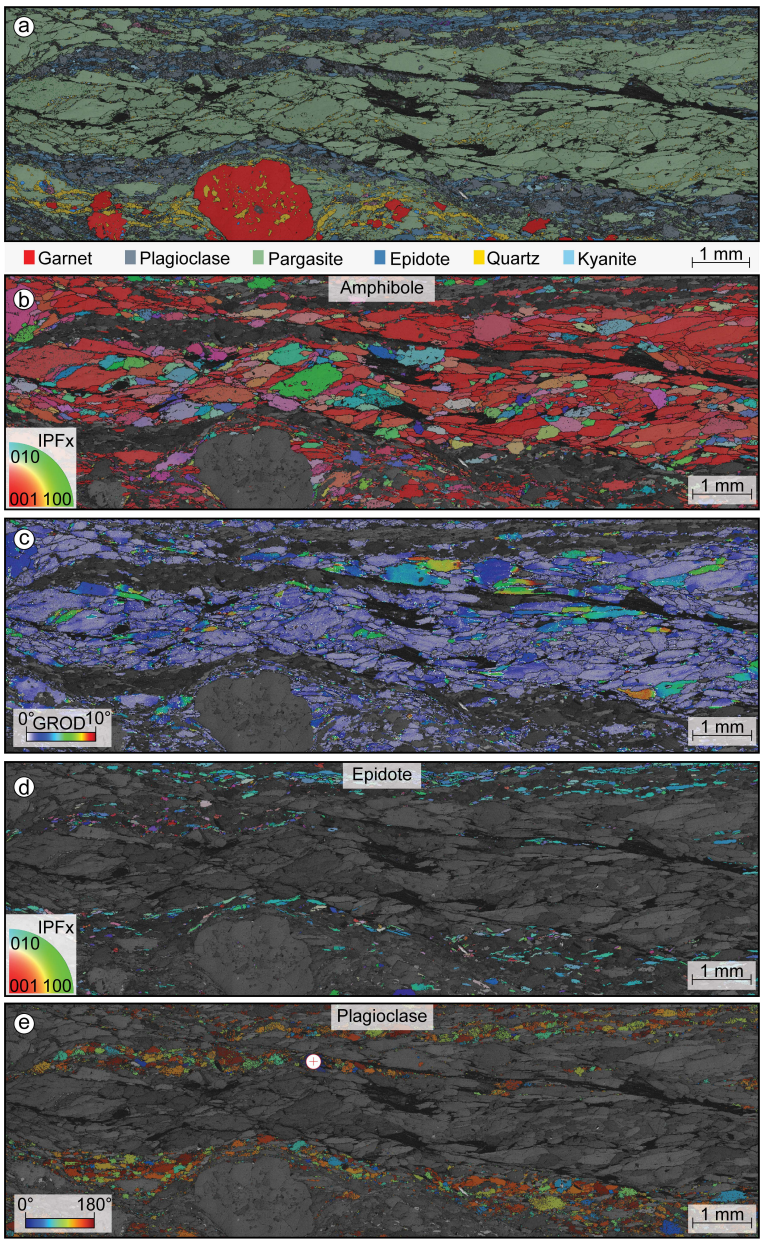

Figure 3.11 Microstructure analysis of the shear zone. (a) Large area phase map of the investigated area obtained by automatic mapping at 6 μm spacing. (b) Inverse Pole Figure (IPFx) EBSD map for amphibole. (c) Grain Reference Orientation Deviation (GROD)-angle orientation map of amphibole. Each pixel is colour coded based on the relative angular deviation from the local misorientation to the mean orientation of the grain. (d) Inverse Pole Figure (IPFx) EBSD map for epidote. (e) Plagioclase grain reference orientation deviation map relative to the reference point indicated by a red cross in the map. High-angle boundaries > 10° are plotted in black.

The amphibole grains record a strong CPO characterized by the alignment of the [001] axes subparallel to lineation and [100] normal to the foliation plane (Figure 3.12). The homogeneous fabric development of amphibole within the shear zone is also emphasised by the homogenous colour distribution in the IPFx orientation maps (Figure 3.11b).

Epidote in the shear zone records a CPO with the [010] axes aligned subparallel to the shear direction (Figure 3.12). [001] axes form a poorly-defined maximum normal to the foliation with the [100] axes defining a girdle (Figure 3.12). Kyanite is scattered along the entire shear zone domain, and it shows a developed CPO characterized by [001] axes aligned sub-parallel to the foliation and [100] axes normal to the foliation (Figure 3.12). In the shear zone, the plagioclase displays a weaker preferred orientation compared to what is observed in the microshear domain of the anorthositic gabbro. In the pole figures, a weak clustering of the [001] axes is subparallel to the foliation normal (Figure 3.12). A fabric strength of M=0.423 is calculated for the plagioclase crystals within the shear zone.

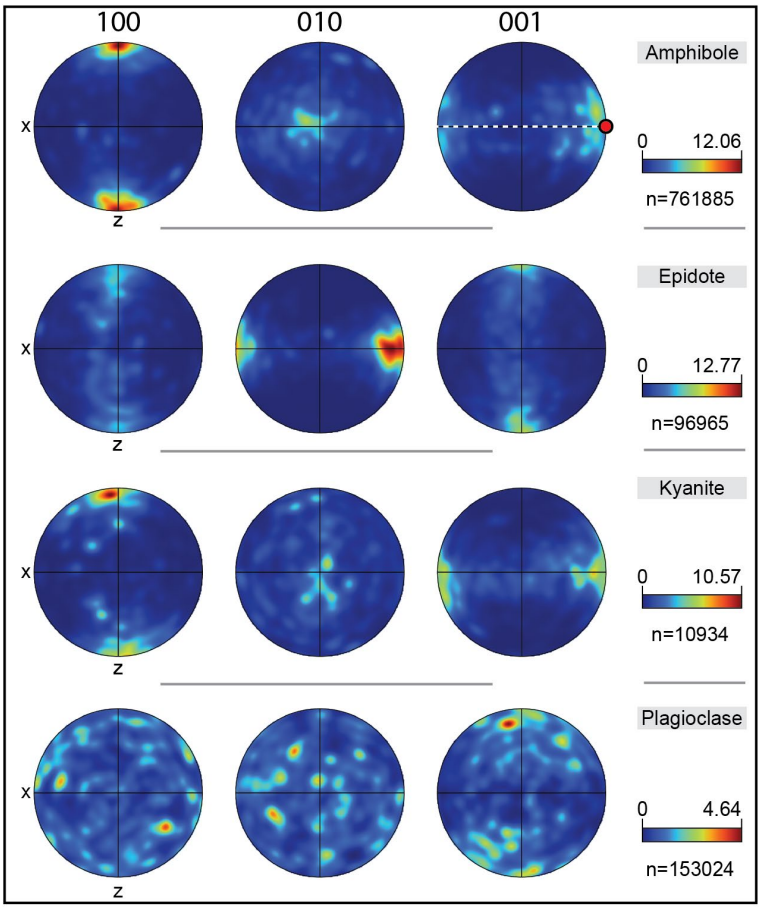

Figure 3.12 Pole figures of amphibole, epidote, kyanite and plagioclase in the shear zone. All the pole figures are presented in the lower hemisphere using an equal-area projection in the sample coordinate system (x-z) where x is the direction parallel to the lineation of the rock. The orientation of the foliation is indicated by the white dashed line, and the lineation is shown by the red dot. The colour coding indicates the density of data points. "n" represents the number of measurement counts.

3.4.3.3 Zircon

Within the shear zone, zircon grains vary from undeformed to showing lattice distortion and low-angle boundary formation (Figure 3.13). Crystallographic misorientation is generally localized to the tips of zircon grains where low-angle grain boundaries predominate (Figure 3.13). Fractures are also observed oriented at high angles to the long axes of the grains. Most of the analysed grains show clustering of misorientation axes parallel to the [111] and [112] directions (Figure 3.13). A general increasing dispersion of the orientations of crystallographic axes is observed with increasing intracrystalline deformation.

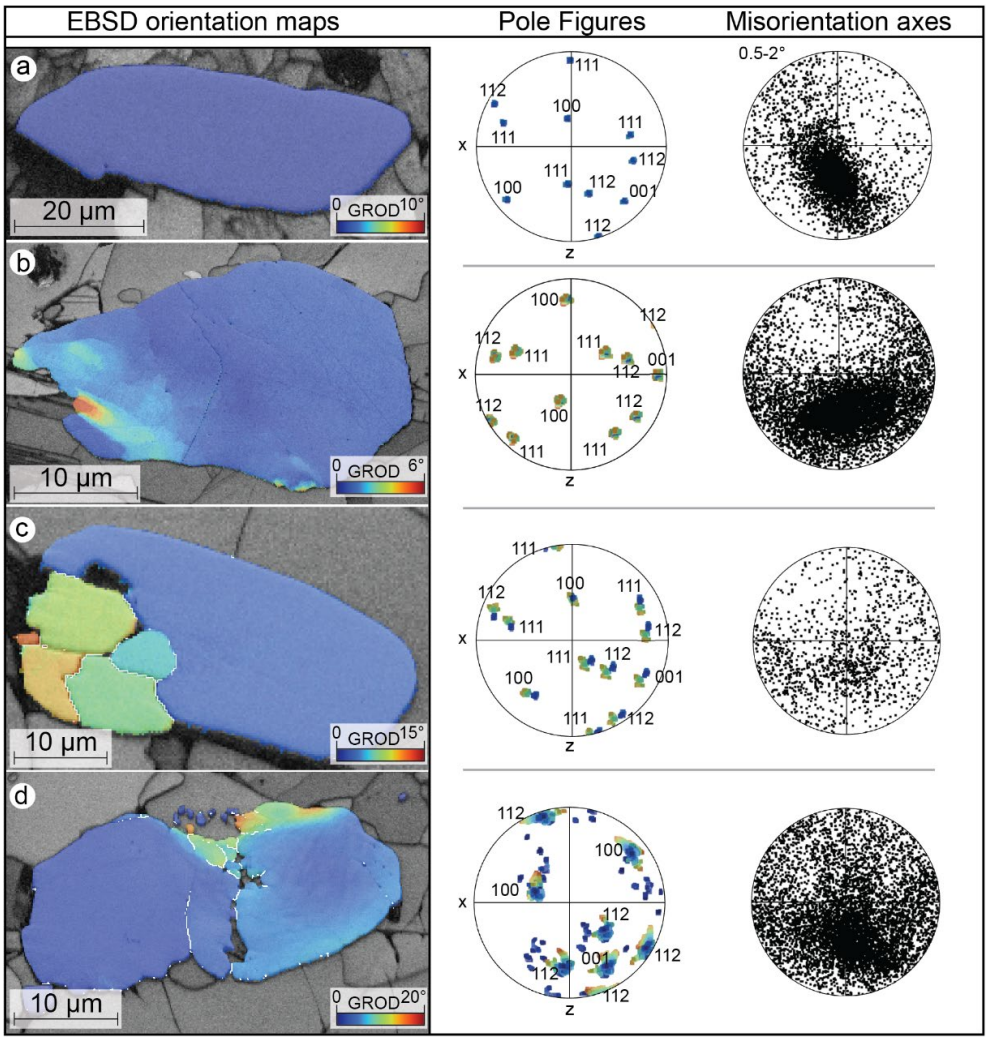

Figure 3.13 Zircon grains EBSD orientation maps (a-d) and stereographic projections of crystallographic data. (a-d) Grain Reference Orientation Deviation (GROD)-angle orientation map. Each pixel is colour coded based on the relative angular deviation from the mean orientation of the grain. Low-angle boundaries (>2°) are plotted in white. (*right)* Pole figures of major crystallographic planes for every data point indexed on the map. Colours correspond to misorientation scales. Plots of misorientation axes for 0.5 – 2° interval. All the plots are lower hemisphere equal area stereographic projections in the sample coordinate system (x-z) where x is the direction parallel to the lineation of the rock.

3.4.4 *P–T* conditions

A *P–T* pseudosection was calculated for the sample representative of the shear zone and presented in Figure 3.14. The preserved stable mineral assemblage within the shear zone is garnet, plagioclase, amphibole, and epidote with minor kyanite, quartz and rutile. The calculation predicts that the peak mineral assemblage is stable within a quadrivariant field that consists of *g-amph-ep-pl-zo-ru-q-ky* located in the high-pressure low-temperature side of the phase diagram (Figure 3.14). This stability field corresponds to *P–T* conditions of 570 to 650 °C at pressures of < 11 to 13 kbar.

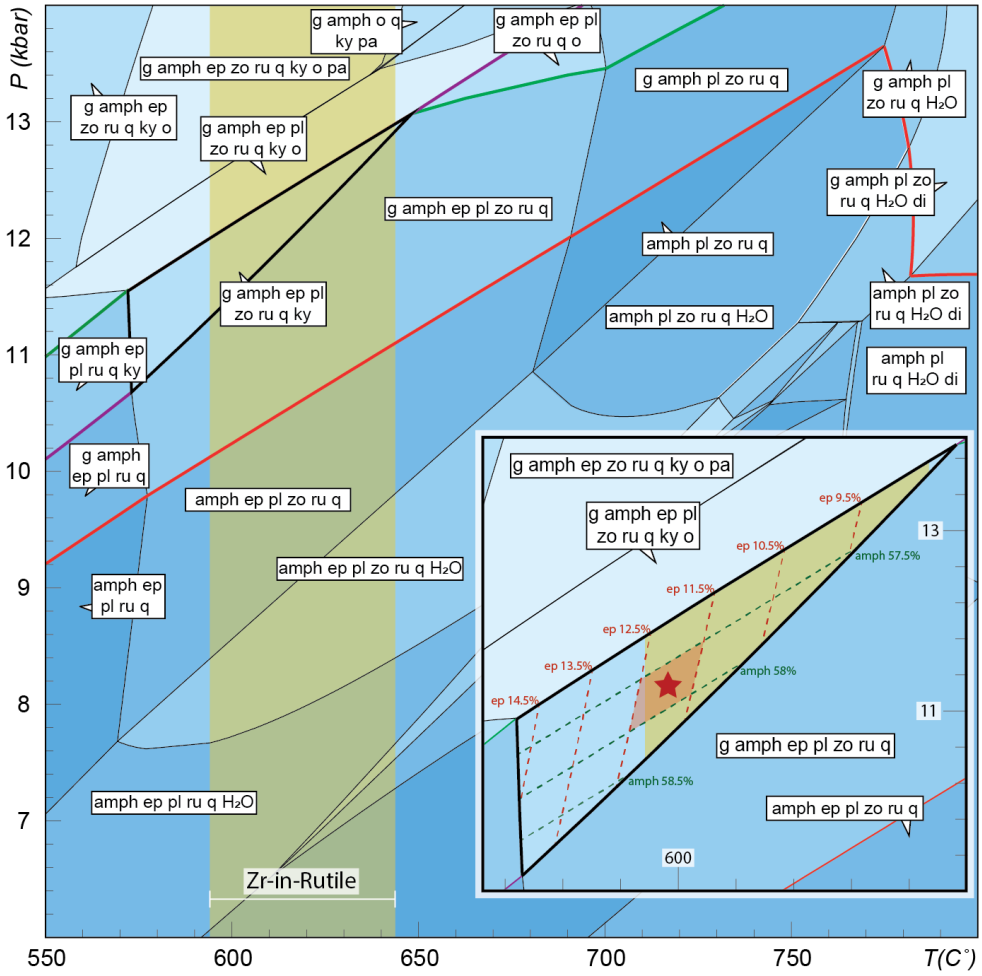

Figure 3.14 P-T section for the shear zone calculated in NCFMASHTO system. Red line is used to indicate garnet-in curve; purple line for kyanite-in curve and green line for omphacite in curve. The orange shaded field reflects the range of temperature obtained by Zr-in-rutile thermometry. Black polygon displays the inferred P-T conditions for the coexistence of the mineral assemblage observed in the rock. The inset shows a close-up of the inferred stability field integrated with isopleths indicating modal percentages of amphibole and epidote obtained from TIMA mapping of the samples. The orange shaded field corresponds to the range of Zr-in-rutile temperatures. The red shaded field corresponds to the modal abundances of pargasite and epidote in the shear zone. Red star indicates the inferred PT conditions of shear zone development.

3.5 Discussion

3.5.1 Conditions of shear zone formation

Phase equilibria modelling of the shear zone sample was key to obtain a *P–T* framework for the deformation and associated fluid-rock interaction. In the modelled *P–T* window, the preserved stable mineral assemblage is stable from 570 °C to 650 °C at pressures of < 11 to 13 kbar. A further temperature constraint is provided by the Zr-in-rutile thermometry which yields a temperature of 619 ± 26 °C. The close textural link between the occurrence of rutile, quartz and the amphibole lineation suggests that rutile formed at equilibrium during the deformational event (Supplementary Figure 3.B.5). This temperature range redefines the estimated conditions for the development of the preserved mineral assemblage in the shear zone from ~ 600 to 650 °C and 11-13 kbar (Figure 3.14). In addition to this, modal abundances for pargasite (57.7 wt%) and epidote (12.3 wt%), obtained from TIMA analyses and normalized with respect to the stable mineral assemblage, intersect with the preserved mineral assemblage further constraining the estimated conditions to ~ 600 °C and ~ 11 kbar (Figure 3.14; Supplementary Table 3.B.3). These conditions are consistent with mid- to lower-crustal levels and upper amphibolite to lower eclogite facies metamorphic conditions for the development of the shear zone at Isdal. These results are in good agreement with *P–T* estimates of < 700°C and 9-12 kbar previously obtained on petrologically similar lithologies found in the Bergen Arcs (Boundy *et al.* 1996; Moore *et al.* 2019; Jamtveit *et al.* 2021 and reference therein). These conditions have been interpreted to represent the deformation conditions of a lower-grade amphibolite facies overprint that occurred during the waning stages of the Caledonian orogeny and potentially linked to the exhumation of the terrane (Boundy *et al.* 1996; Moore *et al.* 2019).

In this study, analysis of REE concentrations for the garnets in the shear zone reveals that the two populations of grains (G-A and G-B) are geochemically distinct. In particular, G-A lacks an Eu anomaly, which becomes slightly negative for G-B. This is consistent with garnet in the shear zone originally forming at higher pressure conditions, in the presence of a minor modal amount of plagioclase in the case of G-A or in its absence during the growth of G-B (Rubatto 2002). Particularly for this bulk composition would be at typical eclogite facies conditions (Newton & Smith 1967). Similar amphibolite facies reworking of an eclogitic protolith is documented elsewhere in the Lindås Nappe and is associated with the

later stages of a clockwise evolution of the anorthositic granulite during the Caledonian Orogeny (Andersen *et al.* 1991; Boundy *et al.* 1992, 1996; Bingen *et al.* 2001; Raimbourg *et al.* 2005; Glodny *et al.* 2008; Bhowany *et al.* 2018). Therefore, the geochemical data obtained in this study, in combination with phase equilibria modelling, are consistent with the mineral assemblage observed in the amphibolite shear zone representing a younger, lower pressure recrystallization stage of the rock, originally formed at higher pressures under eclogite facies conditions. In this scenario, the crystallization of the amphibolite would therefore represent the final recorded stage of the retrograde metamorphic path of the rock suggesting that the shear zone continued to develop under amphibolite facies conditions of < 650 °C and < 13 kbar.

3.5.2 The role of fluids in enhancing replacement reactions

Petrographic and geochemical investigations conducted on the samples collected on Isdal exhibit clear evidence of the essential role of fluids in the retrogression of the original anhydrous granulite facies assemblage to amphibolite (Figure 3.2). From the retrogressed granulite into the shear zone, the unreacted protolith is progressively replaced by a hydrated mineral assemblage throughout the replacement of clinopyroxene and garnet by amphibole and epidote, which become pervasive in the high-strain domain (Figure 3.2).

In the coronitic gabbro anorthosite, the incipient stage of this transformation is manifested by the development of rims of amphibole around coarser grains of garnet (Figures 3.3, 3.9). Similarly, this reaction layer is visible at the interface of clinopyroxene and plagioclase. This observation indicates that the fluid phase required to destabilize the granulitic assemblage infiltrated the rocks along grain boundaries enhancing localized replacement reactions. This is consistent with previous observation conducted on these rocks where sharp reaction fronts of amphibole replacing the clinopyroxene along grain boundaries have been interpreted as the result of dissolution-precipitation (pressure solution) enhanced by the presence of an intergranular fluid phase (Mukai *et al.* 2014; Putnis *et al.* 2017).

In the shear zone, both the mineralogy and the original texture of the rock are completely replaced by strongly elongated mineral aggregates dominated by hydrous minerals (Figure 3.2). The close textural relationship between the well-aligned fabrics displayed by amphibole, epidote, and the kinematic markers of the rock suggests that the development of the rock foliation took place during pervasive overprinting of the dry protolith in the

presence of a fluid phase. This interpretation is consistent with the general interpretation of syn-deformation fluid infiltration suggested for the hydration of the Lindås Nappe (Austrheim 1987; Jamtveit *et al.* 1990).

3.5.3 Mineral deformation during shearing

The weakly deformed coronitic gabbro records deformation microstructures characterized by the development of microshear domains restricted between larger porphyroblasts of clinopyroxene and garnet (Figures 3.3, 3.9). In particular, coarser plagioclase within these microdomains is characterized by the development of subgrain boundaries, followed by a decrease in grain size and progressive crystallographic orientation variation towards the inner sides of the microshear domain (Figures 3.9, 3.10). The elongated fine-grained aggregate of recrystallized plagioclase records a well-developed crystallographic preferred orientation, primarily inherited from the strained parental wall-rock grains (Figure 3.9). In plagioclase, the transition from brittle faulting to dislocation creep strongly depends on temperature, pressure, strain rates and water activity, where temperature is considered to have the most important effect (Tullis & Yund 1992; Stünitz *et al.* 2003). At amphibolite facies conditions, plagioclase undergoes a dramatic change in rheology where both grain boundary diffusion creep and dislocation creep can accommodate strain, the latter resulting in the formation of strong crystallographic preferred orientations (Vernon 1975; Ji & Mainprice 1990; Tullis *et al.* 1996; Stünitz *et al.* 2003; Mancktelow & Pennacchioni 2004; Svahnberg & Piazolo 2010). The microstructural relationships between the coarse-grained plagioclase and the neighbouring recrystallized aggregate therefore suggest a progressive reorganization of the parental plagioclase by dislocation creep, leading to recovery and recrystallization promoting the formation of new, smaller, and oriented dislocation-free plagioclase neoblasts.

The microstructures observed in the shear zone record a strong fabric preserved within the majority of the minerals of the amphibolitic assemblage. In particular, pronounced crystallographic preferred orientations are evident in amphibole and to a minor extent in epidote and kyanite (Figure 3.11). The mechanisms of deformation of amphibole are dominantly controlled by the metamorphic conditions and the applied stress (e.g., Ko & Jung 2015). Generally, the development of crystallographic preferred orientations of amphibole within medium- to high-grade metamorphic rocks is attributed to deformation

accommodated by crystal plasticity (e.g., dislocation creep, Skrotzki 1992). On the other hand, amphibole SPOs and CPOs in the absence of crystal plastic substructures, have been associated with mechanisms such as dissolution-precipitation (Pearce *et al.* 2011; Giuntoli *et al.* 2018), oriented grain growth and rigid body rotation during dissolution creep (Getsinger & Hirth 2014). In this study, however, elongated grains of amphibole display microstructures associated with regions of enhanced intracrystalline distortion, subgrain formation and fish-like geometries (Figure 3.11c). Moreover, the alignment of the [001] axes of amphibole subparallel to lineation and [100] normal to the foliation plane suggests its CPO being associated with the operation of (100) [001] slip system (Type I CPO; Ko & Jung 2015). Slip along [001] in amphibole is among the most common type found in natural systems and it is preferentially activated under high-pressure conditions and relatively high temperature (Getsinger & Hirth 2014). Similarly, the alignment of the [010] axis of epidote parallel to the shear direction is consistent with what reported in experimental deformation of epidote under medium- to high-shear strain conditions (Park *et al.* 2020). Hence, based on the above observations, the documented microstructures in the amphibole from the shear zone are consistent with CPOs generated by dislocation creep, indicating that a strong component of crystal plastic deformation also being active in the shear zone.

Despite the occurrence of conjugate sets of shear bands, and contrarily to what observed in the coronitic gabbro, in the shear zone the pole figures of plagioclase do not display the presence of a crystallographic preferred orientation (Figures 3.11, 3.12). However, the general shape elongation associated with the high fabric strength (M-index= 0.423) suggests that plagioclase grains in the high-strain domain are not completely random, but instead, they record a weaker CPO compared to the other minerals within the matrix (Figure 3.12). If crystal plasticity is the only mechanism of deformation occurring in the shear zone, plagioclase crystals should record a more evident crystallographic preferred orientation. Despite the coarser grain size, the stronger preferred orientation displayed by the other minerals compared to plagioclase can be attributed to a preferential alignment of tabular crystals (e.g., amphibole and epidote) to the stretching direction. This, therefore, does not exclude that a component of granular flow (e.g., diffusive mass transfer) may be present as a concomitant mechanism during deformation with no strong crystallographic control on the plagioclase grain shape.

3.5.4 Crystal plasticity at Isdal: a change of perspective

The microstructures and the crystallographic evolution of the plagioclase feldspars present within the amphibolite shear zone exposed at Isdal have been the subject of a previous investigation by Mukai *et al.* (2014). In their EBSD analyses, the authors showed that plagioclase feldspars within the shear zone are randomly distributed. Conversely, a short-range CPO is indicated by nearest-neighbour misorientations and interpreted to be inherited from pre-existing plagioclase grain orientations. Based on these observations, the authors concluded that pressure solution is the dominant acting deformation mechanism, and that there is little to no contribution of crystal plasticity within the amphibolitic shear zone (Mukai *et al.* 2014; Putnis *et al.* 2017).

In this study, we extend the microstructural results obtained by Mukai *et al.* (2014) by performing large area orientation analyses on multiple minerals of both gabbroic anorthosite and amphibolite assemblages. Contrary to previous observations, EBSD analyses demonstrate the widespread development of subgrain boundaries and intracrystalline lattice distortion both within the plagioclase of the retrogressed metagabbro (Figure 3.10), and in the amphibole of the shear zone (Figure 3.11). In addition, most of the minerals record strong SPOs and CPOs which are consistent with the operation of known natural slip systems (Figures 3.9, 3.12).

The development of CPOs within recrystallized aggregates as well as the alignment of the crystallographic axes with the shear plane and shear direction are mostly generated by crystal plastic behaviour due to dislocation creep (Passchier & Trouw 2005; Bestmann *et al.* 2006). Contrarily, in the absence of subgrain formation, evidence of CPOs development has also been reported as being promoted by dissolution-precipitation mechanisms (e.g. Bons & den Brok 2000; Menegon *et al.* 2008; Pearce *et al.* 2011; Giuntoli *et al.* 2018). For example, pressure solution has been demonstrated to be able to generate CPOs by topoaxial growth on parental grains and nucleation of new grain with similar crystallographic orientation with no crystal plasticity contribution (Giuntoli *et al.* 2018). At Isdal however, there are several observations indicating that the deformation and CPOs development are not dominated by dissolution-precipitation. The strong component of shear displacement visible at the outcrop scale is strongly supported by a well-developed mineral lineation on the foliation plane, subparallel shear bands, σ-type porphyroclasts and fish-like geometries (Figure 3.2). The observed mineral lineation is in agreement with the EBSD data obtained in this study, translated at the grain scale by the development of strong minerals CPOs. In addition, the

drastic reduction in plagioclase grain size accompanied by the development of previously unobserved dislocation microstructures (i.e., subgrain boundaries) is a further compelling indication of deformation occurring by crystal plasticity (Passchier & Trouw 2005).

On the other hand, the microstructures displayed by the analysed zircons found within the shear zone are characterized by various degrees of crystallographic distortion marked by crystal bending and rotation around crystallographic axes (Figure 3.13). These features are consistent with dynamic recrystallization dominated by dislocation creep (Reddy *et al.* 2007). In addition to this, most of the zircon grains in the shear zone are found oriented with their longer axes parallel to the stretching direction (x) and a progressive clustering of the misorientation axes parallel to the foliation axes (y) (Figure 3.13). Geochronology obtained from these zircon grains shows a mean $^{206}Pb/^{238}U$ age of 883 ± 3 Ma (Figure 3.7) which is consistent with ages derived from the granulite facies assemblage (Bingen *et al.* 2001). Moreover, zircon REE record weakly negative to positive europium anomalies, which are also consistent with its growth during the high-temperature Grenvillian metamorphism in the absence of new plagioclase (Rubatto 2002). Hence, the observed zircon deformation microstructures are unlikely to be representative of the original weakly foliated granulitic protolith. On the contrary, this is strongly indicative of a progressive component of rigid body rotation of the zircon grains, as expected in the presence of a non-coaxial deformation (Lloyd *et al.* 1997; Reddy & Buchan 2005; Kaczmarek *et al.* 2011).

Therefore, although pressure solution is likely a dominant mechanism driving the early stages of transformation of the original anhydrous assemblage (Mukai *et al.* 2014; Putnis *et al.* 2017), considering all the above observations we here alternatively interpret the shear zone representing a progressive evolution of grain-scale microstructures in the ductile regime by a dominant mechanism of dislocation creep accompanied by dynamic grain rotation recrystallization. Moreover, the drastic increase in mass percentage of hydrous phases resembles the higher availability of fluids within the shear zone. The introduction of a large amount of fluids would also enable diffusion creep as an additional deformation mechanism which would facilitate the effective deformation (Jamtveit *et al.* 2019).

3.5.5 The interplay between fluid infiltration and enhanced deformability

In this study, the progressive development of the heterogeneous ductile shear zone can be directly observed in a continuous spatial relationship moving from unaltered portions

of the anorthositic protolith towards the high-strain amphibolitic domain, both at the outcrop and micro-scale. From the observations of the microstructures, it is clear that the transformation of the anhydrous mineral assemblage has significantly enhanced the deformability of the aggregate. In a homogeneous protolith, such as the anorthositic granulite, previous studies have shown that the nucleation and development of shear zones are for the most part driven by softening reactions and strain localization mechanisms that occur at the microscale, largely triggered by the presence of mobile fluids (White *et al.* 1980; Kirby 1985; Klaper 1990; Ingles *et al.* 1999; Mancktelow & Pennacchioni 2004, 2005; Oliot *et al.* 2010; Jamtveit *et al.* 2019). Moreover, the presence of water has been previously liked with shear zone development as it increases the efficiency of grain boundary migration, recrystallization, and grain size reduction (Mancktelow & Pennacchioni 2004; Zhou *et al.* 2008). Chemical alteration and/or fluid-assisted softening mechanisms triggered by fluid infiltration towards or within a shear zone, may in turn lead to strain localization and enhanced ductility of the deforming aggregate (Segall & Simpson 1986; Austrheim 2013; Getsinger *et al.* 2013). Here, we propose a sequence of mechanisms where the retrogressed metagabbro represents a snapshot of the incipient stages of protolith deformation which then evolved, through a combination of metamorphic recrystallization and deformation in the presence of fluids, into a ductile shear zone.

The microstructures observed in the retrogressed metagabbro indicate that in the undeformed homogeneous dry granulitic protolith, shear localization initiated between larger crystals of clinopyroxene and garnet resulting in the formation of microshear domains (Figures 3.3, 3.8). The percolation of fluids is mostly restricted along grain boundaries, where static replacement of an anhydrous granulite facies assemblage takes place by dissolution-precipitation reactions (Mukai *et al.* 2014; Putnis *et al.* 2017), without any substantial changes in bulk rock mineralogy. At this stage, as observed from the EBSD microstructures, most of the bulk deformation is partitioned into plagioclase, which therefore behaves as a "soft" mineral, accommodating most of the deformation by crystal plastic processes resulting in a strong CPO that resembles the original orientation of the parental wall-rock grains. The strong rheological contrast between the different mineral phases constituting the coronitic gabbro is, therefore, expected to result in a strain partitioning where the weaker matrix would accommodate most of the deformation (Bell 1985; Vernon 2004; Menegon *et al.* 2008). Moreover, deformation-enhanced fluid distribution in feldspar has the potential to induce a reduction in strength by an order of magnitude lower than the original dry-protolith (Tullis *et al.* 1996). Furthermore, within the microshear zone aggregates of elongated amphiboles are

found surrounding smaller relict garnet porphyroblasts. The formation of these grains and their alignment sub-parallel to the shear direction indicate a more developed stage of garnet breakdown to amphibole enhanced by the deformation.

With the progression of the feedback between hydration softening and deformation following the initial stage of fluid infiltration along grain boundaries, the permeability of the rock becomes significantly higher enhancing fluid transfer, ductility and reactions softening, favouring the nucleation of the shear zone (Géraud *et al.* 1995; Ingles *et al.* 1999; Oliot *et al.* 2010; Austrheim 2013). The greater availability of fluids in the more strained zone results in the pervasive break-down of clinopyroxene, garnet and plagioclase to a finer-grained hydrous assemblage dominated by amphibole, clinozoisite and new plagioclase. At this stage, as observed in the EBSD data, crystals of amphibole and epidote accommodate most of the deformation, resulting in a developed heterogeneous shear zone (Figure 3.11).

The geodynamic implication of the fluid infiltration and consequent mineral alteration into nominally anhydrous rock such as granulites resides in the promotion of local softening processes and strain localization (Austrheim 2013; Jamtveit *et al.* 2019). Although the deformation mechanisms vary as a function of the behaviour of the mineral species, the obtained results show that deformation in the shear zone is fundamentally controlled by the hydration processes. Our results, therefore, provide additional detailed microstructural evidence for the significant rheological weakening caused by fluid-induced recrystallization of the bulk rock volume that contributes to the development of ductile shear zones, with important rheological implications for the strength of the lithosphere.

3.6 Acknowledgements

This work was supported by the Australian Research Council (DP160104637). The authors gratefully acknowledge constructive comments from F. Giuntoli and an anonymous reviewer which significantly improved the quality of the manuscript. We thank L. Menegon for the editorial handling and valuable comments. The corresponding author owes personal thanks to R. Rohrer for precious help in the use of Thermo-Calc software.

3.7 References

Andersen, T., Austrheim, H. & Burke, E.A.J. 1991. Mineral-fluid-melt interactions in high-pressure shear zones in the Bergen Arcs nappe complex, Caledonides of W. Norway: Implications for the fluid regime in Caledonian eclogite-facies metamorphism. *Lithos 27(3),* 187–204. DOI 10.1016/0024-4937(91)90012-A

Austrheim, H. akon & Griffin, W.L. 1985. Shear deformation and eclogite formation within granulite-facies anorthosites of the Bergen Arcs, western Norway. *Chemical Geology 50(1–3),* 267–281.

Austrheim, H. 1987. Eclogitization of lower crustal granulites by fluid migration through shear zones. *Earth and Planetary Science Letters 81(2–3),* 221–232.

Austrheim, H. 2013. Fluid and deformation induced metamorphic processes around Moho beneath continent collision zones: Examples from the exposed root zone of the Caledonian mountain belt, W-Norway. *Tectonophysics 609,* 620–635. DOI 10.1016/j.tecto.2013.08.030

Austrheim, H. & Boundy, T.M. 1994. Pseudotachylytes generated during seismic faulting and eclogitization of the deep crust. *Science 265(5168),* 82–83.

Austrheim, H., Dunkel, K.G., Plümper, O., Ildefonse, B., Liu, Y. & Jamtveit, B. 2017. Fragmentation of wall rock garnets during deep crustal earthquakes. *Science Advances 3(2),* e1602067. DOI 10.1126/sciadv.1602067

Bell, T.H. 1985. Deformation partitioning and porphyroblast rotation in meta-morphic rocks: a radical reinterpretation. *Journal of Metamorphic Geology 3(2),* 109–118. DOI 10.1111/j.1525-1314.1985.tb00309.x

Bestmann, M., Prior, D.J. & Grasemann, B. 2006. Characterisation of deformation and flow mechanics around porphyroclasts in a calcite marble ultramylonite by means of EBSD analysis. *Tectonophysics 413(3–4),* 185–200. DOI 10.1016/j.tecto.2005.10.044

Bhowany, K., Hand, M., Clark, C., Kelsey, D.E., Reddy, S.M., Pearce, M.A., Tucker, N.M. & Morrissey, L.J. 2018. Phase equilibria modelling constraints on *P-T* conditions during fluid

catalysed conversion of granulite to eclogite in the Bergen Arcs, Norway. *Journal of Metamorphic Geology 36(3),* 315–342. DOI 10.1111/jmg.12294

Bingen, B., Davis, W.J. & Austrheim, H. 2001. Zircon U-Pb geochronology in the Bergen arc eclogites and their Proterozoic protoliths, and implications for the pre-Scandian evolution of the Caledonides in western Norway. *Geological Society of America Bulletin,* 10.

Bons, P.D. & den Brok, B. 2000. Crystallographic preferred orientation development by dissolution–precipitation creep. *Journal of Structural Geology 22(11–12),* 1713–1722. DOI 10.1016/S0191-8141(00)00075-4

Boundy, T.M., Fountain, D.M. & Austrheim, H. 1992. Structural development and petrofabrics of eclogite facies shear zones, Bergen Arcs, western Norway: implications for deep crustal deformational processes. *Journal of Metamorphic Geology 10(2),* 127–146.

Boundy, T.M., Essene, E.J., Hall, C.M., Austrheim, H. & Halliday, A.N. 1996. Rapid exhumation of lower crust during continent-continent collision and late extension: Evidence from 40Ar/39Ar incremental heating of hornblendes and muscovites, Caledonian orogen, western Norway. *Geological Society of America Bulletin 108(11),* 1425–1437.

Boyd, F.R. & Mertzman, S.A. 1987. Composition and structure of the Kaapvaal lithosphere, southern Africa. *The Geochemical Society* (1)*,* 12.

Carter, N.L., Kronenberg, A.K., Ross, J.V. & Wiltschko, D.V. 1990. Control of fluids on deformation of rocks. *Geological Society, London, Special Publications 54(1),* 1–13. DOI 10.1144/GSL.SP.1990.054.01.01

Diener, J.F.A. & Powell, R. 2012. Revised activity-composition models for clinopyroxene and amphibole: revised a-x models for cpx & amphibole. *Journal of Metamorphic Geology 30(2),* 131–142. DOI 10.1111/j.1525-1314.2011.00959.x

Diener, J.F.A., Powell, R., White, R.W. & Holland, T.J.B. 2007. A new thermodynamic model for clino- and orthoamphiboles in the system Na_2O-CaO-FeO-MgO-Al_2O_3-SiO_2-H_2O-O. *Journal of Metamorphic Geology 25(6),* 631–656. DOI 10.1111/j.1525-1314.2007.00720.x

Elliott, D. 1973. Diffusion Flow Laws in Metamorphic Rocks. *GSA Bulletin* 1973; 84 (8): 2645–2664.

Géraud, Y., Caron, J. & Faure, P. 1995. Porosity network of a ductile shear zone. *Journal of Structural Geology 17(12),* 1757–1769. DOI 10.1016/0191-8141(95)00067-N

Getsinger, A.J. & Hirth, G. 2014. Amphibole fabric formation during diffusion creep and the rheology of shear zones. *Geology 42(6),* 535–538. DOI 10.1130/G35327.1

Getsinger, A.J., Hirth, G., Stünitz, H. & Goergen, E.T. 2013. Influence of water on rheology and strain localization in the lower continental crust: Water, Rheology, and Strain Localization. *Geochemistry, Geophysics, Geosystems 14(7),* 2247–2264. DOI 10.1002/ggge.20148

Giuntoli, F., Menegon, L. & Warren, C.J. 2018. Replacement reactions and deformation by dissolution and precipitation processes in amphibolites Brown, M. (ed.). *Journal of Metamorphic Geology 36(9),* 1263–1286. DOI 10.1111/jmg.12445

Glodny, J., Kühn, A. & Austrheim, H. 2008. Geochronology of fluid-induced eclogite and amphibolite facies metamorphic reactions in a subduction–collision system, Bergen Arcs, Norway. *Contributions to Mineralogy and Petrology 156(1),* 27–48. DOI 10.1007/s00410-007-0272-y

Green, E., Holland, T. & Powell, R. 2007. An order-disorder model for omphacitic pyroxenes in the system jadeite-diopside-hedenbergite-acmite, with applications to eclogitic rocks. *American Mineralogist 92(7),* 1181–1189. DOI 10.2138/am.2007.2401

Gueydan, F., Leroy, Y.M., Jolivet, L. & Agard, P. 2003. Analysis of continental midcrustal strain localization induced by microfracturing and reaction-softening: continental midcrustal strain localization. *Journal of Geophysical Research: Solid Earth 108(B2).* DOI 10.1029/2001JB000611

Hawemann, F., Mancktelow, N.S., Pennacchioni, G., Wex, S. & Camacho, A. 2019. Weak and Slow, Strong and Fast: How Shear Zones Evolve in a Dry Continental Crust (Musgrave Ranges, Central Australia). *Journal of Geophysical Research: Solid Earth 124(1),* 219–240. DOI 10.1029/2018JB016559

Herring, C. 1950. Diffusional Viscosity of a Polycrystalline Solid. *Journal of Applied Physics 21(5),* 437–445. DOI 10.1063/1.1699681

Holland, T. & Powell, R. 2003. Activity-composition relations for phases in petrological calculations: an asymmetric multicomponent formulation. *Contributions to Mineralogy and Petrology 145(4),* 492–501. DOI 10.1007/s00410-003-0464-z

Holland, T.J.B. & Powell, R. 1998. An internally consistent thermodynamic data set for phases of petrological interest: an internally consistent thermodynamic data set. *Journal of Metamorphic Geology 16(3)*. DOI 10.1111/j.1525-1314.1998.00140.x

Ingles, J., Lamouroux, C., Soula, J.-C., Guerrero, N. & Debat, P. 1999. Nucleation of ductile shear zones in a granodiorite under greenschist facies conditions, NeÂ ouvielle massif, Pyrenees, France. *Journal of Structural Geology,* 22.

Jackson, J. 2002. Strength of the continental. *GSA TODAY,* 5.

Jackson, J., McKenzie, D., Priestley, K. & Emmerson, B. 2008. New views on the structure and rheology of the lithosphere. *Journal of the Geological Society 165(2),* 453–465. DOI 10.1144/0016-76492007-109

Jackson, J.A., Austrheim, H., McKenzie, D. & Priestley, K. 2004. Metastability, mechanical strength, and the support of mountain belts. *Geology 32(7),* 625–628.

Jamtveit, B., Bucher-Nurminen, K. & Austrheim, H. akon. 1990. Fluid controlled eclogitization of granulites in deep crustal shear zones, Bergen arcs, Western Norway. *Contributions to Mineralogy and Petrology 104(2),* 184–193.

Jamtveit, B., Ben-Zion, Y., Renard, F. & Austrheim, H. 2018a. Earthquake-induced transformation of the lower crust. *Nature 556(7702),* 487–491. DOI 10.1038/s41586-018-0045-y

Jamtveit, B., Moulas, E., Andersen, T.B., Austrheim, H., Corfu, F., Petley-Ragan, A. & Schmalholz, S.M. 2018b. High Pressure Metamorphism Caused by Fluid Induced Weakening of Deep Continental Crust. *Scientific Reports 8(1)*. DOI 10.1038/s41598-018-35200-1

Jamtveit, B., Petley-Ragan, A., Incel, S., Dunkel, K.G., Aupart, C., Austrheim, H., Corfu, F., Menegon, L. & Renard, F. 2019. The Effects of Earthquakes and Fluids on the Metamorphism of the Lower Continental Crust. *Journal of Geophysical Research: Solid Earth 124(8),* 7725–7755. DOI 10.1029/2018JB016461

Jamtveit, B., Dunkel, K.G., Petley-Ragan, A., Austrheim, H., Corfu, F. & Schmid, D.W. 2021. Rapid fluid-driven transformation of lower continental crust associated with thrust-induced shear heating. *Lithos 396–397,* 106216. DOI 10.1016/j.lithos.2021.106216

Ji, S. & Mainprice, D. 1990. Recrystallization and Fabric Development in Plagioclase. *The Journal of Geology 98(1),* 65–79. DOI 10.1086/629375

Kaczmarek, M.-A., Reddy, S.M. & Timms, N.E. 2011. Evolution of zircon deformation mechanisms in a shear zone (Lanzo massif, Western-Alps). *Lithos (127) 414–3426*.

Kirby, S.H. 1985. Rock mechanics observations pertinent to the rheology of the continental lithosphere and the localization of strain along shear zones. *Tectonophysics 119(1–4),* 1–27. DOI 10.1016/0040-1951(85)90030-7

Klaper, E.M. 1990. Reaction-enhanced formation of eclogite-facies shear zones in granulite-facies anorthosites. *Geological Society, London, Special Publications 54(1),* 167–173. DOI 10.1144/GSL.SP.1990.054.01.16

Ko, B. & Jung, H. 2015. Crystal preferred orientation of an amphibole experimentally deformed by simple shear. *Nature Communications 6(1),* 6586. DOI 10.1038/ncomms7586

Kylander-Clark, A.R.C., Hacker, B.R. & Cottle, J.M. 2013. Laser-ablation split-stream ICP petrochronology. *Chemical Geology 345,* 99–112. DOI 10.1016/j.chemgeo.2013.02.019

Lloyd, Farmer A.B., & Mainprice D. 1997. Misorientation analysis and the formation and orientation of subgrain and grain boundaries. *Tectonophysics* 279(1–4):55–78.

Mancktelow, N.S. & Pennacchioni, G. 2004. The influence of grain boundary fluids on the microstructure of quartz-feldspar mylonites. *Journal of Structural Geology 26(1),* 47–69. DOI 10.1016/S0191-8141(03)00081-6

Mancktelow, N.S. & Pennacchioni, G. 2005. The control of precursor brittle fracture and fluid–rock interaction on the development of single and paired ductile shear zones. *Journal of Structural Geology 27(4),* 645–661. DOI 10.1016/j.jsg.2004.12.001

Menegon, L., Pennacchioni, G. & Spiess, R. 2008. Dissolution-precipitation creep of K-feldspar in mid-crustal granite mylonites. *Journal of Structural Geology 30(5),* 565–579. DOI 10.1016/j.jsg.2008.02.001

Menegon, L., Campbell, L., Mancktelow, N., Camacho, A., Wex, S., Papa, S., Toffol, G. & Pennacchioni, G. 2021. The earthquake cycle in the dry lower continental crust: insights from two deeply exhumed terranes (Musgrave Ranges, Australia and Lofoten, Norway). *Philosophical Transactions of the Royal Society A: Mathematical, Physical and Engineering Sciences 379(2193),* 20190416. DOI 10.1098/rsta.2019.0416

Moore, J., Beinlich, A., Porter, J.K., Talavera, C., Berndt, J., Piazolo, S., Austrheim, H. & Putnis, A. 2019. Microstructurally controlled trace element (Zr, U–Pb) concentrations in metamorphic rutile: An example from the amphibolites of the Bergen Arcs. *Journal of Metamorphic Geology 38(1),* 103–127. DOI 10.1111/jmg.12514

Mukai, H., Austrheim, H., Putnis, C.V. & Putnis, A. 2014. Textural Evolution of Plagioclase Feldspar across a Shear Zone: Implications for Deformation Mechanism and Rock Strength. *Journal of Petrology 55(8),* 1457–1477. DOI 10.1093/petrology/egu030

Newton, R.C. & Smith, J.V. 1967. Investigations concerning the Breakdown of Albite at Depth in the Earth. *The Journal of Geology 75(3),* 268–286.

Oliot, E., Goncalves, P. & Marquer, D. 2010. Role of plagioclase and reaction softening in a metagranite shear zone at mid-crustal conditions (Gotthard Massif, Swiss Central Alps): Strain localization in granitic rocks. *Journal of Metamorphic Geology 28(8),* 849–871. DOI 10.1111/j.1525-1314.2010.00897.x

Park, Y., Jung, S. & Jung, H. 2020. Lattice Preferred Orientation and Deformation Microstructures of Glaucophane and Epidote in Experimentally Deformed Epidote Blueschist at High Pressure. *Minerals 10(9),* 803. DOI 10.3390/min10090803

Passchier, C.W. & Trouw, R.A.J. 2005. *Microtectonics*. 2nd, rev.enl. ed ed. 366 pp. Springer, Berlin ; New York.

Paton, C., Hellstrom, J., Paul, B., Woodhead, J. & Hergt, J. 2011. Iolite: Freeware for the visualisation and processing of mass spectrometric data. *Journal of Analytical Atomic Spectrometry 26(12),* 2508. DOI 10.1039/c1ja10172b

Pearce, M.A., Wheeler, J. & Prior, D.J. 2011. Relative strength of mafic and felsic rocks during amphibolite facies metamorphism and deformation. *Journal of Structural Geology 33(4),* 662–675. DOI 10.1016/j.jsg.2011.01.002

Pearce, N.J.G., Perkins, W.T., Westgate, J.A., Gorton, M.P., Jackson, S.E., Neal, C.R. & Chenery, S.P. 1997. A Compilation of New and Published Major and Trace Element Data for NIST SRM 610 and NIST SRM 612 Glass Reference Materials. *Geostandards and Geoanalytical Research 21(1),* 115–144. DOI 10.1111/j.1751-908X.1997.tb00538.x

Putnis, A. & John, T. 2010. Replacement Processes in the Earth's Crust. *Elements 6(3),* 159–164. DOI 10.2113/gselements.6.3.159

Putnis, A., Jamtveit, B. & Austrheim, H. 2017. Metamorphic Processes and Seismicity: the Bergen Arcs as a Natural Laboratory. *Journal of Petrology 58(10),* 1871–1898. DOI 10.1093/petrology/egx076

Raimbourg, H., Jolivet, L., Labrousse, L., Leroy, Y. & Avigad, D. 2005. Kinematics of syneclogite deformation in the Bergen Arcs, Norway: implications for exhumation mechanisms. *Geological Society, London, Special Publications 243(1),* 175–192. DOI 10.1144/GSL.SP.2005.243.01.13

Reddy, S.M. & Buchan, C. 2005. Constraining kinematic rotation axes in high-strain zones: a potential microstructural method? *Geological Society, London, Special Publications 243(1),* 1–10. DOI 10.1144/GSL.SP.2005.243.01.02

Reddy, S.M., Timms, N.E., Pantleon, W. & Trimby, P. 2007. Quantitative characterization of plastic deformation of zircon and geological implications. *Contributions to Mineralogy and Petrology 153(6),* 625–645. DOI 10.1007/s00410-006-0174-4

Rubatto, D. 2002. Zircon trace element geochemistry: partitioning with garnet and the link between U–Pb ages and metamorphism. *Chemical Geology 184(1–2),* 123–138. DOI 10.1016/S0009-2541(01)00355-2

Rubie, D.C. 1990. Mechanisms of reaction-enhanced deformability in minerals and rocks. In: *Deformation Processes in Minerals, Ceramics and Rocks*. Springer Netherlands, Dordrecht, 262–295. DOI 10.1007/978-94-011-6827-4_11

Rutter, E. 1983. Pressure solution in nature, theory and experiment. *Journal of the Geological Society*, 140(5), 725-740. http://doi.org/10.1144/gsjgs.140.5.0725.

Scambelluri, M., Pennacchioni, G., Gilio, M., Bestmann, M., Plümper, O. & Nestola, F. 2017. Fossil intermediate-depth earthquakes in subducting slabs linked to differential stress release. *Nature Geoscience 10(12),* 960–966. DOI 10.1038/s41561-017-0010-7

Segall, P. & Simpson, C. 1986. Nucleation of ductile shear zones on dilatant fractures. *,* 4.

Skemer, P., Katayama, I., Jiang, Z. & Karato, S. 2005. The misorientation index: Development of a new method for calculating the strength of lattice-preferred orientation. *Tectonophysics 411(1–4),* 157–167. DOI 10.1016/j.tecto.2005.08.023

Skrotzki, W. 1992. Defect structure and deformation mechanisms in naturally deformed hornblende. *Physica Status Solidi (a) 131(2),* 605–624. DOI 10.1002/pssa.2211310232

Sláma, J., Košler, J., Condon, D.J., Crowley, J.L., Gerdes, A., Hanchar, J.M., Horstwood, M.S.A., Morris, G.A., Nasdala, L., Norberg, N., Schaltegger, U., Schoene, B., Tubrett, M.N. & Whitehouse, M.J. 2008. Plešovice zircon — A new natural reference material for U–Pb and Hf isotopic microanalysis. *Chemical Geology 249(1–2),* 1–35. DOI 10.1016/j.chemgeo.2007.11.005

Stünitz, H. & Tullis, J. 2001. Weakening and strain localization produced by syn-deformational reaction of plagioclase. *International Journal of Earth Sciences 90(1),* 136–148. DOI 10.1007/s005310000148

Stünitz, H., Fitz Gerald, J.D. & Tullis, J. 2003. Dislocation generation, slip systems, and dynamic recrystallization in experimentally deformed plagioclase single crystals. *Tectonophysics 372(3–4),* 215–233. DOI 10.1016/S0040-1951(03)00241-5

Svahnberg, H. & Piazolo, S. 2010. The initiation of strain localisation in plagioclase-rich rocks: Insights from detailed microstructural analyses. *Journal of Structural Geology 32(10),* 1404–1416. DOI 10.1016/j.jsg.2010.06.011

Tomkins, H.S., Powell, R. & Ellis, D.J. 2007. The pressure dependence of the zirconium-in-rutile thermometer. *Journal of Metamorphic Geology 25(6),* 703–713. DOI 10.1111/j.1525-1314.2007.00724.x

Tullis, J. & Yund R. A. 1992. The brittle– ductile transition in feldspar aggregates: an experimental study. In: Evans, B., Wong, T.F. (Eds.), Fault Mechanics and Transport Properties in Rocks. *Academic Press*, New York, pp. 89– 118.

Tullis, J. & Yund, R.A. 1989. Hydrolytic weakening of quartz aggregates: The effects of water and pressure on recovery. *Geophysical Research Letters 16(11),* 1343–1346. DOI 10.1029/GL016i011p01343

Tullis, J., Yund, R. & Farver, J. 1996. Deformation-enhanced fluid distribution in feldspar aggregates and implications for ductile shear zones. *,* 4.

Vernon. 2004. A Practical Guide to Rock Microstructure. 594 pp. Cambridge University Press, Cambridge, UK ; New York.

Vernon, R.H. 1975. Deformation and recrystallization of a plagioclase grain. *American Mineralogist*. 60, 884–888. *,* 5.

Walther, J.V. & Wood, B.J. 1986. Fluid-Rock interactions during metamorphism. Springer-Verlag, New York, Berlin, Heidelberg, Tokyo, 1–218.

Wassmann, S. & Stöckhert, B. 2013. Rheology of the plate interface — Dissolution precipitation creep in high pressure metamorphic rocks. *Tectonophysics 608,* 1–29. DOI 10.1016/j.tecto.2013.09.030

White, J.C. 2004. Instability and localization of deformation in lower crust granulites, Minas fault zone, Nova Scotia, Canada. *Geological Society, London, Special Publications 224(1),* 25–37. DOI 10.1144/GSL.SP.2004.224.01.03

White, R.W., Powell, R., Holland, T.J.B. & Worley, B.A. 2000. The effect of TiO2 and Fe2O3 on metapelitic assemblages at greenschist and amphibolite facies conditions: mineral equilibria calculations in the system K2O–FeO–MgO–Al2O3–SiO2–H2O–TiO2–Fe2O3. *Journal of Meramorphic Geology,* 18, 497-511.

White, R.W., Powell, R. & Holland, T.J.B. 2007. Progress relating to calculation of partial melting equilibria for metapelites. *Journal of Metamorphic Geology 25(5),* 511–527. DOI 10.1111/j.1525-1314.2007.00711.x

White, S.H. & Knipe, R.J. 1978. Transformation- and reaction-enhanced ductility in rocks. *Journal of the Geological Society of London*. 135, 513-516. *,* 4.

White, S.H., Burrows, S.E., Carreras, J., Shaw, N.D. & Humphreys, F.J. 1980. On mylonites in ductile shear zones. *Journal of Structural Geology 2(1–2),* 175–187. DOI 10.1016/0191-8141(80)90048-6

Wiedenbeck, M., Allé, P., Corfu, F., Griffin, W.L., Meier, M., Oberli, F., Quadt, A.V., Roddick, J.C. & Spiegel, W. 1995. Three Natural Zircon Standards for U-TH-PB, LU-HF, Trace Element and REE analyses. *Geostandards and Geoanalytical Research 19(1),* 1–23. DOI 10.1111/j.1751-908X.1995.tb00147.x

Wintsch, R.P. & Yi, K. 2002. Dissolution and replacement creep: a significant deformation mechanism in mid-crustal rocks. *Journal of Structural Geology,* 15.

Yardley, B.W.D. & Valley, J.W. 1997. The petrologic case for a dry lower crust. *Journal of Geophysical Research: Solid Earth 102(B6),* 12173–12185. DOI 10.1029/97JB00508

Zhou, Y., He, C. & Yang, X. 2008. Water contents and deformation mechanism in ductile shear zone of middle crust along the Red River fault in southwestern China. *Science in China Series D: Earth Sciences 51(10),* 1411–1425. DOI 10.1007/s11430-008-0115-3

Chapter 4

Crystal plasticity enhances trace element mobility in garnet

This chapter is published as:

Tacchetto T., Reddy S.M., Fougerouse D., Clark C., Rickard W. D and Saxey D. Crystal plasticity enhances trace element mobility in garnet, *Geology* (2022). https://doi.org/10.1130/G50283.1

Abstract

Chemical heterogeneities along grain boundaries in garnet occur across a wide range of metamorphic conditions, yet the processes underlying their development remain poorly understood. Here, we integrate electron backscattered diffraction (EBSD) and atom probe tomography (APT) to evaluate the mechanisms driving nanoscale trace element mobility to deformation microstructures in a granulitic garnet. This approach shows that low-angle boundaries can be enriched in Ca, Ti, P, Cu, K, Na, Cl and H. Based on the correlation between EBSD and APT data, we propose that solute ions (Ca, Ti, P and Cu) were segregated to the interface during the migration of dislocation associated with ductile deformation of the grain. In contrast, elements such as K, Na, Cl and H are interpreted to reflect diffusion along the low-angle boundary from an externally-derived fluid source. These results provide the missing link between chemical heterogeneity and deformation-related microstructures in garnet. Our approach shows that a combination of microstructural and nanoscale geochemical analyses can provide unprecedented insights into mechanisms of element transfer within minerals.

4.1 Introduction

Garnet is an important rock-forming mineral that occurs in a variety of mineral assemblages, across a wide range of pressure (*P*) and temperature (*T*) conditions, and rock types throughout the Earth's lithosphere (Baxter *et al.* 2013). Owing to its durability and low diffusion rates, garnet geochemistry is widely used as a petrological tool to reconstruct the complex *P*–*T* history of rocks and determine the timing of geological processes (Baxter *et al.* 2017). However, observations at the microscale have suggested that garnet may not be as compositionally robust, especially in regions that have been strongly affected by deformation. Typically, garnet displays a rigid and brittle behaviour in response to deformation occurring in a wide range of crustal metamorphic conditions (Wang & Ji 1999). However, a growing number of studies show that dislocation creep and dynamic recovery can accommodate deformation at high *P*–*T* conditions and low-strain rates (Ji & Martignole 1994; Wang & Ji 1999; Prior *et al.* 2000; Storey & Prior 2005; Bestmann *et al.* 2008; Massey *et al.* 2011; Austrheim *et al.* 2017; Hawemann *et al.* 2019; Phillips & Ji 2021). In garnet deformed by crystal plasticity, compositional heterogeneities have been observed in close proximity to deformation microstructures, highlighting the significance of sub-grain boundaries in compositional re-equilibration (e.g., Chapman *et al.* 2019). Such features have been interpreted to represent the result of either intracrystalline segregation or interface-enhanced element diffusion (e.g., Prior *et al.* 2000; Storey & Prior 2005; Konrad-Schmolke *et al.* 2007; Massey *et al.* 2011; Chapman *et al.* 2019). However, discriminating between these different mechanisms has remained elusive due to the difficulties in analysing compositional variations associated with nanoscale defects.

Here, we integrate detailed microstructural analysis by EBSD with interfacial compositional analysis by APT to investigate mechanisms associated with low-angle boundary formation within a granulite-facies garnet of the Lindås Nappe (western Norway). The results provide evidence for the interlinked relationship between segregation and diffusion of components to deformation microstructures thereby advancing our understanding of element mobility processes during garnet crystal plasticity.

4.2 Samples

The studied sample was collected from within a zoisite-bearing gneiss of the Lindås Nappe of the Bergen arcs (western Norway) (Figure 4.1). The Lindås Nappe comprises Mesoproterozoic-Neoproterozoic orthogneisses recrystallized at granulite-facies conditions (ca. 800-900 °C and < 10 kbar) during the Sveconorwegian orogeny at ~ 930 Ma ± 50 Ma (Bingen *et al.* 2001). Subsequently, these rocks were partially overprinted at upper-amphibolite to eclogite-facies conditions during the Caledonian orogeny between 430 and 410 Ma (Bingen *et al.* 2001). The Caledonian overprint is dominantly linked to the development of ductile shear zones associated with fluid infiltration (Austrheim & Boundy 1994; Austrheim *et al.* 2017).

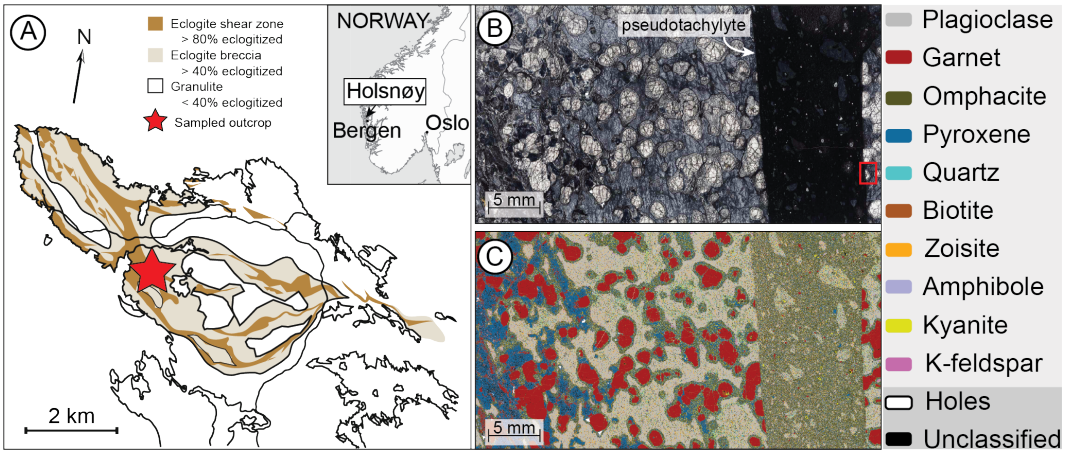

Figure 4.1 a) Simplified geological map of Holsnøy area (modified after Bhowany *et al.* 2018). b, c) Plane-polarized photomicrograph and Tescan integrated mineral analyzer (TIMA) phase map. Red rectangle indicates the area of EBSD and APT analysis.

Within these lithologies, fine-grained dark veins have been described and interpreted as pseudotachylyte based on their characteristic geometric features (e.g., injection veins) (Austrheim & Boundy 1994). Given their close spatial proximity and textural relationship with eclogitic shear zones, the presence of pseudotachylytes has been linked to the Caledonian Orogeny (Austrheim & Boundy 1994; Austrheim *et al.* 2017). Their formation has been interpreted to be the record of frictional melting associated with a seismic event at high-pressure (< 22kbar at < 700°C) induced by the volume decrease associated with the conversion of the granulite-facies assemblage into eclogite (Austrheim & Boundy 1994; Bhowany *et al.* 2018). The timing and the metamorphic conditions of the pseudotachylyte

event remain controversial, being ascribed to either the waning stages of the Grenvillian Orogeny and/or the early stages of the Caledonian Orogeny (Austrheim & Boundy 1994; Bhowany *et al.* 2018).

In thin section, the pseudotachylyte-host gneiss comprises plagioclase (~28 wt%), omphacite (~18 wt%), garnet (~16 wt%), kyanite (~10 wt%) and zoisite (~ 6 wt%) (Figure 4.1, Supplementary Figure 4.C2.1). Coarser grains of garnet and pyroxene are elongated resembling the pre-existing granulite foliation. Garnet is surrounded by coronae that generally comprise fine aggregates of omphacite, kyanite, zoisite and plagioclase. The pseudotachylyte appears as a < 1 cm darker vein crosscutting the rock foliation (Figure 4.1). Mineralogically, the pseudotachylyte preserves a fine-grained (<10 μm) mosaic of omphacite (~ 37 wt%), plagioclase (~ 30 wt%), kyanite (~ 11 wt%), zoisite (~ 6 wt%) and garnet (~ 3 wt%) crystals with minor quartz and K-feldspar (Supplementary Figure 4.C2.1). Within the pseudotachylyte, garnet occurs as small poikilitic euhedral grains, in which quartz is the most abundant mineral inclusion (Supplementary Figure 4.C2.2).

4.3 Methods

We investigated a wall-rock garnet grain that lies in direct contact with the pseudotachylyte (Figures 4.2; Supplementary Figure 4.C2.2). The deformation microstructures were characterized by EBSD orientation mapping. Based on the results of this mapping, a ~ 0.7 ° low-angle boundary was selected for APT analyses. Needle-shaped atom probe specimens were prepared using Pt "button" fiduciaries (Rickard *et al.* 2020). APT analyses yield mass/charge spectra and peaks twice higher than the local background were identified and ranged (Supplementary Table 4.C2.S4). Details of the APT approach for geological materials are given elsewhere (Reddy *et al.* 2020). APT data were reconstructed in 3D using garnet-specific reconstruction parameters (Fougerouse *et al.* 2021b). To estimate the volatile composition of the boundary, OH (17 Da) was quantified as a proxy for H distribution. Additional technical information is provided in the Appendix 4.C.1 and Supplementary Table 4.C2.3.

4.4 Character of the wall-rock garnet

The garnet displays a sharp contact with the pseudotachylyte indicating that the grain was truncated during pseudotachylyte formation. Internally, the remaining garnet fragment is cut by a complex network of fractures (Supplementary Figure 4.C2.2). The EBSD orientation data indicates that the garnet records lattice disorientations up to ~ 15° misorientation, which is localized at the tips of the grain where it is juxtaposed with the pseudotachylyte. Generally, the highest values are due to proximity to fractures (Figure 4.2). The internal strain of the grain is manifested by sub-grain boundaries with < 1° of minimum misorientation (Figure 4.2b, Supplementary Figure 4.C2.3). The EBSD data indicate that the boundary selected for APT analysis does not show evidence of fracture and it is consistent with a tilt boundary geometry formed by the operation of <111>{123} slip system (Figures 4.2c, d). This slip system has been previously identified from EBSD analyses of deformed garnet and is considered to be a common slip system in garnet (e.g., Voegele *et al.* 1998).

Energy-dispersive spectroscopy (EDS) X-ray maps reveal that the analysed garnet is compositionally variable, with a distinct ~ 5-μm-wide rim which has reduced Mg, and increased Fe and Ca (Supplementary Figure 4.C2.5). This compositional variation also occurs in the regions of the grain that exhibit a higher degree of crystal plasticity. The low-angle boundary targeted by APT lies within the Ca and Fe-rich rim domain of the garnet (Supplementary Figure 4.C2.5).

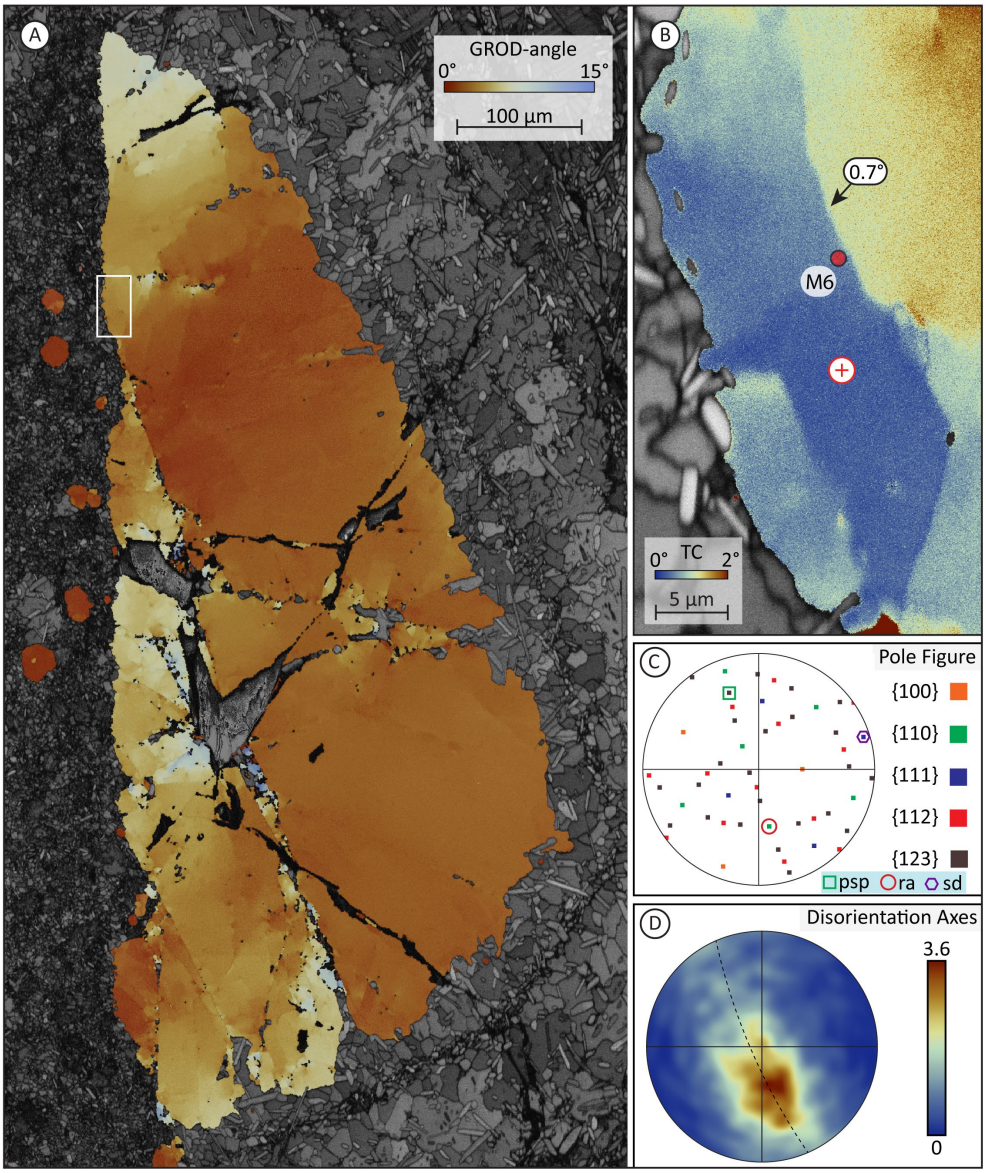

Figure 4.2 (a) EBSD grain reference orientation deviation (GROD)-angle map. Each pixel is colour coded based on the deviation angle relative to the average orientation of the entire grain. (b) Texture Component EBSD map of the region within the white box in (a). Each pixel is colour coded based on the deviation angle relative to the reference point indicated by a red cross in the map. The arrow indicates the low-angle boundary analysed by APT. Location of APT specimen M6 is marked by the red circle. (c) Pole figures of the garnet grain. psp: pole to slip plane; ra: rotation axis; sd: slip direction. (d) Disorientation axes (0.5-1°) plots in sample coordinates for the sub-grain boundary showed in (b). The inferred orientation of the boundary wall is shown by a dashed line.

4.5 Brittle and plastic deformation of garnet

The microstructures displayed by the analyzed garnet are consistent with a dominant component of high-strain rate and brittle deformation, which has been previously interpreted as a result of seismic loading and rupture (Austrheim & Boundy, 1994; Austrheim *et al.* 2017

and therein). In addition, EBSD data reveal that the development of sub-grain boundaries is consistent with the operation of known garnet slip systems, and is the result of crystal plasticity (Figure 4.2, Supplementary Figure 4.C2.3). Despite garnet being a high-strength mineral (Karato *et al.* 1995), ductile behaviour has been reported from wide range of P-T environments, typically from granulite to eclogite facies conditions (e.g., Ji & Martignole 1994; Bestmann *et al.* 2008; Phillips & Ji 2021), and in mantle peridotites (e.g., Prior *et al.* 2002). Previously identified dislocation microstructures in wall-rock garnets from the same study area, were interpreted to represent evidence of crystal plasticity associated with the seismic event responsible for pseudotachylyte formation (Austrheim *et al.* 2017). Hence, the microstructures observed in the analysed grain indicate a heterogeneous distribution of plastic strain where higher stress is concentrated at grain tips and accommodated via a component of dislocation creep.

4.6 Nanochemistry of the low-angle boundary

The bulk composition of six APT needles is consistent with the analysis of garnet. A number of minor peaks represent trace elements (Supplementary Figure 4.C2.6, Supplementary Table 4.C2.2). The distribution of major and trace elements appears homogeneous at the nanoscale (Supplementary Figure 4.C2.7), except for specimen M6, in which trace elements (Cl, Na, K, Ti, P, Cu, H and to a minor extent Ca) are concentrated in planar features oblique to the specimen long-axis and dipping at a high angle (Figure 4.3). These planar features are consistent with the orientation of the low-angle boundary targeted in the EBSD data (Figures 4.2b–d). In particular, the interface is marked by a strong increase in Ti (up to ~ 0.17 at. %), Cl (~ 0.16 at. %), Na (~ 0.17 at. %), K (~ 0.05 at. %) and H (~ 1.43 at. %) (Figure 4.3; Supplementary Table 4.C2.1). At the interface, trace element enrichment is compensated by a decrease in Si, Al, Fe and to a lesser degree Mg (Figure 4.4; Supplementary Table 4.C2.1).

H+ quantification in APT data is difficult because of the potential contamination by chamber-sourced hydrogen. Nevertheless, H+ enrichment in crystal defects has been previously confirmed by APT studies on steels (Chen *et al.* 2020). In addition, studies on olivine demonstrated the OH peak (17 Da) being a good proxy for hydrogen distribution within the specimen (Tacchetto *et al.* 2021; Liu *et al.* 2022). The OH peak is therefore interpreted to reflect H distribution within the analysed specimens.

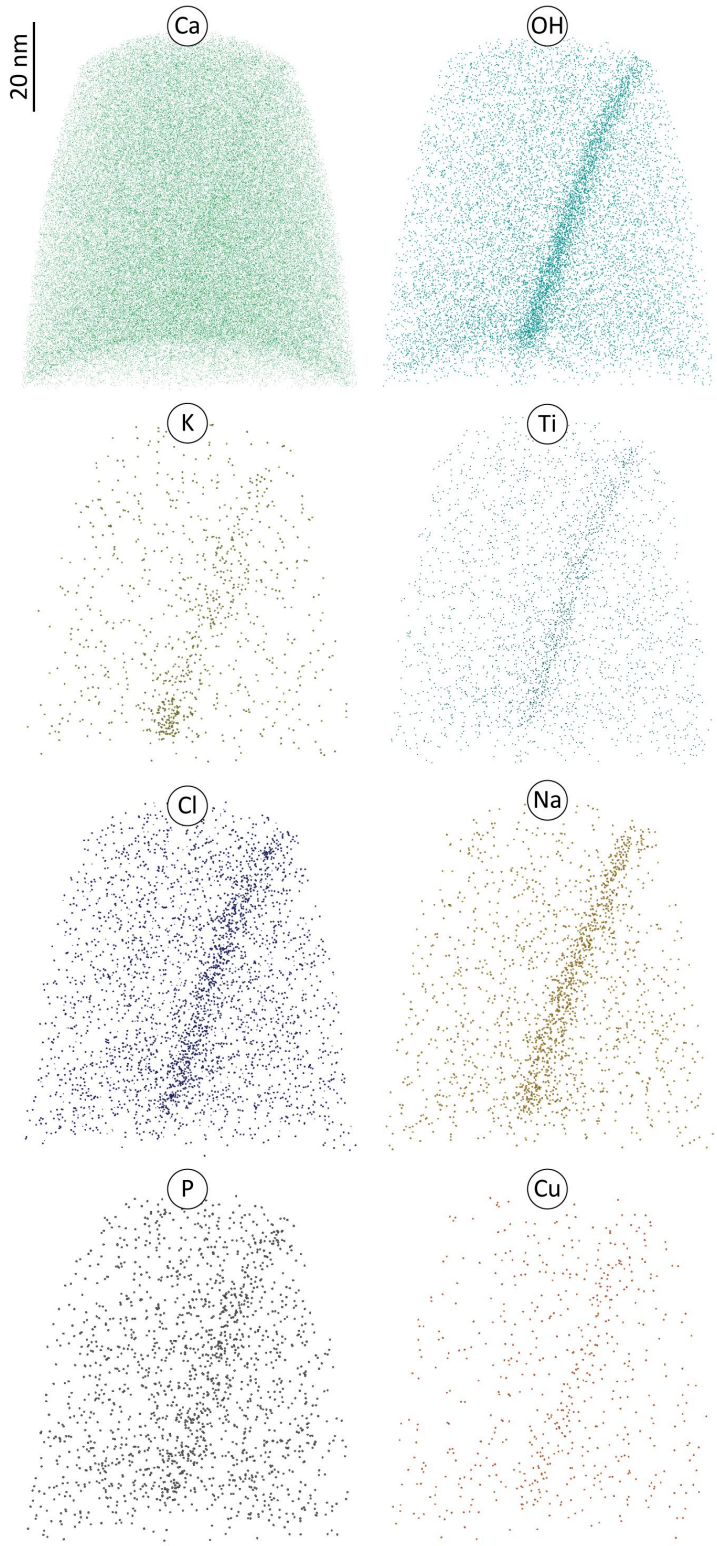

Figure 4.3 Three-dimensional reconstruction of APT specimens M6. Each dot in the atom map images represents one detected ion. Not all detected ions are displayed for clarity.

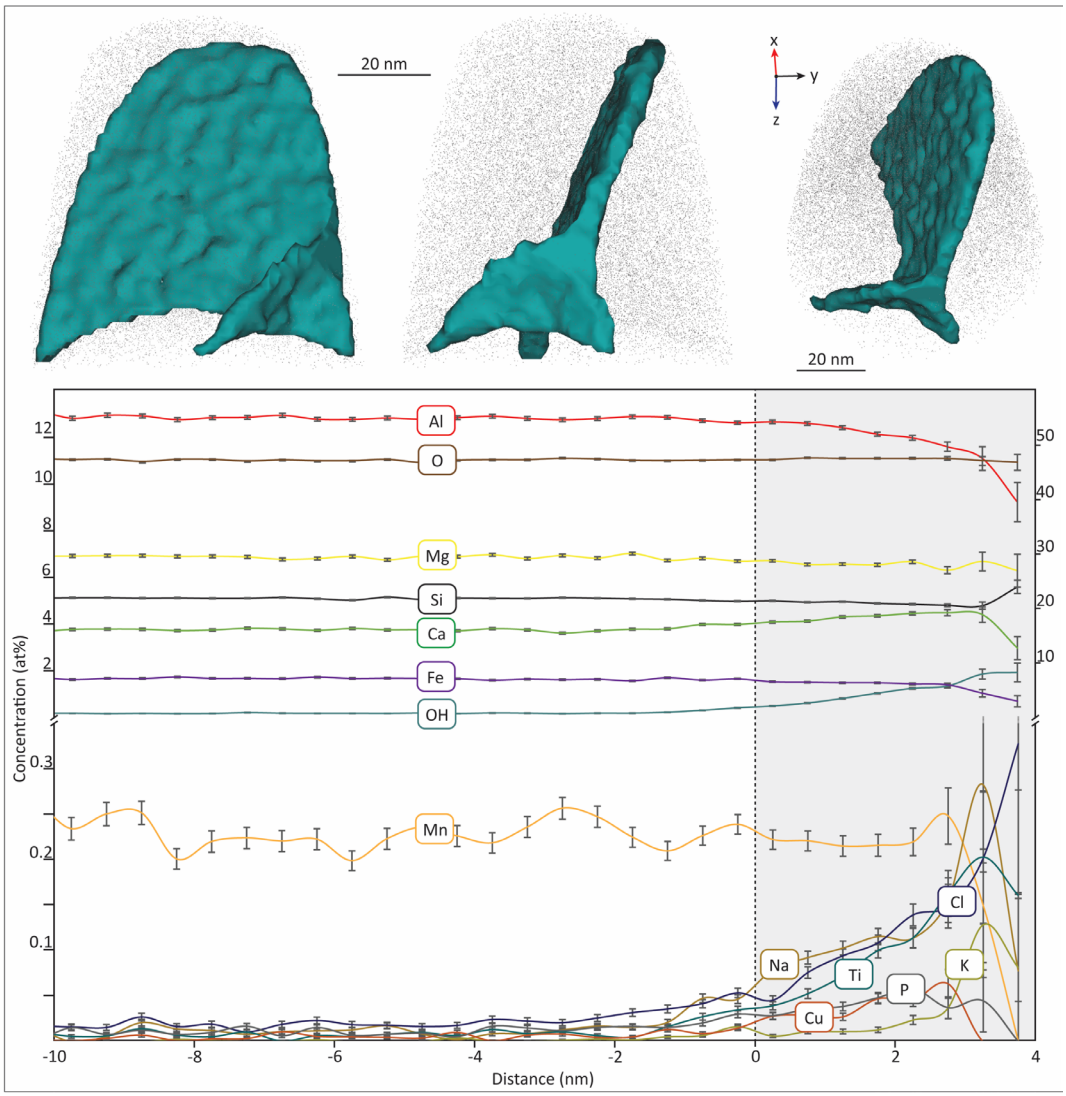

Figure 4.4 Three-dimensional isosurface renderings of the enriched region and relative proximity histogram profiles. Oxygen and Si are plotted with respect to the right y scale; all other elements are plotted with respect to the left *y* scale. Distance zero represents the edges of the interface.

4.7 Trace element segregation and interface diffusion in garnet

APT data show enrichment in Ca, Ti, Cu, K, Na, Cl, P and H along the targeted low-angle boundary (Figure 4.4). Solute enrichment at mineral interfaces is well documented, and it can include mechanisms deriving from interface-enhanced diffusion (e.g., pipe-diffusion; Love 1964), and/or segregation by defect-impurity pair in which trace elements are captured from the crystal lattice by migrating dislocations during dislocation creep (Priester 2013).

A growing number of APT studies have documented the segregation of trace elements to low-angle boundaries in minerals affected by crystal plasticity (e.g., Piazolo *et al.*

2016; Reddy *et al.* 2016; Fougerouse *et al.* 2019, 2021a; Tacchetto *et al.* 2021). In the majority of these studies, enrichment at the interface involves only trace elements that are found in the host mineral. However, the isotopic composition of Pb-enriched interfaces indicates that trace elements may also be derived from an external source (Fougerouse *et al.* 2019). In the garnet studied here, the composition of the interface comprises common trace elements found in the host garnet (Ca, Ti, Cu, P). Based on EBSD and APT data, the enrichment of these elements is interpreted to represent mobility by defect-impurity pair mechanism during crystal plasticity. In contrast, if we take into account the geodynamic and petrological context of these rocks, elements such as K, Na, Cl and H may instead represent components derived from an external source.

In the Lindås Nappe, there is a wide consensus that the transformation of the dry anorthositic protolith is associated with feedback between seismic faulting and fluid infiltration (Austrheim & Boundy 1994; Jamtveit *et al.* 2019). In the present study, garnet coronae and the occurrence of zoisite are consistent with the metasomatism of these rocks induced by the influx of aqueous fluid (Figure 4.1) (Bingen *et al.* 2001; Jamtveit *et al.* 2019).

The zonation pattern for the wall rock garnet containing the low-angle boundary is not truncated by the pseudotachylyte (Supplementary Figure 4.C2.5). This indicates that the process of chemical re-equilibration triggered by the fluid phase pervading the rock must have formed contemporaneously or after the deformation. Moreover, considering the mineral assemblage of the corona replacing the garnet, the resulting fluid composition would be most close to that of a brine, which is typical of subduction zones such as the Bergen Arcs (Manning & Frezzotti 2020). TEM investigations conducted by Austhreim *et al.* (2017), have shown the presence of fluids along the grain boundaries of similar garnets of these rocks. Moreover, the infiltration of brines along grain boundaries at similar metamorphic conditions of this study has been previously observed (Higashino *et al.* 2019). Therefore, based on these considerations our interpretation is that subduction-related fluids present during deformation represent the source of exotic trace elements (Na, Cl, K and H) diffusing along the low-angle boundary.

4.8 Conclusions and geological implications

Previous studies conducted on plastically deformed garnets reported the occurrence of Ca, Mg and Fe compositional gradients (e.g., Prior *et al.* 2000 p. 20; Storey & Prior 2005; Massey *et al.* 2011; Chapman *et al.* 2019). Given the spatial overlap of these chemical anomalies with deformation microstructures, this observation has been interpreted to reflect chemical segregation induced by dislocation creep (Massey *et al.* 2011). However, the activation of pipe-diffusion has been shown to affect garnet microchemistry in geological samples (Chapman *et al.* 2019) and in experimental grain boundaries studies of yttrium aluminum garnet (YAG) (Polednia *et al.* 2020). Our APT results provide the confirmation that compositional heterogeneities associated with deformation microstructures are promoted by the intracrystalline migration of dislocations (Massey *et al.* 2011). Further, they demonstrate that crystal plasticity generates microstructures that may act as fast diffusion pathways enabling the addition of externally derived components, thereby revealing a common link between natural and experimental studies.

Regardless of the dominant mechanism responsible for trace element enrichment, our findings yield important implications. The preservation of garnet peak metamorphic chemistry is of special interest as it is widely used to obtain the timescales of various geological processes (Baxter *et al.* 2017). The observation that intracrystalline deformation can promote addition of externally derived trace elements, highlights the influence of crystal plasticity in increasing the extent of element exchange between rock-forming minerals (Konrad-Schmolke *et al.* 2007; Chapman *et al.* 2019). This, in turn, has the potential to enhance rates of metamorphic reactions, elemental re-equilibration and/or intragranular growth of inclusions with strong implications for its use in petrochronological applications. Our findings motivate a re-examination of deformation microstructures in garnet and question the assumed chemical integrity of important geological minerals.

4.9 References

Austrheim, H. & Boundy, T.M. 1994. Pseudotachylytes generated during seismic faulting and eclogitization of the deep crust. *Science 265(5168),* 82–83.

Austrheim, H., Dunkel, K.G., Plümper, O., Ildefonse, B., Liu, Y. & Jamtveit, B. 2017. Fragmentation of wall rock garnets during deep crustal earthquakes. *Science Advances 3(2),* e1602067. DOI 10.1126/sciadv.1602067

Baxter, E.F., Caddick, M.J. & Ague, J.J. 2013. Garnet: Common Mineral, Uncommonly Useful. *Elements 9(6),* 415–419. DOI 10.2113/gselements.9.6.415

Baxter, E.F., Caddick, M.J. & Dragovic, B. 2017. Garnet: A Rock-Forming Mineral Petrochronometer. *Reviews in Mineralogy and Geochemistry 83(1),* 469–533. DOI 10.2138/rmg.2017.83.15

Bestmann, M., Habler, G., Heidelbach, F. & Thöni, M. 2008. Dynamic recrystallization of garnet and related diffusion processes. *Journal of Structural Geology 30(6),* 777–790. DOI 10.1016/j.jsg.2008.02.007

Bhowany, K., Hand, M., Clark, C., Kelsey, D.E., Reddy, S.M., Pearce, M.A., Tucker, N.M. & Morrissey, L.J. 2018. Phase equilibria modelling constraints on *P-T* conditions during fluid catalysed conversion of granulite to eclogite in the Bergen Arcs, Norway. *Journal of Metamorphic Geology 36(3),* 315–342. DOI 10.1111/jmg.12294

Bingen, B., Davis, W.J. & Austrheim, H. 2001. Zircon U-Pb geochronology in the Bergen arc eclogites and their Proterozoic protoliths, and implications for the pre-Scandian evolution of the Caledonides in western Norway. *Geological Society of America Bulletin,* 10.

Chapman, T., Clarke, G.L., Piazolo, S., Robbins, V.A. & Trimby, P.W. 2019. Grain-scale dependency of metamorphic reaction on crystal plastic strain. *Journal of Metamorphic Geology 37(7),* 1021–1036. DOI 10.1111/jmg.12473

Chen, Y.-S., Lu, H., Liang, J., Rosenthal, A., Liu, H., Sneddon, G., McCarroll, I., Zhao, Z., Li, W., Guo, A. & Cairney, J.M. 2020. Observation of hydrogen trapping at dislocations, grain boundaries, and precipitates. Science 175(2020):171–175. *,* 6.

Fougerouse, D., Reddy, S.M., Kirkland, C.L., Saxey, D.W., Rickard, W.D. & Hough, R.M. 2019. Time-resolved, defect-hosted, trace element mobility in deformed Witwatersrand pyrite. *Geoscience Frontiers 10(1),* 55–63. DOI 10.1016/j.gsf.2018.03.010

Fougerouse, D., Reddy, S.M., Aylmore, M., Yang, L., Guagliardo, P., Saxey, D.W., Rickard, W.D.A. & Timms, N. 2021a. A new kind of invisible gold in pyrite hosted in deformation-related dislocations. *Geology 49(10),* 1225–1229. DOI 10.1130/G49028.1

Fougerouse, D., Saxey, D.W., Rickard, W.D.A., Reddy, S.M. & Verberne, R. 2021b. Standardizing Spatial Reconstruction Parameters for the Atom Probe Analysis of Common Minerals. *Microscopy and Microanalysis,* 1–10. DOI 10.1017/S1431927621013714

Hawemann, F., Mancktelow, N., Wex, S., Pennacchioni, G. & Camacho, A. 2019. Fracturing and crystal plastic behaviour of garnet under seismic stress in the dry lower continental crust (Musgrave Ranges, Central Australia). *Solid Earth 10(5),* 1635–1649. DOI 10.5194/se-10-1635-2019

Higashino, F., Kawakami, T., Tsuchiya, N., Satish-Kumar, M., Ishikawa, M., Grantham, G., Sakata, S. & Hirata, T. 2019. Brine Infiltration in the Middle to Lower Crust in a Collision Zone: Mass Transfer and Microtexture Development Through Wet Grain–Boundary Diffusion. *Journal of Petrology 60(2),* 329–358. DOI 10.1093/petrology/egy116

Jamtveit, B., Petley-Ragan, A., Incel, S., Dunkel, K.G., Aupart, C., Austrheim, H., Corfu, F., Menegon, L. & Renard, F. 2019. The Effects of Earthquakes and Fluids on the Metamorphism of the Lower Continental Crust. *Journal of Geophysical Research: Solid Earth 124(8),* 7725–7755. DOI 10.1029/2018JB016461

Ji, S. & Martignole, J. 1994. Ductility of garnet as an indicator of extremely high temperature deformation. *Journal of Structural Geology 16(7),* 985–996.

Karato, S., Wang, Z., Liu, B. & Fujino, K. 1995. Plastic deformation of garnets: systematics and implications for the rheology of the mantle transition zone. *Earth and Planetary Science Letters,* 18.

Konrad-Schmolke, M., O'Brien, P.J. & Heidelbach, F. 2007. Compositional re-equilibration of garnet: the importance of sub-grain boundaries. *European Journal of Mineralogy 19(4),* 431–438. DOI 10.1127/0935-1221/2007/0019-1749

Liu, J., Taylor, S.D., Qafoku, O., Arey, B.W., Colby, R., Eaton, A., Bartrand, J., Shutthanandan, V., Manandhar, S., and Perea, D.E., 2022, Visualizing the Distribution of Water in Nominally Anhydrous Minerals at the Atomic Scale: Insights From Atom Probe Tomography on Fayalite: *Geophysical Research Letters*, v. 49. doi:10.1029/2021GL094914.

Love G. 1964. Dislocation pipe diffusion. *Acta Metallurgica*, 12(6), 731–737.

Manning, C.E. & Frezzotti, M.L. 2020. Subduction-Zone Fluids. *Elements 16(6),* 395–400. DOI 10.2138/gselements.16.6.395

Massey, M.A., Prior, D.J. & Moecher, D.P. 2011. Microstructure and crystallographic preferred orientation of polycrystalline microgarnet aggregates developed during progressive creep, recovery, and grain boundary sliding. *Journal of Structural Geology 33(4),* 713–730. DOI 10.1016/j.jsg.2010.12.009

Phillips, N.J. & Ji, S. 2021. Constraining the ductile deformation mechanisms of garnet across pressure-temperature space. *Journal of Structural Geology 148,* 104356. DOI 10.1016/j.jsg.2021.104356

Piazolo, S., La Fontaine, A., Trimby, P., Harley, S., Yang, L., Armstrong, R. & Cairney, J.M. 2016. Deformation-induced trace element redistribution in zircon revealed using atom probe tomography. *Nature Communications 7(1).* DOI 10.1038/ncomms10490

Polednia, J., Dohmen, R. & Marquardt, K. 2020. Grain boundary diffusion and its relation to segregation of multiple elements in yttrium aluminum garnet. *European Journal of Mineralogy 32(6),* 675–696. DOI 10.5194/ejm-32-675-2020

Priester, L. 2013. *Grain Boundaries.* Springer Netherlands, Dordrecht, Springer Series in Materials Science. DOI 10.1007/978-94-007-4969-6

Prior, D.J., Wheeler, J., Brenker, F.E., Harte, B., Matthews, M. & Ltd, J.M. 2000. Crystal plasticity of natural garnet: New microstructural evidence. *Geology 28(11),* 1003–1006.

Prior, D.J., Wheeler, J., Peruzzo, L., Spiess, R. & Storey, C. 2002. Some garnet microstructures: an illustration of the potential of orientation maps and misorientation

analysis in microstructural studies. *Journal of Structural Geology 24(6–7),* 999–1011. DOI 10.1016/S0191-8141(01)00087-6

Reddy, S.M., van Riessen, A., Saxey, D.W., Johnson, T.E., Rickard, W.D.A., Fougerouse, D., Fischer, S., Prosa, T.J., Rice, K.P., Reinhard, D.A., Chen, Y. & Olson, D. 2016. Mechanisms of deformation-induced trace element migration in zircon resolved by atom probe and correlative microscopy. *Geochimica et Cosmochimica Acta 195,* 158–170. DOI 10.1016/j.gca.2016.09.019

Reddy, S.M., Saxey, D.W., Rickard, W.D.A., Fougerouse, D., Montalvo, S.D., Verberne, R. & Riessen, A. 2020. Atom Probe Tomography: Development and Application to the Geosciences. *Geostandards and Geoanalytical Research 44(1),* 5–50. DOI 10.1111/ggr.12313

Rickard, W.D.A., Reddy, S.M., Saxey, D.W., Fougerouse, D., Timms, N.E., Daly, L., Peterman, E., Cavosie, A.J. & Jourdan, F. 2020. Novel Applications of FIB-SEM-Based ToF-SIMS in Atom Probe Tomography Workflows. *Microscopy and Microanalysis,* 1–8. DOI 10.1017/S1431927620000136

Storey, C.D. & Prior, D.J. 2005. Plastic Deformation and Recrystallization of Garnet: A Mechanism to Facilitate Diffusion Creep. *Journal of Petrology 46(12),* 2593–2613. DOI 10.1093/petrology/egi067

Tacchetto, T., Reddy, S.M., Saxey, D.W., Fougerouse, D., Rickard, W.D.A. & Clark, C. 2021. Disorientation control on trace element segregation in fluid-affected low-angle boundaries in olivine. *Contributions to Mineralogy and Petrology 176(7),* 59. DOI 10.1007/s00410-021-01815-3

Voegele, V., Cordier, P., Sautter, V., Sharp, T.G., Lardeaux, J.M. & Marques, F.O. 1998. Plastic deformation of silicate garnets II. Deformation microstructures in natural samples. *Physics of the Earth and Planetary Interiors 108,* 319–338.

Wang, Z.C. & Ji, S.C. 1999. Deformation of silicate garnets: brittle ductile transition and its geological implications. Canadian Mineralogist 37, 525–541.

Chapter 5

Disorientation control on trace element segregation in fluid-affected low-angle boundaries in olivine

This chapter is published as:

Tacchetto T., Reddy S. M., Saxey D. W., Fougerouse D., Rickard W. D. and Clark C. Disorientation control on trace element segregation in fluid-affected low-angle boundaries in olivine. *Contributions to Mineralogy and Petrology*, 176(7), 1–16, 2021.
https://doi.org/10.1007/s00410-021-01815-3

Abstract

The geometry and composition of deformation-related low-angle boundaries in naturally-deformed olivine were characterized by electron backscattered diffraction (EBSD) and atom probe tomography (APT). EBSD data show the presence of discrete low-angle tilt boundaries, which formed by sub-grain rotation recrystallisation associated with the (100)[001] slip system during fluid-catalysed metamorphism and deformation. APT analyses of these interfaces show the preferential segregation of olivine-derived trace elements (Ca, Al, Ti, P, Mn, Na and Co) to the low-angle boundaries. Boundaries with < 2° show marked enrichment associated with the presence of multiple, non-parallel dislocation types. However, at larger disorientation angles (> 2°), the interfaces become more ordered and linear enrichment of trace elements coincides with the orientation of dislocations inferred from the EBSD data. These boundaries show a systematic increase of trace element concentration with disorientation angle. Olivine-derived trace elements segregated to the low-angle boundaries are interpreted to be captured and travel with dislocation as they migrate to the sub-grain boundary interfaces. However, the presence of exotic trace elements Cl and H, also enriched in the low-angle boundaries, likely reflect the contribution of an external fluid source during the fluid-present deformation. The observed compositional segregation of trace elements has significant implications for the deformation and transformation of olivine at mantle depth, the interpretation of geophysical data and the redistribution of elements deep in the Earth. The observation that similar features are widely recognised in manufactured materials, indicates that the segregation of trace elements to mineral interfaces is likely to be widespread.

5.1 Introduction

In monomineralic rocks, grain boundaries mark the change in lattice orientation of adjacent crystals. Grain boundary interfaces are only a few nanometres wide, and represent only a small fraction of the rock volume, yet they play a critical role in controlling physical, rheological and mechanical properties of rocks at a broad range of scales. For example, diffusion rates along interfaces are orders of magnitude faster than intracrystalline diffusion (Dohmen & Milke 2010) and grain boundary diffusion may facilitate the localized interdiffusion of material within a rock and promote metamorphic reactions (Putnis & John 2010).

Despite the increasing importance of grain boundary characterization in all rocks, the study of grain boundary properties in geological materials has focused primarily on olivine [$(Mg,Fe)_2SiO_4$], because of its importance in the mantle and therefore its role in large-scale geodynamic processes. A significant focus of this research is the characterization of olivine deformation through the quantification of olivine microstructure in naturally and experimentally deformed olivine-rich rocks. Results illustrate that grain boundaries critically affect a number of mantle properties, such as creep strength during diffusion and dislocation creep, element segregation and diffusion rates, as well as seismic and electrical conductivity properties, all of which have important rheological and geodynamical implications (Wenk 1985; Faul *et al.* 2004; Rohrer 2011; Hansen *et al.* 2012; Dillon *et al.* 2016a; Zhao *et al.* 2019; Yabe & Hiraga 2020). A better understanding of interface properties is key to further developing knowledge of fundamental rock processes.

Detailed microanalytical observations have provided an appreciable visualization of nm-scale structure and composition of grain boundaries in olivine (Suzuki 1987; Kohlstedt 1990; Hiraga *et al.* 2002, 2003; Marquardt *et al.* 2015; Marquardt & Faul 2018). These studies have progressed our understanding of lattice atomic structure (Adjaoud *et al.* 2012), structural and effective width (Ricoult & Kohlstedt 1983; Hiraga *et al.* 2002; Marquardt & Faul 2018), and composition (Hiraga *et al.* 2002, 2003, 2004). Geochemical analyses of high-angle grain boundaries within olivine in deformed mantle rocks have demonstrated the presence of incompatible trace element enrichment, precipitates, and interstitial phases (melt/fluid) at these interfaces (Hiraga *et al.* 2004). Grain boundaries may therefore be a significant repository of geologically important trace elements (Hiraga *et al.* 2003, 2004, 2007). The relationship between adjacent grains and the interface between them can be investigated through the characterization of five geometrical parameters that describe the grain boundary

character distribution (GBCD) of a crystalline material (Lloyd *et al.* 1997). Three of these parameters define the misorientation of the crystal lattice, while the orientation of the boundary plane is constrained by the two additional parameters (Lloyd *et al.* 1997). Since crystallographic orientations and boundary geometries may change during rock deformation, the GBCD may also vary throughout the deformation cycle. Such relationships have been widely investigated in ceramics and metals (e.g. Lejček 2010), but still represent an emerging field of investigation within naturally occurring geological materials (Marquardt & Faul 2018). The variation in the five GBCD parameters leads to a broad range of possible geometrically-distinct grain boundary combinations (> $60x10^3$ for 10° increments in parameter values, Marquardt *et al.* 2015), so only a small number of possible boundaries have been studied in detail (Marquardt & Faul 2018). However, the results of these studies have shown that the different types of grain boundaries in olivine-rich rocks may influence the chemical and mechanical properties of the interface region (Marquardt & Faul 2018). Furthermore, it has been shown that segregation of solute ions, precipitates, or interstitial phases, affects the energy and structure of grain boundaries, which in turn may drive the modification of the GBCD, change the interfacial diffusion rate, and affect the rheological behaviour of mantle rocks (Ando *et al.* 2001; Pang & Wynblatt 2006).

To date, direct observations of mineral grain boundaries have mostly been performed by conventional electron and ion beam-based microscopy techniques (Ando *et al.* 2001; Hiraga *et al.* 2002, 2003; Adjaoud *et al.* 2012; Marquardt *et al.* 2015; Marquardt & Faul 2018 and references therein) and a clear atomically-resolved visualization of trace element distributions within mineral interfaces has been difficult due to the intrinsic analytical limitations associated with the nano-scale width of these features. Furthermore, the primary focus of these studies has been related to the understanding of structural properties in relation to olivine high-angle phase and grain boundaries whereas the investigation of low-angle boundaries has been generally overlooked. Thus, the relationships between low-angle boundary geometry and composition at the early stages of grain boundary formation, and how this affects the rock properties, are still largely unconstrained.

Atom probe tomography (APT) allows a precise, quantitative, 3D-characterization of the sub-nanometre distribution of atoms within grain boundary interfaces (Piazolo *et al.* 2016; Fougerouse *et al.* 2019; Montalvo *et al.* 2019; Cukjati *et al.* 2019; Reddy *et al.* 2020). To date, only a few experimental-based investigations have approached the nanoscale characterization of high-angle olivine grain boundaries by atom probe tomography (Cukjati *et al.* 2019). However, the use of the GBCD as the framework for boundary investigations

has been overlooked. In this contribution, we investigate the relationship between grain boundary disorientation (hereafter used to indicate the minimum angular misorientation between adjacent grains, Wheeler *et al.* 2001) and interfacial segregation within a single olivine grain of a natural peridotite deformed by crystal plastic deformation. We analyze a set of low-angle boundaries with similar boundary geometries that exhibit small disorientation angle variations from 1.3° to 8°. By so doing, we investigate a small, but important region of GBCD related to the formation of low-angle boundaries. Our results represent the first, systematic, three-dimensional analysis of trace element segregation associated with dislocation migration during the formation of low-angle boundaries in naturally deformed olivine. The study provides a significant advance in our understanding of element mobility and segregation processes during deformation by subgrain rotation recrystallisation.

5.2 Geological settings and samples

The investigated samples were collected from a spinel-lherzolite found within the Lindås Nappe of the Bergen Arcs and located on the island of Holsnøy (SW Norway) (Figure 5.1). The region comprises Neoproterozoic anorthositic granulites (930 ± 50 Ma; Austrheim & Griffin 1985; Boundy *et al.* 1992), with minor gabbroic components, mangerites, charnockites and ultramafic lenses (Austrheim 2013). Between ca. 430 and 410 Ma, these rocks were locally overprinted at eclogite-facies conditions during a fluid infiltration event along fractures and shear zones (Austrheim & Griffin 1985; Bhowany *et al.* 2018)

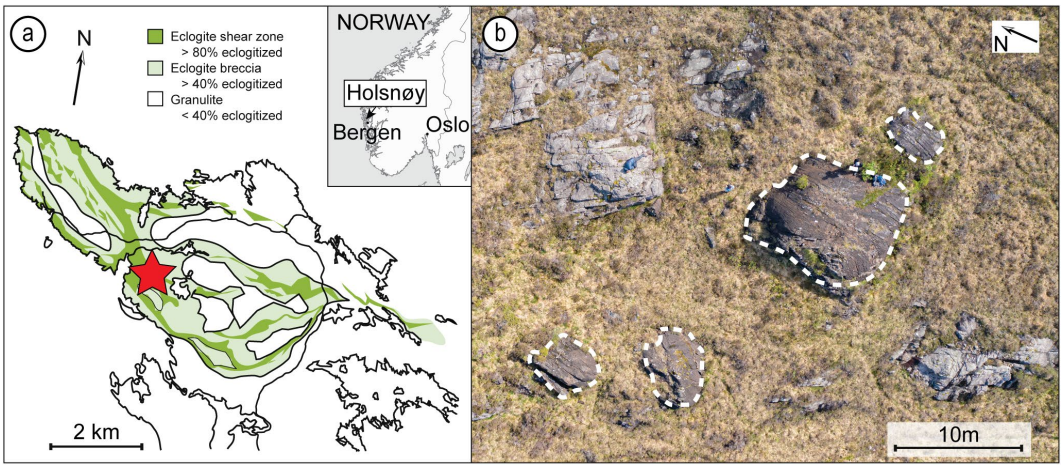

Figure 5.1 (a) Simplified geological map of Holsnøy area (modified after Boundy et al. 1992). (b) Aerial photograph of the ultramafic lenses (dashed lines) outcrop.

The spinel-lherzolites occur as localized lenses enclosed within the partially eclogitized anorthositic granulites and have been interpreted to represent the reworked product of pre-existing cumulate layers (Kühn *et al.* 2000) (Figure 5.1). Within the spinel-lherzolites lenses, a well-developed compositional layering of olivine–pyroxene and garnet-rich bands lies broadly parallel to the granulite-facies foliation in the surrounding anorthositic granulites. The spinel-lherzolites contain abundant centimetre to millimetre wide high-strain zones that crosscut the dominant foliation (Figure 5.2). Mineralogically, the metamorphic transition from the spinel- to garnet-lherzolite is indicative of upper mantle temperature and pressure conditions (O'Neill 1981). Moreover, the presence of minor hydrated minerals (e.g., amphibole) and dolomite are evidence of the presence of fluids during the deformation of these rocks (Kühn *et al.* 2000; Jung *et al.* 2014). Previous work on these high-strain zones has established that these features are related to the high-pressure Caledonian overprint (Kühn *et al.* 2000; Jung *et al.* 2014).

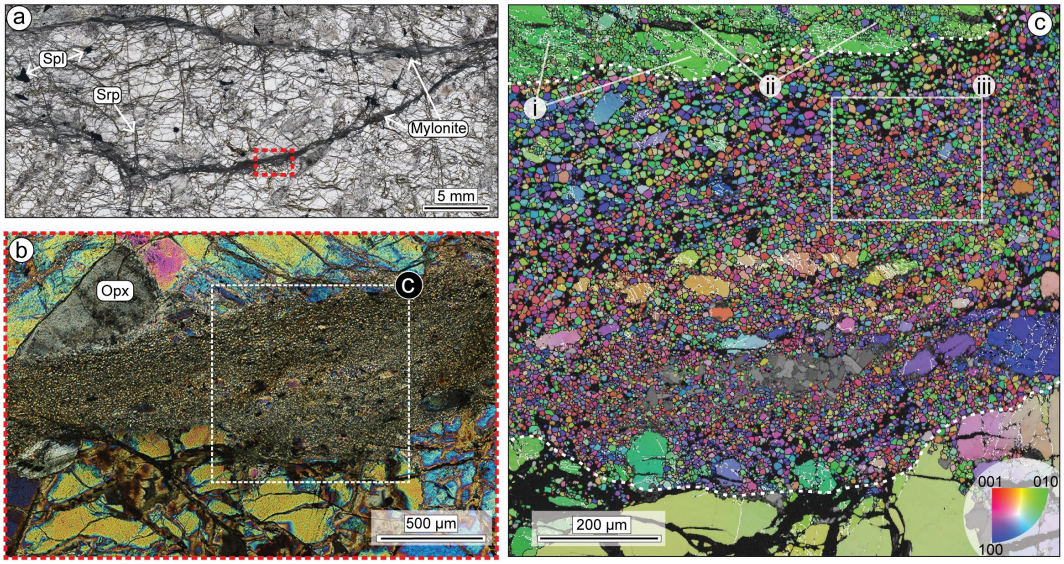

Figure 5.2 (a) Optical plane-polarized photomicrograph of the investigated sample. Red box indicates the investigated EBSD site. Millimetre thick mylonites occur in separate regions of the sample. (b) Crossed-polarized photomicrographs of the investigated section of the lower mylonite (red rectangle). White box represents the area of EBSD shown in c. (c) Inverse Pole Figure (IPF_x) EBSD map highlighting the differences in olivine grain orientations amongst the three different domains (i, ii, iii) of the shear zone. EBSD map step size 0.5 µm.

5.3 Methods

Secondary electron (SE), backscattered electron (BSE) and electron backscattered diffraction (EBSD) data were collected using a Tescan MIRA3 field emission scanning electron microscope (FESEM) housed at the John de Laeter Centre at Curtin University. EBSD data were acquired using an Oxford Instrument Aztec system incorporating a Symmetry EBSD detector and Aztec 4.1 acquisition software using accelerating voltage of 20 kV at 20 mm working distance. EBSD maps were acquired using a step size of 0.5 μm, post-processed using Channel 5.12, and corrected utilizing a standard noise reduction procedure involving the removal of misindexed "wild spikes" and a 6 nearest-neighbour zero solution algorithm. Crystallographic orientation maps and pole figures were constructed using Tango and Mambo sub-components of Channel5 software respectively. Geometrically-necessary dislocation (GND) plots were performed using Aztec Crystal 1.1 software. Detected grains were defined using a critical disorientation of 22° based on molecular dynamic simulations of olivine boundary character (Adjaoud *et al.* 2012; Marquardt *et al.* 2015; Marquardt & Faul 2018) and a minimum disorientation of 1° for boundary completion. Four grain boundaries were specifically selected for detailed atom probe tomography analysis based on similar geometries and disorientation axes. These boundaries have disorientation angles ranging between ~1° and ~8° and are inferred to have formed by similar processes arrested at different degrees of microstructural development.

Needle-shaped specimens for atom probe tomography (APT) and the electron-transparent thin foil for transmission electron microscopy (TEM) were prepared using a Tescan Lyra3 Ga^+ Focused Ion Beam Scanning Electron Microscope (FIB-SEM) at the John de Laeter Centre at Curtin University. The four low-angle boundaries (LAB-1.3°, LAB-2.8°, LAB-4.5°and LAB-8°) were targeted for site specific APT analysis using the "button" method described by Rickard *et al.* (2020). Additionally, during the entire sample preparation procedure, the geometrical orientation of both the interfaces and the atom probe specimens were monitored to allow the reconstructed APT dataset to be geometrically-linked to the boundary trace. Before APT analyses, a final 5 kV polishing stage was performed on all the prepared atom probe specimens to reduce Ga^+ implantation and ion beam damage.

All APT specimens were analysed on a CAMECA LEAP 4000X HR at the Geoscience Atom Probe Facility (John de Laeter Centre, Curtin University) using a base temperature of 50-60 K, an ultraviolet laser (λ= 355nm) with 80-150 pJ pulse energy, 200 kHz frequency and detection rate of 0.008 ions/pulse. Details of the APT technique are

provided elsewhere (Reddy *et al.* 2020). The resulting time-of-flight mass/charge ration spectra were processed and reconstructed in 3D using Cameca's IVAS 3.8.2 software. For the time-of-flight mass spectrum the mass resolving power (M/ΔM) between 1006 and 1096 was measured on the $^{24}Mg^{2+}$ (M = 11.99) peak. The peaks identified within each mass/charge ratio spectrum were compared to the local background and those with peak intensities that were twice above the background level were ranged. Additional details of the acquisition, processing, and reconstruction parameters are provided in the Supplementary Table 5.D.1 (Blum *et al.* 2018). Concentration analysis of the enriched regions was performed using proximity histograms (proxigrams) (Hellman *et al.* 2000) calculated using the ion concentration (at. %) of Ca and Ti (Table 5.1). In order to minimize cross-contamination between enriched domains, the composition of the matrix was obtained using values contained within 3nm of the most distal portions from each enriched interface. The composition of the low-angle boundaries was obtained interpolating the at% obtained from the proxigrams of the interface and the atomic counts within each enriched region. 2D chemical profiles were also used to identify the spatial distribution of the enriched elements along the captured interfaces within the atom probe specimens (Supplementary Figure 5.D.3). In order to estimate the volatile composition of the boundary, OH (17 Da) was quantified as proxy for the H distribution. The accuracy of the approach will be discussed later in this paper.

Bright field (BF) scanning transmission electron microscopy (STEM) and high-angle annular dark-field (HAADF) images of a thin (<200 nm) olivine foil were acquired at 200 kV using a FEI Talos FS200X field emission transmission electron microscope (TEM) housed in the John de Laeter Centre at Curtin University.

5.4 Results

5.4.1 Microstructural characterization of the shear zone

At thin section scale, the undeformed wallrock is coarse-grained and dominated by larger crystals of olivine (< 1 mm) together with ortho- and clinopyroxene. Green spinel is widespread whereas amphibole and carbonates (mainly dolomite) occur as accessory minerals within the rock. Pyroxenes and spinel are often characterized by clusters of microscopic opaque exsolution resulting in a darker optical appearance. Serpentine alteration

is present within the thin section, but is restricted to discrete cracks that cross-cut the shear zones and host olivine grains (Figure 5.2a).

The shear zones form an interconnected network of mm-wide, fine-grained, olivine-rich aggregates with minor orthopyroxene, clinopyroxene, amphibole, spinel and dolomite (Figures 5.2a, b). The contact of the shear zone with the host varies from sharp to irregular with brecciated angular fragments of olivine and pyroxenes scattered within the mylonite matrix (Figure 5.2b). Along the shear zone boundary, crystals of the wall-rock show deformation bands and undulose extinction under crossed polarized light. The transition to the fine-grained shear zone is highlighted by a marked decrease in grain-size (10-15 μm) and a visible variation in mineral orientations from the adjacent host-rock (Figures 5.2b, c). From the wall-rock towards the interior of the mylonite, three microstructurally-distinct domains can be identified in the EBSD data (Figure 5.2c).

Domain (i) represents the deformed host-rock olivine adjacent to the shear zone. Crystals of the host-rock contain low-angle boundaries accommodating small degrees of lattice distortion (< 22°) (Figures 5.2c, 3). Two main trends of low-angle boundary directions can be distinguished, from upper-left to lower-right and from lower-left to upper-right, often intersecting at high angles (Figure 5.3b). The pole figures show that the host-olivine grains of domain (i) are similarly oriented (Figure 5.3b). Disorientation analysis of low-angle boundaries (< 22°) shows an alignment of disorientation axes with the [010] crystallographic direction (Figure 5.3d).

Domain (ii) defines narrow regions that crosscut the host-grain of domain (i). This domain is characterized by the alternation of olivine and orthopyroxene rich bands with minor dolomite, spinel, and clinopyroxene (Figures 5.3a, b). *Domain (ii)* is associated with a noticeable reduction in grain size (< 15 μm in diameter) and the development of olivine neoblasts distinguished by high-angle boundaries (> 22°). The neoblastic olivine grains are progressively reoriented from the host lattice orientation of domain (i) and until they become independent grains surrounded by high-angle boundaries > 22° (Figure 5.3b).

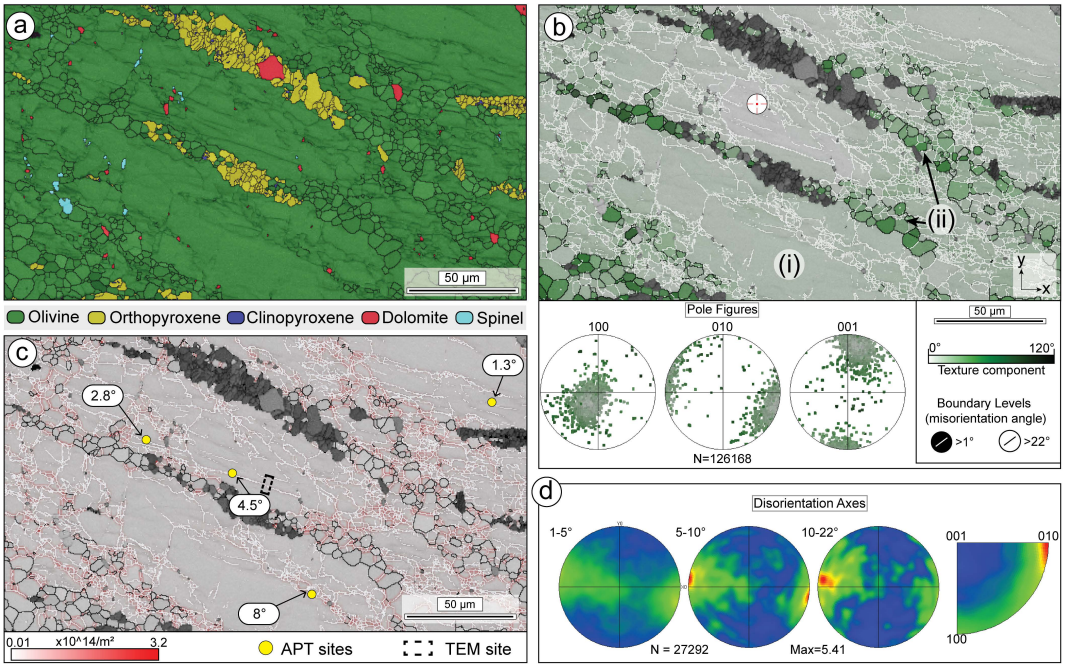

Figure 5.3 Microstructural analysis of domain (i) and (ii) of the shear zone. Sample reference frame is shown in b. (a) Phase map obtained by automated EBSD mapping at 0.5 µm spacing. (b) Olivine grain reference orientation deviation map of domains (i) and (ii) obtained by EBSD mapping highlighting internal substrucutres of the deformed olivine of domain (i). Each pixel is colour coded based on the deviation angle relative to the reference point indicated by a red cross in the map. Low-angle boundaries (1 - 22°) are plotted in white, high-angle boundaries (>22°) in black. Pole figures for domain (i) and (ii) coloured for texture component are also shown. (c) GND density plot of [001] dislocation type. The map colour-scale refers to increasing dislocation densities. The location of the atom probe specimens and TEM analysis are also shown. (d) Disorientation axes plots in sample coordinates (left) and crystal coordinates (right) for the sub-grain boundaries (< 22°) of domain (i) and (ii).

Domain (iii) represents the fine polycrystalline aggregate of the mylonite. The matrix is mainly formed by polygonal olivine grains (10-15 µm in diameter) with 120° triple junctions that show no significant internal misorientation variations (Figures 5.2c, 5.4). Within this domain, larger grains of olivine (up to 50 µm in long dimension) record undulose extinction and internal subgrains that appear similar to those observed in domain (i). Analysis of uncorrelated disorientation angles within the shear zone olivine shows them to be similar to the theoretical random distribution (Figure 5.4). Correlated disorientation angles show a peak at < 10° (Figure 5.4). Using a 1° bin size, a fabric strength (M-index) of 0.082 is calculated for 6802 grains in the shear zone (Skemer *et al.* 2005). These patterns are consistent with the analysis of weakly oriented neoblastic grains containing a small component of incompletely recrystallised grains inherited from the original host [domain (i)] (Figures 5.2c; 5.4). Crystal aggregates of Cl-bearing amphibole are also present in localized portions of the shear zone

whereas individual dolomite, pyroxenes, and spinel grains are scattered within the mylonite matrix.

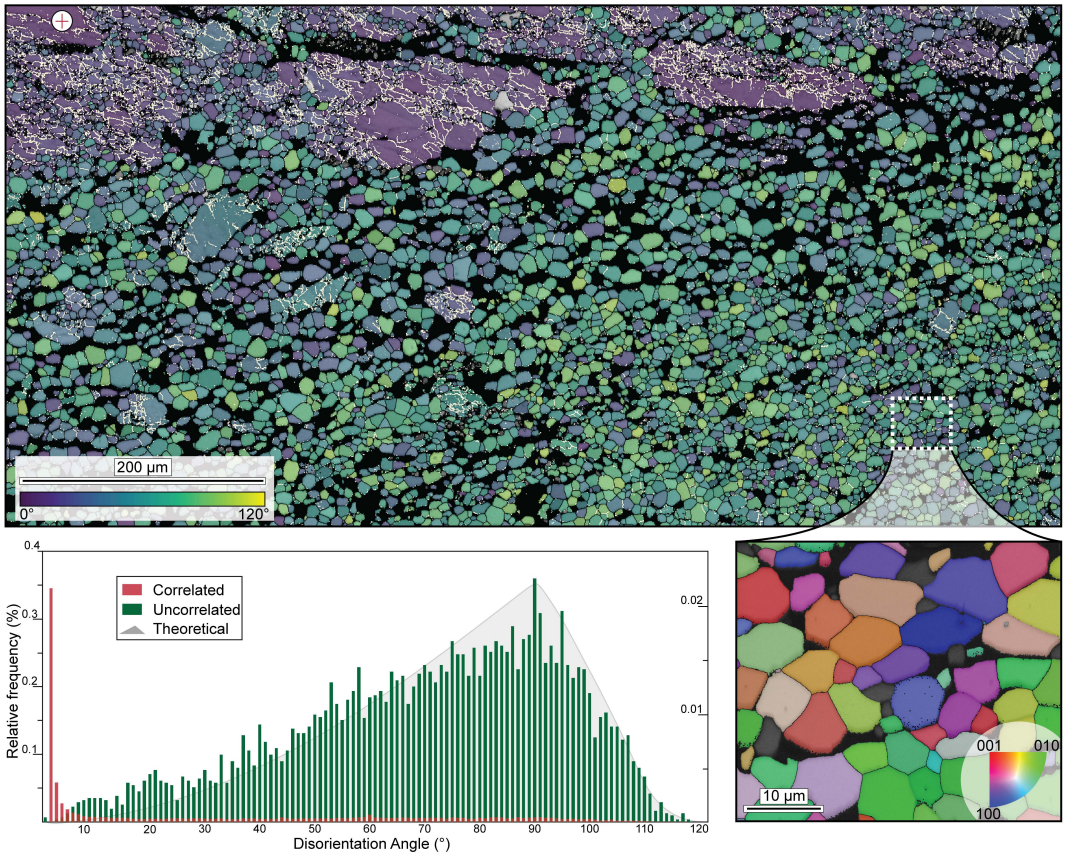

Figure 5.4 EBSD orientation map of the upper part of the shear zone. Each pixel is colour-coded depending on olivine orientation from a reference point indicated with a red cross (upper left). Low-angle boundaries (> 1°) are indicated in white, high-angle boundaries (>22°) in black. Bottom left: Disorientation angle distribution for correlated and uncorrelated disorientations. The grey area represents the theoretical random distribution. Bottom right: Inverse Pole Figure (IPF_x) EBSD map highlighting the differences in olivine grain orientations within the mylonite and the presence of ca. 120° triple junctions. Map step size 50 nm.

To characterize the representative low-angle boundaries for atom probe tomography, the patterns of crystallographic orientation from EBSD data from domain (i) were combined with the geometry of the low-angle boundary trace to infer the slip system responsible for the formation of the observed low-angle boundary (Lloyd *et al.* 1997; Reddy *et al.* 2007). The dominant set of low-angle boundaries (upper-left to lower-right trending) show disorientation axes that are aligned with the [010] crystallographic direction (Figure 5.5). For tilt boundaries, the disorientation axis lies parallel to orientations of dislocations responsible for the lattice distortion. For [010] dislocations and the boundary trace observed in the EBSD maps, there are two possible olivine slip systems (e.g., (100)[001] and (001)[100]). Discrimination between these two possibilities is possible if the geometry of the boundary

in the third dimension is known. This additional information can be found in the 3D APT reconstructions, but was also obtained from a TEM foil across the representative LAB-4.5° (Figure 5.6). The analysis of the lamella on the TEM revealed a complex network of ordered dislocations arranged along two perpendicular principal directions in the foil, a steeply-dipping upper-right to lower-left and a shallower upper-left to lower-right directions (Figure 5.6). These steep and shallow orientations within the foil are consistent with the operation of both the (100)[001] and (001)[100] slip systems respectively. The analysed LAB-4.5° low-angle boundary was taken from the steeply-dipping (ca. 70°) boundary and is consistent with formation by (100)[001] slip (Figure 5.6). For the other analysed boundaries (LAB-1.3°, LAB-2.8° and LAB-8°), the geometry of the interface was measured from the atom probe tomography data, using a similar principle.

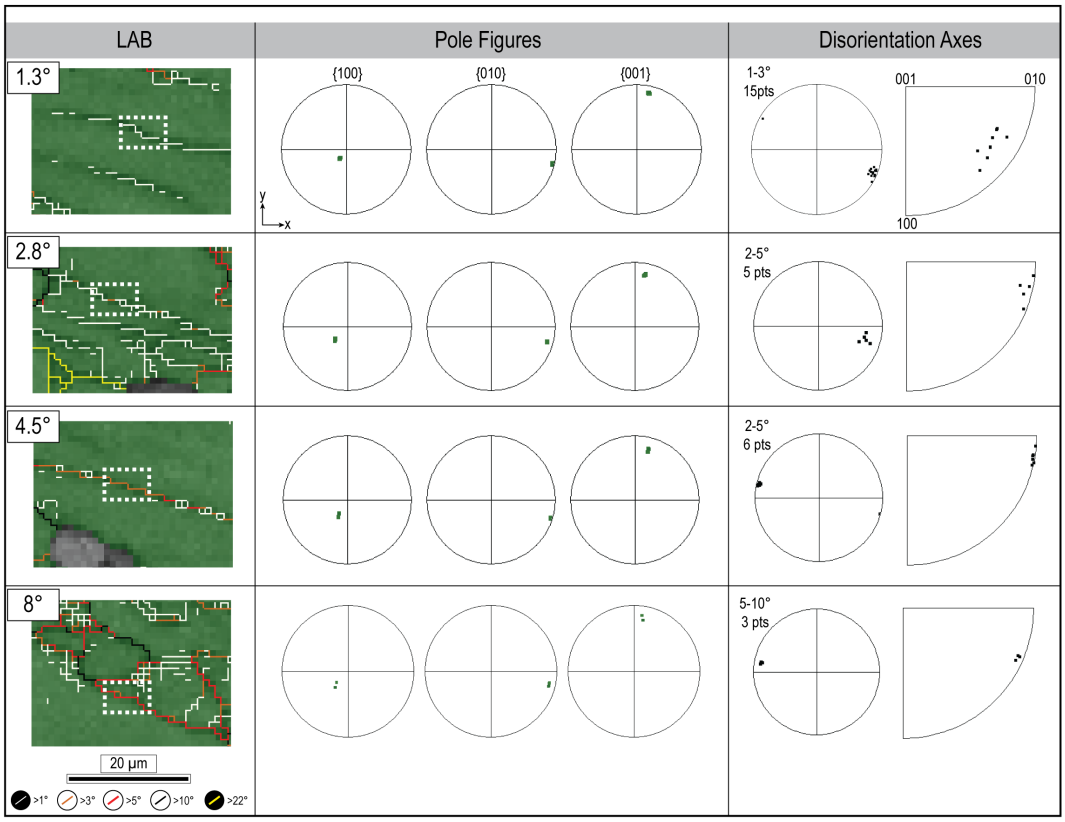

Figure 5.5 Summary of EBSD phase-map (right) and stereographic projections (left) of the investigated low-angle boundaries. Black box in EBSD map shows the subset for the pole figures plots and locations of atom probe tomography specimens lift-out. Grain boundaries are colour coded based on the degree of disorientation as displayed in the legend. Disorientation axes are displayed both in sample and crystal coordinates.

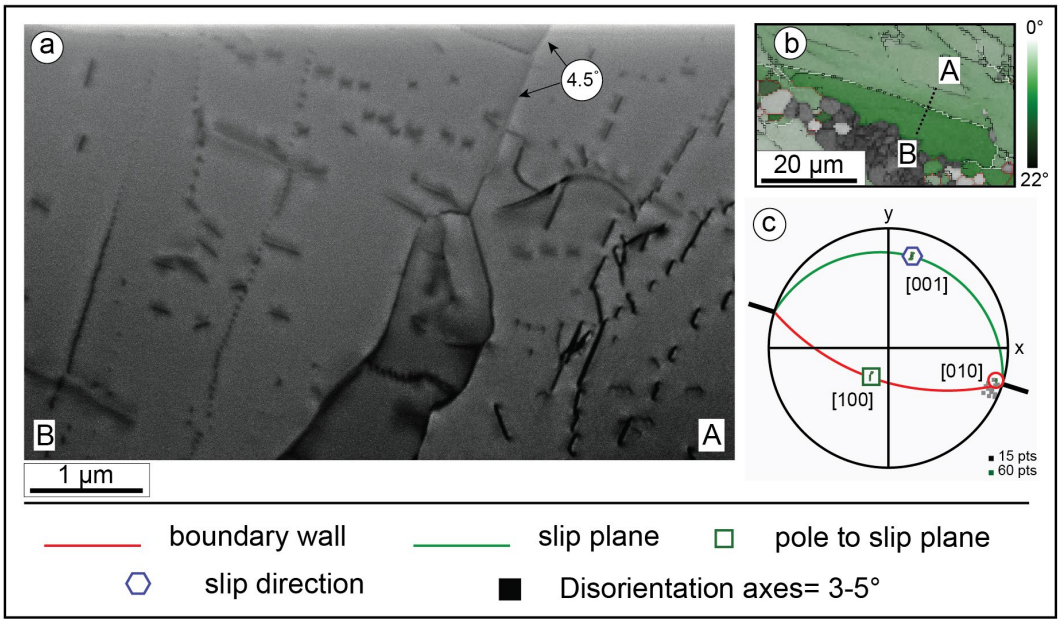

Figure 5.6 (a) HAADF STEM image of olivine lamella obtained across LAB-4.5°. The cross section shows the complexity of domain (i) microstructures. Two main directions of dislocations are distinguishable. (b) GROD-angle orientation map and TEM foil lift-out location. (c) Lower hemisphere and equal area projection of the crystallographic poles of LAB-4.5°. The boundary trace is shown by a thick black line outside the primitive circle. The red curve represents the boundary wall inferred by the tilt boundary geometry of the low angle boundary. The green curved line represents the slip plane (steeply dipping towards B) where the [001] represents the slip direction.

5.4.2 Atom probe tomography

Of the 22 olivine specimens prepared by APT, 10 yielded sufficient data for meaningful analysis. The mass spectra obtained from each of these ten specimens are all similar and record field evaporation of single ions and molecular species at a variety of charge states (Supplementary Figure 5.D.1). The bulk compositions of the reconstructed needles are consistent with the analysis of olivine (Table 5.1). The majority of the mass/charge peaks represent the major elements present within olivine with trace elements forming minor peaks. 3D reconstruction of the APT data reveals the presence of linear and planar domains enriched in particular trace elements compared to the host olivine. Geometrically, the linear domains are broadly consistent with dislocation geometries inferred from the EBSD data, whilst planar domains are consistent with the expected orientation of the targeted steeply-dipping low-angle boundaries (Figure 5.7). Proxigrams obtained from iso-concentration surfaces of the enriched domains show both enrichment and depletion in elements that are not clearly visible in the 3D maps (Figures 5.8, Supplementary Figure 5.D.4).

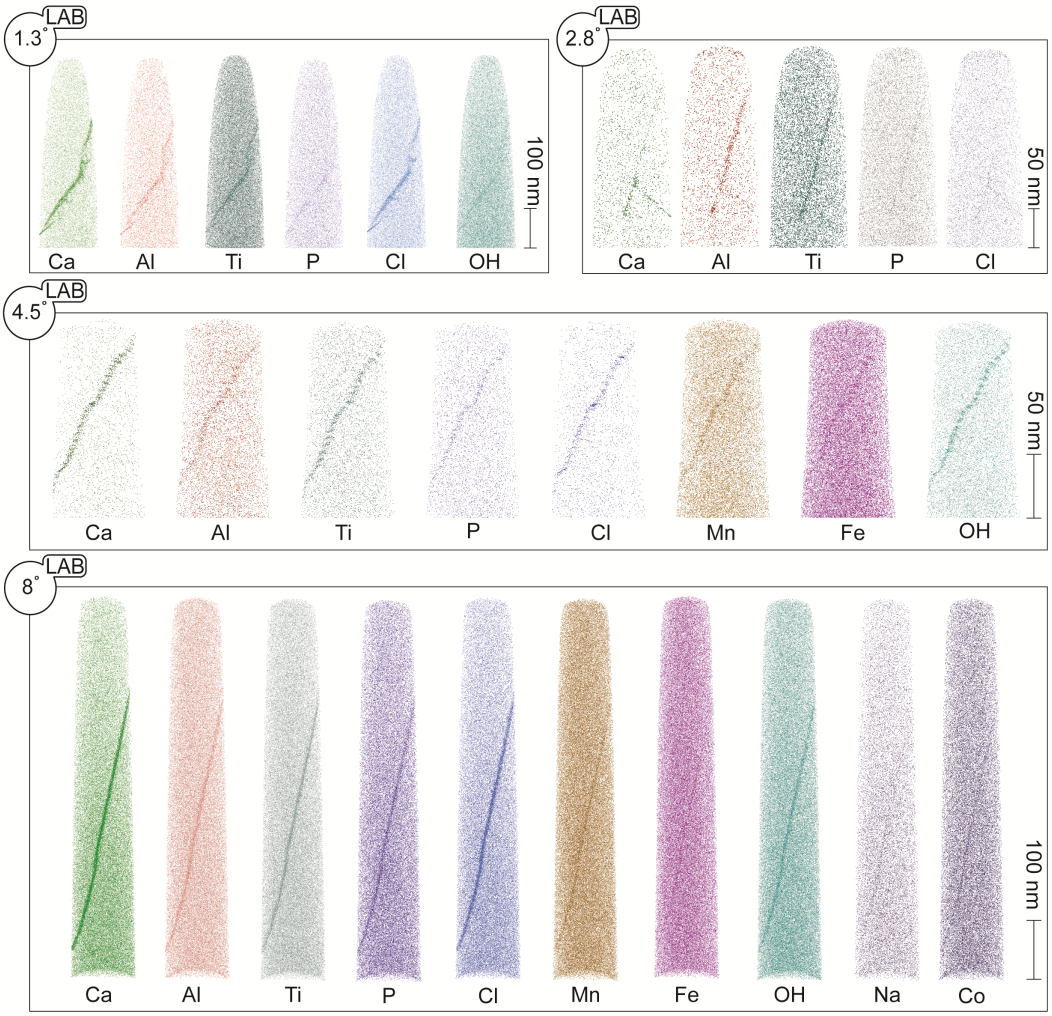

Figure 5.7 3D reconstruction of atom probe specimens for LAB-1.3°, LAB-2.8°, LAB-4.5°, LAB-8°. Each dot in the atom map images represents one detected ionic species. Not all detected atoms are displayed for clarity. The maps show a distinct enrichment of incompatible elements at the targeted interface. An increasing number of elements are found segregated at increasing degrees of disorientation associated with the same crystal slip system. Na and Co segregation is visible only at 8° disorientation angle.

Specimen LAB-1.3° showed a complex boundary geometry. The boundary is characterized by a planar feature constituted by a minimum of three visible sets of linear features intersecting at different angles. These linear features are decorated by Ca, Al, Ti, P, Cl and OH (Figures 5.7, 5.8). The distribution of the enriched elements is heterogeneous as showed by 2D distribution profiles with increasing element concentrations at intersections of the linear features (Supplementary Figure 5.D.3). In particular, a strong increase is visible for Ca up to ca. 0.34 at. %, Cl ca. 0.23 at. %, Ti ca. 0.17 at. %, P ca. 0.08 at. % and OH ca. 0.31 at. % followed by a depletion in O. Mg records a slight decrease in the bulk

concentration but displays a positive detectable increment at the very inner side of the interface (Table 5.1; Supplementary Figure 5.D.4).

Specimen LAB-2.8° contains a main feature highlighted by the local enrichment of Ca (ca. 0.05 at. %), Al (ca. 0.51 at. %), Ti (ca. 0.18 at. %), P (ca. 0.04 at. %), Cl (ca. 0.03 at. %) and Fe, and depletion of O and Mg (Figure 5.7, Table 5.1). The lower zone is also associated with a set of linear features intersecting at a high angle (Figure 5.7).

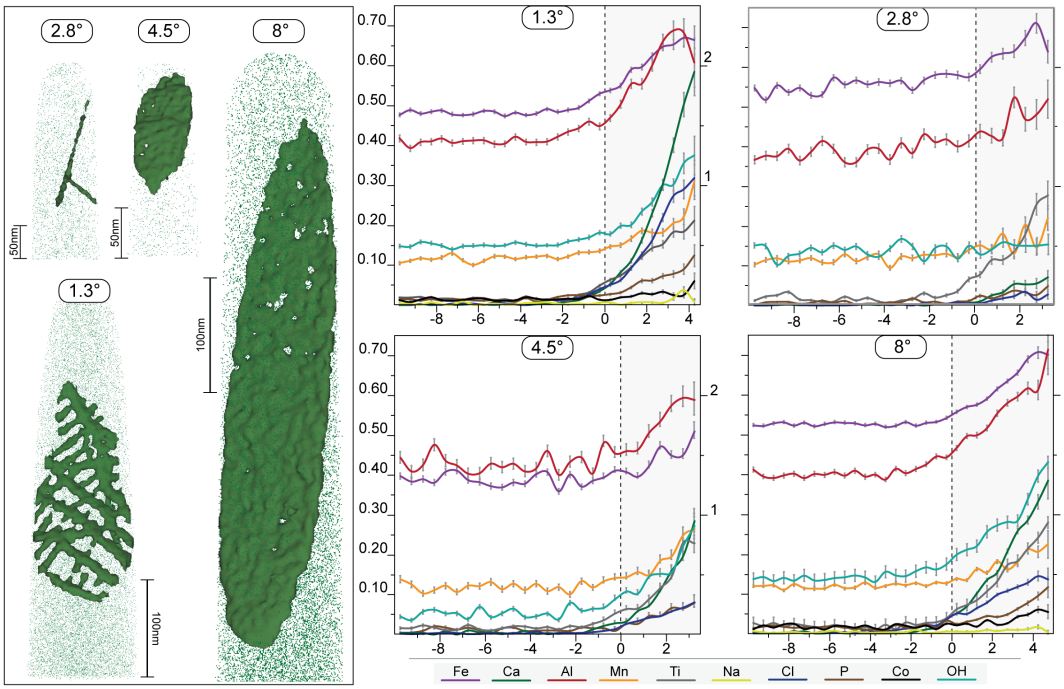

Figure 5.8 3D isosurface renderings of the enriched region of the investigated low-angle boundary based on the concentration of Ca and Ti and relative proximity histogram profiles for visible segregated elements at the interface. The histograms show the gradual increase of concentration expressed in at. % for Ca, Al, Mn, Ti, Na, Cl, P, Co and OH (left y scale) and Fe (right y scale) from the edge (distance 0) towards the inner side of the interface. Distance is expressed in nm.

Within LAB-4.5° the boundary is defined by equally spaced arrays of linear features oriented perpendicular to the vertical axis of the needle tip (Supplementary Figure 5.D.2). The interface is enriched in Ca, Al, Ti, P, Cl, Mn, Fe and OH (Figures 5.7, 5.8). At the interface, Ca shows concentrations of ca. 0.14 at. %, Al ca. 0.58 at. %, Cl ca. 0.06 at. %, Mn ca. 0.20 at. % and OH 0.18 at. %. A decreasing trend of concentration is displayed by Mg and O (Figure 5.8, Supplementary Figure 5.D.4; Table 5.1).

The interface in specimen LAB-8° comprises numerous elongated features and these define a well-developed planar structure (Figures 5.7, Supplementary Figure 5.D.2). The interface shows additional enrichment of Na (ca. 0.01 at. %) and Co (ca. 0.03 at. %). Notably,

the concentrations of the segregated elements are higher compared to LAB-2.8° and LAB-4.5°, with Ca up to ca. 0.23 at. %, Al (ca. 0.63 at. %), Cl (ca. 0.12 at. %) and OH (ca. 0.31 at. %) (Figure 5.8, Table 5.1). Mg, Si and O are reduced within the boundary (Table 5.1; Supplementary Figure 5.D.4).

Table 5.1 Composition of the different olivine specimens and low-angle boundaries obtained from APT. Concentrations are expressed in atomic %.

	LAB-1.3°				**LAB-2.8°**			
Element	Olivine	*σ*	Boundary	σ	Olivine	*σ*	Boundary	σ
O	47.52	*0.06*	46.04	*0.82*	46.85	*0.08*	46.08	*1.23*
Si	20.98	*0.05*	21.15	*0.55*	20.97	*0.07*	21.17	*0.83*
Fe	1.75	*0.01*	2.30	*0.18*	1.95	*0.02*	2.34	*0.28*
Mg	28.91	*0.05*	28.37	*0.64*	29.47	*0.08*	29.17	*0.97*
Ca	0.001	*0.0002*	0.34	*0.07*	0.001	*0.0004*	0.05	*0.04*
Al	0.44	*0.01*	0.69	*0.10*	0.41	*0.01*	0.51	*0.13*
Mn	0.12	*0.004*	0.21	*0.05*	0.12	*0.01*	0.19	*0.08*
Ti	0.02	*0.002*	0.17	*0.05*	0.02	*0.002*	0.18	*0.08*
Na	0.003	*0.001*	0.01	*0.01*	0.005	*0.001*	0.01	*0.02*
Cl	0.002	*0.000*	0.23	*0.06*	0.001	*0.0004*	0.03	*0.03*
P	0.01	*0.001*	0.08	*0.03*	0.01	*0.001*	0.04	*0.03*
Co	0.02	*0.001*	0.03	*0.02*	0.01	*0.002*	0.03	*0.03*
H	0.16	*0.005*	0.31	*0.07*	0.14	*0.01*	0.16	*0.07*
Li	0.00	*0.0003*	0.00	*0.00*	0.001	*0.0004*	0.001	*0.01*
Ni	0.04	*0.002*	0.04	*0.02*	0.04	*0.003*	0.05	*0.04*
Cr	0.01	*0.001*	0.01	*0.01*	0.01	*0.002*	0.01	*0.02*
Sc	0.005	*0.001*	0.01	*0.01*	0.002	*0.01*	0.004	*0.01*

	LAB-4.5°				**LAB-8°**			
Element	Olivine	*σ*	Boundary	σ	Olivine	*σ*	Boundary	σ
O	46.02	*0.11*	45.76	*0.83*	47.39	*0.05*	46.38	*0.41*
Si	20.62	*0.09*	20.77	*0.56*	21.05	*0.04*	20.94	*0.28*
Fe	1.38	*0.03*	1.59	*0.16*	1.90	*0.01*	2.32	*0.09*
Mg	31.24	*0.10*	30.46	*0.68*	28.83	*0.04*	28.51	*0.32*
Ca	0.004	*0.001*	0.14	*0.05*	0.001	*0.0001*	0.23	*0.03*
Al	0.46	*0.01*	0.58	*0.09*	0.43	*0.01*	0.63	*0.05*
Mn	0.13	*0.01*	0.20	*0.06*	0.13	*0.003*	0.19	*0.03*
Ti	0.02	*0.003*	0.14	*0.05*	0.02	*0.001*	0.18	*0.03*
Na	0.003	*0.001*	0.01	*0.01*	0.004	*0.001*	0.01	*0.01*
Cl	0.002	*0.001*	0.06	*0.03*	0.003	*0.0003*	0.12	*0.02*
P	0.01	*0.002*	0.06	*0.03*	0.02	*0.001*	0.06	*0.01*
Co	0.01	*0.002*	0.02	*0.02*	0.02	*0.001*	0.03	*0.01*
H	0.05	*0.005*	0.18	*0.05*	0.15	*0.003*	0.31	*0.03*
Li	0.002	*0.001*	0.001	*0.00*	0.00	*0.000*	0.001	*0.002*
Ni	0.03	*0.004*	0.03	*0.02*	0.04	*0.002*	0.05	*0.01*
Cr	0.01	*0.002*	0.01	*0.01*	0.01	*0.001*	0.01	*0.01*
Sc	0.003	*0.001*	0.004	*0.01*	0.003	*0.0004*	0.01	*0.005*

5.5 Discussion

5.5.1 Microstructural evolution of the olivine mylonite

EBSD orientation data is key to discriminate between different microstructural domains of the shear zone and determine the slip system responsible for the formation of the targeted interfaces for atom probe tomography analysis. In particular, three different microstructurally-distinct domains (*i, ii, iii*) were distinguished showing a systematic increase in disorientation angle associated with the progressive recrystallization of the original host olivine (Figures 5.3, 5.4).

The microstructures associated with *domain (i)* and *domain (ii)* are characterized by the development of subgrains boundaries, grain size decrease, and a change in the character of crystallographic orientations. In particular, a higher density of low-angle boundaries, is apparent in areas adjacent to regions of neoblasts (Figure 5.3b), in agreement with GND density in the order of 10^{14} m^{-2} (Figure 5.3c). These features are consistent with *domain (i)* and *domain (ii)* having formed by the progressive migration and accumulation of dislocations into tilt boundary walls during crystal plasticity. The microstructures associated with the mylonite region (*domain (iii))* are characterized by dislocation-free neoblasts displaying a near-random orientation distribution and the development of triple junctions at ~120°. This suggests the occurrence of recrystallization during deformation and textural equilibrium associated with grain boundary migration within the shear zone. These observations indicate a progressive breakdown of the host olivine by dislocation creep and subgrain rotation recrystallization followed by a switch to grainsize sensitive creep (i.e., diffusion creep) within the shear zone.

The dominant deformation recorded within *domain (i)* is associated with low-angle boundary formation associated with (100)[001] slip system. [001] slip system in olivine is relatively rare, with only a few natural examples having being recorded (Jung *et al.* 2013; Kaczmarek & Reddy 2013). However, the operation of [001] slip in olivine has some important implications as it is preferentially activated during deformation associated with the presence of water and under modest to high-stress conditions (Jung & Karato 2001; Jung *et al.* 2006). In this study, the occurrence of low-angle boundaries dominated by the activity of (100)[001] is therefore consistent with previous interpretations of the Holsnøy peridotites being deformed during the Caledonian orogeny by shear localization in the presence of fluids (Jung *et al.* 2014) and by the regional Caledonian eclogite-facies overprint being localised to zones of fluid-infiltration (Austrheim 2013; Bhowany *et al.* 2018). The presence of

recrystallized Cl-bearing amphibole aggregates and dolomite within the mylonite matrix further supports the presence of a fluid component during the deformation of these rocks.

5.5.2 The relationship between low-angle boundary disorientation, interface structure and trace element composition

A systematic assessment of the relationship between disorientation angle and composition of similarly oriented low-angle boundaries has been undertaken by site-specific atom probe targeting within the deformed host-olivine of *domain (i)*. The atom probe data revealed the enrichment of multiple trace elements (Ca, Al, Ti, P, Mn, Fe, Na, Co, Cl and OH) at these interfaces (Figures 5.7, 5.8).

Three of the low-angle boundaries captured within the analysed specimens (LAB-2.8°, LAB-4.5° and LAB-8°) are characterized by relatively planar surfaces that are internally defined by equally spaced arrays of decorated linear features (Figures 5.7, 5.8). Monitoring of orientation relationships between the thin section and the atom probe specimens during preparation and analysis enables the correlation of the geometrical features in the atom probe data with microstructural information collected from the thin section. This correlation indicates that the linear features within the boundary interfaces are parallel to the disorientation axes inferred from the EBSD analysis of the boundaries. Hence, we interpret these features to represent the preferential segregation of trace elements to dislocations within the low-angle boundaries. In detail, the morphology and distribution of the reconstructed isoconcentration surfaces for these specimens are consistent with the steeply-dipping (100) boundary planes observed in the TEM data being internally defined by arrays of decorated dislocations aligned parallel to the [010] olivine crystallographic direction (Supplementary Figure 5.D.2).

With the exception of LAB-1.3°, the low-angle boundaries LAB-2.8°, LAB-4.5° and LAB-8° display a positive correlation between disorientation angle and trace element enrichment (Figure 5.8, Table 5.1). In detail, LAB-2.8° is enriched in Ca, Al, Ti, P, Cl. In addition to these, Mn, Fe and OH become visible at 4.5° of disorientation. Minor enrichment of Na and Co is only apparent in LAB-8° (Figure 5.7). A concomitant progressive depletion in Mg (and O) is visible from LAB-2.8° to LAB-8° (Supplementary Figure 5.D.4, Table 5.1).

Conversely, at low degrees of lattice distortion, the framework of the boundary captured within LAB-1.3° specimen is defined by a more complex arrangement of elongated

features intersecting at various angles, which are interpreted to represent the intersection of multiple dislocations aligned parallel to the [010], [001] and [011] olivine crystallographic directions (Supplementary Figure 5.D.2). The atomic concentrations of enriched elements registered within LAB-1.3° interface showed a poor correlation compared with the linear trend observed between LAB-2.8°, LAB-4.5° and LAB-8° (Table 5.1). In fact, the concentrations of commonly enriched trace elements within LAB-1.3° are the highest values across all of the analysed specimens. As observed from 2D-chemical profiles for Ca, Cl and Ti, the distribution of the enriched elements within LAB-1.3° is heterogeneous with segregation preferentially localized at dislocation intersections (Supplementary Figure 5.D.3). Similar features have been observed in low-angle boundaries developed within zircon (Piazolo *et al.* 2016; Reddy *et al.* 2016) and pyrite (Fougerouse *et al.* 2019). In such cases, minor lattice distortion (< 3°) is insufficient to form ordered dislocation arrays and the entanglement of geometrically-distinct dislocations is responsible for the local enrichment (i.e., clustering) of segregated elements (Fougerouse *et al.* 2019). It is well known from the Material Science literature that the increasing disorientation between adjacent sub-grains corresponds to a decrease of the spacing between the lattice dislocations that constitute the sub-grain boundary (Read & Shockley 1950; Frank 1951; Priester 2013). At higher lattice distortion the individual dislocations contributing to the formation of a subgrain boundary gradually overlap, until the formation of high-angle boundaries is reached, in which the identification of singular dislocations is no longer possible. Therefore, one possible explanation of the increased trace element concentrations in LAB-1.3°is that, at really low-angle of disorientation, the dominant dislocation sets had no time to mature and the observed boundary structure and trace element enrichment represent the result of a mixture of different slip system required for plastic deformation of a single grain ("von Mises criteria").

With the exception of the trace element concentrations within LAB-1.3°, which is complicated by the presence of multiple dislocations types, the quantitative geochemical data strongly suggest the presence of a systematic relationship between the degree of lattice misorientation, the structure of the grain boundary, and the extent of trace element segregation at those interfaces.

5.5.3 Mechanisms of trace element segregation to low-angle boundaries

The enrichment of solute ions at mineral interfaces is a well-known phenomenon in manufactured material and is considered to reflect the minimization of the elastic strain energy derived by non-stoichiometric atoms within the crystal lattice and space charge compensation (Hondros & Seah 1977; Priester 2013). This enrichment can include mechanisms deriving from the ability of static dislocations to attract interstitial elements ("Cottrell atmosphere", Cottrell & Bilby 1949) or the coupled mobility of trace elements with dislocations as they migrate towards low-angle boundaries during deformation (e.g. Reddy *et al.* 2006, 2007).

In this study, crystal plasticity accommodated by subgrain rotation recrystallization is interpreted to be responsible for the development of *domains (i)* and *(ii)* during deformation (Figure 5.3). Apart from the boundary with the smallest disorientation angle, which is microstructurally distinct from the other studied low-angle boundaries due to the complexity in dislocation types, the boundaries show increasing trace element enrichment with increasing disorientation angle. The elements that are enriched in the boundaries show some similarities with the composition of high-angle grain boundaries in natural and experimentally deformed olivine (Ando *et al.* 2001; Hiraga *et al.* 2002, 2003, 2004; Marquardt *et al.* 2015; Marquardt & Faul 2018; Cukjati *et al.* 2019). These elements are, by enlarge, trace elements that are found within natural olivine (De Hoog *et al.* 2010). The segregation of incompatible trace elements (e.g., Ca, Al and Ti) has been previously reported from studies of olivine grain boundaries, and it is mostly dictated by the bulk composition of the rock and the crystal chemistry (Hiraga *et al.* 2002, 2003, 2004; Marquardt & Faul 2018). Similar observations have also been reported in atom probe studies of low-angle boundaries in zircon and pyrite (Piazolo *et al.* 2016; Reddy *et al.* 2016; Fougerouse *et al.* 2019) and observation in metals and alloys also show an increase of trace element segregation with the number of accumulated dislocation within a boundary (Watanabe 1985).

HREM and AEM studies have demonstrated that local enrichment of particular elements can also be attributed to the occurrence of thin intergranular phases such as amorphous layers or interstitial precipitates (e.g. Wirth 1996; Marquardt *et al.* 2015). In this study, however, the observation that elements segregation at low-angle boundary interfaces is followed by a concomitant depletion in elements such as Si, O and Mg, indicates the preservation of olivine stoichiometry (Hiraga *et al.* 2004). Moreover, the concentration of trace elements at the analysed interfaces does not exceed a few at%. This implies that at the

nanometre scale the interface is still dominated by the typical olivine composition. These observations, therefore, allow us to exclude the presence of an independent intergranular phase between adjacent grains.

Based on EBSD and APT data, we interpret the enrichment of elements such as Ca, Al, Ti, P, Mn, Fe, Na, and Co to reflect the capture and migration of olivine-hosted trace elements in dislocations that migrate to the low-angle boundary during deformation. Our results are consistent with a dynamic and progressive migration and accumulation of dislocations at low-angle boundaries, the associated mobility of trace elements along with these migrating dislocations, and the equilibrium segregation of these trace elements at newly formed sub-grain interfaces (Figure 5.9). The site-specific targeting of low-angle boundaries characterized by a similar tilt-boundary geometry provides information from a small, but important, subset of GBCD variables, and shows a systematic relationship between sub-grain boundary disorientation and composition. Since the GBCD and interfacial segregation are two interlinked manifestations of grain boundary energy minimization, associated with both surface energy and impurity-related elastic strain, these results show the likelihood of a complex structure-property relationship between microstructure and grain boundary composition.

In addition to non-stoichiometric ions, the low-angle boundaries captured with APT are found to be enriched in Cl and OH. The evidence for a [001] slip and previous studies on the same outcrops argue for shear zone formation in a fluid-present geochemical environment (Kühn *et al.* 2000; Austrheim 2013; Jung *et al.* 2014; Bhowany *et al.* 2018). Therefore, although concentrated along the targeted microstructures, there is the possibility that Cl and OH represent exotic components derived from the fluid phase. The presence of H^+ at the analysed interfaces (evaporated as hydroxide anion) is not trivial to assess with atom probe data. It is possible that detected H^+ may represent chamber-sourced hydrogen within the local evaporation field of the planar interfaces during the analysis. However, recent studies using coupled cryogenic sample preparation techniques and APT, have confirmed hydrogen segregation within crystal defects, including interfaces (Chen *et al.* 2020). Furthermore, since the occurrence of H^+ in olivine is strongly attributed to Ti point defects (Berry *et al.* 2005; Walker *et al.* 2007; Demouchy & Alard 2021), the segregation of Ti to grain boundaries is consistent with the observed enrichment of hydrogen in the low-angle interfaces. Moreover, the concentration of hydrogen in the different boundaries is consistent with the systematic Ti enrichment observed within LAB-2.8°, LAB-4.5° and LAB-8°. The role of interfaces, formed during sub-grain rotation recrystallization, as pathways for

subsequent addition of externally-derived trace elements has been shown by Pb isotope analysis intragrain boundaries in pyrite (Fougerouse *et al.* 2019). Therefore, considering the available dataset and both the geological and petrological context of the sample, we can speculate the Cl and H^+ signature detected within the low-angle boundaries to be real and reflecting an externally-derived Cl-bearing fluid present during deformation (Figure 5.9). The progressive increase of atomic concentrations of these trace elements with increasing disorientation may reflect increasingly easier diffusion in boundaries with higher dislocation densities.

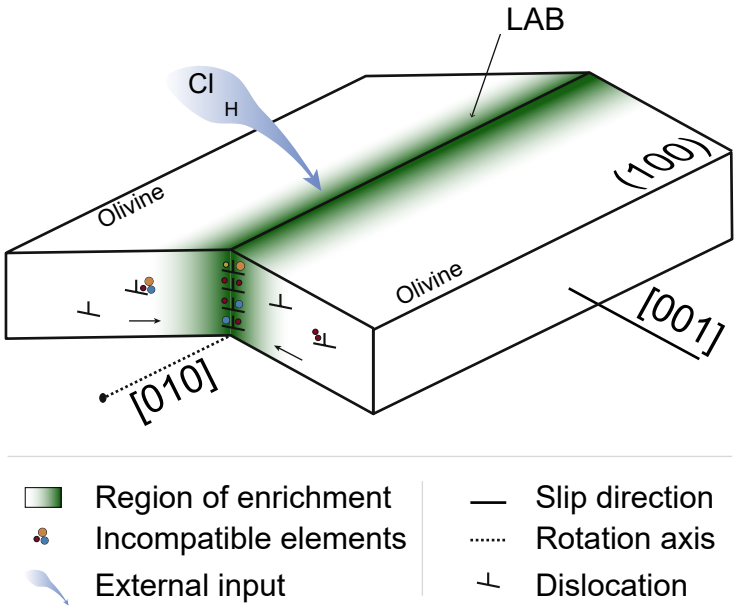

Figure 5.9 Schematic representation of the proposed model of incompatible element segregation along the interface of a symmetric low-angle tilt boundary (modified after Reddy et *al.* 2007). The migration of dislocations facilitates the mobility of solute ions towards the low angle boundary during deformation. The infiltration of Cl and H from an external fluid source is here represented by the blue arrow.

Segregation of solute ions to grain boundaries and intergranular precipitation in response to variation in thermodynamic variables, such as decrease of temperature, is a well-known phenomenon in material science (Dillon *et al.* 2016). The cooling of the sample, for example, generates a decrease in solubility of incompatible trace elements within the crystal lattice and the less-ordered grain boundaries become energetically more favourable as sites of segregation (Priester 2013). The EBSD and APT data presented here indicate a systematic relationship between disorientation and trace element concentrations in the boundaries and there is no evidence for significant modification of low-angle boundary composition after their formation. Unlike many manufactured materials, the segregation of trace elements to

grain boundaries in olivine may not represent a continuous equilibrium process during cooling, but may instead represent the composition shortly after boundary formation. This lack of exchange may reflect the inability of trace elements to migrate through the olivine lattice by volume diffusion once deformation has ceased at temperatures < 700 °C (Cherniak & Liang 2014).

5.5.4 Geological implications

The microstructural and compositional analysis of low-angle boundaries in natural olivine presented in this study shows a previously unidentified structure-chemistry relationship between the amount of lattice distortion and trace element segregation. Although it is generally considered that grain boundaries in polycrystalline materials represent sites of preferential diffusion pathways, for example being an order of magnitude faster than intracrystalline diffusion (Dohmen & Milke 2010), our data shows that different amount of lattice disorientation in tilt-boundaries, associated with the activity of the same slip system, leads to marked compositional differences within the boundary interface. Since element diffusion along 2-dimensional grain boundaries is strongly controlled by the chemistry of the interface (Wuensch & Vasilos 1966), then this has the potential to affect grain boundary diffusion, which in turn can affect viscosity properties (Marquardt & Faul 2018 and references therein) and diffusion rates (Priester 2011; Cukjati *et al.* 2019). Furthermore, the presence of solute atoms segregated at grain boundaries will modify the structure of the interface, thereby affecting the energy of the grain boundary, which is an important factor controlling the grainsize of polycrystalline aggregates (Hiraga *et al.* 2007; Priester 2013). Grainsize is a critical property of materials and controls deformation mechanisms and the properties of rocks during deformation. The nanoscale data presented in this study might therefore have the potential to yield important implications for the intrinsic properties of the rock during crystal plastic deformation highlighting the importance of the geometry of grain boundary interfaces in controlling the migration of solute ions.

The localization of H^+ in the boundary interfaces within olivine has significant implications for the rheological properties of mantle rocks during deformation (Mei & Kohlstedt 2000). In addition, the heterogeneity of hydrogen within nominally anhydrous minerals, such as olivine, can drastically affect physico-chemical properties of the aggregate. The distribution of hydrogen at grain boundaries will have major consequences of decreasing

the strength in dislocation and diffusion creep regime (Mei & Kohlstedt 2000), facilitate and promote chemical reactions and phase transitions, and will modify geophysical properties such as electrical conductivity (Wang *et al.* 2006) and seismic energy attenuation (Karato & Jung 1998).

Previous studies investigating compositional variations associated with low-angle boundaries have suggested that variation in the Fe content of olivine can play an important control in localizing phase transformations in the mantle, which may promote seismicity within deeply subducted lithosphere (Ando *et al.* 2001). This previous study utilized electron beam techniques to show variations at the scale of ~ 200nm (Ando *et al.* 2001). The obtained APT data in this study show that variations in Fe content associated with low-angle boundaries is at a much-finer scale than previously measured - only restricted to a few nanometres. The results also show that Fe enrichment is heterogeneous within these grain boundaries, generally segregating to dislocations within the boundary interface. Moreover, these observations may also imply that phase transformation of olivine, facilitated by Fe heterogeneity, can affect the strength of the upper mantle at early stages of deformation without requiring the application of high differential stress.

5.6 Conclusions

The characterization of the nanostructure and chemistry of low-angle boundaries in olivine obtained by atom probe tomography provides unprecedented evidence of trace elements segregation to low-angle boundary interfaces during deformation. This study reports a direct positive correlation between disorientation angle and the degree of interfacial segregation of solute ions. In addition, the results show a relationship between the composition of low-angle boundaries and the level of grain-boundary complexity. The process of segregation identified in this study involves the capture and the transportation of solute ions within mobile dislocations. Potentially exotic trace elements, such as Cl and H, likely reflect a small, but significant, contribution of an external fluid source also being localized along the grain boundaries. The compositional variations associated with low-angle boundaries have implications for grain deformation and phase transformation of olivine in the depth Earth as well as interpretation of geophysical data, such as electrical conductivity and seismic energy attenuation.

5.6 Acknowledgments

The authors gratefully acknowledge constructive comments from T. Hiraga and an anonymous reviewer which helped improve the quality of the manuscript. We thank D. Canil for the editorial handling and valuable comments that helped improve the final version. The corresponding author owes personal thanks to Joseph C. for helpful discussions.

5.7 References

Adjaoud, O., Marquardt, K. & Jahn, S. 2012. Atomic structures and energies of grain boundaries in Mg2SiO4 forsterite from atomistic modeling. *Physics and Chemistry of Minerals 39(9),* 749–760. DOI 10.1007/s00269-012-0529-5

Ando, J., Shibata, Y., Okajima, Y., Kanagawa, K., Furusho, M. & Tomioka, N. 2001. Striped iron zoning of olivine induced by dislocation creep in deformed peridotites. *Nature 414(6866),* 893–895. DOI 10.1038/414893°

Austrheim, H. akon & Griffin, W.L. 1985. Shear deformation and eclogite formation within granulite-facies anorthosites of the Bergen Arcs, western Norway. *Chemical Geology 50(1–3),* 267–281.

Austrheim, H. 2013. Fluid and deformation induced metamorphic processes around Moho beneath continent collision zones: Examples from the exposed root zone of the Caledonian mountain belt, W-Norway. *Tectonophysics 609,* 620–635. DOI 10.1016/j.tecto.2013.08.030

Berry, A.J., Hermann, J., O'Neill, H.S.C. & Foran, G.J. 2005. Fingerprinting the water site in mantle olivine. *Geology 33(11),* 869. DOI 10.1130/G21759.1

Bhowany, K., Hand, M., Clark, C., Kelsey, D.E., Reddy, S.M., Pearce, M.A., Tucker, N.M. & Morrissey, L.J. 2018. Phase equilibria modelling constraints on *P-T* conditions during fluid catalysed conversion of granulite to eclogite in the Bergen Arcs, Norway. *Journal of Metamorphic Geology 36(3),* 315–342. DOI 10.1111/jmg.12294

Blum, T.B., Darling, J.R., Kelly, T.F., Larson, D.J., Moser, D.E., Perez-Huerta, A., Prosa, T.J., Reddy, S.M., Reinhard, D.A., Saxey, D.W., Ulfig, R.M. & Valley, J.W. 2018. Best Practices for Reporting Atom Probe Analysis of Geological Materials. In: Moser, D.E., Corfu, F., Darling, J.R., Reddy, S.M. & Tait, K. (eds) *Geophysical Monograph Series*. John Wiley & Sons, Inc., Hoboken, NJ, USA, 369–373. DOI 10.1002/9781119227250.ch18

Boundy, T.M., Fountain, D.M. & Austrheim, H. 1992. Structural development and petrofabrics of eclogite facies shear zones, Bergen Arcs, western Norway: implications for deep crustal deformational processes. *Journal of Metamorphic Geology 10(2),* 127–146.

Chen, Y.-S., Lu, H., Liang, J., Rosenthal, A., Liu, H., Sneddon, G., McCarroll, I., Zhao, Z., Li, W., Guo, A. & Cairney, J.M. 2020. Observation of hydrogen trapping at dislocations, grain boundaries, and precipitates. Science 175(2020):171–175. *,* 6.

Cherniak, D.J. & Liang, Y. 2014. Titanium diffusion in olivine. *Geochimica et Cosmochimica Acta 147,* 43–57. DOI 10.1016/j.gca.2014.10.016

Cottrell, A.H. & Bilby, B.A. 1949. Dislocation Theory of Yielding and Strain Ageing of Iron. *Proceedings of the Physical Society. Section A 62(1),* 49–62. DOI 10.1088/0370-1298/62/1/308

Cukjati, J.T., Cooper, R.F., Parman, S.W., Zhao, N., Akey, A.J. & Laiginhas, F.A.T.P. 2019. Differences in chemical thickness of grain and phase boundaries: an atom probe tomography study of experimentally deformed wehrlite. *Physics and Chemistry of Minerals 46(9),* 845–859. DOI 10.1007/s00269-019-01045-x

De Hoog, J.C.M., Gall, L. & Cornell, D.H. 2010. Trace-element geochemistry of mantle olivine and application to mantle petrogenesis and geothermobarometry. *Chemical Geology 270(1–4),* 196–215. DOI 10.1016/j.chemgeo.2009.11.017

Demouchy, S. & Alard, O. 2021. Hydrogen, trace, and ultra-trace element distribution in natural olivines. *Contributions to Mineralogy and Petrology 176(4),* 26. DOI 10.1007/s00410-021-01778-5

Dillon, S.J., Tai, K. & Chen, S. 2016. The importance of grain boundary complexions in affecting physical properties of polycrystals. *Current Opinion in Solid State and Materials Science 20(5),* 324–335. DOI 10.1016/j.cossms.2016.06.003

Dohmen, R. & Milke, R. 2010. Diffusion in Polycrystalline Materials: Grain Boundaries, Mathematical Models, and Experimental Data. *Reviews in Mineralogy and Geochemistry 72(1),* 921–970. DOI 10.2138/rmg.2010.72.21

Faul, U.H., Fitz Gerald, J.D. & Jackson, I. 2004. Shear wave attenuation and dispersion in melt-bearing olivine polycrystals: 2. Microstructural interpretation and seismological implications: ATTENUATION IN MELT-BEARING OLIVINE 2. *Journal of Geophysical Research: Solid Earth 109(B6).* DOI 10.1029/2003JB002407

Fougerouse, D., Reddy, S.M., Kirkland, C.L., Saxey, D.W., Rickard, W.D. & Hough, R.M. 2019. Time-resolved, defect-hosted, trace element mobility in deformed Witwatersrand pyrite. *Geoscience Frontiers 10(1),* 55–63. DOI 10.1016/j.gsf.2018.03.010

Frank F.C. 1951. The resultant content of dislocations in an arbitrary intercrystalline boundary. Report on a symposium on plastic deformation of crystalline solids. Carnegie Institute of Technology and Office of Naval Research, pp 150–154.

Hansen, L.N., Zimmerman, M.E. & Kohlstedt, D.L. 2012. The influence of microstructure on deformation of olivine in the grain-boundary sliding regime: effect of microstructure on deformation. *Journal of Geophysical Research: Solid Earth 117(B9).* DOI 10.1029/2012JB009305

Hellman, O.C., Vandenbroucke, J.A., Rüsing, J., Isheim, D. & Seidman, D.N. 2000. Analysis of Three-dimensional Atom-probe Data by the Proximity Histogram. *Microscopy and Microanalysis 6(05),* 437–444. DOI 10.1007/S100050010051

Hiraga, T., Anderson, I., Zimmerman, M., Mei, S. & Kohlstedt, D. 2002. Structure and chemistry of grain boundaries in deformed, olivine + basalt and partially molten lherzolite aggregates: evidence of melt-free grain boundaries. *Contributions to Mineralogy and Petrology 144(2),* 163–175. DOI 10.1007/s00410-002-0394-1

Hiraga, T., Anderson I.M., & Kohlstedt D.L. 2003. Chemistry of grain boundaries in mantle rocks. *American Mineralogist* 88(6976):1015–1019.

Hiraga, T., Anderson I.M., & Kohlstedt D.L. 2004. Grain boundaries as reservoirs of incompatible elements in the Earth's mantle. *Nature* 427(6976):699–703.

Hiraga, T., Hirschmann, M.M. & Kohlstedt, D.L. 2007. Equilibrium interface segregation in the diopside–forsterite system II: Applications of interface enrichment to mantle geochemistry. *Geochimica et Cosmochimica Acta 71(5),* 1281–1289. DOI 10.1016/j.gca.2006.11.020

Hondros, E.D. & Seah, M.P. 1977. Segregation to interfaces. *International Metals Reviews 22(1),* 262–301. DOI 10.1179/imtr.1977.22.1.262

Jung, H. & Karato, S.-I. 2001. Effects of water on dynamically recrystallized grain-size of olivine. *Journal of Structural Geology 23(9),* 1337–1344.

Jung, H., Katayama, I., Jiang, Z., Hiraga, T. & Karato, S. 2006. Effect of water and stress on the lattice-preferred orientation of olivine. *Tectonophysics 421(1–2),* 1–22. DOI 10.1016/j.tecto.2006.02.011

Jung, H., Lee, J., Ko, B., Jung, S., Park, M., Cao, Y. & Song, S. 2013. Natural type-C olivine fabrics in garnet peridotites in North Qaidam UHP collision belt, NW China. *Tectonophysics 594,* 91–102. DOI 10.1016/j.tecto.2013.03.025

Jung, S., Jung, H. & Austrheim, H. akon. 2014. Characterization of olivine fabrics and mylonite in the presence of fluid and implications for seismic anisotropy and shear localization. *Earth, Planets and Space 66(1),* 46.

Kaczmarek, M.-A. & Reddy, S.M. 2013. Mantle deformation during rifting: Constraints from quantitative microstructural analysis of olivine from the East African Rift (Marsabit, Kenya). *Tectonophysics 608,* 1122–1137. DOI 10.1016/j.tecto.2013.06.034

Karato S.I. & Jung H. 1998. Water, partial melting and the origin of the seismic low velocity and high attenuation zone in the upper mantle, *Earth and Planetary Science Letters*, 157, 193–207.

Kohlstedt, D.L. 1990. Chemical analysis of grain boundaries in an olivine-basalt aggregate using high-resolution, analytical electron microscopy. In: Duba, A.G., Durham, W.B., Handin, J.W. & Wang, H.F. (eds) *Geophysical Monograph Series.* American Geophysical Union, Washington, D. C., 211–218. DOI 10.1029/GM056p0211

Kühn A., Glodny J., Iden K., & Austrheim H. 2000. Retention of Precambrian Rb/Sr phlogopite ages through Caledonian Eclogite facies metamorphism, Bergen Arcs Complex, W-Norway. *Lithos* 51, 305–330.

Lejček, P. 2010. *Grain Boundary Segregation in Metals*. Springer, New York, NY, Springer series in materials science.

Lloyd, Farmer A.B., & Mainprice D. 1997. Misorientation analysis and the formation and orientation of subgrain and grain boundaries. *Tectonophysics* 279(1–4):55–78.

Marquardt, K. & Faul, U.H. 2018. The structure and composition of olivine grain boundaries: 40 years of studies, status and current developments. *Physics and Chemistry of Minerals 45(2),* 139–172. DOI 10.1007/s00269-017-0935-9

Marquardt, K., Rohrer, G.S., Morales, L., Rybacki, E., Marquardt, H. & Lin, B. 2015. The most frequent interfaces in olivine aggregates: the GBCD and its importance for grain boundary related processes. *Contributions to Mineralogy and Petrology 170(4)*. DOI 10.1007/s00410-015-1193-9

Mei, S. & Kohlstedt, D.L. 2000. Influence of water on plastic deformation of olivine aggregates 2. Dislocation creep regime. *Journal of Geophysical Research* 105(B9):21471–21481.

Montalvo, S.D., Reddy, S.M., Saxey, D.W., Rickard, W.D.A., Fougerouse, D., Quadir, Z. & Johnson, T.E. 2019. Nanoscale constraints on the shock-induced transformation of zircon to reidite. *Chemical Geology 507,* 85–95. DOI 10.1016/j.chemgeo.2018.12.039

O'Neill, H.St.C. 1981. The transition between spinel lherzolite and garnet lherzolite, and its use as a Geobarometer. *Contributions to Mineralogy and Petrology 77(2),* 185–194. DOI 10.1007/BF00636522

Pang, Y. & Wynblatt, P. 2006. Effects of Nb Doping and Segregation on the Grain Boundary Plane Distribution in TiO2. *Journal of the American Ceramic Society 89(2),* 666–671. DOI 10.1111/j.1551-2916.2005.00759.x

Piazolo, S., La Fontaine, A., Trimby, P., Harley, S., Yang, L., Armstrong, R. & Cairney, J.M. 2016. Deformation-induced trace element redistribution in zircon revealed using atom probe tomography. *Nature Communications 7(1)*. DOI 10.1038/ncomms10490

Priester, L. (ed.). 2011. Grain Boundaries and Crystalline Plasticity. 344 pp. ISTE ; *Wiley*, London : Hoboken, NJ.

Priester, L. 2013. Grain Boundaries. Springer Netherlands, Dordrecht, *Springer Series in Materials Science*. DOI 10.1007/978-94-007-4969-6

Putnis, A. & John, T. 2010. Replacement Processes in the Earth's Crust. *Elements 6(3),* 159–164. DOI 10.2113/gselements.6.3.159

Read W.T. & Shockley W. 1950. Dislocation models of crystal grain boundaries. *Physical Reviews* 78:275–289.

Reddy, S.M., Timms, N.E., Trimby, P., Kinny, P.D., Buchan, C. & Blake, K. 2006. Crystal-plastic deformation of zircon: A defect in the assumption of chemical robustness. *Geology 34(4),* 257. DOI 10.1130/G22110.1

Reddy, S.M., Timms, N.E., Pantleon, W. & Trimby, P. 2007. Quantitative characterization of plastic deformation of zircon and geological implications. *Contributions to Mineralogy and Petrology 153(6),* 625–645. DOI 10.1007/s00410-006-0174-4

Reddy, S.M., van Riessen, A., Saxey, D.W., Johnson, T.E., Rickard, W.D.A., Fougerouse, D., Fischer, S., Prosa, T.J., Rice, K.P., Reinhard, D.A., Chen, Y. & Olson, D. 2016. Mechanisms of deformation-induced trace element migration in zircon resolved by atom probe and correlative microscopy. *Geochimica et Cosmochimica Acta 195,* 158–170. DOI 10.1016/j.gca.2016.09.019

Reddy, S.M., Saxey, D.W., Rickard, W.D.A., Fougerouse, D., Montalvo, S.D., Verberne, R. & Riessen, A. 2020. Atom Probe Tomography: Development and Application to the Geosciences. *Geostandards and Geoanalytical Research 44(1),* 5–50. DOI 10.1111/ggr.12313

Rickard, W.D.A., Reddy, S.M., Saxey, D.W., Fougerouse, D., Timms, N.E., Daly, L., Peterman, E., Cavosie, A.J. & Jourdan, F. 2020. Novel Applications of FIB-SEM-Based ToF-SIMS in Atom Probe Tomography Workflows. *Microscopy and Microanalysis,* 1–8. DOI 10.1017/S1431927620000136

Ricoult, D.L. & Kohlstedt, D.L. 1983. Structural width of low-angle grain boundaries in olivine. *Physics and Chemistry of Minerals 9(3–4),* 133–138. DOI 10.1007/BF00308370

Rohrer, G.S. 2011. Grain boundary energy anisotropy: a review. *Journal of Materials Science 46(18),* 5881–5895. DOI 10.1007/s10853-011-5677-3

Skemer, P., Katayama, I., Jiang, Z. & Karato, S. 2005. The misorientation index: Development of a new method for calculating the strength of lattice-preferred orientation. *Tectonophysics 411(1–4),* 157–167. DOI 10.1016/j.tecto.2005.08.023

Suzuki K. 1987. Grain-boundary enrichment of incompatible elements in some mantle peridotites. *Chemical Geology*, 63, 319–334.

Walker, A.M., Hermann, J., Berry, A.J. & O'Neill, H.St.C. 2007. Three water sites in upper mantle olivine and the role of titanium in the water weakening mechanism. *Journal of Geophysical Research 112(B5).* DOI 10.1029/2006JB004620

Wang, D., Mookherjee, M., Xu, Y. & Karato, S. 2006. The effect of water on the electrical conductivity of olivine. *Nature 443(7114),* 977–980. DOI 10.1038/nature05256

Watanabe, T. 1985. Structural effects on grain boundary segregation, hardening and fracture. *Le Journal de Physique Colloques 46(C4),* C4-555-C4-566. DOI 10.1051/jphyscol:1985462

Wenk H.R. 1985. Preferred Orientation in Deformed Metal and Rocks: An Introduction to Modern Texture Analysis. *Academic Press Inc*, New York.

Wheeler, J., Prior, D., Jiang, Z., Spiess, R. & Trimby, P. 2001. The petrological significance of misorientations between grains. *Contributions to Mineralogy and Petrology 141(1),* 109–124. DOI 10.1007/s004100000225

Wirth, R. 1996. Thin amorphous films (1-2 nm) at olivine grain boundaries in mantle xenoliths from San Carlos, Arizona. *Contributions to Mineralogy and Petrology 124(1),* 44–54. DOI 10.1007/s004100050172

Wuensch, B.J. & Vasilos, T. 1966. Origin of Grain-Boundary Diffusion in MgO. *Journal of the American Ceramic Society 49(8),* 433–436. DOI 10.1111/j.1151-2916.1966.tb15411.x

Yabe, K. & Hiraga, T. 2020. Grain-Boundary Diffusion Creep of Olivine: 2. Solidus Effects and Consequences for the Viscosity of the Oceanic Upper Mantle. *Journal of Geophysical Research: Solid Earth 125(8).* DOI 10.1029/2020JB019416

Zhao, N., Hirth, G., Cooper, R.F., Kruckenberg, S.C. & Cukjati, J. 2019. Low viscosity of mantle rocks linked to phase boundary sliding. *Earth and Planetary Science Letters 517,* 83–94. DOI 10.1016/j.epsl.2019.04.019

Chapter 6

Synthesis and Thesis Conclusions

This doctoral thesis aims to investigate metamorphic processes of fluid-rock interactions at the nanometre scale. In this research, the application of a systematic stepwise workflow, which combines microanalytical techniques such as SEM, EBSD, ToF-SIMS and LA-ICPMS together with TEM and atom probe tomography, allows to characterize the nanoscale manifestation of trace element mobility occurring at the interplay between deformation, fluid infiltration and metamorphism.

This project investigates two main case studies, isolated in four investigations, and included in this thesis as individual chapters (*Chapters 2–5*). Although separated, these studies are closely related in that each provides a detailed microstructural and geochemical picture of different mechanisms occurring during the complex fluid-mediated metamorphism and/or deformation that can occur within lower crustal lithologies. As indicated in the thesis structure of the introductory chapter, the four studies are presented in order of increasing complexity of the investigated system. In detail, the research initially applied nanoscale techniques of characterization to an undeformed closed system such as melt inclusions (*Chapter 2*). Thereafter, the perspective shifted towards a complex open system of fluid-mediated deformation by quantifying deformation microstructures in metasomatic shear zones *(Chapter 3*). The linking between deformation and trace element mobility at the nanoscale was then investigated by targeting low-angle boundaries within deformed garnet and olivine (*Chapter 4,5*). As one of the results of *Chapter 2*, the first part of this synthesis addresses the importance of integrating techniques such as atom probe tomography into the conventional analytical workflow to investigate features previously challenged by their size. Building off the outcome of *Chapter 2*, the following sections bring together also *Chapters 3,4 and 5* intending to summarize and discuss the information obtained from metre to nanometre scale investigation of fluid infiltration, metamorphism, grain-scale and element mobility mechanisms. Finally, before concluding the thesis, some recommendations for the use of APT are outlined for future investigations.

6.1 Trace element distribution in anatectic glassy inclusions

For the past decade, the presence of crystal-free glassy melt inclusions trapped within peritectic minerals of migmatitic and granulitic terranes has been a matter of debate (see Cesare *et al.* 2009; Clemens 2009; Ferrero *et al.* 2012; Bartoli *et al.* 2016; Bartoli 2020). Despite the slow cooling rates of the host rocks (~ 3–6 °C/Ma; Cenki *et al.* 2004), observations

conducted by both conventional optical and scanning electron microscopy techniques (e.g., SEM), do not indicate evidence of solid phases crystallized within the entrapped fluid. However, these inclusions are commonly found coexisting with partially, or/and totally crystallized inclusions (nanogranitoids; Cesare *et al.* 2015), to which they are both microstructurally and compositionally related.

In *Chapter 2* of this research, high spatial resolution analyses conducted on glassy inclusions revealed the presence of chemical heterogeneities within the preserved amorphous material. Based on ToF-SIMS data, at the microscale, the inclusions are characterized by patchy distributions of Na and K within the glass and along inclusion edges. At the nanoscale, TEM and APT analyses revealed the presence of compositional clusters enriched in Fe, Al, and trace elements. Based on their systematic distribution at the inclusion edges (sites of daughter mineral nucleation, Roedder 1984), the geometrical similarities with nanostructures observed in synthetic and volcanic glasses and the chemical compatibility with common crystallized phases in partially crystallized inclusions, we interpreted these domains to represent pre-nucleation clusters. Hence, glassy inclusions represent former nanogranitoids "captured" at an earlier stage of crystallization. The formation of these clusters has been linked to the existence of a short-range diffusion gradient induced by the shape maturation of the inclusions after their formation (e.g., Cesare *et al.* 2021). Moreover, integration of our results with previously published work on melt inclusions suggests that the impediment to crystallization might not only be facilitated by the small volume of these cavities, but also by the H_2O contents of the entrapped melt.

The micro- to the nanoscale characterisation of natural glassy inclusions conducted in *Chapter 2* provides a robust indication for the common origin of both glassy and nanogranitoid inclusions, shedding light on the oddity of glass preservation in slowly cooled rocks. In addition, results show the absence of a detectable diffusional exchange between the two mineral phases, confirming the pristine character of these inclusions for geochemical studies. *Chapter 2*, therefore, not only establishes that APT can resolve the chemistry of melt inclusions and produce high-quality datasets, but also that the integration of the technique into the analytical workflow can provide insights into previously unobserved mechanisms of distribution and mobility of elements.

6.2 The impact of fluid-assisted deformation on grain-scale microstructures

In the thesis introduction, it is discussed the key role that fluids *s.l.* have in modifying both the mechanical and chemical properties of rocks. The introduction of a fluid phase into a rock has the potential to generate thermodynamic conditions of disequilibrium, causing the re-equilibration of the host by metasomatic reactions. Importantly, fluids modify the rheological response of minerals to deformation, with larger impacts on the rheology of the entire aggregate. For example, fluid infiltration into metastable rocks such as granulites promotes softening reactions thereby facilitating the deformation of the aggregate. On the other hand, deformation is one of the main mechanisms responsible for increasing permeability by the formation of fractures and shear zones, which in turn facilitates the infiltration of a fluid phase into the rock. Therefore, it is clear that there is a strong relationship between deformation, fluid infiltration and metasomatism. This relationship has been noted and discussed by several previous studies and in different geological contexts (e.g., Austrheim 1987, 2013; Carter *et al.* 1990; Jamtveit *et al.* 1990, 2019, 2021; Mancktelow & Pennacchioni 2005; Getsinger *et al.* 2013; Petley-Ragan *et al.* 2018; Hawemann *et al.* 2019; Petley-Ragan *et al.* 2019). However, applying nanoscale techniques to understand trace element mobility during these metasomatic mechanisms is challenged by the complexity of the system.

In this scenario, the combination of metre- to nanoscale analyses conducted on the shear zone exposed at Isdal (*Chapter 3*), provided the information necessary to extract and reconstruct the evolutionary history of such complex interactions. The interpretation of the microstructures presents a sequence of mechanisms where at an initial stage of deformation, grain size reduction is accommodated by crystal plastic processes, whereas mineral replacement reactions are dominated by dissolution-precipitation creep (pressure solution) at the on-set between mineral interfaces (Mukai *et al.* 2014; Putnis *et al.* 2017). With the progress of deformation, the increased permeability of the rock enhances fluid flow, reaction softening and ductility favouring the formation of the shear zone. *Chapter* 3 highlights how the quantification of deformation microstructures on large areas of the samples and for a variety of minerals provides a complete picture of the impact that fluid-aided deformation has at grain scale levels. By doing so, the study also provides a re-evaluation of the dominant deformation mechanisms responsible for the development of the ductile shear zone exposed at Isdal, contributing to a better understanding of lower crust weakening processes.

Importantly, this chapter helped to delineate an analytical workflow to understand and identify "where to find" deformation microstructures (e.g., sub-grain boundaries) within complex systems, which are therefore suitable for the evaluation of the impact of deformation element mobility, setting the basis for the subsequent investigation by APT performed in *Chapters 4 and 5*.

6.3 Trace element mobility during fluid-enhanced deformation

One of the main aims of this doctoral research is to improve our understanding of the feedback of fluid-interaction mechanisms on the mobility of elements. By analysing amorphous silicate glass trapped as inclusions in garnets, *Chapter 2* revealed the presence of mechanisms of elemental reorganization into pre-nucleation clusters driven, in a closed undeformed system, by short-range gradients of diffusion. In a deformed open system, *Chapter 3* showed that, at the micro-scale, fluids find their way into a rock along grain boundaries enabling mass-transfer mechanisms such as pressure solution. On the other hand, *Chapter 4* demonstrated that, at the nanoscale, the distribution of elements during fluid-aided deformation can be modified by coupled mechanisms.

In *Chapter* 4, the analysis of a garnet low-angle boundary formed by crystal plasticity revealed the presence of trace elements such as Cl, Na, K, Ti, P, Cu, H and to a minor extent Ca, concentrated along the planar interface. Considering the geological context of these rocks, the observed enrichment of trace elements is interpreted to be the result of two concomitant mechanisms acting during the formation of the interface. Ca, Ti, P and Cu are interpreted to reflect the preferential segregation of solute ions transported to the low-angle boundary by migrating dislocations during dislocation creep (i.e., defect-impurity pair). Contrarily, K, Na, Cl and H enrichment is attributed to an external fluid phase (e.g., a brine) present during deformation and transported along the interface by diffusion mechanisms. Although being representative of an open system, the nanoscale investigation conducted on a single low-angle boundary allowed the complexity of the investigation to be reduced. By targeting a low-angle boundary formed within garnet with APT, *Chapter 4* not only reveals that trace elements can be mobilised by the intracrystalline migration of dislocations but also shows that crystal plastic deformation has the potential to generate pathways for diffusion of externally derived components into a mineral. Independent of the dominant mechanism promoting trace element enrichment, the results obtained by this study provide evidence of

the role that deformation has on element mobility at the nanoscale. Moreover, these findings are unprecedented and have the potential to yield strong implications for the robustness of garnet geochemistry.

At this stage of the research, the application of APT to deformation microstructures demonstrates how, during fluid-induced deformation, the mobility of trace elements along interfaces can be promoted by a combination of mass-transport mechanisms. However, the impact that different amounts of deformation might have on the extent of trace element segregation has not been established yet. In this regard, *Chapter 5* aims to address this aspect by performing APT analyses on deformation-related low-angle boundaries in olivine. The investigation is undertaken on a set of low-angle boundaries with increasing disorientation angles (i.e., increasing degree of deformation). Moreover, in order to be representative, the study has been performed in a conventional framework of grain boundaries investigation by the use of a smaller subset of the grain boundary character distribution (GBCD; e.g., Marquardt *et al.* 2015). In detail, this has been obtained by investigating a monomineralic system (a single crystal of olivine), low-angle boundaries formed by the same slip system and characterised by the same crystallographic geometries. Based on the findings of the previous study, crystal plasticity is expected to have influenced the transport of elements. Here, APT analyses of olivine show enrichment of Ca, Al, Ti, P, Mn, Fe, Na, Co, Cl and H to the targeted interfaces. Moreover, the enrichment of elements allows to observe the evolution of the atomic structure of each boundary (i.e., dislocations). In detail, boundaries with $< 2°$ show marked enrichment associated with the presence of multiple, non-parallel dislocation types. At larger disorientation, the interfaces become more ordered and defined by linear enrichment of trace elements. Importantly, the comparison of the chemistry obtained from APT reconstruction shows a systematic increase of trace element concentration with disorientation angle. Once again, a combination of observations indicates that multiple different mechanisms played a role in the enrichment of trace elements. Olivine-derived impurities such as Ca, Al, Ti, P, Mn, Fe, Na and Co are interpreted to be segregated to the interfaces by defect-impurity pair during dislocation creep, whereas higher concentrations of Cl and H are attributed to the diffusion of fluid-derived components. The microstructural and nanoscale compositional outcome of this study yields significant implications that help provide a better understanding of mechanisms of element mobility in the deep Earth. Firstly, APT analysis of a set of low-angle boundaries revealed the presence of a previously unobserved structure-chemistry relationship between the amount of lattice distortion and

trace element segregation. Similarly, diffusion in boundaries is enhanced by higher dislocation densities.

6.4 Trace element segregation to mineral interfaces: the rule rather than the exception

From this summary, one important aspect outlined by this research is the role of deformation microstructures, crystal defects, and interfaces, in enhancing the redistribution of trace elements throughout geological materials. In particular, APT data acquired from both garnet and olivine indicate that low-angle boundaries behave as sites of preferential trace element segregation driven by coupled mechanisms of mass transport.

As discussed in *Chapters 4 and 5*, grain boundary segregation is a well-known phenomenon in material science, where the term is used to describe any local modification of the chemical composition of grain boundaries in solids (Priester 2011). Although such process is widely explored in manufactured materials (e.g., Lejček 2010; Priester 2011, 2013; Lejček *et al.* 2018; Lejček & Hofmann 2021), evidence of trace element segregation in minerals and its link to geological implications still represent a developing field of investigation.

The introduction of laser-assisted APT has seen a rapid increase in geological publications of studies exploring nanoscale compositional heterogeneity associated with mineral defects in various geological contexts (see Reddy et al., 2020 for a review). In particular, segregation within dislocations and along low-angle boundaries have been documented within deformed zircon (e.g., Piazolo *et al.* 2016; Reddy *et al.* 2016; Montalvo *et al.* 2019), monazite (Fougerouse *et al.* 2018, 2021a), titanite (Kirkland *et al.* 2018) and pyrite (Fougerouse *et al.* 2019, 2021a), as well as within undeformed zircon (Verberne *et al.* 2022) and olivine (Cukjati *et al.* 2019). Hence, to date, the focus of APT geological investigations has been given almost exclusively to accessory minerals, particularly for their routine use in geochronological applications.

This doctoral research has expanded this investigation by examining interfaces within grains of fundamental minerals of the lower continental crust and the upper mantle, such as garnet and olivine. Although promoted by different rheological regimes (brittle and ductile), the analysed interfaces share a common formation by dislocation creep in the presence of a fluid phase. Both datasets obtained in *Chapters 4 and* 5 demonstrate that similar to what was previously reported, trace elements are preferentially segregated to low-angle boundaries.

This common outcome is of critical importance as it demonstrates that segregation is not a phenomenon exclusively occurring within accessory phases, but also extends to other more fundamental rock-forming minerals. Importantly, the APT characterization of grain boundaries conducted in this thesis is applied to a single geometry of tilt-boundary, which limits the observations to a very small subset of possible geometrically distinct grain boundary combinations (Marquardt *et al.* 2015). Considering the nanoscale compositional evidence obtained in this thesis, and integrating these with what is reported in the APT literature, the general conclusion is that, independently of the deformed or unaltered nature of the system, we can expect trace element segregation to be a common feature within the majority of geological materials and in different geometrical configurations of the interfaces. These considerations yield fundamental larger-scale geological implications.

From a rheological point of view, segregation can affect mechanical changes of grain boundary properties. For example, it is known from material science studies that intergranular cohesion, which is the parameter controlling a fracture mode of an interface, can be strongly affected by its chemistry. Hence, one of the main effects of segregation is generally an increased intergranular embrittlement under loading (e.g., Lejček *et al.* 2017). Similarly, the energy of the grain boundary is dependent on the density, the arrangement and the chemistry of dislocations as segregated ions can change the boundary structure by modifying atomic bonds and decreasing vacancies concentrations (Mei & Kohlstedt 2000; Hiraga *et al.* 2007). This in turn controls the grain size of the polycrystalline aggregate with a strong effect on the selective activation of different deformation mechanisms (Watanabe 1985; Hiraga *et al.* 2007; Priester 2013). Previous studies conducted in olivine grain boundaries have observed that the chemistry of the interface is mostly dependent on the bulk composition of the crystal chemistry (Hiraga *et al.* 2002, 2003, 2004; Marquardt & Faul 2018). The results obtained in *Chapter 5* show that the chemistry of low-angle boundaries varies with the degree of deformation, and it can be further affected by the surrounding system by the inter-diffusion of externally derived components. This means that the observed variation in chemistry will translate into variations in the creep strength of the grain boundary at different stages of deformation, with consequences for the rheological behaviour of the aggregate. Importantly, *Chapter 5* highlighted how the segregation of Fe to low-angle boundaries, might have implications for olivine phase transformation and therefore the rheology of the upper mantle.

On the other hand, diffusion along crystalline defects is known to represent fast diffusion pathways for element mobility (Dohmen & Milke 2010). Once again, diffusion is

dependent on the chemistry of the interface (Wuensch & Vasilos 1966). In particular, the segregation of particular elements has the potential to decrease diffusion properties. For example, experimental studies of grain boundary diffusion in YAG have shown that segregation of Ti to grain boundaries has a major retaining effect on La (Polednia *et al.* 2020). Similarly, segregation can also affect grain boundary migration rates by impurity-drag effects (e.g., Vilenkin 2001). Therefore, the ubiquitous fractionation of trace elements observed in the studies presented here indicates that segregation can also impact diffusion properties in a variety of minerals.

From a geochemical point of view, the nanoscale compositional characterisation obtained in *Chapters 4 and 5* demonstrates that crystal-plastic deformation-induced low-angle boundaries coincide with sites of local trace element enrichment. Furthermore, low-angle boundaries act as entry points for the infiltration of external fluid-derived components. These observations highlight the impact that deformation microstructures might have in enhancing the compositional re-equilibration of their host. Significantly, if we consider the widespread occurrence of both garnet and olivine in lithospheric lithologies, trace element segregation might therefore represent an important mechanism of element mobility within the deep Earth's crust. On the other hand, the localised enrichment of particular elements might lead to chemical overestimations and/or compromise geochronological estimations. This aspect becomes very important, especially when analysing trace element concentrations with small volume analytical techniques (e.g., SIMS).

6.5 OH^+ as a proxy for molecular water in minerals interfaces?

This thesis has explored the important role that crustal fluids and deformation play in modifying lower crustal lithologies. In particular, each study has provided a detailed structural and geochemical picture of the manifestation of fluid-rock interaction mechanisms at different scales and geological environments. Considering the ubiquitous involvement of a fluid phase in all the case studies, it is therefore expected to detect a fluid-like signature in the acquired geochemical data.

Section *1.6* of the introduction highlighted the role of grain boundaries as the first entry point of fluids within a rock. Significantly, *Chapter 3* provides a natural record of the paths followed by infiltrating fluids within rocks undergoing deformation. In this case, evidence of fluid percolation along mineral interfaces is given by rims of amphibole around

the pyroxene of the rock and promoted by fluid-induced replacement reactions (pressure solution).

Considering the microstructural observations obtained in *Chapter 3*, if present, the chemical signature of a fluid phase is therefore expected to be localized along mineral interfaces. As predicted, at the nanoscale, results from *Chapters 4 and 5* record OH^+ peaks occurring at 17 Da in all of the analysed low-angle boundaries, both in garnet and olivine. As discussed in these chapters, the absolute discrimination and quantification of H^+ from chamber-derived hydrogen ions remains difficult to resolve in APT data. Nevertheless, by comparing the close microstructural relationship between fluid-enhanced deformation-induced low-angle boundaries with petrological observations and, in the case of olivine, the segregation of Ti, in *Chapters 4 and 5* it was concluded the OH^+ peak representing the signature of hydrogen enrichment, inherited from the fluid phase infiltrating the rocks during deformation. The pattern of OH^+ enrichment in the acquired datasets of this thesis appears systematically associated with Na and Cl, and this relationship is consistent across all the representative specimens. Recently, Liu *et al.* (2022) demonstrated that the association of hydroxide species (OH_2^+ at 18 Da and $FeOH_2^+$ at 37 Da) with Na (23 Da) in APT analysis of olivine, is indicative of hydrated defects. Hence, considering all the above observations, the clear relationship between the nanoscale composition of the interfaces and larger-scale petrological observations provides a solid argument to suggest the peaks association OH^+ - Na - Cl as a good starting point for the identification and quantification of molecular water in APT datasets of metamorphic minerals. Despite the absence of interface segregation, the glassy melt inclusions analysed in *Chapter 2* are known to contain a distinct amount of H_2O (Bartoli *et al.* 2016). One could argue that the lack of preferential segregation at the phase boundary may be due to the absence of deformation in a closed system. Hence, the possibility that OH^+ peaks in the glass datasets similarly reflect the hydrated component of the silicate amorphous cannot be excluded.

The possibility of routinely identifying water in APT analyses has the potential to represent an important breakthrough for the nanoscale identification of hydrogen within fundamental rock-forming minerals. Hydrogen drastically decreases mineral strength during deformation by the so-called hydraulic-weakening effect (e.g., Tullis & Yund 1989), increases electrical conductivity (Yoshino *et al.* 2006), enhances plastic deformation (Mei & Kohlstedt 2000) and determines the activation of preferential slip systems (Jung *et al.* 2006). Therefore, measuring the precise location of hydrogen atoms within materials is of crucial importance for many polycrystalline materials. For example, there is a considerable discussion about the

potential association of water with olivine defects and the role that hydrogen might have in promoting electrical conductivities anomalies and controlling the strength of the upper mantle (Yoshino *et al.* 2006; Sommer *et al.* 2008; Ohtani 2020; Liu *et al.* 2022). Therefore, gaining information about hydrogen mobility within mantle-derived minerals such as olivine has broad implications to infer large-scale dynamics of the deep Earth and water estimates of the upper mantle. In this regard, *Chapter 5* of this thesis revealed various amounts of hydrogen enrichments at intracrystalline defects (dislocations) and along interfaces (low-angle boundaries), with implications for the deformation and phase transformation of olivine at mantle depth. These results indicate that important information on hydrogen distribution can be obtained by APT of low-angle boundaries, opening up new targets for future research.

6.6 APT advances and recommendations (i): technical approaches

Although aware of the significant advantages of the capabilities of atom probe tomography, one of the main challenges encountered along the course of this research is the really small, point-specific volume of localised analysis in a natural system (typically < 0.02 μm^3, Reddy *et al.* 2020). In the case of analysis conducted in experimentally reproduced mineral microstructures, this problem is overcome by the constrained extrinsic conditions of the experiment (e.g., Cukjati *et al.* 2019). In order to make this small volume of material representative in a natural sample, APT data must be (i) placed into a known scientific geological context and (ii) integrated with other larger length-scale analytical techniques. In this thesis (i) has been achieved by using well-studied samples reported in the literature, whereas (ii) is achieved by the application of multiple micro-analytical techniques. For instance, the analysis of the metasomatic shear zone in *Chapter 3* demonstrated the ability of fluid-mediated deformation to generate microstructures suitable for the application of atom probe tomography (i.e., sub-grain boundaries). The use of EBSD is therefore a prerequisite before preparing APT specimens in order to build a representative microstructural framework of investigation and to identify suitable areas within deformed regions of the sample (e.g., *Chapters 4, 5*). Similarly, TEM characterization can also provide important microstructural and crystallographic information on the character of the samples, providing a solid base for interpretation of APT datasets (e.g., *Chapters 2, 5*).

The individual chapters of this thesis show how the application of APT tomography enables the visualization of trace element heterogeneities within different materials at the scale of an individual dislocation. However, in order to correctly estimate the extent and level

of trace element enrichments, a crucial aspect of any APT experiments is determining the accurate composition of the analysed sample. In particular, the chemical component of data reconstructions involves the identification of detected ions in the obtained mass-to-charge ratio spectra. When analysing phases such as silicates, this interpretation is complicated by the high number of element peaks some of which are commonly overlapping. For example, in garnet and olivine, Al^{+} overlaps with Fe^{++} at 27Da, Ca^{+} with MgO^{+} at 40 Da, Co^{+} and AlO_2^{+} at 59 Da, FeO^{+} and Si_2O^{+} at 72 Da in the mass-to-charge ratio spectra. Similarly, NaO^{+} overlaps with K^{+} at 39 Da in silicate glass. Discriminating between overlapping element peaks of silicates is therefore challenging and a good knowledge of the chemistry of the sample is recommended before the APT investigation is undertaken.

Secondly, uncertainties can be introduced by analytical artefacts in the reconstructed three-dimensional model. In *Chapter 2* the analysis of adjacent distinct phases with different evaporation fields resulted in the display of an enriched layer within the garnet with a similar pattern to chemical heterogeneities observed along grain boundaries interfaces (e.g., *Chapter 4,* 5). A detailed 2D and 3D analysis of the reconstruction showed that this enrichment corresponds with a localised region of increased atomic density. Considering the known incompatibility of the enriched elements in garnet, the observed pattern is interpreted as a local reconstruction artefact generated by a local magnification effect. Therefore, care must be taken when handling APT datasets from similar complex phase boundaries, as analytical artefacts can be generated, leading to incorrect interpretation of the results.

6.7 APT advances and recommendations (ii): specimen yield

To date, the application of APT to geological material represents an innovative approach (e.g., Reddy *et al.* 2020). As with any developing technique, a few limitations associated with its use remain. For example, fracturing and destruction of the specimen are frequent during APT experiments (Prosa *et al.* 2019). This is due to the large stress conditions induced by the intense electric field applied near the apex of the specimen tip in order to promote ions evaporation (Kölling & Vandervorst 2009; Larson *et al.* 2013; Reddy *et al.* 2020). The mechanical failure can be promoted by extrinsic factors deriving from sample preparation such as rupture of the platinum weld, shape irregularities of the specimen or polishing defects (Kölling & Vandervorst 2009). On the other hand, the survivability of the specimen is strongly controlled by the intrinsic properties of the analysed material, such as optical absorption, thermo-conductivity, atomic volume, crystallinity, and/or microstructural

characteristics. For example, grain and phase boundaries are known to represent weaker regions of the material, where delamination and fracture can occur during evaporation of such interfaces (Larson *et al.* 2013). Similarly, a high density of lattice defects can induce fracture, and therefore result in low data yield (e.g., Montalvo *et al.* 2019). On the other hand, APT analyses of amorphous materials such as silicate glass are often challenged by the strong instability of the tip under the electrical field due to the high variability of composition and density of the material (e.g., Gin *et al.* 2017). Consequently, while extrinsic factors can somehow be reduced by careful sample preparation, the optimization of the acquisition conditions based on the constitutive properties of the individual material is essential to improve the quality of APT data. While there has been substantial progress in the optimization of running conditions of accessory minerals (Saxey *et al.* 2018; Verberne *et al.* 2019; Joseph *et al.* 2021 and references therein), only a few studies have aimed at the characterization of more common rock-forming minerals by mean of APT (Cukjati *et al.* 2019; Fougerouse *et al.* 2021b; Liu *et al.* 2022). The following section aims to outline the practice used for the analysis of "less known" minerals and provide a starting point for similar future investigations.

In this research, the application of APT to different minerals (olivine, garnet) and materials (silicate glass) with various amounts of intracrystalline deformation and variable composition, required selective adjusting of the running conditions to maximise the yield for each specimen. During the course of this study, a total number of 53 APT specimens were prepared. This number comprises samples from both the melt inclusions from Ronda (*Chapter* 2) as well as the garnet and the olivine grains from the Lindås Nappe (*Chapters 4,5*). Of the prepared specimens, 42 were effectively analysed by APT with a survivability rate of 33%, resulting in a total collection of 1,474,022,533 ions (~ 322 hours of acquisition time) (Supplementary Table 6.E.1).

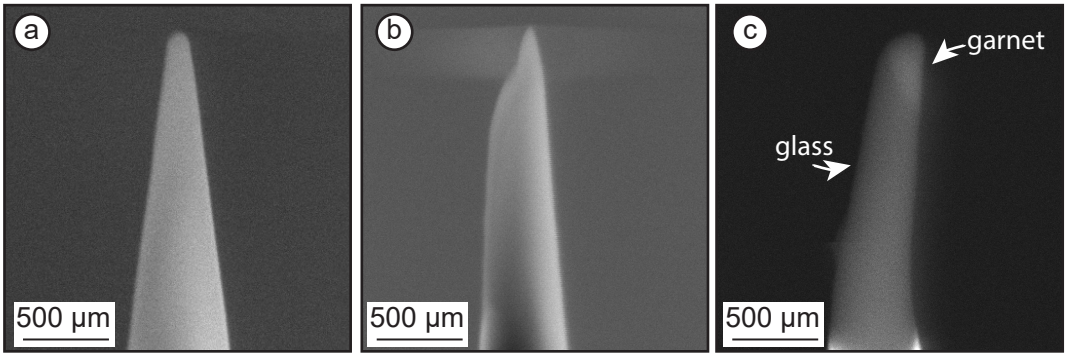

Figure 6.1 Series of SE images of APT specimens affected by complex phase boundaries. (a) single phase of garnet allows the fabrication of a good specimen shape. (b-c) topographic irregularities and bending deriving from different robustness of garnet and glass during later stages of Ga^+.

The analysis of the silicate glass–host garnet interface was mostly complicated by the composite nature of the specimens. Firstly, during sample preparation, garnet is a much more robust material during Ga^+ milling compared to glass. This often resulted in morphological irregularities in the needle-shaped specimens (Figure 6.1). In the atom probe, the interface between the two adjacent phases resulted being highly unstable, mostly attributed to the strong differences in crystallinity (e.g., amorphous vs cubic symmetry). Therefore, due to the variability in compositions and specimens morphologies, the APT running conditions were individually optimized to maximise the yield for each specimen (Supplementary Table 6.E.1).

As discussed in *Chapter 2* silicate glass requires a higher evaporation field compared to garnet. During the analyses, it was observed that glass is particularly prone to premature fracture and the production of a very small dataset. In order to decrease the stress induced by the electrical field, the laser pulse varied between 350 and 500 pJ at a detection rate ranging between 0.002 and 0.006 ions/pulse. Finally, representative results of glass were obtained using a base temperature of 60K, 480 pJ laser pulse energy and 0.003 to 0.005 ions/pulse detection rate. Similar parameters (400-450 pJ, 0.003-0.004 ions/pules) were in turn tested for garnet. Moreover, in order to create optimal conditions when evaporating the phase boundary, the APT specimens were manufactured so that the garnet lies above the glass. This was achieved by targeting the host-inclusion interface from above the edges of carefully selected semi-exposed glassy inclusions (Figure 6.2). Importantly, this approach improved the specimens yield allowing to resolve the complex phase boundary and produce more consistent datasets.

For the analyses of grain boundaries in garnet and olivine (*Chapters 4,* 5) the running conditions varied for each individual mineral, except for the base temperature and the laser frequency which were set at 60 K and 200 kHz, respectively. In detail, garnet running conditions were optimized at 380 pJ and a detection rate of 0.005 ions/pulse. Olivine specimens were analysed with a maximum laser pulse energy of 150 pJ and detection rate of 0.008 ions/pulse. Comparing the laser pulse energies with the percentage of single hits (i.e., good hits %) optimal conditions were achieved at 150 pJ and 0.008 ions/pulse (Figure 6.3). In both datasets, there is no apparent correlation between the specimen failures and the analysis of the targeted interfaces. The failures have been therefore attributed to the achievement of high voltages (typically ~8 – 9 kV).

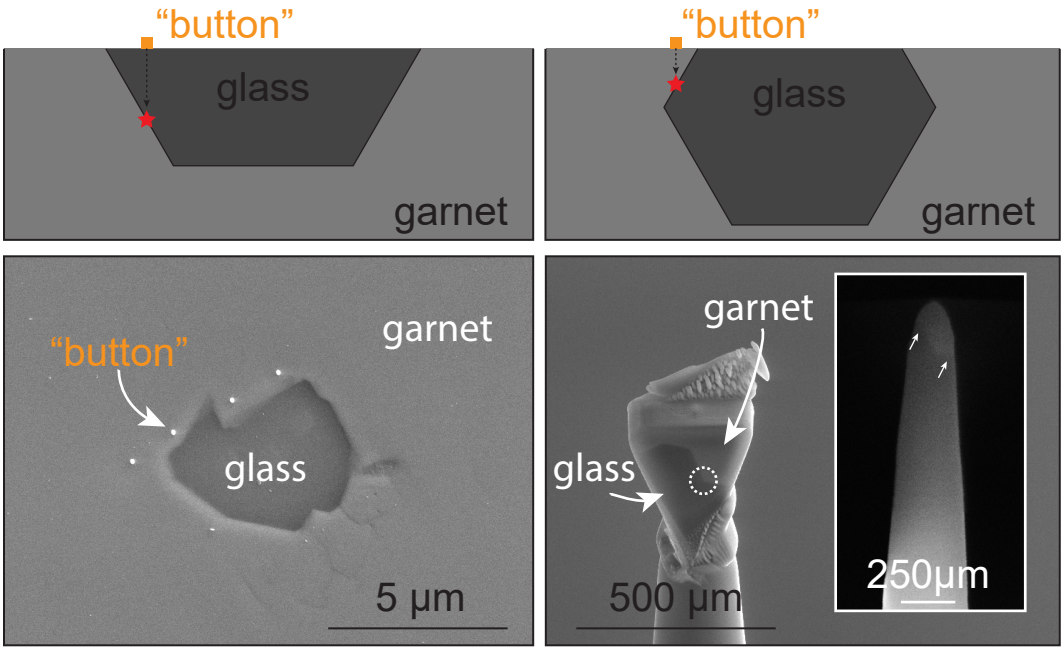

Figure 6.2 Series of SE images detailing the "button" method for the target of the interface between garnet and glass explained in the tex. By targeting the interface from semi-exposed inclusion, it is possible to obtain garnet on top of glass in the APT specimen. At the final stage of preparation, the interface highlighted by the white circle is contained in the specimen.

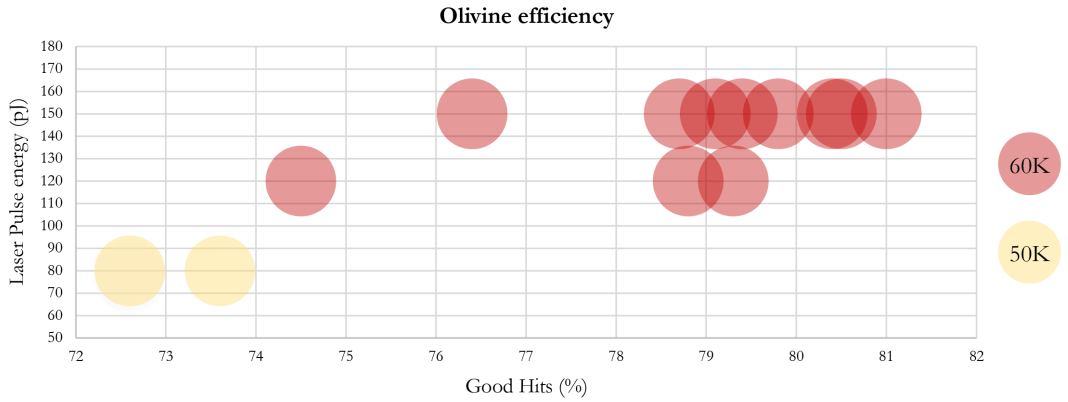

Figure 6.3 Graph showing the olivine efficiency expressed in percentages of good hits (single hits) at increasing laser pulse and temperature at a constant detection rate of 0.008 ions/pulse. Optimal results can be achieved at 60K and 150 pJ of energy pulse.

With an average detection of 1*10^7 ions, 80 % single hits and 15 hours of acquisition time prior to fracture, this research shows that olivine represents an excellent mineral for APT analyses. Similarly, garnet can provide high-quality datasets. These minerals are therefore an excellent target for future studies of grain boundaries in geological material and of fundamental metamorphic processes. The APT data acquired in this research show how several parameters can influence the quality of the analyses. For a given material, an initial series of tests is strongly recommended to successfully apply atom probe tomography. Importantly, care must be taken when analysing composite materials characterized by strong differences in field of evaporation and degree of crystallinity.

6.8 Thesis conclusions

This doctoral thesis represents an important breakthrough in the characterization of complex metamorphic mechanisms of fluid-rock interactions. Using a combined correlative analytical techniques approach, this research has enabled direct correlation of metre- to micro- to nanoscale textural structures with chemical compositions. Common to all the works presented in the main body of this thesis, the multiscale characterizations showed that, independent of the nature of the fluid phase (aqueous or melt), the distribution of trace elements is affected by a variety of factors and mechanisms. These include gradients of diffusion, bulk compositions, deformation microstructures and segregation along crystallographic defects. Importantly, the application of APT has enabled identification and assessment of the contribution of the different mechanisms responsible for the coupled trace element mobility, and allowed insights on the larger scale implications associated with the individual geological context. The study of different crustal proxies such as melt inclusions and granulites from the Bergen Arcs has provided access to investigate deep continental processes otherwise inaccessible. Moreover, the study of different lithologies (granulites, eclogites and spinel-lherzolites) allowed the comparison of the results of the same process in rocks of different bulk compositions that could represent, with good approximation, the average lower continental crust and the upper mantle, providing a broad range of new insights into the migration and distribution of trace elements at different crustal levels. The observation that trace elements are enriched at garnet and olivine interfaces indicates that these features are likely to be widespread between other rock-forming minerals. The results show the powerful role of atom probe tomography as a tool to unveil the nanoscale manifestation of complex natural metamorphic processes. The technique enabled unprecedented characterization of the structures and chemistry of grain, phase boundaries and silicate glass with sub-nanometre scale resolution. This research shows that the study of really small features is possible by APT, with the potential to change our understanding of processes of mass transfer throughout rocks. The workflow developed in this thesis offers a wide range of potential new studies for the analysis of metamorphic minerals, opening new frontiers of exploration to enhance our understanding of fundamental rock processes.

6.9 References

Austrheim, H. 1987. Eclogitization of lower crustal granulites by fluid migration through shear zones. *Earth and Planetary Science Letters 81(2–3),* 221–232. DOI 10.1016/0012-821X(87)90158-0

Austrheim, H. 2013. Fluid and deformation induced metamorphic processes around Moho beneath continent collision zones: Examples from the exposed root zone of the Caledonian mountain belt, W-Norway. *Tectonophysics 609,* 620–635. DOI 10.1016/j.tecto.2013.08.030

Bartoli, O. 2020. Characterizing fluid and melt in high-grade metamorphic rocks. In: Lecumberri-Sanchez P, Steele-McInnis M (eds) Fluid inclusions, , Short Course Ser. *Mineral Association of Canada,* 36.

Bartoli, O., Acosta-Vigil, A., Tajčmanová, L., Cesare, B. & Bodnar, R.J. 2016. Using nanogranitoids and phase equilibria modeling to unravel anatexis in the crustal footwall of the Ronda peridotites (Betic Cordillera, S Spain). *Lithos 256–257,* 282–299. DOI 10.1016/j.lithos.2016.03.016

Carter, N.L., Kronenberg, A.K., Ross, J.V. & Wiltschko, D.V. 1990. Control of fluids on deformation of rocks. *Geological Society, London, Special Publications 54(1),* 1–13. DOI 10.1144/GSL.SP.1990.054.01.01

Cenki, B., Braun, I. & Bröcker, M. 2004. Evolution of the continental crust in the Kerala Khondalite Belt, southernmost India: evidence from Nd isotope mapping, U–Pb and Rb–Sr geochronology. *Precambrian Research 134(3–4),* 275–292. DOI 10.1016/j.precamres.2004.06.002

Cesare, B., Ferrero, S., Salvioli-Mariani, E., Pedron, D. & Cavallo, A. 2009. "Nanogranite" and glassy inclusions: The anatectic melt in migmatites and granulites. *Geology 37(7),* 627–630.

Cesare, B., Acosta-Vigil, A., Bartoli, O. & Ferrero, S. 2015. What can we learn from melt inclusions in migmatites and granulites? *Lithos 239,* 186–216. DOI 10.1016/j.lithos.2015.09.028

Cesare, B., Parisatto, M., Mancini, L., Peruzzo, L., Franceschi, M., Tacchetto, T., Reddy, S., Spiess, R., Nestola, F. & Marone, F. 2021. Mineral inclusions are not immutable: Evidence of post-entrapment thermally-induced shape change of quartz in garnet. *Earth and Planetary Science Letters 555,* 116708. DOI 10.1016/j.epsl.2020.116708

Clemens, J.D. 2009. The message in the bottle: "Melt" inclusions in migmatitic garnets. *Geology 37(7),* 671–672. DOI 10.1130/focus072009.1

Cukjati, J.T., Cooper, R.F., Parman, S.W., Zhao, N., Akey, A.J. & Laiginhas, F.A.T.P. 2019. Differences in chemical thickness of grain and phase boundaries: an atom probe tomography study of experimentally deformed wehrlite. *Physics and Chemistry of Minerals 46(9),* 845–859. DOI 10.1007/s00269-019-01045-x

Dohmen, R. & Milke, R. 2010. Diffusion in Polycrystalline Materials: Grain Boundaries, Mathematical Models, and Experimental Data. *Reviews in Mineralogy and Geochemistry 72(1),* 921–970. DOI 10.2138/rmg.2010.72.21

Ferrero, S., Bartoli, O., Cesare, B., Salvioli-Mariani, E., Acosta-Vigil, A., Cavallo, A., Groppo, C. & Battiston, S. 2012. Microstructures of melt inclusions in anatectic metasedimentary rocks: anatectic melt inclusions in migmatites. *Journal of Metamorphic Geology 30(3),* 303–322. DOI 10.1111/j.1525-1314.2011.00968.x

Fougerouse, D., Reddy, S.M., Saxey, D.W., Erickson, T.M., Kirkland, C.L., Rickard, W.D.A., Seydoux-Guillaume, A.-M., Clark, C. & Buick, I.S. 2018. Nanoscale distribution of Pb in monazite revealed by atom probe microscopy. *Chemical Geology 479,* 251–258. DOI 10.1016/j.chemgeo.2018.01.020

Fougerouse, D., Reddy, S.M., Kirkland, C.L., Saxey, D.W., Rickard, W.D. & Hough, R.M. 2019. Time-resolved, defect-hosted, trace element mobility in deformed Witwatersrand pyrite. *Geoscience Frontiers 10(1),* 55–63. DOI 10.1016/j.gsf.2018.03.010

Fougerouse, D., Reddy, S.M., Seydoux-Guillaume, A.-M., Kirkland, C.L., Erickson, T.M., Saxey, D.W., Rickard, W.D.A., Jacob, D., Leroux, H. & Clark, C. 2021a. Mechanical twinning of monazite expels radiogenic lead. *Geology 49(4),* 417–421. DOI 10.1130/G48400.1

Fougerouse, D., Saxey, D.W., Rickard, W.D.A., Reddy, S.M. & Verberne, R. 2021b. Standardizing Spatial Reconstruction Parameters for the Atom Probe Analysis of Common Minerals. *Microscopy and Microanalysis,* 1–10. DOI 10.1017/S1431927621013714

Getsinger, A.J., Hirth, G., Stünitz, H. & Goergen, E.T. 2013. Influence of water on rheology and strain localization in the lower continental crust: Water, Rheology, and Strain Localization. *Geochemistry, Geophysics, Geosystems 14(7),* 2247–2264. DOI 10.1002/ggge.20148

Gin, S., Jollivet, P., Barba Rossa, G., Tribet, M., Mougnaud, S., Collin, M., Fournier, M., Cadel, E., Cabie, M. & Dupuy, L. 2017. Atom-Probe Tomography, TEM and ToF-SIMS study of borosilicate glass alteration rim: A multiscale approach to investigating rate-limiting mechanisms. *Geochimica et Cosmochimica Acta 202,* 57–76. DOI 10.1016/j.gca.2016.12.029

Hawemann, F., Mancktelow, N.S., Pennacchioni, G., Wex, S. & Camacho, A. 2019. Weak and Slow, Strong and Fast: How Shear Zones Evolve in a Dry Continental Crust (Musgrave Ranges, Central Australia). *Journal of Geophysical Research: Solid Earth 124(1),* 219–240. DOI 10.1029/2018JB016559

Hiraga, T., Anderson, I., Zimmerman, M., Mei, S. & Kohlstedt, D. 2002. Structure and chemistry of grain boundaries in deformed, olivine + basalt and partially molten lherzolite aggregates: evidence of melt-free grain boundaries. *Contributions to Mineralogy and Petrology 144(2),* 163–175. DOI 10.1007/s00410-002-0394-1

Hiraga, T., Anderson I.M., & Kohlstedt D.L. 2003. Chemistry of grain boundaries in mantle rocks. *American Mineralogist* 88(6976):1015–1019.

Hiraga, T., Anderson I.M., & Kohlstedt D.L. 2004. Grain boundaries as reservoirs of incompatible elements in the Earth's mantle. *Nature* 427(6976):699–703.

Hiraga, T., Hirschmann, M.M. & Kohlstedt, D.L. 2007. Equilibrium interface segregation in the diopside–forsterite system II: Applications of interface enrichment to mantle geochemistry. *Geochimica et Cosmochimica Acta 71(5),* 1281–1289. DOI 10.1016/j.gca.2006.11.020

Jamtveit, B., Bucher-Nurminen, K. & Austrheim, H. akon. 1990. Fluid controlled eclogitization of granulites in deep crustal shear zones, Bergen arcs, Western Norway. *Contributions to Mineralogy and Petrology 104(2),* 184–193.

Jamtveit, B., Petley-Ragan, A., Incel, S., Dunkel, K.G., Aupart, C., Austrheim, H., Corfu, F., Menegon, L. & Renard, F. 2019. The Effects of Earthquakes and Fluids on the Metamorphism of the Lower Continental Crust. *Journal of Geophysical Research: Solid Earth 124(8),* 7725–7755. DOI 10.1029/2018JB016461

Jamtveit, B., Dunkel, K.G., Petley-Ragan, A., Austrheim, H., Corfu, F. & Schmid, D.W. 2021. Rapid fluid-driven transformation of lower continental crust associated with thrust-induced shear heating. *Lithos 396–397,* 106216. DOI 10.1016/j.lithos.2021.106216

Joseph, C., Fougerouse, D., Saxey, D.W., Verberne, R., Reddy, S.M. & Rickard, W.D.A. 2021. Xenotime at the Nanoscale: U-Pb Geochronology and Optimisation of Analyses by Atom Probe Tomography. *Geostandards and Geoanalytical Research 45(3),* 443–456. DOI 10.1111/ggr.12398

Jung, H., Katayama, I., Jiang, Z., Hiraga, T. & Karato, S. 2006. Effect of water and stress on the lattice-preferred orientation of olivine. *Tectonophysics 421(1–2),* 1–22. DOI 10.1016/j.tecto.2006.02.011

Kirkland, C.L., Fougerouse, D., Reddy, S.M., Hollis, J. & Saxey, D.W. 2018. Assessing the mechanisms of common Pb incorporation into titanite. *Chemical Geology 483,* 558–566. DOI 10.1016/j.chemgeo.2018.03.026

Kölling, S. & Vandervorst, W. 2009. Failure mechanisms of silicon-based atom-probe tips. *Ultramicroscopy 109(5),* 486–491. DOI 10.1016/j.ultramic.2008.11.013

Larson, D.J., Prosa, T.J., Ulfig, R.M., Geiser, B.P. & Kelly, T.F. 2013. *Local Electrode Atom Probe Tomography*. Springer New York, New York, NY. DOI 10.1007/978-1-4614-8721-0

Lejček, P. 2010. *Grain Boundary Segregation in Metals*. Springer, New York, NY, Springer series in materials science.

Lejček, P. & Hofmann, S. 2021. Entropy-Driven Grain Boundary Segregation: Prediction of the Phenomenon. *Metals 11(8),* 1331. DOI 10.3390/met11081331

Lejček, P., Šob, M. & Paidar, V. 2017. Interfacial segregation and grain boundary embrittlement: An overview and critical assessment of experimental data and calculated results. *Progress in Materials Science 87,* 83–139. DOI 10.1016/j.pmatsci.2016.11.001

Lejček, P., Všianská, M. & Šob, M. 2018. Recent trends and open questions in grain boundary segregation. *Journal of Materials Research 33(18),* 2647–2660. DOI 10.1557/jmr.2018.230

Liu, J., Taylor, S.D., Qafoku, O., Arey, B.W., Colby, R., Eaton, A., Bartrand, J., Shutthanandan, V., Manandhar, S. & Perea, D.E. 2022. Visualizing the Distribution of Water in Nominally Anhydrous Minerals at the Atomic Scale: Insights From Atom Probe Tomography on Fayalite. *Geophysical Research Letters 49(2).* DOI 10.1029/2021GL094914

Mancktelow, N.S. & Pennacchioni, G. 2005. The control of precursor brittle fracture and fluid–rock interaction on the development of single and paired ductile shear zones. *Journal of Structural Geology 27(4),* 645–661. DOI 10.1016/j.jsg.2004.12.001

Marquardt, K. & Faul, U.H. 2018. The structure and composition of olivine grain boundaries: 40 years of studies, status and current developments. *Physics and Chemistry of Minerals 45(2),* 139–172. DOI 10.1007/s00269-017-0935-9

Marquardt, K., Rohrer, G.S., Morales, L., Rybacki, E., Marquardt, H. & Lin, B. 2015. The most frequent interfaces in olivine aggregates: the GBCD and its importance for grain boundary related processes. *Contributions to Mineralogy and Petrology 170(4).* DOI 10.1007/s00410-015-1193-9

Mei, S. & Kohlstedt, D.L. 2000. Influence of water on plastic deformation of olivine aggregates 2. Dislocation creep regime. J Geophys Res 105(B9):21471–21481.

Montalvo, S.D., Reddy, S.M., Saxey, D.W., Rickard, W.D.A., Fougerouse, D., Quadir, Z. & Johnson, T.E. 2019. Nanoscale constraints on the shock-induced transformation of zircon to reidite. *Chemical Geology 507,* 85–95. DOI 10.1016/j.chemgeo.2018.12.039

Mukai, H., Austrheim, H., Putnis, C.V. & Putnis, A. 2014. Textural Evolution of Plagioclase Feldspar across a Shear Zone: Implications for Deformation Mechanism and Rock Strength. *Journal of Petrology 55(8),* 1457–1477. DOI 10.1093/petrology/egu030

Ohtani, E. 2020. The role of water in Earth's mantle. *National Science Review 7(1),* 224–232. DOI 10.1093/nsr/nwz071

Petley-Ragan, A., Dunkel, K.G., Austrheim, H., Ildefonse, B. & Jamtveit, B. 2018. Microstructural Records of Earthquakes in the Lower Crust and Associated Fluid-Driven Metamorphism in Plagioclase-Rich Granulites. *Journal of Geophysical Research: Solid Earth 123(5),* 3729–3746. DOI 10.1029/2017JB015348

Petley-Ragan, A., Ben-Zion, Y., Austrheim, H., Ildefonse, B., Renard, F. & Jamtveit, B. 2019. Dynamic earthquake rupture in the lower crust. *Science Advances 5(7),* eaaw0913. DOI 10.1126/sciadv.aaw0913

Piazolo, S., La Fontaine, A., Trimby, P., Harley, S., Yang, L., Armstrong, R. & Cairney, J.M. 2016. Deformation-induced trace element redistribution in zircon revealed using atom probe tomography. *Nature Communications 7(1).* DOI 10.1038/ncomms10490

Polednia, J., Dohmen, R. & Marquardt, K. 2020. Grain boundary diffusion and its relation to segregation of multiple elements in yttrium aluminum garnet. *European Journal of Mineralogy 32(6),* 675–696. DOI 10.5194/ejm-32-675-2020

Priester, L. (ed.). 2011. *Grain Boundaries and Crystalline Plasticity*. 344 pp. ISTE ; Wiley, London : Hoboken, NJ.

Priester, L. 2013. *Grain Boundaries*. Springer Netherlands, Dordrecht, Springer Series in Materials Science. DOI 10.1007/978-94-007-4969-6

Prosa, T.J., Strennen, S., Olson, D., Lawrence, D. & Larson, D.J. 2019. A Study of Parameters Affecting Atom Probe Tomography Specimen Survivability. *Microscopy and Microanalysis 25(2),* 425–437. DOI 10.1017/S1431927618015258

Putnis, A., Jamtveit, B. & Austrheim, H. 2017. Metamorphic Processes and Seismicity: the Bergen Arcs as a Natural Laboratory. *Journal of Petrology 58(10),* 1871–1898. DOI 10.1093/petrology/egx076

Reddy, S.M., van Riessen, A., Saxey, D.W., Johnson, T.E., Rickard, W.D.A., Fougerouse, D., Fischer, S., Prosa, T.J., Rice, K.P., Reinhard, D.A., Chen, Y. & Olson, D. 2016. Mechanisms of deformation-induced trace element migration in zircon resolved by atom probe and correlative microscopy. *Geochimica et Cosmochimica Acta 195,* 158–170. DOI 10.1016/j.gca.2016.09.019

Reddy, S.M., Saxey, D.W., Rickard, W.D.A., Fougerouse, D., Montalvo, S.D., Verberne, R. & Riessen, A. 2020. Atom Probe Tomography: Development and Application to the Geosciences. *Geostandards and Geoanalytical Research 44(1),* 5–50. DOI 10.1111/ggr.12313

Roedder, E. 1984. *Fluid Inclusions*. Mineralogical Society of America, Reviews in Mineralogy.

Saxey, D.W., Moser, D.E., Piazolo, S., Reddy, S.M. & Valley, J.W. 2018. Atomic worlds: Current state and future of atom probe tomography in geoscience. *Scripta Materialia 148,* 115–121. DOI 10.1016/j.scriptamat.2017.11.014

Sommer, H., Regenauer-Lieb, K., Gasharova, B. & Siret, D. 2008. Grain boundaries: a possible water reservoir in the Earth's mantle? *Mineralogy and Petrology 94(1–2),* 1–8. DOI 10.1007/s00710-008-0002-9

Tullis, J. & Yund, R.A. 1989. Hydrolytic weakening of quartz aggregates: The effects of water and pressure on recovery. *Geophysical Research Letters 16(11),* 1343–1346. DOI 10.1029/GL016i011p01343

Verberne R., Saxey D., Reddy S., Rickard W., Fougerouse D., & Clark C. 2019. Analysis of Natural Rutile (TiO2) by Laser-assisted Atom Probe Tomography. Microscopy and Microanalysis, 1-8. doi:10.1017/S1431927618015477.

Verberne, R., Reddy, S.M., Saxey, D.W., Fougerouse, D., Rickard, W.D.A., Quadir, Z., Evans, N.J. & Clark, C. 2022. Dislocations in minerals: Fast-diffusion pathways or trace-element traps? *Earth and Planetary Science Letters 584,* 117517. DOI 10.1016/j.epsl.2022.117517

Vilenkin, A. 2001. Interaction of Solute Impurity with Grain Boundary: The Impurity Drag Effect. *Interface Science 9(3/4),* 323–329. DOI 10.1023/A:1015186905631

Watanabe, T. 1985. Structural effects on grain boundary segregation, hardening and fracture. *Le Journal de Physique Colloques 46(C4),* C4-555-C4-566. DOI 10.1051/jphyscol:1985462

Wuensch, B.J. & Vasilos, T. 1966. Origin of Grain-Boundary Diffusion in MgO. *Journal of the American Ceramic Society 49(8),* 433–436. DOI 10.1111/j.1151-2916.1966.tb15411.x

Yoshino, T., Matsuzaki, T., Yamashita, S. & Katsura, T. 2006. Hydrous olivine unable to account for conductivity anomaly at the top of the asthenosphere. *Nature 443(7114),* 973–976. DOI 10.1038/nature05223

Appendix A

2.A Supplementary Figures and Data Tables to Chapter 2

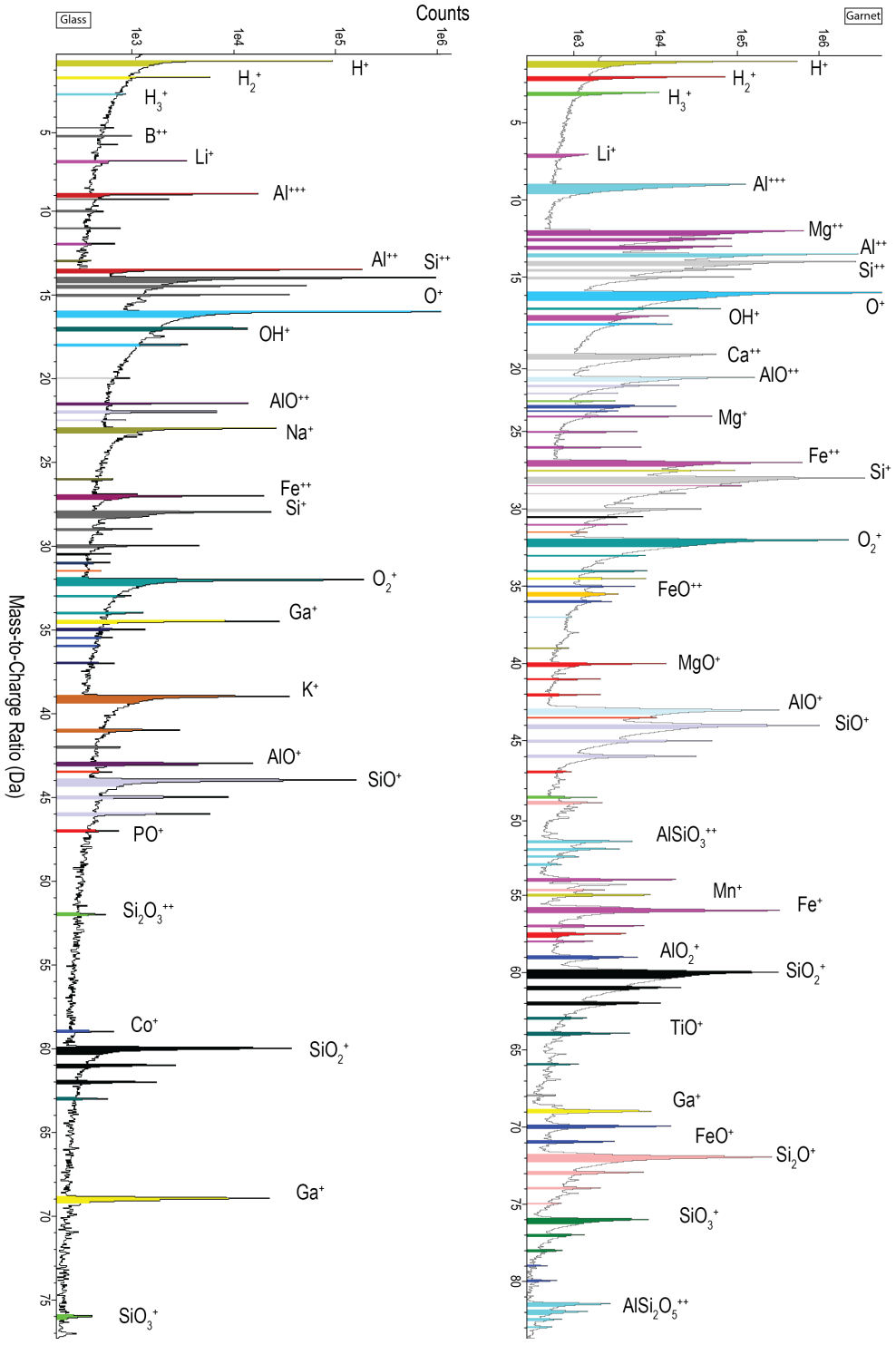

Figure 2.A.1 Representative atom probe tomography mass spectrum of silicate glass (left) and garnet (right) from sample Gl1 and Grt1 respectively.

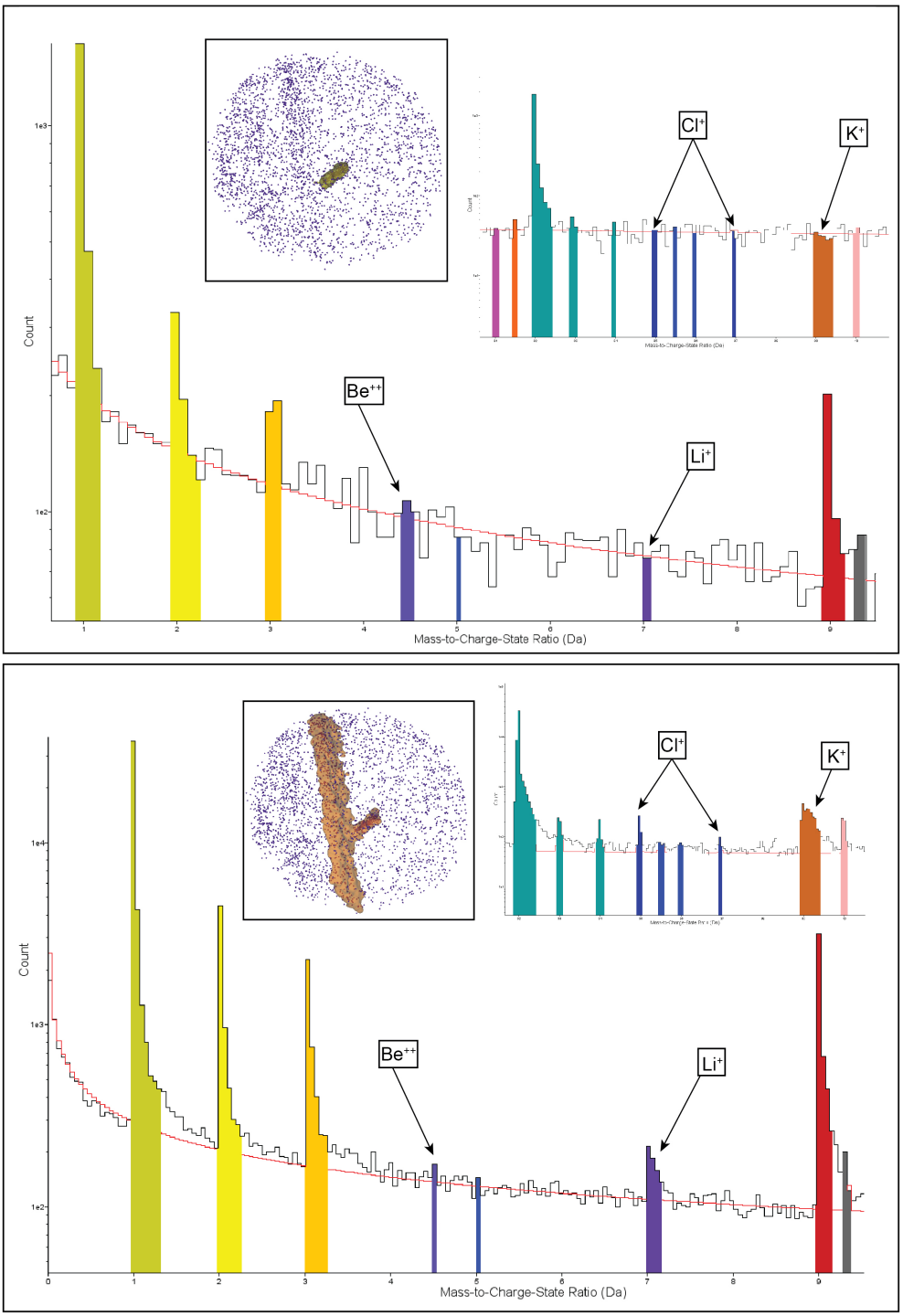

Figure 2.A.2. 3D isosurface renderings and mass spectra comparison for the elongated feature and the boundary interface. Red curve shows the estimated background. The mass spectra extracted from the linear feature shows how the element enrichment is mostly produced by a noise artefact during acquisition whereas above background within the phase boundary.

Table 2.A.1 APT data acquisition settings and data summary compiled following the recommendation of Blum et al. (2018). The table shows details of instrumentation, reconstruction software, conditions of acquisitions, outcome and 3D reconstruction parameters.

Data set/specimen	**Grt-1**	**Grt-2**	**Grt-3**	**Gl-1**	**Gl-2**	**PB-1**	**PB-2a**	**PB-2b**
Instrument model	LEAP 4000X HR	LEAP 4000X HR	LEAP 4000X HR	LEAP 4000X HR	LEAP 4000X HR	LEAP 4000X HR	LEAP 4000X HR	LEAP 4000X HR
Instrument settings								
Laser wavelenth (nm)	355	355	355	355	355	355	355	355
Laser pulse energy (pJ)	450	480	400	480	480	480	500	500
Pulse frequency (kHz)	200	200	200	200	200	200	200	200
Evaporation control	dec rate	dec rate	dec rate	dec rate	dec rate	dec rate	dec rate	dec rate
Targeted det. Rate (ions/pulse)	0.3	0.4	0.4	0.3	0.5	0.4	0.6	0.6
Nominal flight path (mm)	382	382	382	382	382	382	382	382
Set point temperature (K)	60	60	60	60	60	60	60	60
Sample Temperature (K)	69.2	69.2	69.2	69.2	69.2	69.2	69.2	69.2
Chamber Pressure (torr)	3.2 E-11	3.2 E-11	3.1 E-11	3.2 E-11	3.0 E-11	3.2 E-11	3.1 E-11	3.0 E-11
Data summary								
LAS Root version	15.41.342l	15.41.342l	15.41.342l	15.41.342l	15.41.342l	15.41.342l	15.41.342l	15.41.342l
CAMECAROOT version	18.46.428	18.46.428	18.46.428	18.46.428	18.46.428	18.46.428	18.46.428	18.46.428
Analysis Software	IVAS 3.8.2	IVAS 3.8.3	IVAS 3.8.4	IVAS 3.8.2	IVAS 3.8.2	IVAS 3.8.3	IVAS 3.8.3	IVAS 3.8.3
Total ions	45074104	28420181	31212039	3155285	6199347	7077336	21462038	6857985
single (%)	86	81.2	82.8	77.20	85.8	83.3	80.2	84.1
multiple (%)	13.6	18.4	16.7	22.20	13.9	16.3	19.5	15.5
partial (%)	0.4	0.4	0.4	0.50	0.3	0.4	0.4	0.4
Volt./bowl corr. Peak (Da)	16	16	16	16	16	16	16	16
Mass Clib (peaks/interp)	10/Lin.	10/Lin.	10/Lin.	8/Lin.	8/Lin.	9/Lin.	9/Lin.	10/Lin.
*(M/ΔM) for $16O^{2+}$	1040	1001.6	1017.5	950.7	990	998.6	922.3	909
**(M/ΔM10)	213.9	155.3	121.2	200.1	227.3	200.8	139.6	168.8
Time independent background (ppm/ns)	16.77	10.82	11.37	31.144	33.6	25.871	13.121	39.691
Reconsruction								
Final specimen state	Intact	Intact	Intact	Fractured	Fractured	Fractured	Intact	Fractured
pre-/post analysis imaging	SEM	SEM	SEM	SEM	SEM	Sem	Sem	Sem
Radius evolution model	voltage	voltage	voltage	tip profile	voltage	shank angle	voltage	voltage
Field factor(k)	3.3	3.3	3.3	3.3	3.3	3.3	3.3	3.3
Image compression factor	1.65	1.65	1.65	1.65	1.65	1.65	1.65	1.65
Assumed E-field (V/nm)	20	19	18	36	28	25	25	20
Detector efficiency	0.36	0.36	0.36	0.36	0.36	0.36	0.36	0.36
vg. Atomic volume (nm3)	0.00986	0.00986	0.00986	0.0125	0.0125	0.00986	0.00986	0.00986
Vinitial;Vfinal (V)	3043.5-7558.8	2875.0-6645.0	2750.5-5472.0	2925.8-4284.5	5755.0-8550.5	2467.5-6407.1	3548-6777.4	6126.3-6972

*ΔM is full width at half maximum

** ΔM10 is full width at tenth maximum

det. = detection; Volt. = voltage; corr. = correction; Calib. = calibration; interp. = interpolation; Lin. = linearization method; Avg. = average

Table 2.A.2 APT composition of the successful specimens. Concentrations are expressed in atomic %. n.d = not detected

	Sample								
Ion	**Grt1**	**Grt2**	**Grt3**	**Grt-PB1**	**Grt-PB2**	**Gl1**	**Gl2**	**Gl-PB1**	**Gl-PB2**
Si	30.36	30.55	30.47	30.42	30.14	32.16	32.77	31.28	31.90
O	47.90	47.81	48.49	47.89	49.28	59.79	58.82	62.87	59.59
Ti	0.06	0.05	0.05	0.06	0.04	0.07	0.09	0.05	0.05
Al	11.35	11.48	11.47	12.12	11.35	5.64	5.48	3.56	5.39
Fe	5.46	4.86	4.22	4.04	4.02	0.56	0.81	0.70	0.58
Mn	0.42	0.37	0.36	0.44	0.36	0.05	0.07	0.03	0.03
Mg	4.01	4.44	4.43	4.65	4.40	0.02	0.02	0.16	0.01
Ca	0.35	0.37	0.42	0.28	0.32	0.02	0.03	0.03	0.02
Na	0.02	0.01	0.01	0.01	0.01	0.42	0.23	0.48	0.75
K	0.01	0.004	0.004	0.01	0.003	0.81	1.04	0.46	1.31
Li	0.01	0.01	0.01	0.01	0.02	0.03	0.03	0.09	0.08
B	*n.d*	*n.d*	*n.d*	*n.d*	*n.d*	0.14	0.17	0.12	0.11
P	0.03	0.02	0.02	0.03	0.02	0.18	0.24	0.08	0.08
Cl	0.003	0.002	0.004	0.01	0.004	0.08	0.13	0.05	0.07
Zn	0.01	0.004	0.004	0.01	0.005	*n.d*	*n.d*	*n.d*	*n.d*
Sr	0.03	0.03	0.04	0.03	0.05	0.03	0.05	0.02	0.02

Appendix B

3.B Supplementary Figures and Data Tables to Chapter 3

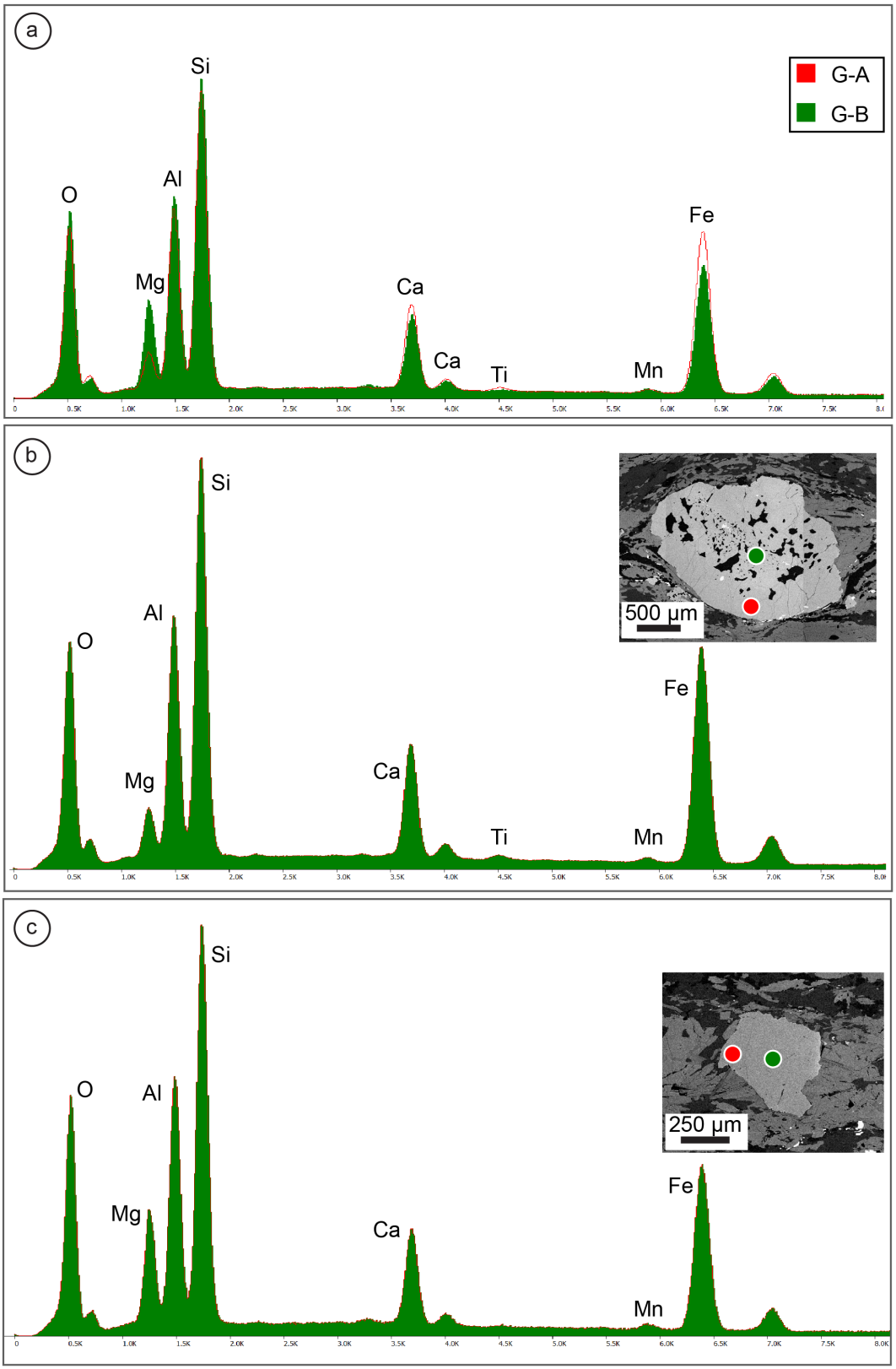

Figure 3.B.1 (a) Overlapped EDS-Xray spectra of garnets G-A and G-B of the shear zone. Higher concentrations of Mg, Ca and Fe are visible in G-A. (b, c) Spot analyses at the core (green) and rim (red) for G-A (b) and G-B (c). No variations in chemical composition between the two regions of the grain are visible.

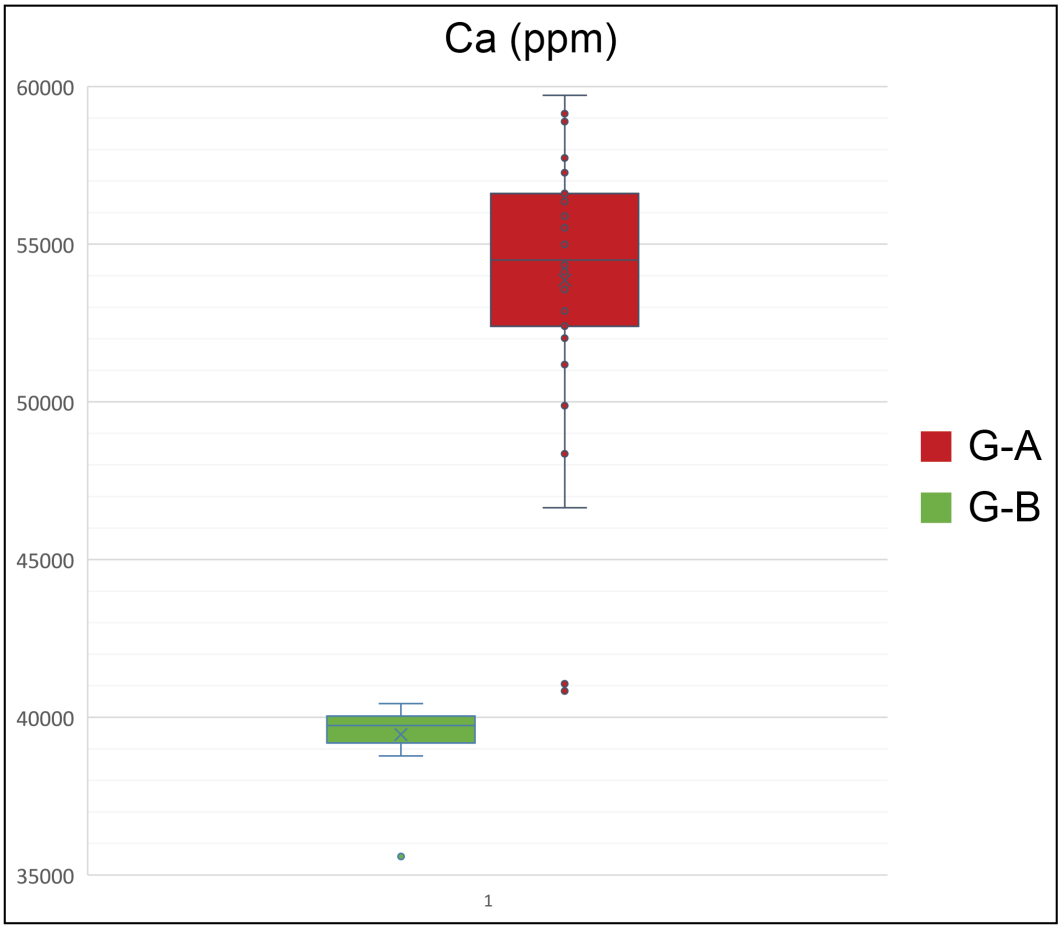

Figure 3.B.2 Box and Whiskers plots of Ca concentration for garnet G-A and G-B obtained by laser ablation. Concentrations are expressed in ppm.

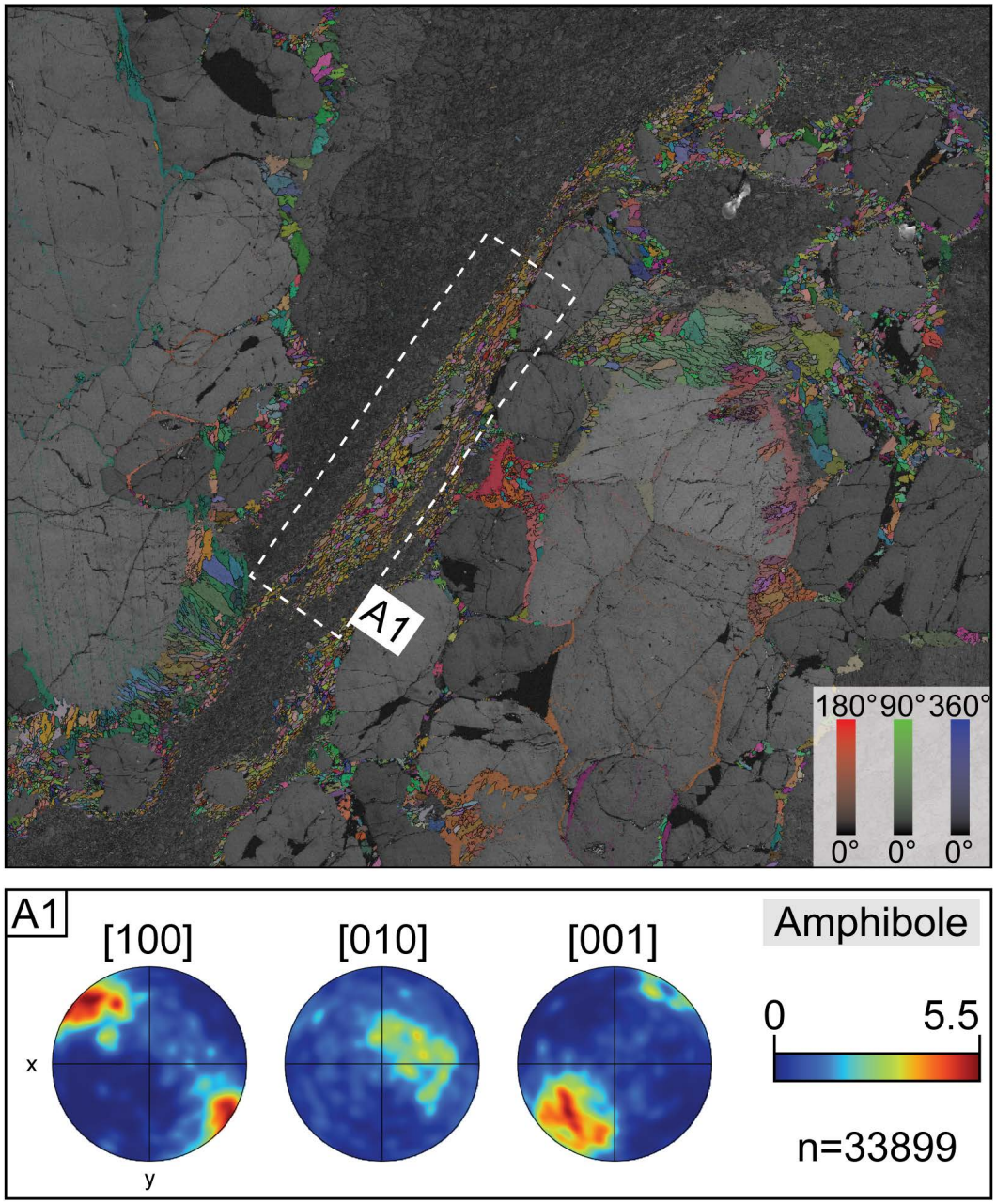

Figure 3.B.3 All-Euler angles EBSD map highlighting the distribution and orientation of amphibole crystals within the micro-shear domain. Each pixel represents an orientation colour coded with respect to its Euler angles. The orientation of amphibole in the subdomain [A1] are presented as contoured pole figures (equal area and lower hemisphere). The colour coding indicates the density of data points. "n" represents the number of grains. Map step size 0.7 μm.

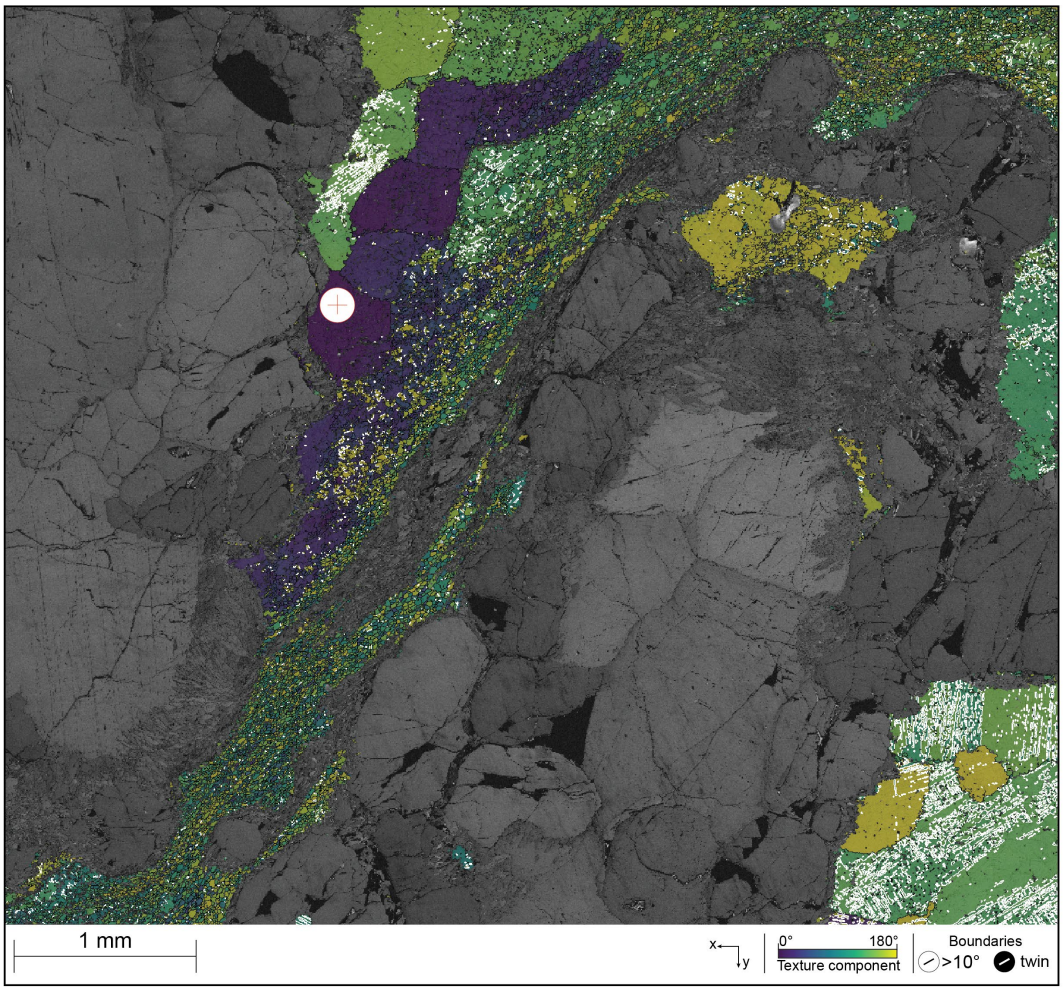

Figure 3.B.4 Enlarged version of the plagioclase grain reference orientation deviation map obtained by EBSD. Each pixel is colour coded based on the deviation angle relative to the reference point indicated by a red cross in the map. High-angle boundaries (>10 °) are plotted in black, twin boundaries (<010>180°) are plotted in white.

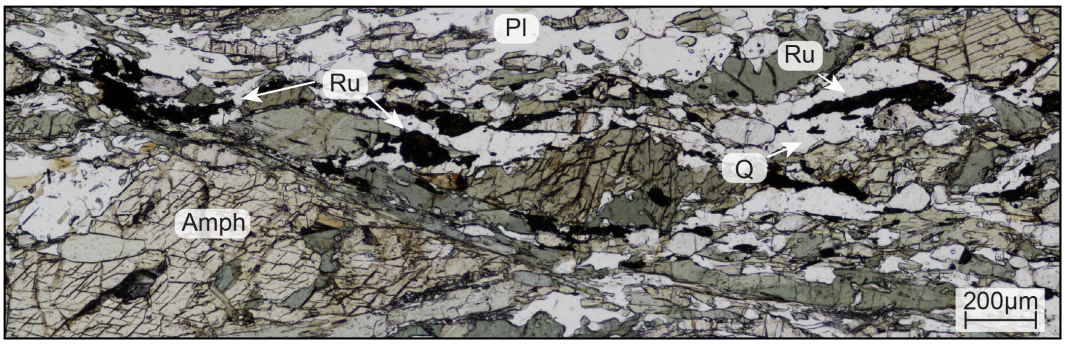

Figure 3.B.5 Optical plane-polarized photomicrograph showing the occurrence of rutile in textural occurrence with quartz and amphibole in the shear zone. Plagioclase is also present in the matrix.

Table 3.B.1 Representative trace element analyses of zircon, and garnet obtained form LA-ICP-MS.

Lithology	Shear zone		Anorthosite Gabbro		Shear zone		Shear zone	
Mineral	Zircon		Garnet		Garnet A		Garnet B	
	ppm	*stdv*	ppm	*stdv*	ppm	*stdv*	ppm	*stdv*
Ca			41103.02	*829.8*	47313.58	*9525.5*	39452.77	*1136.3*
Y			1.47	*0.4*	83.41	*73.3*	99.75	*18.5*
La	0.6	*2.8*	0.005	*0.03*	4.93	*46.7*	0.01	*0.03*
Ce	16.4	*6.9*	0.05	*0.05*	10.09	*95.2*	0.10	*0.1*
Pr	35.3	*129.9*	0.03	*0.01*	1.05	*9.6*	0.11	*0.03*
Nd	8.5	*10.7*	0.45	*0.1*	4.31	*33.0*	2.44	*0.3*
Sm	17.2	*21.9*	0.32	*0.04*	2.73	*3.5*	4.05	*0.4*
Eu	32.4	*33.5*	0.67	*0.05*	1.95	*1.0*	1.59	*0.1*
Gd	38.1	*31.6*	0.39	*0.1*	9.86	*3.9*	10.73	*0.7*
Tb	63.0	*53.6*	0.05	*0.01*	2.33	*1.1*	2.36	*0.2*
Dy	92.9	*77.0*	0.29	*0.1*	15.86	*10.7*	17.49	*1.8*
Ho	129.7	*100.2*	0.05	*0.01*	3.18	*2.8*	3.93	*0.7*
Er	183.2	*152.0*	0.15	*0.1*	8.33	*8.8*	11.45	*3.0*
Tm	235.9	*186.0*	0.02	*0.01*	1.05	*1.3*	1.60	*0.5*
Yb	339.9	*269.1*	0.17	*0.1*	6.60	*8.7*	10.97	*4.3*
Lu	419.9	*329.6*	0.03	*0.02*	0.90	*1.3*	1.58	*0.7*
Lu_N/Sm_N	22.9	*10.4*	*0.60*	*0.4*	1.90	*2.2*	2.44	*1.3*
Eu/Eu*	1.4	*0.7*	5.91	*0.7*	1.21	*0.1*	0.74	*0.03*

Table 3.B.2 Representative trace element analyses of Zr-in rutile temperatures

Analytical spot	Zr (ppm)	2s	Temp (°C)
16IS2-2-3 - 1.d	212	6	631
16IS2-2-3 - 2.d	221	6	634
16IS2-2-3 - 3.d	221	9	634
16IS2-2-3 - 4.d	218	5	633
16IS2-2-3 - 5.d	184	9	620
16IS2-2-3 - 6.d	211	7	631
16IS2-2-3 - 7.d	195	5	625
16IS2-2-3 - 8.d	178	5	618
16IS2-2-3 - 9.d	146	5	603
16IS2-2-3 - 10.d	188	8	622
16IS2-2-3 - 11.d	192	5	623
16IS2-2-3 - 12.d	202	22	627
16IS2-2-3 - 13.d	141	5	601
16IS2-2-3 - 14.d	119	8	589
16IS2-2-3 - 15.d	167	5	613
16IS2-2-3 - 18.d	200	7	627
16IS2-2-3 - 19.d	128	5	594
16IS2-2-3 - 20.d	169	4	614
Average			**619**

Table 3.B.3 Mineral abundances obtained from TIMA analyses. Values are expressed in wt%. Shear zone PT represent the normalized modal abundances of the minerals in the stable mineral assemblage.

Lithology	Anorthosite Gabbro	Shear zone	Shear zone PT
Phase			
	wt%	wt%	wt%
Pargasite	8.49	54.53	57.7
Plagioclase	59.84	23.42	24.8
Epidote	0.12	11.61	12.3
Quartz	0.33	3.65	3.9
Biotite	0.83	3.04	-
Clinopyroxene	11.11	1.28	-
K-Feldspar	-	0.65	-
Garnet A	18.01	0.45	0.5
Garnet B	-	0.42	0.4
Kyanite	0.68	0.23	0.2
Apatite	-	0.19	-
Kaolinite	0.38	0.18	-
Rutile	-	0.16	0.2
Pyrite	-	0.12	-
The rest	0.19	0.06	0.1
Total	100.00	100.00	100.00

Table 3.B.4 Whole-rock geochemistry analyses for the amphibolite sample used in the thermodynamic model. Concentrations are expressed in molar percentages.

	Amphibolite
Oxides	Mol%
SiO_2	50.09
Al_2O_3	11.89
FeO	5.64
MgO	10.77
CaO	12.41
Na_2O	2.73
TiO_2	0.32
H_2O	5.2
O	0.97

Table 3.B.5 LA-ICP-MS trace elements analyses from zircon of the amphibolite shear zone. Concentrations are expressed in ppm.

Grain #	La	La_2σ	Ce	Ce_2σ	Pr	Pr_2σ	Nd	Nd_2σ	Sm	Sm_2σ	Eu	Eu_2σ	Gd	Gd_2σ
z2 - 3			10.93	0.9			1.9	1.2	2.7	1.7	1.12	0.5	5.7	1.6
z6 - 2	-0.084	0.099	11.12	0.93	0.88	0.27	6.1	2.4	1.63	0.99	2.6	1	7.7	1.7
z4 - 4	0.16	0.18	7.94	0.98	1.6	1.1	7.7	4.2	2.8	1.7	1.28	0.66	4.6	1.9
z1 - 4	-0.42	0.33	10.66	0.9	64	20	4	2.2	1.4	1.1	2.58	0.7	5.9	1.4
z1 - 5	0.098	0.038	7.8	1.3	2.2	1.2	4.4	2.8	2.1	1.4	1.73	0.67	6.2	1.7
z4 - 1	0.09	0.1	8.2	1	4.3	1.7	8.3	3.3	1.9	1	3.01	0.91	3.8	1.6
z1 - 8	0.005	0.084	10.2	1.1			3.1	2.3			1.5	0.65	10	1.9
z6 - 3	-0.06	0.12	12.95	0.87			5.6	2.5	3.9	1.4	2.6	1	13.3	2
z1 - 3	-0.24	0.32	6.37	0.85	9.9	4.4	1.45	0.89					2.3	1.1
z2 - 4			10.8	1.4					2.8	1.4	1.01	0.44	6.6	1.6
z3 - 1	0.08	0.1	11.8	2.1	0.37	0.18	1.2	1.1	4	1.6	1.29	0.76	9	2.6
z11 - 1	-0.03	0.12	22.3	1.2	2.64	0.58	15.7	4.3	10.8	2.4	5.41	0.97	25.5	2.7
z1 - 7	0.071	0.058	9.4	1.2	1.06	0.42	8.4	3.7	4.8	2.3	2.29	0.93	11.8	2.3
z1 - 9	-0.17	0.15	17.6	1.3	3.24	0.76	20.5	7.3	14.4	3.4	8.9	1.3	26.3	4.1
z1 - 1			5.88	0.85			0.67	0.63	1.07	0.94			1.2	1.1
z6 - 1	0.03	0.047	4.35	0.73									2.72	0.73
z5 - 2			4.99	0.88					0.63	0.69	0.6	0.53	1.35	0.85
z5 - 1			7.6	0.94			1.8	1.3	1.7	1.1	0.74	0.44	4.1	1.2
z2 - 5			14.3	1.3					3.1	1.9	1.39	0.58	8	2.2
z1 - 10	0.017	0.088	13.6	1.1	0.75	0.47	6.6	2.7	2.4	1.2	3.3	1.1	14	2.7
z10 - 1			8.5	1.2			1.7	1.2			0.68	0.47	5	1.8
z1 - 6	-0.08	0.13	6.1	1.3	0.65	0.43	1.4	1.3			1.78	0.91	2.9	1
z2 - 2			10.6	1.2	0.22	0.15			2.7	1.7	1.01	0.65	7.2	1.6
z14 - 1	2.907	0.075	6.2	1.4							0.2	0.18	3.02	0.98
z7 - 1			7.99	0.92							1.37	0.51	3.9	1.4
z6 - 4	-0.08	0.13	18.35	0.79			4.6	1.9	4.5	1.7	3.5	1.5	12.8	3.3
z14 - 2	1.92	0.039	6.13	0.79									4.77	0.99
z5 - 3			8.72	0.67			3.3	2.7	1.9	0.69	0.95	0.52	2.7	1.4
average	0.23	0.12	10.05	1.08	7.06	2.44	5.42	2.50	3.56	1.52	2.12	0.75	7.58	1.77
stdev	0.82	0.08	4.23	0.29	17.30	5.40	5.04	1.56	3.33	0.65	1.86	0.30	6.29	0.78

Table 3.B.5 Continued

Grain #	Tb	Tb_2σ	Dy	Dy_2σ	Ho	Ho_2σ	Er	Er_2σ	Tm	Tm_2σ	Yb	Yb_2σ	Lu	Lu_2σ	Hf	Hf_2σ
z2 - 3	2.23	0.47	22.50	2.40	7.56	0.93	29.70	2.10	7.33	0.77	65.00	4.50	11.90	1.00	7080.00	190.00
z6 - 2	2.38	0.28	20.40	2.60	6.05	0.68	23.70	3.40	5.54	0.64	41.80	5.10	7.70	0.98	6740.00	180.00
z4 - 4	1.22	0.32	8.50	1.30	3.37	0.58	10.90	1.80	1.84	0.29	19.30	2.30	3.56	0.70	6520.00	190.00
z1 - 4	1.50	0.28	18.50	2.80	4.63	0.61	20.20	1.90	3.94	0.45	33.10	3.90	7.41	0.64	6540.00	160.00
z1 - 5	2.20	0.51	24.70	3.90	6.70	1.30	28.40	3.70	5.17	0.88	48.10	7.60	9.10	1.40	6810.00	160.00
z4 - 1	1.07	0.35	5.60	1.50	1.58	0.34	5.60	1.20	0.99	0.28	7.38	0.89	1.39	0.23	6480.00	180.00
z1 - 8	2.50	0.56	27.90	3.30	8.18	0.82	32.70	3.00	7.20	0.64	72.60	5.00	14.99	0.78	7010.00	150.00
z6 - 3	4.33	0.39	37.30	2.30	11.80	1.20	52.80	3.50	10.79	0.81	100.70	7.10	18.70	1.00	7010.00	160.00
z1 - 3	0.56	0.16	5.90	1.20	1.65	0.36	5.30	1.10	1.02	0.27	7.60	1.30	1.49	0.33	6270.00	110.00
z2 - 4	1.74	0.31	20.20	3.40	7.07	0.76	31.50	2.60	6.33	0.89	60.90	5.40	10.85	0.90	7030.00	170.00
z3 - 1	2.65	0.38	31.40	2.70	11.20	1.30	40.00	3.30	9.53	0.84	87.90	7.50	18.20	1.70	6980.00	180.00
z11 - 1	8.00	0.87	80.90	7.10	20.50	1.40	88.20	4.60	17.23	0.87	154.70	8.10	28.70	1.70	7160.00	240.00
z1 - 7	3.01	0.57	30.90	4.40	9.97	0.97	38.70	4.20	7.87	0.85	73.10	5.80	13.60	1.50	6880.00	170.00
z1 - 9	7.92	0.72	69.70	3.90	21.50	1.30	92.30	4.00	16.30	1.00	146.60	5.80	28.50	1.60	6650.00	190.00
z1 - 1	0.51	0.16	4.60	1.50	1.44	0.32	3.77	0.85	0.91	0.27	7.90	2.00	1.13	0.24	6180.00	110.00
z6 - 1	0.65	0.21	5.20	1.30	1.45	0.38	5.60	1.10	0.73	0.17	8.30	1.80	1.36	0.31	6600.00	150.00
z5 - 2	0.64	0.17	5.80	1.50	1.57	0.30	4.50	0.92	0.76	0.29	7.00	1.50	1.25	0.38	6800.00	190.00
z5 - 1	1.31	0.30	14.50	1.50	5.76	0.60	19.70	2.10	4.17	0.70	38.60	4.90	7.27	0.82	6660.00	200.00
z2 - 5	2.69	0.48	28.30	2.90	9.34	0.65	41.00	4.00	9.41	0.86	77.40	4.90	16.08	0.74	7130.00	130.00
z1 - 10	3.66	0.70	40.90	2.60	12.24	0.86	49.30	4.30	8.98	0.79	92.20	5.20	16.70	1.40	6710.00	160.00
z10 - 1	1.03	0.25	11.10	2.60	4.02	0.76	16.90	3.50	3.60	1.10	33.60	5.00	6.00	1.20	6920.00	170.00
z1 - 6	0.73	0.25	9.50	1.80	2.10	0.47	10.00	1.90	1.82	0.37	18.00	2.40	2.93	0.65	6580.00	130.00
z2 - 2	2.13	0.32	23.30	1.60	7.84	0.89	34.00	1.70	6.57	0.79	66.70	5.20	14.26	0.87	7110.00	170.00
z14 - 1	0.76	0.22	7.40	2.20	2.10	0.41	6.90	1.50	1.65	0.33	12.40	2.60	2.46	0.66	6740.00	110.00
z7 - 1	1.33	0.28	13.40	1.90	4.67	0.65	19.80	2.30	3.96	0.40	41.70	4.30	8.49	0.60	6780.00	190.00
z6 - 4	4.20	0.53	48.20	3.10	16.60	1.30	75.30	3.90	14.20	1.20	142.20	7.00	26.00	1.90	7360.00	230.00
z14 - 2	1.00	0.36	7.30	1.70	2.81	0.37	8.10	1.40	1.76	0.41	16.60	2.90	3.43	0.45	6790.00	150.00
z5 - 3	1.55	0.30	16.20	2.10	6.11	0.41	26.00	2.40	5.50	0.43	51.00	3.40	10.49	0.68	6890.00	110.00
average	2.27	0.38	22.86	2.54	7.14	0.75	29.32	2.58	5.90	0.63	54.73	4.41	10.50	0.91	6800.36	165.36
stdev	1.93	0.18	18.95	1.25	5.51	0.35	24.32	1.17	4.65	0.29	43.32	2.05	8.24	0.48	271.42	33.50

Table 3.B.6 Condrite-normalized trace elements analyses from zircon of the amphibolite shear zone.

Grain #	La	Ce	Pr	Nd	Sm	Eu	Gd	Tb	Dy	Ho	Er	Tm	Yb	Lu	Lu/Sm	Eu/Eu*
z2 - 3	0.00	17.83	0.00	4.16	18.24	20.00	28.64	61.94	91.46	137.45	185.63	293.20	403.73	476.00	26.09	0.87
z6 - 2	-0.35	18.14	9.46	13.35	11.01	46.43	38.69	66.11	82.93	110.00	148.13	221.60	259.63	308.00	27.97	2.25
z4 - 4	0.68	12.95	17.20	16.85	18.92	22.86	23.12	33.89	34.55	61.27	68.13	73.60	119.88	142.40	7.53	1.09
z1 - 4	-1.77	17.39	688.17	8.75	9.46	46.07	29.65	41.67	75.20	84.18	126.25	157.60	205.59	296.40	31.33	2.75
z1 - 5	0.41	12.72	23.66	9.63	14.19	30.89	31.16	61.11	100.41	121.82	177.50	206.80	298.76	364.00	25.65	1.47
z4 - 1	0.38	13.38	46.24	18.16	12.84	53.75	19.10	29.72	22.76	28.73	35.00	39.60	45.84	55.60	4.33	3.43
z1 - 8	0.02	16.64	0.00	6.78	0.00	26.79	50.25	69.44	113.41	148.73	204.38	288.00	450.93	599.60		
z6 - 3	-0.25	21.13	0.00	12.25	26.35	46.43	66.83	120.28	151.63	214.55	330.00	431.60	625.47	748.00	28.39	1.11
z1 - 3	-1.01	10.39	106.45	3.17	0.00	0.00	11.56	15.56	23.98	30.00	33.13	40.80	47.20	59.60		
z2 - 4	0.00	17.62	0.00	0.00	18.92	18.04	33.17	48.33	82.11	128.55	196.88	253.20	378.26	434.00	22.94	0.72
z3 - 1	0.34	19.25	3.98	2.63	27.03	23.04	45.23	73.61	127.64	203.64	250.00	381.20	545.96	728.00	26.94	0.66
z11 - 1	-0.13	36.38	28.39	34.35	72.97	96.61	128.14	222.22	328.86	372.73	551.25	689.20	960.87	1148.00	15.73	1.00
z1 - 7	0.30	15.33	11.40	18.38	32.43	40.89	59.30	83.61	125.61	181.27	241.88	314.80	454.04	544.00	16.77	0.93
z1 - 9	-0.72	28.71	34.84	44.86	97.30	158.93	132.16	220.00	283.33	390.91	576.88	652.00	910.56	1140.00	11.72	1.40
z1 - 1	0.00	9.59	0.00	1.47	7.23	0.00	6.03	14.17	18.70	26.18	23.56	36.40	49.07	45.20	6.25	
z6 - 1	0.13	7.10	0.00	0.00	0.00	0.00	13.67	18.06	21.14	26.36	35.00	29.20	51.55	54.40		
z5 - 2	0.00	8.14	0.00	0.00	4.26	10.71	6.78	17.78	23.58	28.55	28.13	30.40	43.48	50.00	11.75	1.99
z5 - 1	0.00	12.40	0.00	3.94	11.49	13.21	20.60	36.39	58.94	104.73	123.13	166.80	239.75	290.80	25.32	0.86
z2 - 5	0.00	23.33	0.00	0.00	20.95	24.82	40.20	74.72	115.04	169.82	256.25	376.40	480.75	643.20	30.71	0.86
z1 - 10	0.07	22.19	8.06	14.44	16.22	58.93	70.35	101.67	166.26	222.55	308.13	359.20	572.67	668.00	41.19	1.74
z10 - 1	0.00	13.87	0.00	3.72	0.00	12.14	25.13	28.61	45.12	73.09	105.63	144.00	208.70	240.00		
z1 - 6	-0.34	9.95	6.99	3.06	0.00	31.79	14.57	20.28	38.62	38.18	62.50	72.80	111.80	117.20		
z2 - 2	0.00	17.29	2.37	0.00	18.24	18.04	36.18	59.17	94.72	142.55	212.50	262.80	414.29	570.40	31.27	0.70
z14 - 1	12.27	10.11	0.00	0.00	0.00	3.57	15.18	21.11	30.08	38.18	43.13	66.00	77.02	98.40		
z7 - 1	0.00	13.03	0.00	0.00	0.00	24.46	19.60	36.94	54.47	84.91	123.75	158.40	259.01	339.60		
z6 - 4	-0.34	29.93	0.00	10.07	30.41	62.50	64.32	116.67	195.93	301.82	470.63	568.00	883.23	1040.00	34.20	1.41
z14 - 2	8.12	10.00	0.00	0.00	0.00	0.00	23.97	27.78	29.67	51.09	50.63	70.40	103.11	137.20		
z5 - 3	0.00	14.23	0.00	7.22	12.84	16.96	13.57	43.06	65.85	111.09	162.50	220.00	316.77	419.60	32.68	1.29
average	0.6	16.4	35.3	8.5	17.2	32.4	38.1	63.0	92.9	129.7	183.2	235.9	339.9	419.9	22.9	1.4
stdev	2.80	6.91	129.88	10.74	21.90	33.48	31.62	53.58	77.04	100.21	152.03	185.96	269.07	329.56	10.39	0.75

Table 3.B.7 U-Pb ages data obtained from trace element analyses of zircon. Rejected outliners analyses are highlighted in dark grey.

Grain #	U^{238}/Pb^{206}	U^{238}/Pb^{206} ±2σ	Pb^{207}/Pb^{206}	Pb^{207}/Pb^{206} ±2σ	Grain #	U^{238}/Pb^{206}	U^{238}/Pb^{206} ±2σ	Pb^{207}/Pb^{206}	Pb^{207}/Pb^{206} ±2σ
z5 - 1	6.69	0.21	0.07	0.00	z14 - 1	6.63	0.33	0.07	0.00
z5 - 2	6.70	0.27	0.07	0.00	z14 - 2	6.41	0.30	0.07	0.00
z5 - 3	6.41	0.45	0.07	0.00	z17 - 1			no value	NAN
z7 - 1	6.62	0.26	0.07	0.00	z26 - 1			no value	NAN
z9 - 1	8.64	0.31	0.07	0.00	z13 - 1	6.95	0.44	0.14	0.01
z22 - 1	6.91	0.28	0.08	0.01	z15 - 1	8.16	0.42	0.09	0.00
z12 - 1	18.59	1.80	0.13	0.02	z8 - 1	7.15	0.38	0.09	0.01
z4 - 1	7.06	0.26	0.07	0.00	z8 - 2	10.82	0.45	0.06	0.00
z4 - 2	7.49	0.29	0.08	0.00	z1 - 1	6.72	0.28	0.07	0.00
z4 - 3	6.93	0.28	0.07	0.00	z1 - 2	7.18	0.47	0.08	0.01
z4 - 4	7.24	0.33	0.07	0.00	z1 - 3	6.82	0.35	0.07	0.00
z4 - 5	7.68	0.35	0.09	0.00	z1 - 4	7.17	0.30	0.07	0.00
z16 - 1			no value	NAN	z1 - 5	7.15	0.36	0.07	0.00
z3 - 1	6.78	0.38	0.07	0.00	z1 - 6	6.65	0.31	0.07	0.00
z3 - 2	8.26	0.38	0.07	0.00	z1 - 7	6.73	0.33	0.07	0.00
z3 - 3	8.18	0.58	0.07	0.00	z1 - 8	6.98	0.29	0.07	0.00
z3 - 4	10.32	0.49	0.07	0.00	z1 - 9	6.73	0.25	0.07	0.00
z10 - 1	6.65	0.34	0.07	0.00	z1 - 10	6.67	0.31	0.07	0.00
z2 - 1	6.98	0.36	0.14	0.02	z11 - 1	6.76	0.27	0.07	0.00
z2 - 2	6.64	0.35	0.07	0.00	z6 - 1	6.72	0.25	0.07	0.00
z2 - 3	7.45	0.32	0.07	0.00	z6 - 2	7.30	0.28	0.07	0.00
z2 - 4	6.78	0.32	0.07	0.00	z6 - 3	6.93	0.37	0.07	0.00
z2 - 5	6.68	0.30	0.07	0.00	z6 - 4	6.57	0.26	0.07	0.00
z27 - 1	5.35	0.43	0.61	0.01	z19 - 1	13.89	1.02	0.13	0.01

Table 3.B.8 LA-ICP-MS trace elements analyses from rutile of the amphibolite shear zone. Concentrations are expressed in ppm.

Grain #	Al	Al_2σ	Si	Si_2σ	Ca	Ca_2σ	V	V_2σ	Cr	Cr_2σ	Fe	Fe_2σ	Ni	Ni_2σ
16IS2-2-3 - 1.d	87.08	6.91	2060.00	2058.04	399.24	616.64	826.21	23.22	49.64	4.27	2927.96	326.17	-0.66	0.52
16IS2-2-3 - 2.d	147.21	12.50	511.29	2824.88	618.13	613.45	848.90	19.17	50.62	3.55	2548.05	181.29	0.15	0.98
16IS2-2-3 - 3.d	69.29	5.62	260.55	2472.54	144.35	596.62	847.88	34.64	62.12	4.42	10092.98	2359.74	-0.18	0.56
16IS2-2-3 - 4.d	134.03	18.55	3348.14	2720.47	323.23	629.63	832.67	23.67	43.45	4.61	2052.38	97.03	0.87	1.06
16IS2-2-3 - 5.d	2407.17	371.49	599470.96	150580.58	1597.53	2317.06	806.05	25.20	60.45	14.52	2934.38	305.03	8.18	5.14
16IS2-2-3 - 6.d	7065.75	4483.97	29554.74	17836.65	5295.36	3462.53	809.28	25.61	89.11	7.96	22498.22	8928.12	34.21	19.73
16IS2-2-3 - 7.d	7734.06	373.42	52619.14	3882.46	2299.04	972.30	741.18	22.05	103.02	5.98	10423.38	1539.70	92.93	15.62
16IS2-2-3 - 8.d	629.64	76.68	117071.91	6122.48	1192.83	891.84	805.84	17.31	48.63	3.30	5826.44	663.76	2.67	1.33
16IS2-2-3 - 9.d	27133.78	4012.02	102260.00	13686.19	23018.61	3475.28	793.76	23.42	43.32	5.48	53968.25	8101.95	96.35	21.07
16IS2-2-3 - 10.d	1660.11	513.03	458489.53	171484.49	39156.53	23891.33	959.47	37.79	85.38	28.82	24820.22	3518.22	24.52	10.21
16IS2-2-3 - 11.d	55.42	6.73	132.19	3325.37	40.93	577.69	804.76	36.24	29.37	4.54	5174.27	273.66	0.16	1.13
16IS2-2-3 - 12.d	3344.61	1152.30	84776.45	44001.55	663657.68	89606.15	887.16	29.65	46.12	23.57	13157.52	1987.83	36.63	13.96
16IS2-2-3 - 13.d	363.85	47.86	11437.30	5345.76	277.30	906.40	794.74	19.32	29.74	6.07	2913.81	252.75	2.15	1.34
16IS2-2-3 - 14.d	36797.45	4498.29	610359.01	130225.74	3582.28	3566.42	869.84	26.00	69.96	24.65	16560.49	2816.21	72.46	23.35
16IS2-2-3 - 15.d	67.65	26.38	2462.98	4188.10	34.15	697.15	792.09	16.52	49.86	7.88	5017.33	535.58	-0.10	1.14
16IS2-2-3 - 18.d	178.73	23.61	7035.47	4021.78	974.39	913.37	809.02	21.43	39.75	7.55	2145.73	168.25	0.47	1.37
16IS2-2-3 - 19.d	209.01	23.70	153256.75	8369.55	1969.04	1347.61	834.21	20.82	94.89	8.52	3314.52	271.27	3.53	2.10
16IS2-2-3 - 20.d	1161.55	131.30	6131.02	4724.80	104.05	898.66	738.64	16.13	57.96	7.22	5840.28	360.83	16.15	3.20

Table 3.B.8 Continued

Grain #	Zr	Zr_2σ	Nb	Nb_2σ	Mo	Mo_2σ	Sn	Sn_2σ	Sb	Sb_2σ	Ta	Ta_2σ	W	W_2σ
16IS2-2-3 - 1.d	211.81	6.19	551.33	17.57	15.14	1.82	36.74	3.09	5.51	0.80	9.41	0.77	4.75	0.49
16IS2-2-3 - 2.d	221.11	5.70	756.22	16.54	15.62	1.93	44.59	3.04	5.63	0.71	18.27	0.89	4.94	0.55
16IS2-2-3 - 3.d	220.67	8.54	664.67	17.00	14.87	1.86	40.32	2.46	4.94	0.64	46.97	2.15	4.68	0.50
16IS2-2-3 - 4.d	218.27	4.79	232.56	6.72	12.51	1.89	35.28	2.29	7.62	1.03	9.45	0.88	3.60	0.57
16IS2-2-3 - 5.d	183.63	8.56	655.13	32.11	11.16	3.55	29.12	3.70	6.02	1.25	37.54	6.09	6.02	1.38
16IS2-2-3 - 6.d	210.92	7.01	493.01	19.12	12.59	1.57	35.74	2.98	7.57	1.21	9.39	1.12	3.42	0.50
16IS2-2-3 - 7.d	195.30	4.72	1089.80	24.67	21.47	2.53	43.85	3.20	7.19	1.03	26.34	2.71	4.04	0.49
16IS2-2-3 - 8.d	177.90	4.96	416.72	14.67	13.37	1.36	37.98	2.46	5.83	0.83	8.23	0.90	3.57	0.43
16IS2-2-3 - 9.d	146.24	4.93	497.91	18.47	10.93	2.56	29.98	2.83	7.21	1.16	19.39	1.56	3.55	0.55
16IS2-2-3 - 10.d	188.19	8.45	945.97	47.47	14.72	4.31	270.68	120.33	7.20	1.92	59.73	4.18	6.82	1.30
16IS2-2-3 - 11.d	191.97	5.26	878.44	32.94	13.81	1.91	44.33	4.37	7.83	1.18	37.89	1.40	5.52	0.58
16IS2-2-3 - 12.d	202.45	22.38	1195.22	30.10	13.24	3.87	324.17	79.63	11.18	2.84	86.80	3.43	7.69	1.86
16IS2-2-3 - 13.d	140.80	5.37	157.07	13.14	9.42	1.50	51.54	5.96	6.57	1.07	5.83	1.15	3.55	0.71
16IS2-2-3 - 14.d	119.25	8.26	880.28	30.38	12.02	3.56	125.07	38.23	10.60	2.56	40.54	4.24	4.29	1.20
16IS2-2-3 - 15.d	166.95	5.34	713.49	20.31	14.42	2.51	58.50	7.04	8.12	1.29	29.04	1.58	7.10	0.84
16IS2-2-3 - 18.d	200.12	6.68	391.99	11.38	13.82	2.87	60.32	6.55	8.30	1.49	10.26	0.91	6.98	0.94
16IS2-2-3 - 19.d	127.74	5.00	1240.22	34.18	20.44	3.47	64.35	7.17	10.03	1.79	39.01	3.12	7.41	0.81
16IS2-2-3 - 20.d	169.49	4.43	538.43	15.48	15.14	1.83	47.32	4.11	7.50	1.31	12.56	0.89	5.56	0.69

Table 3.B.9 LA-ICP-MS trace elements analyses from garnet of the retrogressed anorthosite. Concentrations are expressed in ppm.

Sample #	Ca	± 2σ	Y	± 2σ	La	± 2σ	Ce	± 2σ	Pr	± 2σ	Nd	± 2σ	Sm	± 2σ	Eu	± 2σ
idl01_usd_grtA1 - 1.d	39904.64	480.64	1.91	0.035	0.0010	0.0004	0.024	0.0026	0.0178	0.0017	0.32	0.024	0.26	0.02	0.60	0.0165
idl01_usd_grtA1 - 2.d	40950.70	427.31	1.99	0.042	0.0024	0.0007	0.027	0.0026	0.0202	0.0020	0.33	0.023	0.28	0.02	0.62	0.0169
idl01_usd_grtA1 - 3.d	40423.88	506.22	2.01	0.036	0.0007	0.0004	0.020	0.0024	0.0164	0.0015	0.29	0.018	0.28	0.02	0.60	0.0180
idl01_usd_grtA1 - 4.d	40933.53	498.53	1.91	0.031	0.0010	0.0004	0.028	0.0027	0.0243	0.0021	0.36	0.025	0.29	0.02	0.63	0.0162
idl01_usd_grtA2 - 1.d	41336.61	456.37	1.80	0.037	0.0021	0.0006	0.056	0.0032	0.0397	0.0030	0.47	0.032	0.28	0.02	0.67	0.0180
idl01_usd_grtA2 - 2.d	41172.67	390.87	1.89	0.033	0.0025	0.0007	0.060	0.0039	0.0374	0.0028	0.50	0.031	0.30	0.02	0.69	0.0157
idl01_usd_grtA2 - 3.d	41791.35	437.47	1.92	0.037	0.0025	0.0007	0.065	0.0048	0.0376	0.0027	0.52	0.028	0.32	0.03	0.70	0.0157
idl01_usd_grtA2 - 4.d	42014.06	451.31	1.94	0.037	0.0029	0.0007	0.062	0.0039	0.0396	0.0028	0.53	0.030	0.30	0.03	0.70	0.0177
idl01_usd_grtA2 - 5.d	41600.25	445.66	1.83	0.032	0.0035	0.0008	0.058	0.0039	0.0333	0.0023	0.45	0.026	0.28	0.02	0.68	0.0169
idl01_usd_grtA2 - 6.d	41945.44	414.67	1.85	0.028	0.0014	0.0005	0.044	0.0036	0.0332	0.0024	0.45	0.028	0.30	0.02	0.69	0.0151
idl01_usd_grtA2 - 7.d	41115.87	519.86	1.87	0.036	0.0023	0.0007	0.029	0.0025	0.0221	0.0023	0.34	0.022	0.25	0.02	0.64	0.0173
idl01_usd_grtA3 - 1.d	41322.19	401.68	1.93	0.037	0.0034	0.0008	0.066	0.0034	0.0394	0.0028	0.51	0.030	0.33	0.02	0.67	0.0157
idl01_usd_grtA3 - 2.d	41738.72	425.09	2.00	0.033	0.0031	0.0008	0.074	0.0043	0.0419	0.0030	0.52	0.031	0.32	0.03	0.69	0.0182
idl01_usd_grtA3 - 3.d	41751.81	444.27	2.01	0.037	0.0037	0.0009	0.079	0.0043	0.0457	0.0030	0.52	0.029	0.35	0.03	0.70	0.0169
idl01_usd_grtA3 - 4.d	41545.82	423.61	2.07	0.034	0.0035	0.0008	0.087	0.0048	0.0466	0.0028	0.55	0.033	0.34	0.03	0.71	0.0175
idl01_usd_grtA3 - 5.d	41489.99	429.87	2.04	0.037	0.0025	0.0007	0.081	0.0041	0.0423	0.0027	0.54	0.030	0.32	0.03	0.71	0.0185
idl01_usd_grtA3 - 6.d	41157.02	456.37	1.97	0.035	0.0014	0.0005	0.063	0.0032	0.0388	0.0027	0.50	0.029	0.30	0.02	0.67	0.0157
idl01_usd_grtA3 - 7.d	40708.07	458.05	1.95	0.034	0.0016	0.0005	0.042	0.0032	0.0302	0.0023	0.41	0.024	0.31	0.02	0.63	0.0173
idl01_usd_grtA4 - 1.d	40415.73	457.50	1.60	0.034	0.0019	0.0006	0.049	0.0035	0.0310	0.0026	0.43	0.030	0.26	0.02	0.65	0.0186
idl01_usd_grtA4 - 2.d	40597.92	395.46	1.65	0.032	0.0013	0.0005	0.042	0.0028	0.0298	0.0022	0.38	0.028	0.30	0.02	0.63	0.0179
idl01_usd_grtA4 - 3.d	40902.16	379.95	1.60	0.032	0.0010	0.0005	0.038	0.0031	0.0282	0.0022	0.38	0.026	0.28	0.02	0.63	0.0153
idl01_usd_grtA5 - 1.d	41023.16	474.64	1.47	0.032	0.0010	0.0004	0.039	0.0030	0.0311	0.0026	0.46	0.029	0.33	0.03	0.65	0.0166
idl01_usd_grtA5 - 2.d	41541.96	442.45	1.45	0.031	0.0014	0.0006	0.045	0.0027	0.0333	0.0026	0.47	0.027	0.38	0.03	0.68	0.0177
idl01_usd_grtA5 - 3.d	41621.84	388.39	1.48	0.033	0.0006	0.0003	0.041	0.0024	0.0310	0.0026	0.44	0.027	0.37	0.03	0.68	0.0182
idl01_usd_grtA5 - 4.d	41541.60	500.07	1.46	0.026	0.0005	0.0003	0.040	0.0037	0.0339	0.0027	0.46	0.032	0.36	0.02	0.71	0.0203
idl01_usd_grtA5 - 5.d	41961.73	408.33	1.47	0.024	0.0015	0.0011	0.047	0.0033	0.0349	0.0026	0.51	0.030	0.35	0.02	0.69	0.0176
idl01_usd_grtA5 - 6.d	41493.15	465.12	1.41	0.032	0.0006	0.0004	0.043	0.0026	0.0344	0.0028	0.49	0.031	0.34	0.02	0.68	0.0159
idl01_usd_grtA5 - 7.d	41259.01	389.45	1.43	0.025	0.0009	0.0004	0.035	0.0027	0.0298	0.0023	0.46	0.026	0.34	0.02	0.67	0.0151
idl01_usd_grtA5 - 8.d	41711.05	501.35	1.50	0.038	0.0014	0.0006	0.052	0.0032	0.0359	0.0026	0.49	0.029	0.36	0.03	0.67	0.0167
idl01_usd_grtA5 - 9.d	42351.43	459.01	1.48	0.029	0.0019	0.0005	0.055	0.0036	0.0351	0.0025	0.50	0.027	0.36	0.03	0.68	0.0159
idl01_usd_grtA5 - 10.d	41537.24	512.25	1.43	0.029	0.0009	0.0004	0.040	0.0032	0.0287	0.0022	0.42	0.029	0.36	0.03	0.65	0.0194
idl01_usd_grtA6 - 1.d	40415.00	439.77	1.07	0.026	0.0010	0.0005	0.052	0.0035	0.0406	0.0028	0.55	0.030	0.38	0.03	0.71	0.0179
idl01_usd_grtA6 - 2.d	40941.80	421.10	1.23	0.026	0.0014	0.0005	0.050	0.0031	0.0380	0.0028	0.54	0.027	0.42	0.03	0.74	0.0189
idl01_usd_grtA6 - 3.d	40545.09	425.97	1.21	0.025	0.0009	0.0004	0.037	0.0031	0.0327	0.0030	0.50	0.029	0.37	0.03	0.72	0.0173

Table 3.B.9 LA-ICP-MS Continued

Sample #	Gd	± 2σ	Tb	± 2σ	Dy	± 2σ	Ho	± 2σ	Er	± 2σ	Tm	± 2σ	Yb	± 2σ	Lu	± 2σ
idl01_usd_grtA1 - 1.d	0.3526	0.024	0.056	0.0038	0.34	0.019	0.074	0.0055	0.20	0.014	0.029	0.0026	0.19	0.019	0.038	0.0036
idl01_usd_grtA1 - 2.d	0.3735	0.023	0.061	0.0038	0.36	0.022	0.075	0.0047	0.21	0.014	0.028	0.0028	0.23	0.020	0.037	0.0033
idl01_usd_grtA1 - 3.d	0.3731	0.024	0.062	0.0042	0.36	0.022	0.072	0.0044	0.20	0.014	0.031	0.0032	0.23	0.021	0.034	0.0029
idl01_usd_grtA1 - 4.d	0.3596	0.024	0.058	0.0036	0.35	0.019	0.076	0.0047	0.20	0.014	0.030	0.0029	0.21	0.020	0.039	0.0029
idl01_usd_grtA2 - 1.d	0.3189	0.027	0.046	0.0036	0.29	0.018	0.071	0.0046	0.23	0.015	0.039	0.0033	0.35	0.025	0.062	0.0047
idl01_usd_grtA2 - 2.d	0.3105	0.022	0.050	0.0038	0.31	0.018	0.068	0.0041	0.24	0.016	0.036	0.0028	0.36	0.026	0.062	0.0038
idl01_usd_grtA2 - 3.d	0.3488	0.027	0.047	0.0035	0.31	0.019	0.071	0.0047	0.24	0.014	0.036	0.0034	0.38	0.027	0.066	0.0044
idl01_usd_grtA2 - 4.d	0.3288	0.023	0.047	0.0037	0.33	0.019	0.071	0.0043	0.24	0.013	0.044	0.0035	0.36	0.023	0.071	0.0041
idl01_usd_grtA2 - 5.d	0.3169	0.023	0.046	0.0035	0.31	0.019	0.071	0.0048	0.23	0.016	0.038	0.0029	0.36	0.022	0.062	0.0036
idl01_usd_grtA2 - 6.d	0.3134	0.023	0.044	0.0032	0.30	0.020	0.071	0.0046	0.24	0.012	0.038	0.0034	0.33	0.025	0.066	0.0041
idl01_usd_grtA2 - 7.d	0.3088	0.020	0.047	0.0034	0.30	0.018	0.070	0.0046	0.23	0.013	0.037	0.0034	0.36	0.021	0.070	0.0041
idl01_usd_grtA3 - 1.d	0.3518	0.026	0.050	0.0041	0.30	0.021	0.075	0.0043	0.23	0.015	0.040	0.0028	0.34	0.027	0.058	0.0047
idl01_usd_grtA3 - 2.d	0.3286	0.021	0.050	0.0037	0.33	0.020	0.074	0.0046	0.23	0.015	0.038	0.0030	0.37	0.027	0.064	0.0040
idl01_usd_grtA3 - 3.d	0.3389	0.024	0.050	0.0034	0.31	0.019	0.071	0.0043	0.25	0.015	0.041	0.0034	0.37	0.026	0.069	0.0037
idl01_usd_grtA3 - 4.d	0.3328	0.026	0.051	0.0042	0.32	0.019	0.075	0.0041	0.23	0.014	0.045	0.0042	0.36	0.024	0.071	0.0042
idl01_usd_grtA3 - 5.d	0.3559	0.028	0.050	0.0038	0.34	0.021	0.078	0.0042	0.24	0.016	0.040	0.0034	0.37	0.024	0.069	0.0050
idl01_usd_grtA3 - 6.d	0.3313	0.020	0.046	0.0035	0.31	0.019	0.074	0.0052	0.25	0.017	0.039	0.0032	0.34	0.024	0.068	0.0045
idl01_usd_grtA3 - 7.d	0.3015	0.023	0.046	0.0039	0.30	0.018	0.071	0.0053	0.24	0.017	0.042	0.0037	0.37	0.023	0.073	0.0046
idl01_usd_grtA4 - 1.d	0.3417	0.025	0.047	0.0035	0.29	0.020	0.060	0.0044	0.19	0.013	0.027	0.0027	0.22	0.022	0.040	0.0035
idl01_usd_grtA4 - 2.d	0.3791	0.024	0.051	0.0033	0.28	0.019	0.059	0.0045	0.18	0.013	0.028	0.0029	0.24	0.020	0.040	0.0041
idl01_usd_grtA4 - 3.d	0.3668	0.026	0.049	0.0035	0.30	0.020	0.059	0.0040	0.18	0.013	0.026	0.0026	0.23	0.022	0.036	0.0028
idl01_usd_grtA5 - 1.d	0.5188	0.032	0.077	0.0053	0.35	0.018	0.054	0.0040	0.11	0.009	0.012	0.0019	0.09	0.012	0.012	0.0018
idl01_usd_grtA5 - 2.d	0.5417	0.035	0.072	0.0041	0.34	0.020	0.056	0.0042	0.10	0.010	0.013	0.0017	0.07	0.010	0.012	0.0017
idl01_usd_grtA5 - 3.d	0.5199	0.034	0.075	0.0048	0.35	0.024	0.054	0.0037	0.10	0.010	0.013	0.0019	0.09	0.012	0.013	0.0020
idl01_usd_grtA5 - 4.d	0.5119	0.035	0.075	0.0044	0.36	0.018	0.053	0.0040	0.11	0.009	0.012	0.0017	0.09	0.011	0.015	0.0019
idl01_usd_grtA5 - 5.d	0.5267	0.029	0.070	0.0043	0.36	0.019	0.051	0.0039	0.11	0.008	0.013	0.0019	0.09	0.011	0.018	0.0022
idl01_usd_grtA5 - 6.d	0.5247	0.031	0.069	0.0038	0.36	0.022	0.051	0.0047	0.11	0.008	0.013	0.0017	0.08	0.011	0.016	0.0021
idl01_usd_grtA5 - 7.d	0.5121	0.032	0.075	0.0042	0.34	0.021	0.051	0.0034	0.11	0.009	0.013	0.0018	0.09	0.011	0.016	0.0022
idl01_usd_grtA5 - 8.d	0.5189	0.032	0.076	0.0044	0.36	0.019	0.052	0.0040	0.11	0.010	0.014	0.0019	0.08	0.011	0.015	0.0019
idl01_usd_grtA5 - 9.d	0.5297	0.030	0.074	0.0046	0.36	0.018	0.056	0.0040	0.11	0.008	0.014	0.0020	0.08	0.011	0.018	0.0019
idl01_usd_grtA5 - 10.d	0.5065	0.024	0.073	0.0044	0.33	0.018	0.049	0.0033	0.11	0.010	0.013	0.0016	0.09	0.011	0.016	0.0018
idl01_usd_grtA6 - 1.d	0.4023	0.026	0.049	0.0036	0.24	0.015	0.038	0.0033	0.10	0.008	0.011	0.0018	0.06	0.011	0.010	0.0017
idl01_usd_grtA6 - 2.d	0.3794	0.024	0.051	0.0037	0.27	0.017	0.049	0.0035	0.13	0.011	0.013	0.0018	0.08	0.012	0.015	0.0021
idl01_usd_grtA6 - 3.d	0.4005	0.027	0.051	0.0038	0.25	0.017	0.046	0.0037	0.11	0.009	0.014	0.0019	0.09	0.013	0.017	0.0027

Table 3.B.9 LA-ICP-MS Continued

Sample #	Ca	± 2σ	Y	± 2σ	La	± 2σ	Ce	± 2σ	Pr	± 2σ	Nd	± 2σ	Sm	± 2σ	Eu	± 2σ
idl01_usd_grtA6 - 4.d	41002.32	456.61	1.09	0.022	0.0006	0.0003	0.029	0.0028	0.0280	0.0024	0.46	0.031	0.37	0.02	0.71	0.0198
idl01_usd_grtA6 - 5.d	40881.04	353.06	1.10	0.024	0.0008	0.0004	0.043	0.0030	0.0362	0.0026	0.53	0.032	0.40	0.03	0.71	0.0153
idl01_usd_grtA7 - 1.d	40102.50	371.14	1.86	0.033	0.0016	0.0006	0.045	0.0034	0.0289	0.0024	0.41	0.023	0.29	0.03	0.65	0.0179
idl01_usd_grtA7 - 2.d	40880.15	350.22	1.80	0.033	0.0016	0.0006	0.051	0.0033	0.0340	0.0025	0.45	0.023	0.31	0.02	0.66	0.0199
idl01_usd_grtA7 - 3.d	40948.02	395.28	1.82	0.027	0.0013	0.0005	0.051	0.0036	0.0334	0.0026	0.43	0.025	0.27	0.02	0.67	0.0168
idl01_usd_grtA7 - 4.d	40700.23	448.83	1.79	0.035	0.0014	0.0005	0.050	0.0034	0.0295	0.0023	0.42	0.027	0.28	0.02	0.67	0.0161
idl01_usd_grtA7 - 5.d	40805.37	491.41	1.82	0.032	0.0024	0.0007	0.050	0.0029	0.0304	0.0022	0.43	0.028	0.29	0.02	0.67	0.0169
idl01_usd_grtA7 - 6.d	40136.31	586.26	1.78	0.036	0.0011	0.0004	0.042	0.0030	0.0285	0.0020	0.42	0.021	0.28	0.02	0.63	0.0162
idl01_usd_grtA8 - 1.d	40371.75	673.40	1.59	0.042	0.0039	0.0011	0.049	0.0040	0.0338	0.0026	0.47	0.029	0.29	0.02	0.65	0.0144
idl01_usd_grtA8 - 2.d	39715.80	453.65	1.62	0.031	0.0006	0.0003	0.013	0.0018	0.0135	0.0014	0.28	0.022	0.24	0.02	0.60	0.0146
idl01_usd_grtA9 - 1.d	40599.57	343.76	1.36	0.024	0.0016	0.0006	0.061	0.0041	0.0377	0.0033	0.47	0.029	0.30	0.03	0.67	0.0180
idl01_usd_grtA9 - 2.d	40720.55	326.19	1.36	0.028	0.0054	0.0013	0.066	0.0044	0.0424	0.0054	0.48	0.025	0.30	0.02	0.67	0.0186
idl01_usd_grtA9 - 3.d	41043.95	367.13	1.41	0.026	0.0021	0.0006	0.056	0.0034	0.0350	0.0029	0.47	0.024	0.31	0.03	0.67	0.0153
idl01_usd_grtA9 - 4.d	40669.59	435.26	1.36	0.026	0.0016	0.0005	0.053	0.0032	0.0314	0.0021	0.44	0.030	0.32	0.02	0.65	0.0150
idl01_usd_grtA9 - 5.d	40981.40	499.54	1.39	0.031	0.0012	0.0005	0.046	0.0034	0.0318	0.0024	0.39	0.023	0.29	0.02	0.66	0.0163
idl01_usd_grtA10 - 1.d	39771.49	415.88	1.67	0.033	0.0021	0.0006	0.032	0.0030	0.0189	0.0023	0.29	0.021	0.25	0.02	0.62	0.0172
idl01_usd_grtA10 - 2.d	39673.91	407.06	1.69	0.030	0.0115	0.0017	0.055	0.0045	0.0274	0.0022	0.38	0.028	0.27	0.02	0.62	0.0165
idl01_usd_grtA10 - 3.d	40232.01	370.07	1.74	0.030	0.0122	0.0015	0.057	0.0032	0.0292	0.0026	0.39	0.031	0.26	0.02	0.64	0.0156
idl01_usd_grtA11 - 1.d	40128.77	438.38	0.73	0.019	0.0025	0.0007	0.051	0.0026	0.0336	0.0025	0.45	0.025	0.35	0.03	0.66	0.0166
idl01_usd_grtA11 - 2.d	40691.49	349.33	0.74	0.016	0.0028	0.0008	0.061	0.0039	0.0371	0.0026	0.50	0.026	0.34	0.02	0.67	0.0150
idl01_usd_grtA11 - 3.d	40942.84	372.70	0.73	0.018	0.0019	0.0007	0.058	0.0038	0.0369	0.0025	0.51	0.030	0.33	0.02	0.67	0.0164
idl01_usd_grtA11 - 4.d	41328.31	505.89	0.74	0.020	0.0030	0.0007	0.065	0.0040	0.0412	0.0030	0.54	0.028	0.33	0.02	0.68	0.0183
idl01_usd_grtA11 - 5.d	40988.94	596.62	0.74	0.019	0.0021	0.0005	0.062	0.0036	0.0405	0.0024	0.53	0.029	0.36	0.03	0.70	0.0162
idl01_usd_grtA11 - 6.d	41750.34	475.40	0.77	0.016	0.0010	0.0004	0.036	0.0027	0.0280	0.0020	0.46	0.026	0.36	0.03	0.67	0.0171
idl01_usd_grtA11 - 7.d	41705.32	569.16	0.74	0.017	0.0016	0.0005	0.045	0.0032	0.0319	0.0022	0.47	0.029	0.35	0.02	0.70	0.0187
idl01_usd_grtA11 - 8.d	41297.77	573.87	0.73	0.018	0.0019	0.0005	0.056	0.0031	0.0363	0.0027	0.51	0.028	0.35	0.02	0.69	0.0170
idl01_usd_grtA11 - 9.d	40707.99	765.90	0.73	0.021	0.0018	0.0006	0.059	0.0037	0.0391	0.0030	0.51	0.028	0.34	0.02	0.69	0.0175
idl01_usd_grtA11 - 10.d	40646.78	738.81	0.73	0.017	0.0026	0.0006	0.066	0.0036	0.0407	0.0025	0.53	0.027	0.35	0.03	0.67	0.0185
idl01_usd_grtA11 - 11.d	41601.28	603.91	0.77	0.017	0.0021	0.0006	0.066	0.0038	0.0420	0.0026	0.57	0.028	0.39	0.03	0.71	0.0143
idl01_usd_grtA11 - 12.d	41216.88	574.67	0.80	0.020	0.0018	0.0006	0.058	0.0043	0.0386	0.0024	0.51	0.030	0.35	0.03	0.70	0.0171
idl01_usd_grtA12 - 1.d	40874.85	364.55	0.76	0.016	0.0037	0.0009	0.072	0.0042	0.0441	0.0028	0.50	0.028	0.37	0.03	0.70	0.0171
idl01_usd_grtA12 - 2.d	41380.85	453.87	0.76	0.018	0.0036	0.0009	0.076	0.0038	0.0435	0.0031	0.52	0.028	0.33	0.02	0.72	0.0184
idl01_usd_grtA12 - 3.d	41582.02	419.04	0.76	0.017	0.0025	0.0007	0.076	0.0044	0.0441	0.0032	0.55	0.028	0.35	0.02	0.72	0.0164
idl01_usd_grtA12 - 4.d	41268.17	553.79	0.74	0.018	0.0034	0.0009	0.080	0.0042	0.0448	0.0028	0.57	0.030	0.34	0.03	0.72	0.0165

Table 3.B.9 LA-ICP-MS Continued

Sample #	Gd	± 2σ	Tb	± 2σ	Dy	± 2σ	Ho	± 2σ	Er	± 2σ	Tm	± 2σ	Yb	± 2σ	Lu	± 2σ
idl01_usd_grtA6 - 4.d	0.3827	0.029	0.051	0.0041	0.22	0.014	0.038	0.0030	0.09	0.009	0.013	0.0020	0.07	0.014	0.016	0.0020
idl01_usd_grtA6 - 5.d	0.3701	0.025	0.047	0.0035	0.25	0.016	0.042	0.0033	0.10	0.009	0.011	0.0016	0.08	0.011	0.011	0.0016
idl01_usd_grtA7 - 1.d	0.3540	0.024	0.057	0.0033	0.34	0.021	0.069	0.0044	0.18	0.014	0.025	0.0028	0.16	0.018	0.027	0.0029
idl01_usd_grtA7 - 2.d	0.3573	0.023	0.059	0.0038	0.35	0.018	0.070	0.0054	0.17	0.011	0.025	0.0028	0.17	0.016	0.028	0.0030
idl01_usd_grtA7 - 3.d	0.3636	0.024	0.058	0.0040	0.35	0.020	0.067	0.0049	0.18	0.011	0.024	0.0025	0.19	0.017	0.026	0.0024
idl01_usd_grtA7 - 4.d	0.3413	0.025	0.060	0.0042	0.32	0.020	0.067	0.0043	0.16	0.011	0.023	0.0021	0.17	0.016	0.027	0.0025
idl01_usd_grtA7 - 5.d	0.3778	0.024	0.056	0.0043	0.34	0.018	0.066	0.0042	0.18	0.011	0.025	0.0021	0.19	0.020	0.028	0.0025
idl01_usd_grtA7 - 6.d	0.3590	0.025	0.053	0.0034	0.34	0.020	0.066	0.0042	0.17	0.013	0.025	0.0022	0.17	0.017	0.030	0.0024
idl01_usd_grtA8 - 1.d	0.3149	0.025	0.045	0.0036	0.27	0.018	0.057	0.0040	0.19	0.011	0.028	0.0031	0.25	0.020	0.042	0.0035
idl01_usd_grtA8 - 2.d	0.3455	0.024	0.048	0.0039	0.30	0.018	0.064	0.0048	0.18	0.012	0.029	0.0028	0.25	0.025	0.049	0.0040
idl01_usd_grtA9 - 1.d	0.3762	0.026	0.052	0.0042	0.27	0.019	0.053	0.0036	0.12	0.010	0.017	0.0020	0.13	0.015	0.019	0.0023
idl01_usd_grtA9 - 2.d	0.3791	0.027	0.054	0.0039	0.30	0.022	0.050	0.0034	0.13	0.011	0.017	0.0022	0.13	0.015	0.021	0.0022
idl01_usd_grtA9 - 3.d	0.3624	0.025	0.050	0.0038	0.29	0.017	0.049	0.0037	0.12	0.011	0.017	0.0020	0.12	0.014	0.023	0.0023
idl01_usd_grtA9 - 4.d	0.3793	0.025	0.056	0.0039	0.27	0.018	0.051	0.0032	0.13	0.010	0.018	0.0021	0.13	0.016	0.020	0.0025
idl01_usd_grtA9 - 5.d	0.3732	0.026	0.052	0.0036	0.29	0.020	0.048	0.0040	0.14	0.010	0.020	0.0022	0.14	0.015	0.024	0.0026
idl01_usd_grtA10 - 1.d	0.3229	0.024	0.047	0.0039	0.29	0.018	0.061	0.0046	0.19	0.013	0.032	0.0034	0.26	0.022	0.053	0.0034
idl01_usd_grtA10 - 2.d	0.3282	0.023	0.052	0.0041	0.28	0.019	0.057	0.0049	0.21	0.015	0.033	0.0027	0.29	0.024	0.050	0.0036
idl01_usd_grtA10 - 3.d	0.3525	0.025	0.054	0.0039	0.30	0.018	0.069	0.0044	0.20	0.013	0.032	0.0029	0.28	0.021	0.054	0.0042
idl01_usd_grtA11 - 1.d	0.3236	0.024	0.039	0.0035	0.18	0.015	0.026	0.0029	0.06	0.008	0.006	0.0013	0.05	0.009	0.009	0.0015
idl01_usd_grtA11 - 2.d	0.3619	0.023	0.040	0.0036	0.18	0.014	0.025	0.0025	0.06	0.006	0.007	0.0012	0.04	0.007	0.010	0.0014
idl01_usd_grtA11 - 3.d	0.3443	0.026	0.041	0.0028	0.17	0.012	0.025	0.0028	0.06	0.008	0.007	0.0012	0.05	0.006	0.009	0.0014
idl01_usd_grtA11 - 4.d	0.3540	0.028	0.040	0.0033	0.18	0.014	0.026	0.0026	0.06	0.006	0.007	0.0012	0.05	0.011	0.008	0.0014
idl01_usd_grtA11 - 5.d	0.3579	0.027	0.039	0.0030	0.17	0.014	0.028	0.0025	0.05	0.007	0.005	0.0011	0.06	0.010	0.009	0.0016
idl01_usd_grtA11 - 6.d	0.3508	0.023	0.041	0.0034	0.19	0.013	0.027	0.0023	0.06	0.006	0.006	0.0012	0.05	0.010	0.009	0.0015
idl01_usd_grtA11 - 7.d	0.3665	0.022	0.041	0.0029	0.16	0.010	0.025	0.0027	0.05	0.006	0.006	0.0013	0.05	0.009	0.010	0.0017
idl01_usd_grtA11 - 8.d	0.3521	0.022	0.038	0.0034	0.17	0.014	0.026	0.0026	0.06	0.007	0.007	0.0011	0.05	0.009	0.009	0.0015
idl01_usd_grtA11 - 9.d	0.3455	0.024	0.037	0.0033	0.17	0.012	0.024	0.0021	0.06	0.006	0.006	0.0012	0.06	0.008	0.009	0.0014
idl01_usd_grtA11 - 10.d	0.3448	0.022	0.038	0.0028	0.17	0.012	0.029	0.0027	0.05	0.006	0.007	0.0012	0.05	0.007	0.009	0.0013
idl01_usd_grtA11 - 11.d	0.3496	0.023	0.041	0.0033	0.18	0.014	0.025	0.0024	0.06	0.007	0.008	0.0014	0.05	0.008	0.010	0.0017
idl01_usd_grtA11 - 12.d	0.3515	0.026	0.041	0.0028	0.18	0.013	0.027	0.0030	0.06	0.006	0.006	0.0011	0.05	0.009	0.009	0.0013
idl01_usd_grtA12 - 1.d	0.3438	0.024	0.039	0.0034	0.19	0.014	0.027	0.0031	0.06	0.008	0.007	0.0013	0.04	0.009	0.010	0.0018
idl01_usd_grtA12 - 2.d	0.3479	0.027	0.041	0.0034	0.17	0.012	0.027	0.0025	0.07	0.006	0.007	0.0013	0.04	0.007	0.010	0.0018
idl01_usd_grtA12 - 3.d	0.3720	0.024	0.042	0.0035	0.18	0.013	0.028	0.0026	0.06	0.007	0.007	0.0013	0.05	0.008	0.009	0.0016
idl01_usd_grtA12 - 4.d	0.3767	0.025	0.041	0.0034	0.18	0.014	0.027	0.0022	0.05	0.007	0.007	0.0013	0.05	0.008	0.009	0.0014

Table 3.B.9 LA-ICP-MS Continued

Sample #	Ca	± 2σ	Y	± 2σ	La	± 2σ	Ce	± 2σ	Pr	± 2σ	Nd	± 2σ	Sm	± 2σ	Eu	± 2σ
idl01_usd_grtA13 - 1.d	40690.09	400.67	1.55	0.032	0.0039	0.0009	0.069	0.0043	0.0395	0.0030	0.53	0.032	0.30	0.02	0.67	0.0174
idl01_usd_grtA13 - 2.d	41306.66	344.52	1.62	0.028	0.0033	0.0008	0.085	0.0040	0.0441	0.0028	0.51	0.031	0.30	0.02	0.68	0.0168
idl01_usd_grtA13 - 3.d	41384.00	448.87	1.63	0.030	0.0023	0.0007	0.086	0.0042	0.0406	0.0030	0.49	0.030	0.28	0.02	0.68	0.0161
idl01_usd_grtA13 - 4.d	41677.41	431.52	1.66	0.029	0.0036	0.0008	0.077	0.0035	0.0437	0.0031	0.52	0.029	0.31	0.02	0.70	0.0192
idl01_usd_grtA13 - 5.d	41605.79	425.46	1.56	0.030	0.0018	0.0005	0.060	0.0038	0.0375	0.0025	0.48	0.031	0.29	0.02	0.68	0.0170
idl01_usd_grtA13 - 6.d	41464.70	466.70	1.58	0.030	0.0022	0.0007	0.070	0.0041	0.0423	0.0030	0.50	0.028	0.30	0.02	0.68	0.0167
idl01_usd_grtA13 - 7.d	41278.54	497.80	1.61	0.030	0.0015	0.0006	0.068	0.0033	0.0387	0.0025	0.51	0.028	0.29	0.02	0.69	0.0151
idl01_usd_grtA13 - 8.d	41194.99	519.67	1.63	0.029	0.0020	0.0006	0.064	0.0034	0.0383	0.0026	0.46	0.028	0.29	0.02	0.68	0.0168
idl01_usd_grtA14 - 1.d	40607.53	509.89	1.70	0.035	0.0023	0.0007	0.044	0.0030	0.0290	0.0023	0.41	0.026	0.30	0.02	0.62	0.0164
idl01_usd_grtA15 - 1.d	39786.98	438.50	1.53	0.027	0.0009	0.0004	0.038	0.0026	0.0273	0.0022	0.37	0.031	0.26	0.02	0.62	0.0169
idl01_usd_grtA15 - 2.d	41169.63	437.15	1.64	0.036	0.0012	0.0006	0.041	0.0038	0.0318	0.0022	0.43	0.027	0.30	0.02	0.67	0.0163
idl01_usd_grtA15 - 3.d	41895.84	400.38	1.72	0.034	0.0037	0.0011	0.048	0.0034	0.0346	0.0030	0.45	0.031	0.27	0.02	0.70	0.0185
idl01_usd_grtA15 - 4.d	41771.32	418.45	1.71	0.031	0.0017	0.0006	0.048	0.0035	0.0351	0.0022	0.44	0.026	0.29	0.03	0.70	0.0148
idl01_usd_grtA16 - 1.d	40764.04	414.97	1.70	0.032	0.0012	0.0005	0.024	0.0024	0.0185	0.0018	0.30	0.020	0.27	0.03	0.62	0.0154
idl01_usd_grtA16 - 2.d	41734.27	388.01	1.76	0.031	0.0009	0.0004	0.028	0.0026	0.0222	0.0019	0.35	0.025	0.29	0.03	0.63	0.0157
idl01_usd_grtA16 - 3.d	41107.18	509.02	1.84	0.038	0.0007	0.0003	0.026	0.0026	0.0237	0.0023	0.35	0.024	0.29	0.02	0.66	0.0145
idl01_usd_grtA16 - 4.d	41566.37	459.83	1.84	0.034	0.0005	0.0003	0.019	0.0019	0.0192	0.0016	0.34	0.027	0.26	0.02	0.65	0.0164
idl02_usd_grtA17 - 1.d	40777.53	360.53	1.18	0.027	0.0011	0.0005	0.046	0.0040	0.0335	0.0025	0.46	0.026	0.30	0.03	0.66	0.0156
idl02_usd_grtA17 - 2.d	40997.84	371.80	1.18	0.024	0.0020	0.0006	0.052	0.0034	0.0364	0.0025	0.47	0.028	0.31	0.02	0.70	0.0148
idl02_usd_grtA17 - 3.d	41492.86	429.84	1.22	0.028	0.0021	0.0006	0.064	0.0039	0.0396	0.0029	0.49	0.022	0.30	0.03	0.70	0.0162
idl02_usd_grtA17 - 4.d	41771.51	433.90	1.25	0.026	0.0018	0.0006	0.066	0.0038	0.0392	0.0031	0.50	0.027	0.34	0.02	0.70	0.0162
idl02_usd_grtA17 - 5.d	41213.63	458.81	1.28	0.026	0.0017	0.0006	0.062	0.0030	0.0399	0.0034	0.52	0.029	0.31	0.02	0.70	0.0167
idl02_usd_grtA17 - 6.d	41618.75	449.72	1.31	0.024	0.0030	0.0007	0.068	0.0042	0.0414	0.0028	0.52	0.028	0.33	0.03	0.71	0.0191
idl02_usd_grtA17 - 7.d	41474.42	414.31	1.35	0.031	0.0026	0.0007	0.067	0.0040	0.0394	0.0028	0.47	0.024	0.31	0.02	0.68	0.0154
idl02_usd_grtA18 - 1.d	40395.85	461.84	1.78	0.034	0.0022	0.0007	0.054	0.0040	0.0347	0.0027	0.46	0.027	0.28	0.02	0.65	0.0146
idl02_usd_grtA18 - 2.d	40955.67	366.47	1.85	0.033	0.0019	0.0006	0.052	0.0027	0.0351	0.0026	0.45	0.025	0.31	0.02	0.67	0.0174
idl02_usd_grtA18 - 3.d	41413.26	378.72	1.89	0.030	0.0015	0.0005	0.054	0.0033	0.0346	0.0024	0.46	0.024	0.31	0.02	0.68	0.0163
idl02_usd_grtA18 - 4.d	41228.22	545.08	1.86	0.035	0.0015	0.0006	0.044	0.0034	0.0306	0.0024	0.42	0.022	0.30	0.02	0.66	0.0182
idl02_usd_grtA19 - 1.d	40516.55	394.82	1.67	0.024	0.0019	0.0006	0.050	0.0036	0.0316	0.0025	0.44	0.029	0.28	0.02	0.66	0.0138
idl02_usd_grtA19 - 2.d	40949.42	418.68	1.67	0.032	0.0013	0.0005	0.041	0.0034	0.0298	0.0024	0.43	0.028	0.29	0.02	0.68	0.0189
idl02_usd_grtA19 - 3.d	40816.39	389.41	1.70	0.033	0.0088	0.0012	0.052	0.0032	0.0240	0.0017	0.35	0.022	0.25	0.02	0.62	0.0148
idl02_usd_grtA19 - 4.d	41486.54	426.70	1.76	0.032	0.0035	0.0010	0.059	0.0036	0.0363	0.0026	0.48	0.027	0.28	0.02	0.68	0.0175
idl02_usd_grtA20 - 1.d	39675.88	456.39	1.92	0.034	0.0007	0.0004	0.027	0.0023	0.0207	0.0021	0.34	0.025	0.28	0.03	0.60	0.0186
idl02_usd_grtA20 - 2.d	40462.80	373.12	1.95	0.038	0.0008	0.0004	0.029	0.0022	0.0215	0.0020	0.38	0.018	0.28	0.02	0.63	0.0148

Table 3.B.9 LA-ICP-MS Continued

Sample #	Gd	± 2σ	Tb	± 2σ	Dy	± 2σ	Ho	± 2σ	Er	± 2σ	Tm	± 2σ	Yb	± 2σ	Lu	± 2σ
idl01_usd_grtA13 - 1.d	0.3434	0.026	0.051	0.0034	0.29	0.020	0.059	0.0045	0.16	0.012	0.025	0.0023	0.19	0.019	0.037	0.0031
idl01_usd_grtA13 - 2.d	0.3362	0.026	0.054	0.0039	0.31	0.016	0.060	0.0040	0.18	0.012	0.028	0.0025	0.21	0.019	0.041	0.0035
idl01_usd_grtA13 - 3.d	0.3541	0.022	0.053	0.0043	0.29	0.017	0.058	0.0033	0.17	0.012	0.028	0.0030	0.24	0.021	0.039	0.0033
idl01_usd_grtA13 - 4.d	0.3300	0.022	0.050	0.0031	0.30	0.021	0.061	0.0036	0.19	0.012	0.028	0.0026	0.24	0.020	0.040	0.0030
idl01_usd_grtA13 - 5.d	0.3671	0.028	0.052	0.0037	0.30	0.017	0.059	0.0039	0.16	0.011	0.026	0.0029	0.19	0.017	0.034	0.0028
idl01_usd_grtA13 - 6.d	0.3405	0.023	0.050	0.0033	0.30	0.019	0.059	0.0037	0.18	0.012	0.024	0.0020	0.21	0.016	0.038	0.0032
idl01_usd_grtA13 - 7.d	0.3267	0.021	0.052	0.0037	0.29	0.017	0.058	0.0039	0.18	0.012	0.027	0.0023	0.21	0.017	0.038	0.0032
idl01_usd_grtA13 - 8.d	0.3423	0.025	0.050	0.0031	0.32	0.018	0.056	0.0035	0.18	0.012	0.031	0.0029	0.23	0.019	0.041	0.0033
idl01_usd_grtA14 - 1.d	0.3154	0.025	0.050	0.0041	0.31	0.020	0.061	0.0046	0.19	0.013	0.033	0.0031	0.28	0.022	0.049	0.0039
idl01_usd_grtA15 - 1.d	0.3324	0.025	0.054	0.0034	0.29	0.015	0.058	0.0043	0.16	0.011	0.024	0.0027	0.18	0.014	0.031	0.0030
idl01_usd_grtA15 - 2.d	0.3597	0.026	0.051	0.0039	0.31	0.021	0.061	0.0042	0.17	0.011	0.024	0.0026	0.20	0.018	0.032	0.0027
idl01_usd_grtA15 - 3.d	0.3674	0.025	0.053	0.0038	0.31	0.018	0.059	0.0042	0.18	0.012	0.025	0.0024	0.20	0.019	0.032	0.0031
idl01_usd_grtA15 - 4.d	0.3581	0.029	0.054	0.0040	0.32	0.018	0.060	0.0046	0.18	0.013	0.028	0.0030	0.19	0.015	0.035	0.0031
idl01_usd_grtA16 - 1.d	0.3087	0.023	0.045	0.0035	0.29	0.015	0.066	0.0047	0.21	0.013	0.035	0.0028	0.31	0.024	0.060	0.0043
idl01_usd_grtA16 - 2.d	0.3176	0.023	0.044	0.0030	0.29	0.017	0.066	0.0038	0.22	0.012	0.038	0.0029	0.34	0.025	0.066	0.0039
idl01_usd_grtA16 - 3.d	0.3114	0.025	0.046	0.0036	0.29	0.020	0.069	0.0046	0.25	0.014	0.044	0.0034	0.36	0.023	0.073	0.0046
idl01_usd_grtA16 - 4.d	0.2985	0.023	0.047	0.0036	0.31	0.019	0.074	0.0049	0.24	0.015	0.043	0.0037	0.37	0.028	0.071	0.0048
idl02_usd_grtA17 - 1.d	0.3753	0.026	0.056	0.0039	0.27	0.016	0.044	0.0040	0.10	0.008	0.011	0.0019	0.07	0.011	0.010	0.0018
idl02_usd_grtA17 - 2.d	0.3884	0.028	0.056	0.0040	0.26	0.016	0.041	0.0036	0.09	0.008	0.010	0.0015	0.07	0.011	0.010	0.0017
idl02_usd_grtA17 - 3.d	0.3805	0.023	0.057	0.0044	0.28	0.018	0.041	0.0037	0.08	0.008	0.009	0.0015	0.06	0.009	0.011	0.0018
idl02_usd_grtA17 - 4.d	0.3839	0.027	0.058	0.0040	0.28	0.021	0.047	0.0036	0.09	0.009	0.011	0.0018	0.07	0.011	0.011	0.0016
idl02_usd_grtA17 - 5.d	0.3906	0.029	0.060	0.0044	0.29	0.016	0.045	0.0037	0.09	0.010	0.010	0.0016	0.06	0.011	0.011	0.0017
idl02_usd_grtA17 - 6.d	0.4014	0.022	0.062	0.0036	0.31	0.017	0.045	0.0036	0.10	0.010	0.010	0.0015	0.07	0.011	0.012	0.0016
idl02_usd_grtA17 - 7.d	0.4067	0.027	0.059	0.0040	0.31	0.018	0.049	0.0036	0.10	0.009	0.012	0.0019	0.06	0.011	0.010	0.0017
idl02_usd_grtA18 - 1.d	0.3543	0.029	0.055	0.0034	0.32	0.019	0.065	0.0048	0.20	0.013	0.030	0.0028	0.22	0.023	0.047	0.0043
idl02_usd_grtA18 - 2.d	0.3684	0.032	0.059	0.0042	0.34	0.018	0.064	0.0038	0.19	0.013	0.033	0.0026	0.25	0.020	0.045	0.0037
idl02_usd_grtA18 - 3.d	0.3589	0.021	0.057	0.0034	0.34	0.020	0.070	0.0043	0.20	0.015	0.030	0.0028	0.26	0.020	0.044	0.0034
idl02_usd_grtA18 - 4.d	0.3462	0.026	0.053	0.0035	0.35	0.019	0.069	0.0037	0.19	0.012	0.031	0.0030	0.25	0.023	0.044	0.0036
idl02_usd_grtA19 - 1.d	0.3399	0.028	0.052	0.0036	0.30	0.017	0.066	0.0043	0.19	0.013	0.028	0.0028	0.28	0.027	0.045	0.0031
idl02_usd_grtA19 - 2.d	0.3473	0.023	0.051	0.0036	0.31	0.018	0.062	0.0040	0.19	0.014	0.029	0.0027	0.26	0.023	0.048	0.0038
idl02_usd_grtA19 - 3.d	0.3330	0.021	0.054	0.0033	0.34	0.020	0.058	0.0040	0.20	0.013	0.034	0.0026	0.24	0.021	0.046	0.0034
idl02_usd_grtA19 - 4.d	0.3675	0.026	0.053	0.0033	0.33	0.020	0.064	0.0042	0.20	0.013	0.032	0.0030	0.27	0.023	0.052	0.0036
idl02_usd_grtA20 - 1.d	0.3350	0.025	0.054	0.0042	0.36	0.022	0.068	0.0047	0.20	0.013	0.029	0.0028	0.21	0.020	0.037	0.0031
idl02_usd_grtA20 - 2.d	0.3573	0.024	0.058	0.0045	0.34	0.020	0.070	0.0049	0.20	0.012	0.026	0.0025	0.22	0.020	0.040	0.0036

Table 3.B.9 LA-ICP-MS Continued

Sample #	Ca	± 2σ	Y	± 2σ	La	± 2σ	Ce	± 2σ	Pr	± 2σ	Nd	± 2σ	Sm	± 2σ	Eu	± 2σ
idl02_usd_grtA21 - 1.d	39517.52	336.44	1.73	0.029	0.0106	0.0017	0.025	0.0027	0.0073	0.0011	0.14	0.017	0.21	0.02	0.51	0.0140
idl02_usd_grtA21 - 2.d	40524.01	439.12	1.80	0.036	0.0054	0.0010	0.014	0.0020	0.0073	0.0010	0.19	0.017	0.26	0.02	0.58	0.0161
idl02_usd_grtA22 - 1.d	34256.52	1445.43	1.38	0.095	0.3284	0.0488	0.576	0.0800	0.0668	0.0094	0.33	0.031	0.19	0.02	0.38	0.0408
idl02_usd_grtA22 - 2.d	40810.32	347.40	1.63	0.027	0.0114	0.0018	0.036	0.0035	0.0174	0.0021	0.29	0.021	0.25	0.03	0.61	0.0170
idl02_usd_grtA22 - 3.d	41039.27	439.45	1.67	0.034	0.0014	0.0005	0.023	0.0021	0.0203	0.0017	0.34	0.024	0.27	0.02	0.64	0.0172
idl02_usd_grtA22 - 4.d	41182.80	485.69	1.72	0.034	0.0058	0.0013	0.033	0.0025	0.0176	0.0017	0.32	0.023	0.25	0.02	0.64	0.0185
idl02_usd_grtA23 - 1.d	41234.56	427.69	1.61	0.031	0.0013	0.0005	0.038	0.0035	0.0280	0.0023	0.44	0.032	0.30	0.02	0.63	0.0152
idl02_usd_grtA23 - 2.d	41485.68	413.36	1.69	0.029	0.0020	0.0006	0.051	0.0036	0.0320	0.0023	0.45	0.030	0.31	0.02	0.66	0.0148
idl02_usd_grtA23 - 3.d	41720.81	401.07	1.73	0.037	0.0018	0.0006	0.047	0.0034	0.0316	0.0023	0.48	0.026	0.32	0.03	0.67	0.0157
idl02_usd_grtA23 - 4.d	42179.67	273.60	1.77	0.028	0.0007	0.0003	0.040	0.0029	0.0296	0.0023	0.46	0.026	0.32	0.02	0.69	0.0164
idl02_usd_grtA23 - 5.d	41847.11	392.38	1.71	0.026	0.0015	0.0005	0.042	0.0029	0.0342	0.0027	0.47	0.025	0.32	0.02	0.68	0.0150
idl02_usd_grtA23 - 6.d	42018.82	399.37	1.69	0.030	0.0019	0.0006	0.053	0.0039	0.0341	0.0024	0.48	0.027	0.32	0.02	0.68	0.0158
idl02_usd_grtA24 - 1.d	40966.16	384.49	0.79	0.019	0.0018	0.0005	0.046	0.0030	0.0363	0.0025	0.50	0.032	0.34	0.02	0.71	0.0179
idl02_usd_grtA24 - 2.d	41274.02	419.08	0.81	0.019	0.0018	0.0006	0.051	0.0032	0.0399	0.0031	0.51	0.029	0.38	0.03	0.73	0.0163
idl02_usd_grtA24 - 3.d	41674.91	370.74	0.81	0.018	0.0019	0.0007	0.053	0.0034	0.0369	0.0026	0.52	0.029	0.37	0.02	0.73	0.0173
idl02_usd_grtA24 - 4.d	42093.80	394.90	0.84	0.021	0.0021	0.0007	0.068	0.0191	0.0394	0.0026	0.56	0.034	0.40	0.03	0.76	0.0150
idl02_usd_grtA24 - 5.d	42276.94	355.31	0.86	0.018	0.0044	0.0010	0.071	0.0044	0.0404	0.0028	0.57	0.026	0.38	0.02	0.77	0.0188
idl02_usd_grtA24 - 6.d	41718.58	409.37	0.85	0.016	0.0101	0.0116	0.073	0.0036	0.0427	0.0027	0.59	0.027	0.38	0.03	0.76	0.0190
idl02_usd_grtA24 - 7.d	41498.80	419.88	0.84	0.021	0.0025	0.0006	0.073	0.0037	0.0438	0.0028	0.55	0.028	0.38	0.03	0.75	0.0169
idl02_usd_grtA24 - 8.d	41112.06	722.01	0.84	0.018	0.0025	0.0008	0.067	0.0037	0.0413	0.0021	0.57	0.030	0.39	0.02	0.76	0.0197
idl02_usd_grtA25 - 1.d	41596.91	405.52	1.55	0.032	0.0018	0.0006	0.039	0.0029	0.0292	0.0024	0.45	0.025	0.32	0.02	0.63	0.0163
idl02_usd_grtA25 - 2.d	41528.42	328.99	1.54	0.025	0.0011	0.0005	0.038	0.0028	0.0302	0.0021	0.41	0.028	0.36	0.03	0.64	0.0155
idl02_usd_grtA25 - 3.d	41840.07	376.65	1.54	0.025	0.0030	0.0009	0.036	0.0033	0.0281	0.0022	0.41	0.026	0.34	0.02	0.66	0.0155
idl02_usd_grtA25 - 4.d	41332.79	526.28	1.47	0.026	0.0006	0.0003	0.038	0.0030	0.0305	0.0024	0.46	0.027	0.36	0.03	0.66	0.0172
idl02_usd_grtA25 - 5.d	41802.17	430.34	1.44	0.027	0.0025	0.0007	0.045	0.0037	0.0338	0.0028	0.50	0.033	0.36	0.02	0.69	0.0173
idl02_usd_grtA25 - 6.d	41998.89	432.83	1.41	0.026	0.0007	0.0004	0.044	0.0034	0.0343	0.0025	0.47	0.029	0.37	0.02	0.71	0.0181
idl02_usd_grtA25 - 7.d	41831.32	436.58	1.42	0.029	0.0014	0.0005	0.046	0.0033	0.0355	0.0027	0.49	0.028	0.39	0.03	0.70	0.0153
idl02_usd_grtA25 - 8.d	42022.89	363.63	1.41	0.023	0.0023	0.0008	0.051	0.0040	0.0352	0.0021	0.48	0.029	0.38	0.03	0.70	0.0166
idl02_usd_grtA25 - 9.d	41771.64	451.65	1.39	0.027	0.0018	0.0006	0.039	0.0028	0.0338	0.0025	0.48	0.028	0.35	0.03	0.67	0.0145
idl02_usd_grtA25 - 10.d	41749.15	424.51	1.41	0.027	0.0012	0.0005	0.050	0.0033	0.0334	0.0027	0.47	0.026	0.35	0.02	0.69	0.0164
idl02_usd_grtA25 - 11.d	41931.07	362.71	1.42	0.024	0.0048	0.0009	0.043	0.0033	0.0300	0.0024	0.46	0.029	0.38	0.02	0.68	0.0162
idl02_usd_grtA25 - 12.d	42034.71	427.64	1.43	0.029	0.0041	0.0008	0.030	0.0029	0.0223	0.0018	0.42	0.026	0.37	0.02	0.66	0.0166
idl02_usd_grtA25 - 13.d	41437.89	358.88	1.43	0.027	0.0052	0.0010	0.031	0.0026	0.0225	0.0022	0.38	0.026	0.35	0.03	0.65	0.0165
idl02_usd_grtA25 - 14.d	41106.89	460.28	1.45	0.027	0.0090	0.0014	0.028	0.0028	0.0173	0.0018	0.32	0.026	0.35	0.02	0.64	0.0177

Table 3.B.9 LA-ICP-MS Continued

Sample #	Gd	± 2σ	Tb	± 2σ	Dy	± 2σ	Ho	± 2σ	Er	± 2σ	Tm	± 2σ	Yb	± 2σ	Lu	± 2σ
idl02_usd_grtA21 - 1.d	0.3402	0.027	0.054	0.0033	0.33	0.020	0.064	0.0037	0.18	0.011	0.026	0.0026	0.24	0.021	0.045	0.0033
idl02_usd_grtA21 - 2.d	0.3566	0.027	0.056	0.0039	0.32	0.020	0.066	0.0045	0.20	0.012	0.032	0.0027	0.25	0.023	0.044	0.0038
idl02_usd_grtA22 - 1.d	0.2516	0.032	0.039	0.0051	0.24	0.025	0.052	0.0051	0.14	0.013	0.022	0.0026	0.19	0.017	0.032	0.0033
idl02_usd_grtA22 - 2.d	0.3068	0.024	0.044	0.0034	0.28	0.019	0.063	0.0037	0.19	0.013	0.033	0.0029	0.28	0.020	0.054	0.0045
idl02_usd_grtA22 - 3.d	0.3277	0.021	0.049	0.0034	0.28	0.015	0.062	0.0042	0.20	0.013	0.032	0.0030	0.30	0.021	0.059	0.0036
idl02_usd_grtA22 - 4.d	0.3297	0.023	0.050	0.0036	0.30	0.019	0.066	0.0049	0.20	0.012	0.035	0.0030	0.31	0.022	0.055	0.0035
idl02_usd_grtA23 - 1.d	0.2934	0.018	0.041	0.0036	0.27	0.016	0.062	0.0040	0.19	0.012	0.027	0.0025	0.22	0.019	0.036	0.0032
idl02_usd_grtA23 - 2.d	0.3269	0.020	0.045	0.0035	0.26	0.019	0.065	0.0043	0.19	0.014	0.030	0.0032	0.24	0.020	0.033	0.0031
idl02_usd_grtA23 - 3.d	0.3285	0.022	0.047	0.0033	0.28	0.016	0.064	0.0035	0.19	0.015	0.030	0.0027	0.23	0.020	0.037	0.0036
idl02_usd_grtA23 - 4.d	0.3233	0.022	0.047	0.0038	0.28	0.017	0.066	0.0043	0.20	0.012	0.028	0.0025	0.22	0.020	0.036	0.0032
idl02_usd_grtA23 - 5.d	0.3332	0.026	0.044	0.0029	0.28	0.020	0.062	0.0037	0.19	0.015	0.032	0.0029	0.24	0.019	0.036	0.0031
idl02_usd_grtA23 - 6.d	0.3413	0.026	0.039	0.0033	0.28	0.020	0.063	0.0036	0.20	0.014	0.029	0.0031	0.22	0.019	0.038	0.0031
idl02_usd_grtA24 - 1.d	0.3729	0.023	0.043	0.0033	0.18	0.014	0.029	0.0028	0.06	0.007	0.006	0.0012	0.04	0.009	0.007	0.0016
idl02_usd_grtA24 - 2.d	0.3705	0.023	0.042	0.0034	0.19	0.013	0.027	0.0028	0.06	0.007	0.008	0.0014	0.04	0.007	0.007	0.0015
idl02_usd_grtA24 - 3.d	0.3710	0.024	0.045	0.0035	0.19	0.012	0.030	0.0032	0.07	0.007	0.008	0.0014	0.04	0.008	0.008	0.0013
idl02_usd_grtA24 - 4.d	0.3716	0.026	0.043	0.0039	0.19	0.012	0.030	0.0030	0.06	0.007	0.007	0.0011	0.05	0.009	0.008	0.0013
idl02_usd_grtA24 - 5.d	0.3701	0.022	0.044	0.0032	0.20	0.013	0.029	0.0030	0.07	0.008	0.007	0.0014	0.05	0.009	0.009	0.0016
idl02_usd_grtA24 - 6.d	0.3797	0.024	0.044	0.0036	0.18	0.015	0.029	0.0023	0.06	0.006	0.007	0.0012	0.06	0.009	0.010	0.0016
idl02_usd_grtA24 - 7.d	0.4134	0.028	0.044	0.0033	0.20	0.013	0.033	0.0028	0.07	0.008	0.008	0.0014	0.06	0.009	0.008	0.0013
idl02_usd_grtA24 - 8.d	0.3925	0.025	0.044	0.0032	0.19	0.014	0.030	0.0030	0.06	0.007	0.006	0.0012	0.05	0.007	0.009	0.0014
idl02_usd_grtA25 - 1.d	0.5474	0.035	0.075	0.0043	0.39	0.023	0.057	0.0038	0.12	0.010	0.012	0.0018	0.08	0.011	0.015	0.0019
idl02_usd_grtA25 - 2.d	0.5554	0.037	0.077	0.0047	0.37	0.019	0.060	0.0037	0.11	0.009	0.015	0.0020	0.09	0.011	0.014	0.0019
idl02_usd_grtA25 - 3.d	0.5269	0.031	0.080	0.0046	0.37	0.021	0.058	0.0035	0.13	0.012	0.012	0.0018	0.08	0.011	0.013	0.0018
idl02_usd_grtA25 - 4.d	0.5021	0.027	0.072	0.0041	0.36	0.020	0.051	0.0042	0.12	0.011	0.012	0.0017	0.09	0.012	0.014	0.0019
idl02_usd_grtA25 - 5.d	0.5298	0.034	0.077	0.0048	0.36	0.018	0.053	0.0047	0.11	0.009	0.012	0.0017	0.08	0.011	0.015	0.0019
idl02_usd_grtA25 - 6.d	0.5359	0.030	0.071	0.0043	0.36	0.021	0.051	0.0035	0.11	0.009	0.014	0.0018	0.09	0.010	0.014	0.0022
idl02_usd_grtA25 - 7.d	0.5655	0.030	0.076	0.0041	0.35	0.019	0.053	0.0042	0.12	0.010	0.012	0.0017	0.09	0.012	0.018	0.0021
idl02_usd_grtA25 - 8.d	0.5492	0.030	0.074	0.0046	0.35	0.020	0.051	0.0035	0.11	0.009	0.010	0.0017	0.08	0.012	0.015	0.0021
idl02_usd_grtA25 - 9.d	0.5157	0.032	0.070	0.0040	0.33	0.018	0.050	0.0036	0.11	0.010	0.011	0.0016	0.09	0.012	0.016	0.0019
idl02_usd_grtA25 - 10.d	0.5225	0.033	0.073	0.0040	0.34	0.019	0.050	0.0037	0.10	0.008	0.012	0.0018	0.08	0.013	0.017	0.0022
idl02_usd_grtA25 - 11.d	0.5174	0.031	0.072	0.0037	0.34	0.019	0.052	0.0033	0.10	0.009	0.013	0.0016	0.08	0.012	0.015	0.0020
idl02_usd_grtA25 - 12.d	0.5409	0.035	0.076	0.0045	0.34	0.019	0.054	0.0037	0.10	0.008	0.013	0.0017	0.09	0.012	0.015	0.0019
idl02_usd_grtA25 - 13.d	0.5366	0.032	0.076	0.0053	0.35	0.019	0.050	0.0040	0.10	0.008	0.012	0.0016	0.09	0.012	0.014	0.0016
idl02_usd_grtA25 - 14.d	0.5295	0.031	0.075	0.0044	0.37	0.017	0.053	0.0033	0.10	0.010	0.012	0.0016	0.09	0.012	0.016	0.0020

Table 3.B.9 LA-ICP-MS Continued

Sample #	Ca	± 2σ	Y	± 2σ	La	± 2σ	Ce	± 2σ	Pr	± 2σ	Nd	± 2σ	Sm	± 2σ	Eu	± 2σ
idl02_usd_grtA25 - 15.d	41226.84	376.20	1.45	0.023	0.0128	0.0016	0.035	0.0026	0.0179	0.0019	0.33	0.024	0.38	0.02	0.63	0.0161
idl02_usd_grtA25 - 16.d	40723.79	399.59	1.42	0.026	0.0028	0.0007	0.014	0.0016	0.0139	0.0014	0.31	0.020	0.31	0.02	0.62	0.0155
idl02_usd_grtA25 - 17.d	40905.35	391.84	1.43	0.029	0.0014	0.0005	0.014	0.0015	0.0152	0.0017	0.32	0.023	0.36	0.02	0.61	0.0166
idl02_usd_grtA25 - 18.d	39675.36	444.88	1.46	0.022	0.0004	0.0003	0.012	0.0014	0.0134	0.0017	0.27	0.019	0.33	0.03	0.61	0.0178
idl02_usd_grtA26 - 1.d	40818.16	419.02	1.45	0.027	0.0010	0.0004	0.031	0.0023	0.0234	0.0019	0.40	0.028	0.31	0.02	0.59	0.0157
idl02_usd_grtA26 - 2.d	40957.14	398.94	1.51	0.024	0.0012	0.0005	0.035	0.0021	0.0241	0.0024	0.39	0.025	0.33	0.02	0.62	0.0152
idl02_usd_grtA27 - 1.d	40702.70	432.21	1.47	0.028	0.0033	0.0009	0.062	0.0039	0.0374	0.0023	0.44	0.030	0.30	0.02	0.65	0.0175
idl02_usd_grtA27 - 2.d	41045.22	376.47	1.48	0.028	0.0032	0.0008	0.073	0.0044	0.0446	0.0034	0.54	0.030	0.30	0.03	0.69	0.0151

Table 3.B.9 LA-ICP-MS Continued

Sample #	Gd	± 2σ	Tb	± 2σ	Dy	± 2σ	Ho	± 2σ	Er	± 2σ	Tm	± 2σ	Yb	± 2σ	Lu	± 2σ
idl02_usd_grtA25 - 15.d	0.5094	0.026	0.073	0.0041	0.36	0.020	0.056	0.0038	0.11	0.010	0.010	0.0015	0.09	0.010	0.015	0.0020
idl02_usd_grtA25 - 16.d	0.5378	0.033	0.075	0.0043	0.36	0.019	0.054	0.0039	0.10	0.010	0.014	0.0018	0.08	0.010	0.015	0.0018
idl02_usd_grtA25 - 17.d	0.5208	0.030	0.076	0.0041	0.37	0.021	0.059	0.0038	0.11	0.010	0.011	0.0016	0.09	0.012	0.013	0.0018
idl02_usd_grtA25 - 18.d	0.5046	0.031	0.074	0.0040	0.37	0.020	0.055	0.0044	0.11	0.008	0.013	0.0015	0.09	0.013	0.014	0.0017
idl02_usd_grtA26 - 1.d	0.4884	0.029	0.074	0.0044	0.37	0.020	0.055	0.0039	0.12	0.010	0.012	0.0015	0.07	0.011	0.011	0.0017
idl02_usd_grtA26 - 2.d	0.5572	0.033	0.076	0.0047	0.39	0.019	0.059	0.0037	0.13	0.010	0.012	0.0017	0.08	0.012	0.012	0.0016
idl02_usd_grtA27 - 1.d	0.3532	0.027	0.052	0.0034	0.29	0.018	0.054	0.0042	0.13	0.010	0.018	0.0023	0.14	0.015	0.020	0.0022
idl02_usd_grtA27 - 2.d	0.3912	0.024	0.050	0.0037	0.30	0.019	0.052	0.0041	0.12	0.010	0.017	0.0024	0.11	0.015	0.016	0.0022

Table 3.B.10 LA-ICP-MS trace elements analyses from garnet of the amphibolite shear zone. Concentrations are expressed in ppm.

Sample #	Ca	± 2σ	Y	± 2σ	La	± 2σ	Ce	± 2σ	Pr	± 2σ	Nd	± 2σ	Sm	± 2σ	Eu	± 2σ
idl08_sz_grtB4 - 1.d	55186.17	557.32	28.49	0.32	0.0005	0.0003	0.004	0.0010	0.004	0.0009	0.14	0.014	0.72	0.037	0.68	0.018
idl08_sz_grtB4 - 2.d	54269.59	567.05	37.52	0.34	0.0000	0.0000	0.005	0.0008	0.007	0.0009	0.20	0.018	1.00	0.034	0.95	0.016
idl08_sz_grtB4 - 3.d	57993.15	524.93	47.49	0.46	0.0000	0.0000	0.006	0.0009	0.008	0.0011	0.29	0.022	1.41	0.053	1.25	0.020
idl08_sz_grtB4 - 4.d	55474.20	479.66	54.47	0.71	0.0000	0.0000	0.010	0.0015	0.011	0.0013	0.33	0.022	1.40	0.055	1.28	0.021
idl08_sz_grtB5 - 1.d	55199.46	607.50	31.03	0.41	0.0002	0.0002	0.006	0.0012	0.006	0.0009	0.22	0.018	0.95	0.045	0.81	0.021
idl08_sz_grtB5 - 2.d	34837.36	401.80	186.61	5.23	0.0012	0.0005	0.045	0.0036	0.047	0.0029	1.09	0.048	3.21	0.094	2.32	0.057
idl08_sz_grtA14 - 1.d	51698.41	532.96	39.67	0.45	0.0095	0.0014	0.024	0.0023	0.012	0.0013	0.33	0.024	1.31	0.047	1.01	0.022
idl08_sz_grtA15 - 1.d	68973.52	6280.19	56.25	2.59	0.0496	0.0148	0.133	0.0380	0.032	0.0080	0.33	0.048	0.92	0.060	0.74	0.026
idl08_sz_grtA16 - 1.d	52568.64	504.45	20.86	0.17	0.0006	0.0003	0.022	0.0023	0.025	0.0023	0.62	0.033	2.48	0.074	2.15	0.036
idl08_sz_grtA16 - 2.d	58527.07	588.53	40.44	0.53	0.0000	0.0000	0.010	0.0014	0.010	0.0015	0.29	0.024	1.36	0.055	1.31	0.023
idl08_sz_grtA16 - 3.d	53306.09	453.38	22.75	0.41	443.2878	57.1610	903.093	114.2136	91.197	11.5814	313.52	39.852	33.88	4.076	7.64	0.747
idl08_sz_grtA16 - 4.d	52732.91	475.13	11.36	0.12	0.4418	0.1657	1.297	0.5311	0.117	0.0359	0.95	0.156	2.48	0.077	2.05	0.032
idl08_sz_grtA16 - 5.d	49956.58	464.40	19.26	0.21	0.0039	0.0026	0.052	0.0283	0.033	0.0025	0.81	0.039	2.65	0.076	2.06	0.036
idl08_sz_grtA16 - 6.d	47425.24	549.08	14.09	0.27	0.0102	0.0112	0.033	0.0045	0.030	0.0034	0.68	0.038	2.25	0.070	1.83	0.040
idl08_sz_grtA16 - 7.d	56118.52	539.61	32.04	0.37	0.0055	0.0020	0.026	0.0030	0.021	0.0019	0.55	0.031	2.25	0.066	2.00	0.030
idl08_sz_grtA17 - 1.d	44937.43	334.75	60.00	1.04	0.0009	0.0004	0.039	0.0030	0.046	0.0030	1.12	0.050	3.22	0.120	2.53	0.063
idl08_sz_grtA17 - 2.d	38052.63	272.63	113.67	2.22	0.0012	0.0005	0.035	0.0028	0.040	0.0030	0.99	0.042	2.95	0.083	2.44	0.050
idl08_sz_grtA17 - 3.d	44684.15	525.12	106.84	1.54	0.0006	0.0003	0.027	0.0024	0.032	0.0021	0.86	0.041	2.76	0.075	2.38	0.030
idl08_sz_grtA17 - 4.d	48392.42	473.60	22.33	0.35	0.0159	0.0020	0.059	0.0037	0.028	0.0024	0.66	0.035	2.50	0.073	2.15	0.032
idl08_sz_grtA18 - 1.d	55528.00	578.48	39.61	0.49	0.0003	0.0002	0.011	0.0016	0.012	0.0015	0.36	0.025	1.58	0.063	1.49	0.029
idl08_sz_grtA18 - 2.d	56610.13	509.99	42.85	0.41	0.0000	0.0000	0.011	0.0013	0.013	0.0013	0.41	0.027	1.68	0.056	1.58	0.028
idl08_sz_grtA18 - 3.d	56348.34	422.87	24.98	0.29	0.0024	0.0007	0.010	0.0015	0.006	0.0009	0.18	0.015	0.87	0.049	0.78	0.016
idl08_sz_grtA18 - 4.d	55136.48	473.05	41.60	0.54	0.0002	0.0002	0.009	0.0014	0.013	0.0016	0.36	0.024	1.54	0.046	1.39	0.028
idl08_sz_grtA18 - 5.d	57303.48	603.23	46.02	0.61	0.0000	0.0001	0.010	0.0014	0.015	0.0016	0.41	0.025	1.79	0.066	1.65	0.028
idl08_sz_grtA18 - 6.d	52399.87	463.36	39.62	0.43	0.0001	0.0002	0.009	0.0015	0.013	0.0015	0.32	0.023	1.38	0.060	1.21	0.024
idl08_sz_grtA18 - 7.d	54347.12	552.68	43.57	0.56	0.0031	0.0008	0.014	0.0017	0.011	0.0015	0.34	0.022	1.49	0.060	1.37	0.025
idl08_sz_grtA18 - 8.d	34040.47	504.26	173.84	4.16	0.0085	0.0014	0.066	0.0048	0.052	0.0034	1.18	0.048	3.45	0.108	2.80	0.057
idl08_sz_grtA18 - 9.d	52834.59	548.83	38.12	0.52	0.0000	0.0000	0.010	0.0016	0.011	0.0014	0.33	0.021	1.41	0.048	1.29	0.025
idl08_sz_grtA18 - 10.d	51150.78	569.75	35.93	0.47	0.0000	0.0000	0.011	0.0015	0.013	0.0015	0.33	0.021	1.37	0.058	1.21	0.021
idl08_sz_grtA19 - 1.d	56820.78	616.38	44.30	0.55	0.0000	0.0000	0.006	0.0010	0.008	0.0014	0.23	0.017	1.20	0.049	1.14	0.020
idl08_sz_grtA19 - 2.d	57851.86	477.62	58.56	0.67	0.0006	0.0004	0.010	0.0017	0.013	0.0016	0.34	0.027	1.62	0.055	1.43	0.026
idl08_sz_grtA19 - 3.d	52969.47	630.34	39.68	0.48	0.0007	0.0004	0.014	0.0017	0.015	0.0017	0.42	0.024	1.58	0.057	1.45	0.029
idl08_sz_grtA19 - 4.d	57721.39	583.93	45.75	0.58	0.0231	0.0029	0.069	0.0073	0.025	0.0026	0.52	0.029	1.90	0.072	1.74	0.033
idl08_sz_grtA19 - 5.d	34950.45	302.14	238.70	1.51	0.0048	0.0010	0.074	0.0040	0.071	0.0036	1.66	0.061	4.28	0.098	3.27	0.047

Sample #	Gd	± 2σ	Tb	± 2σ	Dy	± 2σ	Ho	± 2σ	Er	± 2σ	Tm	± 2σ	Yb	± 2σ	Lu	± 2σ
idl08_sz_grtB4 - 1.d	4.85	0.10	1.22	0.025	7.31	0.12	1.19	0.025	2.43	0.048	0.24	0.008	1.23	0.045	0.14	0.006
idl08_sz_grtB4 - 2.d	5.90	0.12	1.46	0.024	9.03	0.14	1.55	0.022	3.40	0.052	0.34	0.010	1.77	0.057	0.23	0.008
idl08_sz_grtB4 - 3.d	7.75	0.14	1.87	0.032	11.34	0.17	1.94	0.027	4.23	0.071	0.43	0.010	2.21	0.055	0.28	0.010
idl08_sz_grtB4 - 4.d	7.31	0.15	1.80	0.031	11.87	0.18	2.24	0.036	5.31	0.100	0.58	0.016	3.27	0.081	0.42	0.011
idl08_sz_grtB5 - 1.d	5.38	0.10	1.30	0.025	7.63	0.14	1.23	0.026	2.51	0.056	0.24	0.009	1.16	0.044	0.15	0.007
idl08_sz_grtB5 - 2.d	13.48	0.30	3.68	0.093	30.07	0.80	7.16	0.229	21.30	0.743	2.98	0.114	20.09	0.812	3.03	0.138
idl08_sz_grtA14 - 1.d	6.71	0.15	1.57	0.030	9.44	0.13	1.58	0.027	3.32	0.075	0.34	0.011	1.94	0.067	0.24	0.009
idl08_sz_grtA15 - 1.d	5.63	0.23	1.48	0.063	10.67	0.44	2.33	0.110	6.62	0.342	0.90	0.052	5.91	0.320	0.89	0.052
idl08_sz_grtA16 - 1.d	8.99	0.17	1.48	0.023	6.18	0.11	0.76	0.015	1.26	0.032	0.11	0.005	0.50	0.026	0.06	0.004
idl08_sz_grtA16 - 2.d	7.74	0.16	1.90	0.033	10.81	0.18	1.54	0.026	2.76	0.063	0.24	0.009	1.06	0.042	0.12	0.007
idl08_sz_grtA16 - 3.d	18.82	1.32	2.14	0.082	7.71	0.21	0.83	0.023	1.26	0.048	0.10	0.006	0.41	0.029	0.04	0.004
idl08_sz_grtA16 - 4.d	8.04	0.15	1.16	0.018	4.00	0.09	0.39	0.011	0.53	0.021	0.04	0.003	0.17	0.015	0.02	0.002
idl08_sz_grtA16 - 5.d	8.56	0.14	1.38	0.025	5.65	0.10	0.67	0.016	1.07	0.033	0.09	0.006	0.47	0.027	0.05	0.004
idl08_sz_grtA16 - 6.d	7.47	0.19	1.17	0.027	4.46	0.12	0.48	0.016	0.67	0.029	0.05	0.003	0.22	0.018	0.02	0.002
idl08_sz_grtA16 - 7.d	9.48	0.18	1.85	0.034	8.69	0.14	1.20	0.026	2.14	0.045	0.20	0.009	0.99	0.040	0.11	0.005
idl08_sz_grtA17 - 1.d	12.09	0.30	2.54	0.049	14.35	0.30	2.25	0.054	4.43	0.100	0.43	0.014	2.21	0.077	0.26	0.010
idl08_sz_grtA17 - 2.d	12.01	0.27	2.96	0.065	21.34	0.44	4.23	0.093	10.51	0.239	1.26	0.030	7.04	0.183	0.89	0.027
idl08_sz_grtA17 - 3.d	11.40	0.14	2.74	0.031	19.69	0.26	4.09	0.065	10.86	0.195	1.36	0.032	8.29	0.252	1.10	0.035
idl08_sz_grtA17 - 4.d	9.00	0.14	1.52	0.023	6.66	0.11	0.83	0.019	1.48	0.040	0.15	0.006	0.70	0.039	0.09	0.005
idl08_sz_grtA18 - 1.d	7.95	0.16	1.75	0.039	9.80	0.16	1.55	0.031	3.10	0.070	0.30	0.010	1.46	0.051	0.18	0.008
idl08_sz_grtA18 - 2.d	8.43	0.14	1.89	0.027	10.56	0.16	1.67	0.027	3.41	0.060	0.35	0.010	1.74	0.068	0.21	0.007
idl08_sz_grtA18 - 3.d	5.08	0.11	1.19	0.023	6.66	0.11	1.01	0.019	1.94	0.039	0.18	0.006	0.90	0.043	0.12	0.007
idl08_sz_grtA18 - 4.d	7.52	0.17	1.70	0.027	9.88	0.17	1.64	0.032	3.48	0.082	0.36	0.011	1.82	0.067	0.23	0.007
idl08_sz_grtA18 - 5.d	8.80	0.17	1.95	0.035	11.19	0.19	1.83	0.035	3.77	0.076	0.39	0.012	2.04	0.065	0.25	0.010
idl08_sz_grtA18 - 6.d	6.84	0.12	1.56	0.026	9.34	0.14	1.63	0.029	3.60	0.056	0.37	0.010	1.91	0.065	0.25	0.008
idl08_sz_grtA18 - 7.d	7.57	0.16	1.75	0.032	10.35	0.15	1.76	0.035	3.87	0.071	0.40	0.011	2.10	0.061	0.26	0.009
idl08_sz_grtA18 - 8.d	14.28	0.32	3.77	0.087	29.77	0.69	6.73	0.165	19.59	0.541	2.62	0.075	16.79	0.491	2.39	0.068
idl08_sz_grtA18 - 9.d	6.94	0.15	1.59	0.028	9.40	0.16	1.53	0.028	3.16	0.072	0.31	0.008	1.50	0.057	0.18	0.008
idl08_sz_grtA18 - 10.d	6.79	0.12	1.54	0.026	8.95	0.13	1.49	0.029	3.15	0.062	0.32	0.008	1.58	0.055	0.19	0.009
idl08_sz_grtA19 - 1.d	7.27	0.15	1.75	0.036	10.79	0.18	1.82	0.035	3.86	0.081	0.40	0.012	2.10	0.066	0.25	0.009
idl08_sz_grtA19 - 2.d	8.38	0.15	2.02	0.032	12.91	0.22	2.33	0.041	5.44	0.110	0.60	0.016	3.32	0.083	0.42	0.011
idl08_sz_grtA19 - 3.d	7.46	0.19	1.61	0.029	9.32	0.14	1.57	0.029	3.49	0.077	0.37	0.010	2.00	0.061	0.26	0.011
idl08_sz_grtA19 - 4.d	8.54	0.15	1.85	0.030	10.60	0.17	1.78	0.035	3.99	0.080	0.43	0.012	2.34	0.079	0.29	0.008
idl08_sz_grtA19 - 5.d	17.06	0.25	4.58	0.045	38.07	0.29	9.39	0.081	29.62	0.224	4.28	0.053	29.89	0.310	4.54	0.052

Table 3.B.10 Continued

Sample #	Ca	± 2σ	Y	± 2σ	La	± 2σ	Ce	± 2σ	Pr	± 2σ	Nd	± 2σ	Sm	± 2σ	Eu	± 2σ
idl08_sz_grtA19 - 6.d	37013.73	493.71	214.39	2.93	0.0018	0.0006	0.067	0.0040	0.067	0.0038	1.56	0.055	4.24	0.098	3.29	0.061
idl08_sz_grtB6 - 1.d	44656.98	445.79	104.94	1.15	0.0004	0.0003	0.020	0.0021	0.025	0.0019	0.63	0.035	2.19	0.070	1.68	0.024
idl08_sz_grtB6 - 2.d	37409.09	428.07	267.60	4.54	0.0008	0.0004	0.052	0.0032	0.057	0.0036	1.40	0.053	3.90	0.098	2.91	0.066
idl08_sz_grtA20 - 1.d	30499.94	338.51	234.50	2.50	0.0012	0.0005	0.047	0.0038	0.047	0.0030	1.11	0.044	3.05	0.081	2.14	0.038
idl08_sz_grtA20 - 2.d	36020.74	533.43	261.13	4.25	0.0181	0.0020	0.109	0.0051	0.084	0.0040	1.72	0.054	4.46	0.121	3.02	0.054
idl08_sz_grtA20 - 3.d	30351.54	318.37	203.10	2.07	0.0127	0.0016	0.066	0.0036	0.051	0.0034	1.05	0.044	2.81	0.071	1.92	0.033
idl08_sz_grtA20 - 4.d	33853.75	571.90	187.40	2.26	0.0033	0.0008	0.056	0.0035	0.049	0.0027	1.06	0.038	2.99	0.078	2.09	0.039
idl08_sz_grtA20 - 5.d	38829.14	476.42	194.48	1.69	0.0005	0.0003	0.035	0.0025	0.042	0.0029	1.15	0.046	3.35	0.083	2.05	0.031
idl08_sz_grtA20 - 6.d	30869.13	337.14	235.40	3.81	0.0011	0.0005	0.043	0.0031	0.045	0.0024	0.98	0.034	2.68	0.076	1.87	0.028
idl08_sz_grtA20 - 7.d	36190.46	514.68	196.78	2.06	0.0128	0.0014	0.061	0.0036	0.041	0.0031	1.01	0.039	3.03	0.069	1.91	0.033
idl08_sz_grtA21 - 1.d	53558.36	555.43	42.46	0.68	0.0045	0.0085	0.013	0.0071	0.024	0.0160	0.33	0.024	1.43	0.047	1.24	0.026
idl08_sz_grtA21 - 2.d	52217.92	342.24	46.82	0.70	0.0000	0.0000	0.011	0.0015	0.014	0.0016	0.44	0.029	1.74	0.062	1.41	0.026
idl08_sz_grtA21 - 3.d	37019.00	347.33	75.72	0.47	0.0012	0.0005	0.050	0.0032	0.054	0.0032	1.29	0.047	3.30	0.081	2.48	0.038
idl08_sz_grtA21 - 4.d	37916.89	726.06	146.36	2.40	0.0021	0.0006	0.056	0.0040	0.052	0.0030	1.27	0.073	3.27	0.132	2.57	0.080
idl08_sz_grtA21 - 5.d	30514.65	361.29	123.75	0.97	0.0025	0.0006	0.042	0.0029	0.041	0.0027	0.97	0.036	2.57	0.064	2.05	0.032
idl08_sz_grtA21 - 6.d	32710.86	397.87	199.77	2.51	0.0019	0.0007	0.049	0.0032	0.050	0.0028	1.16	0.049	3.04	0.091	2.15	0.040
idl08_sz_grtA21 - 7.d	47972.69	536.20	58.58	1.21	0.0003	0.0002	0.015	0.0017	0.019	0.0020	0.52	0.027	1.94	0.055	1.59	0.031
idl08_sz_grtA22 - 1.d	55518.04	534.09	40.69	0.42	0.0007	0.0004	0.007	0.0013	0.007	0.0012	0.24	0.020	1.09	0.052	1.02	0.026
idl08_sz_grtA22 - 2.d	57735.97	468.79	48.42	0.54	0.0078	0.0013	0.023	0.0026	0.012	0.0016	0.32	0.023	1.43	0.058	1.28	0.026
idl08_sz_grtA22 - 3.d	56372.12	571.69	40.36	0.53	0.0000	0.0000	0.007	0.0012	0.009	0.0013	0.26	0.022	1.12	0.048	1.03	0.024
idl08_sz_grtA22 - 4.d	58886.38	718.41	48.58	0.72	0.0005	0.0003	0.016	0.0020	0.017	0.0018	0.48	0.027	1.95	0.061	1.84	0.035
idl08_sz_grtA22 - 5.d	59723.53	567.77	49.51	0.54	0.0005	0.0003	0.015	0.0018	0.018	0.0019	0.48	0.027	2.05	0.072	1.83	0.030
idl08_sz_grtA22 - 6.d	58976.51	769.36	48.83	0.66	0.0004	0.0003	0.013	0.0020	0.015	0.0016	0.45	0.028	1.87	0.065	1.73	0.038
idl08_sz_grtA22 - 7.d	57265.83	637.18	56.89	0.82	0.0000	0.0000	0.009	0.0016	0.010	0.0015	0.30	0.021	1.51	0.061	1.38	0.028
idl08_sz_grtA22 - 8.d	59142.53	729.64	43.84	0.75	0.0004	0.0003	0.006	0.0012	0.008	0.0015	0.24	0.016	1.20	0.048	1.14	0.024
idl08_sz_grtB8 - 1.d	36391.85	387.69	3.71	0.06	0.0168	0.0020	0.446	0.0096	0.275	0.0078	3.88	0.095	3.74	0.086	1.61	0.030
idl08_sz_grtB8 - 2.d	36993.19	340.14	3.87	0.05	0.0175	0.0019	0.449	0.0105	0.281	0.0081	3.95	0.081	3.86	0.096	1.64	0.026

Sample #	Gd	± 2σ	Tb	± 2σ	Dy	± 2σ	Ho	± 2σ	Er	± 2σ	Tm	± 2σ	Yb	± 2σ	Lu	± 2σ
idl08_sz_grtA19 - 6.d	16.72	0.37	4.41	0.080	35.49	0.63	8.30	0.144	24.99	0.401	3.50	0.065	23.28	0.446	3.45	0.065
idl08_sz_grtB6 - 1.d	9.86	0.17	2.59	0.044	19.01	0.26	3.93	0.059	10.24	0.170	1.26	0.027	7.49	0.217	0.98	0.033
idl08_sz_grtB6 - 2.d	16.42	0.30	4.70	0.092	40.76	0.78	10.23	0.196	31.93	0.635	4.56	0.105	30.63	0.714	4.48	0.107
idl08_sz_grtA20 - 1.d	13.21	0.24	3.93	0.074	35.49	0.55	8.94	0.118	27.24	0.328	3.75	0.056	24.09	0.406	3.21	0.050
idl08_sz_grtA20 - 2.d	17.56	0.36	4.83	0.084	40.57	0.75	9.68	0.180	28.84	0.486	4.00	0.077	26.71	0.435	3.67	0.063
idl08_sz_grtA20 - 3.d	11.77	0.20	3.48	0.049	30.79	0.40	7.54	0.082	22.45	0.305	3.03	0.043	19.60	0.278	2.57	0.033
idl08_sz_grtA20 - 4.d	12.05	0.19	3.36	0.045	28.74	0.39	6.90	0.108	20.87	0.287	2.97	0.049	20.39	0.348	2.81	0.047
idl08_sz_grtA20 - 5.d	14.57	0.21	4.08	0.061	33.63	0.42	7.52	0.085	20.45	0.221	2.56	0.031	15.38	0.193	1.93	0.030
idl08_sz_grtA20 - 6.d	11.47	0.22	3.47	0.058	32.50	0.51	8.91	0.167	30.72	0.684	4.97	0.119	38.51	0.958	5.94	0.158
idl08_sz_grtA20 - 7.d	13.33	0.21	3.83	0.059	32.89	0.39	7.65	0.094	21.91	0.266	2.89	0.039	18.21	0.224	2.37	0.033
idl08_sz_grtA21 - 1.d	7.69	0.17	1.78	0.035	10.29	0.18	1.65	0.036	3.51	0.078	0.38	0.013	1.88	0.076	0.24	0.010
idl08_sz_grtA21 - 2.d	8.40	0.17	1.93	0.035	11.07	0.17	1.77	0.035	3.66	0.072	0.37	0.009	1.99	0.065	0.25	0.011
idl08_sz_grtA21 - 3.d	11.10	0.17	2.39	0.028	15.17	0.17	2.65	0.028	6.18	0.084	0.72	0.014	4.22	0.090	0.51	0.012
idl08_sz_grtA21 - 4.d	12.52	0.41	3.10	0.085	23.80	0.55	5.27	0.093	15.11	0.204	2.12	0.030	14.20	0.167	2.03	0.025
idl08_sz_grtA21 - 5.d	10.20	0.16	2.59	0.036	19.94	0.25	4.42	0.052	12.49	0.143	1.70	0.022	11.28	0.191	1.55	0.020
idl08_sz_grtA21 - 6.d	12.53	0.25	3.55	0.058	30.46	0.43	7.60	0.121	23.58	0.352	3.38	0.063	22.51	0.374	3.38	0.062
idl08_sz_grtA21 - 7.d	9.05	0.20	2.08	0.036	12.77	0.24	2.22	0.049	5.13	0.141	0.60	0.023	3.44	0.125	0.45	0.018
idl08_sz_grtA22 - 1.d	6.21	0.13	1.51	0.027	9.61	0.16	1.66	0.031	3.67	0.066	0.39	0.012	2.00	0.068	0.25	0.008
idl08_sz_grtA22 - 2.d	7.50	0.14	1.79	0.028	11.25	0.17	1.95	0.034	4.32	0.079	0.44	0.012	2.37	0.086	0.28	0.012
idl08_sz_grtA22 - 3.d	6.33	0.14	1.54	0.031	9.56	0.16	1.65	0.034	3.62	0.076	0.38	0.012	2.03	0.084	0.24	0.008
idl08_sz_grtA22 - 4.d	9.03	0.15	1.93	0.040	11.12	0.21	1.93	0.038	4.40	0.084	0.47	0.016	2.63	0.089	0.34	0.012
idl08_sz_grtA22 - 5.d	9.33	0.15	2.01	0.029	11.66	0.17	1.95	0.032	4.37	0.082	0.46	0.010	2.52	0.069	0.32	0.011
idl08_sz_grtA22 - 6.d	9.02	0.17	1.98	0.035	11.43	0.20	1.92	0.035	4.25	0.084	0.45	0.012	2.52	0.083	0.30	0.010
idl08_sz_grtA22 - 7.d	8.40	0.17	2.00	0.034	12.72	0.18	2.32	0.041	5.33	0.108	0.56	0.013	3.06	0.093	0.39	0.012
idl08_sz_grtA22 - 8.d	7.02	0.16	1.73	0.039	10.70	0.21	1.79	0.041	3.86	0.092	0.38	0.011	2.02	0.068	0.25	0.010
idl08_sz_grtB8 - 1.d	4.18	0.09	0.45	0.013	1.51	0.05	0.12	0.007	0.14	0.009	0.01	0.002	0.03	0.008	0.00	0.001
idl08_sz_grtB8 - 2.d	4.30	0.09	0.48	0.012	1.58	0.05	0.14	0.008	0.17	0.012	0.01	0.002	0.04	0.009	0.00	0.001

Table 3.B.10 Continued

Sample #	Ca	± 2σ	Y	± 2σ	La	± 2σ	Ce	± 2σ	Pr	± 2σ	Nd	± 2σ	Sm	± 2σ	Eu	± 2σ
idl09_sz_grtA1 - 1.d	46647.78	299.63	65.94	1.13	0.0008	0.0004	0.033	0.0031	0.038	0.0026	1.03	0.043	3.87	0.098	3.48	0.054
idl09_sz_grtA1 - 2.d	53563.71	436.29	25.59	0.26	0.0000	0.0000	0.006	0.0011	0.007	0.0013	0.23	0.020	1.07	0.044	0.99	0.028
idl09_sz_grtA1 - 3.d	54125.35	449.50	40.30	0.72	0.0000	0.0001	0.018	0.0022	0.021	0.0020	0.60	0.031	2.58	0.076	2.56	0.047
idl09_sz_grtA1 - 4.d	54494.77	477.55	29.23	0.21	0.0000	0.0000	0.014	0.0017	0.017	0.0015	0.44	0.031	1.69	0.061	1.59	0.026
idl09_sz_grtA1 - 5.d	40336.91	336.91	299.70	2.63	0.0114	0.0014	0.090	0.0047	0.081	0.0044	1.85	0.061	5.05	0.117	4.17	0.056
idl09_sz_grtA1 - 6.d	49881.51	333.34	22.17	0.66	0.0000	0.0000	0.010	0.0012	0.014	0.0014	0.40	0.030	1.55	0.065	1.47	0.043
idl09_sz_grtA1 - 7.d	53733.37	419.36	32.69	0.30	0.0004	0.0003	0.009	0.0013	0.011	0.0012	0.31	0.023	1.35	0.054	1.18	0.020
idl09_sz_grtA1 - 8.d	48354.25	547.33	79.06	0.93	0.0006	0.0003	0.040	0.0026	0.046	0.0025	1.31	0.053	4.45	0.087	3.93	0.050
idl09_sz_grtA1 - 9.d	35540.76	546.80	218.44	2.89	0.0322	0.0029	0.124	0.0058	0.068	0.0037	1.35	0.047	3.72	0.104	3.08	0.052
idl09_sz_grtA1 - 10.d	54441.03	561.65	34.17	0.45	0.0000	0.0000	0.009	0.0014	0.011	0.0013	0.36	0.022	1.44	0.050	1.31	0.026
idl09_sz_grtA2 - 1.d	32086.52	519.34	51.93	0.95	0.0019	0.0007	0.045	0.0037	0.046	0.0034	1.10	0.042	2.95	0.085	2.33	0.053
idl09_sz_grtA3 - 1.d	33987.29	334.56	202.73	0.96	0.0014	0.0005	0.069	0.0042	0.069	0.0037	1.66	0.054	4.27	0.101	2.85	0.036
idl09_sz_grtA4 - 1.d	41065.34	478.46	67.00	1.79	0.0015	0.0005	0.036	0.0026	0.036	0.0033	1.02	0.062	3.13	0.131	2.49	0.089
idl09_sz_grtA5 - 1.d	52882.52	561.20	29.11	0.41	0.0005	0.0003	0.010	0.0017	0.013	0.0017	0.38	0.023	1.55	0.062	1.34	0.032
idl09_sz_grtA6 - 1.d	38301.36	614.56	96.35	1.10	0.0015	0.0005	0.025	0.0025	0.028	0.0024	0.70	0.033	2.11	0.077	1.46	0.026
idl09_sz_grtB1 - 1.d	36055.84	293.52	70.32	0.66	0.0038	0.0015	0.097	0.0064	0.119	0.0047	2.72	0.071	4.07	0.098	2.46	0.034
idl09_sz_grtB1 - 2.d	35924.32	415.90	69.46	0.93	0.0133	0.0022	0.085	0.0094	0.104	0.0052	2.73	0.075	3.99	0.091	2.47	0.040
idl09_sz_grtA7 - 1.d	38371.01	488.55	131.65	1.92	0.0054	0.0014	0.091	0.0050	0.080	0.0040	1.94	0.067	5.01	0.128	3.54	0.060
idl09_sz_grtA8 - 1.d	40831.11	782.78	95.96	1.25	0.0018	0.0005	0.056	0.0033	0.057	0.0031	1.31	0.047	3.64	0.109	2.90	0.058
idl09_sz_grtA9 - 1.d	36540.23	354.08	130.51	1.80	0.0044	0.0011	0.064	0.0046	0.058	0.0035	1.37	0.049	3.56	0.106	2.71	0.048
idl09_sz_grtA9 - 2.d	37815.70	312.58	110.48	1.55	0.0050	0.0010	0.049	0.0069	0.028	0.0022	0.68	0.035	2.18	0.073	1.80	0.030
idl09_sz_grtA10 - 1.d	52024.74	577.38	25.37	0.49	0.0000	0.0000	0.007	0.0013	0.009	0.0012	0.27	0.018	1.25	0.051	1.11	0.027
idl09_sz_grtA10 - 3.d	35752.62	383.62	123.54	1.53	0.0011	0.0005	0.066	0.0036	0.066	0.0038	1.58	0.051	4.14	0.101	3.35	0.055
idl09_sz_grtA11 - 1.d	37430.03	416.15	214.00	2.82	0.0014	0.0005	0.055	0.0031	0.057	0.0026	1.37	0.059	3.85	0.108	2.73	0.051
idl09_sz_grtA12 - 1.d	55889.31	588.34	34.86	0.45	0.0000	0.0000	0.001	0.0004	0.002	0.0005	0.07	0.011	0.38	0.023	0.36	0.012
idl09_sz_grtB2 - 1.d	50701.15	718.98	50.53	0.40	0.0000	0.0000	0.009	0.0013	0.011	0.0013	0.34	0.023	1.45	0.052	1.24	0.023
idl09_sz_grtA13 - 1.d	54311.04	420.66	27.94	0.32	0.0247	0.0022	0.066	0.0040	0.019	0.0017	0.34	0.026	1.32	0.054	1.21	0.024
idl09_sz_grtA13 - 2.d	54989.48	493.58	26.60	0.29	0.0093	0.0014	0.039	0.0038	0.019	0.0019	0.38	0.025	1.45	0.046	1.47	0.025

Sample #	Gd	± 2σ	Tb	± 2σ	Dy	± 2σ	Ho	± 2σ	Er	± 2σ	Tm	± 2σ	Yb	± 2σ	Lu	± 2σ
idl09_sz_grtA1 - 1.d	15.06	0.24	3.10	0.046	16.63	0.32	2.47	0.062	4.79	0.119	0.46	0.017	2.21	0.081	0.26	0.011
idl09_sz_grtA1 - 2.d	5.60	0.15	1.26	0.028	6.82	0.12	1.02	0.020	1.84	0.043	0.16	0.008	0.78	0.040	0.08	0.005
idl09_sz_grtA1 - 3.d	11.31	0.24	2.27	0.042	11.08	0.24	1.49	0.032	2.61	0.072	0.23	0.009	1.04	0.053	0.11	0.007
idl09_sz_grtA1 - 4.d	7.56	0.13	1.53	0.023	7.70	0.09	1.15	0.020	2.24	0.049	0.22	0.007	1.13	0.045	0.14	0.007
idl09_sz_grtA1 - 5.d	20.32	0.27	5.71	0.067	47.78	0.50	11.70	0.136	35.22	0.365	4.87	0.051	31.87	0.390	4.55	0.054
idl09_sz_grtA1 - 6.d	6.72	0.20	1.28	0.036	6.14	0.19	0.77	0.024	1.34	0.049	0.13	0.008	0.73	0.058	0.08	0.006
idl09_sz_grtA1 - 7.d	6.58	0.12	1.46	0.024	8.19	0.14	1.31	0.026	2.71	0.045	0.26	0.010	1.36	0.045	0.17	0.006
idl09_sz_grtA1 - 8.d	16.82	0.30	3.51	0.059	19.43	0.25	3.02	0.051	6.04	0.098	0.60	0.013	3.10	0.072	0.36	0.010
idl09_sz_grtA1 - 9.d	15.10	0.31	4.28	0.076	35.93	0.55	8.51	0.130	24.48	0.380	3.23	0.048	20.22	0.303	2.72	0.042
idl09_sz_grtA1 - 10.d	7.05	0.16	1.56	0.033	8.83	0.16	1.37	0.030	2.83	0.066	0.27	0.008	1.46	0.057	0.18	0.008
idl09_sz_grtA2 - 1.d	10.33	0.23	2.24	0.059	12.60	0.29	1.78	0.030	3.00	0.067	0.26	0.010	1.12	0.043	0.11	0.005
idl09_sz_grtA3 - 1.d	17.39	0.27	4.57	0.058	35.46	0.28	7.53	0.062	19.16	0.179	2.22	0.030	12.46	0.235	1.50	0.032
idl09_sz_grtA4 - 1.d	12.14	0.48	2.62	0.103	15.21	0.56	2.34	0.070	4.95	0.163	0.53	0.026	2.93	0.205	0.39	0.034
idl09_sz_grtA5 - 1.d	7.05	0.17	1.48	0.033	7.59	0.15	1.07	0.023	1.87	0.049	0.16	0.007	0.76	0.037	0.08	0.004
idl09_sz_grtA6 - 1.d	9.36	0.19	2.49	0.045	18.23	0.28	3.51	0.049	8.13	0.133	0.87	0.017	4.34	0.100	0.49	0.012
idl09_sz_grtB1 - 1.d	7.32	0.14	1.50	0.026	11.32	0.15	2.71	0.041	8.87	0.144	1.39	0.024	10.81	0.184	1.67	0.028
idl09_sz_grtB1 - 2.d	7.20	0.13	1.49	0.030	11.19	0.20	2.65	0.042	8.57	0.148	1.34	0.023	10.46	0.196	1.60	0.032
idl09_sz_grtA7 - 1.d	18.24	0.29	4.21	0.067	27.57	0.46	4.76	0.091	9.45	0.169	0.89	0.021	4.04	0.108	0.38	0.011
idl09_sz_grtA8 - 1.d	13.59	0.26	3.03	0.055	19.25	0.30	3.50	0.064	8.40	0.156	0.98	0.022	5.65	0.111	0.70	0.019
idl09_sz_grtA9 - 1.d	13.81	0.28	3.40	0.068	24.75	0.48	4.78	0.071	11.59	0.185	1.31	0.024	7.57	0.138	0.90	0.017
idl09_sz_grtA9 - 2.d	9.24	0.16	2.47	0.037	19.14	0.32	4.21	0.071	11.18	0.177	1.32	0.028	7.46	0.142	0.90	0.018
idl09_sz_grtA10 - 1.d	5.94	0.16	1.26	0.032	6.72	0.13	1.02	0.027	1.92	0.054	0.17	0.007	0.84	0.043	0.10	0.006
idl09_sz_grtA10 - 3.d	15.96	0.30	3.93	0.072	25.98	0.43	4.50	0.075	9.09	0.162	0.85	0.017	4.05	0.089	0.41	0.012
idl09_sz_grtA11 - 1.d	15.89	0.27	4.39	0.078	35.38	0.61	7.86	0.122	21.20	0.320	2.59	0.043	15.50	0.354	1.99	0.039
idl09_sz_grtA12 - 1.d	3.01	0.07	0.94	0.021	6.97	0.14	1.32	0.028	2.96	0.067	0.31	0.010	1.68	0.061	0.22	0.008
idl09_sz_grtB2 - 1.d	7.72	0.16	1.81	0.031	11.18	0.13	1.98	0.027	4.61	0.077	0.51	0.014	2.95	0.110	0.39	0.016
idl09_sz_grtA13 - 1.d	6.56	0.13	1.38	0.025	7.35	0.12	1.12	0.023	2.26	0.046	0.22	0.008	1.13	0.043	0.15	0.007
idl09_sz_grtA13 - 2.d	6.98	0.12	1.37	0.017	7.13	0.13	1.04	0.021	2.08	0.043	0.22	0.009	1.18	0.044	0.15	0.006

Appendix C

4.C1 Supplementary Methods to Chapter 4

Preliminary petrographic observations were conducted by optical microscopy in transmitted light. Characterization by scanning electron microscopy (SEM) used both a TESCAN Mira3 FESEM and a TESCAN Integrated Mineral Analyzer (TIMA) housed at the John de Laeter Centre at Curtin University. TIMA analyses were conducted in dot mapping mode using a 3 μm pixel size for backscattered imaging and 27 μm spacing for energy dispersive spectroscopy (EDS) analyses. The instrument was operated using 25 kV at 15 mm working distance. Post-processing of the data was performed using TIMA software v.2.5.2. Electron backscattered diffraction (EBSD) data were collected using the Tescan Clara field emission gun scanning electron microscope (FEG-SEM) equipped with an Oxford Instruments Symmetry EBSD detector housed at the John de Laeter Centre at Curtin University. EBSD data were acquired using 20 kV at 20 mm working distance using a step size from 500 to 50 nm. EDS X-ray maps of the garnet were acquired synchronously to the EBSD data. EBSD maps were post-processed using AZtec Crystal 2.1 software, corrected utilizing a standard noise reduction procedure involving the removal of misindexed "wild spikes", a six nearest-neighbour zero solution algorithm and colour coded using a perceptually uniform Roma colour scheme (Crameri 2018). To improve the visualization of subgrain boundaries with misorientation < 1° a Kuwahara filter function has been applied (Humphrey's *et al.* 2001). Grain boundaries were defined using a critical misorientation of 10° for high-angle boundaries. Within the analysed garnet a 0.7° low-angle boundary was selected for atom probe tomography (APT) analyses.

Needle-shaped specimens for APT were prepared using a Tescan Lyra3 Ga+ focused ion beam scanning electron microscope (FIB-SEM) at the John de Laeter Centre at Curtin University. the targeting of the interface was performed using the "button" method described by Rickard et *al.* (2020). Before APT analyses, a final 5 kV polishing stage was performed on all the prepared atom probe specimens to reduce the layer affected by high-energy Ga^+ ions. APT specimens were analyzed on a CAMECA LEAP 4000X HR Geoscience Atom Probe in the John de Laeter Centre at Curtin University. The specimens were analysed in laser-assisted mode with a UV laser (λ = 355 nm), pulsed between 250 and 200 kHz. The laser pulse energy varied from 350 to 380 pJ. The base temperature of the specimens was

maintained at 60 K and the automated detection rate was between 0.005 to 0.006 ions/pulse. The resulting time-of-flight mass/charge ration spectra were post-processed and reconstructed in 3D using Cameca's IVAS 3.8.2 software. Peaks twice higher than the background were identified and ranged (Supplementary Table 4.C2.4). For the 3D dimensional reconstruction of the analysed samples, the standardized parameters for garnet provided by Fougerouse et al. 2021 were used. Additional detail about data acquisition and reconstruction parameters are given in the Supplementary Table 4.C2.3 compiled following the recommendation of Blum et *al.* (2018). Further details on the application of APT technique applied to geological materials are provided in Reddy et *al.* (2020). The composition of the interface was calculated by extracting the composition of an isoconcentration surface defined by the ion concentration (at%) of OH and Na. In order to minimize cross-contamination between enriched domains, the composition of the matrix was obtained using values contained within 3 nm of the most distal portions from each enriched interface. The composition of the low-angle boundary was obtained by interpolating the at % obtained from the proxigram of the interface and the atomic counts within each enriched region.

4.C1.1 References

Blum, T.B., Darling, J.R., Kelly, T.F., Larson, D.J., Moser, D.E., Perez-Huerta, A., Prosa, T.J., Reddy, S.M., Reinhard, D.A., Saxey, D.W., Ulfig, R.M. & Valley, J.W. 2018. Best Practices for Reporting Atom Probe Analysis of Geological Materials. In: Moser, D.E., Corfu, F., Darling, J.R., Reddy, S.M. & Tait, K. (eds) *Geophysical Monograph Series*. John Wiley & Sons, Inc., Hoboken, NJ, USA, 369–373. DOI 10.1002/9781119227250.ch18

Crameri, F. 2018. *Scientific Colour Maps. Zenodo. Http://Doi.Org/10.5281/Zenodo.1243862.*

Fougerouse, D., Saxey, D.W., Rickard, W.D.A., Reddy, S.M. & Verberne, R. 2021. Standardizing Spatial Reconstruction Parameters for the Atom Probe Analysis of Common Minerals. *Microscopy and Microanalysis,* 1–10. DOI 10.1017/S1431927621013714

Humphreys, F.J., Bate, P.S. and Hurley, P.J. (2001), Orientation averaging of electron backscattered diffraction data. *Journal of Microscopy,* 201: 50-58. https://doi.org/10.1046/j.1365-2818.2001.00777.x

Reddy, S.M., Saxey, D.W., Rickard, W.D.A., Fougerouse, D., Montalvo, S.D., Verberne, R. & Riessen, A. 2020. Atom Probe Tomography: Development and Application to the Geosciences. *Geostandards and Geoanalytical Research 44(1),* 5–50. DOI 10.1111/ggr.12313

Rickard, W.D.A., Reddy, S.M., Saxey, D.W., Fougerouse, D., Timms, N.E., Daly, L., Peterman, E., Cavosie, A.J. & Jourdan, F. 2020. Novel Applications of FIB-SEM-Based ToF-SIMS in Atom Probe Tomography Workflows. *Microscopy and Microanalysis,* 1–8. DOI 10.1017/S1431927620000136

4.C2 Supplementary Figures and Tables to Chapter 4

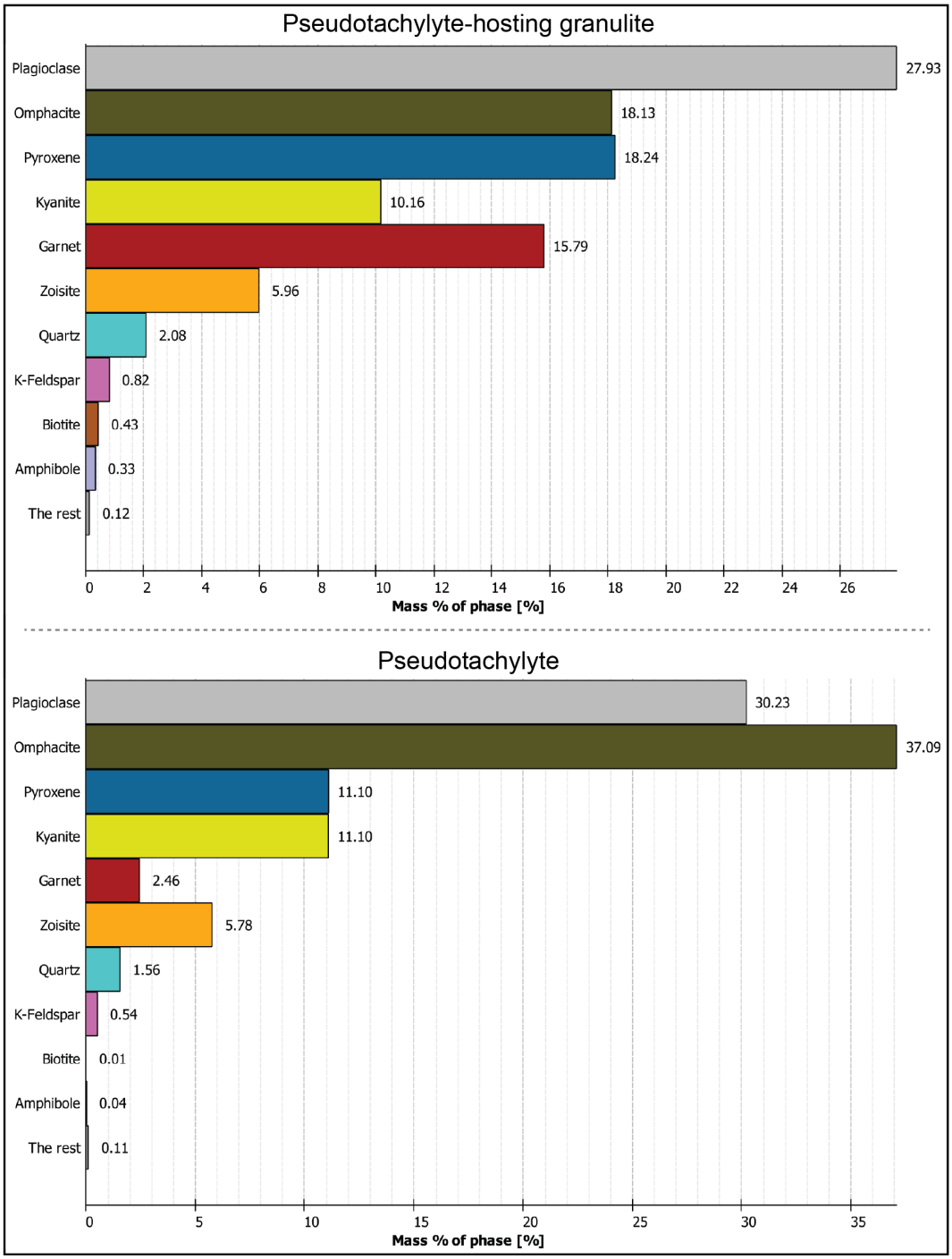

Figure 4.C2.1 Mineral proportions of the investigated sample obtained by TIMA analyses and expressed in wt%.

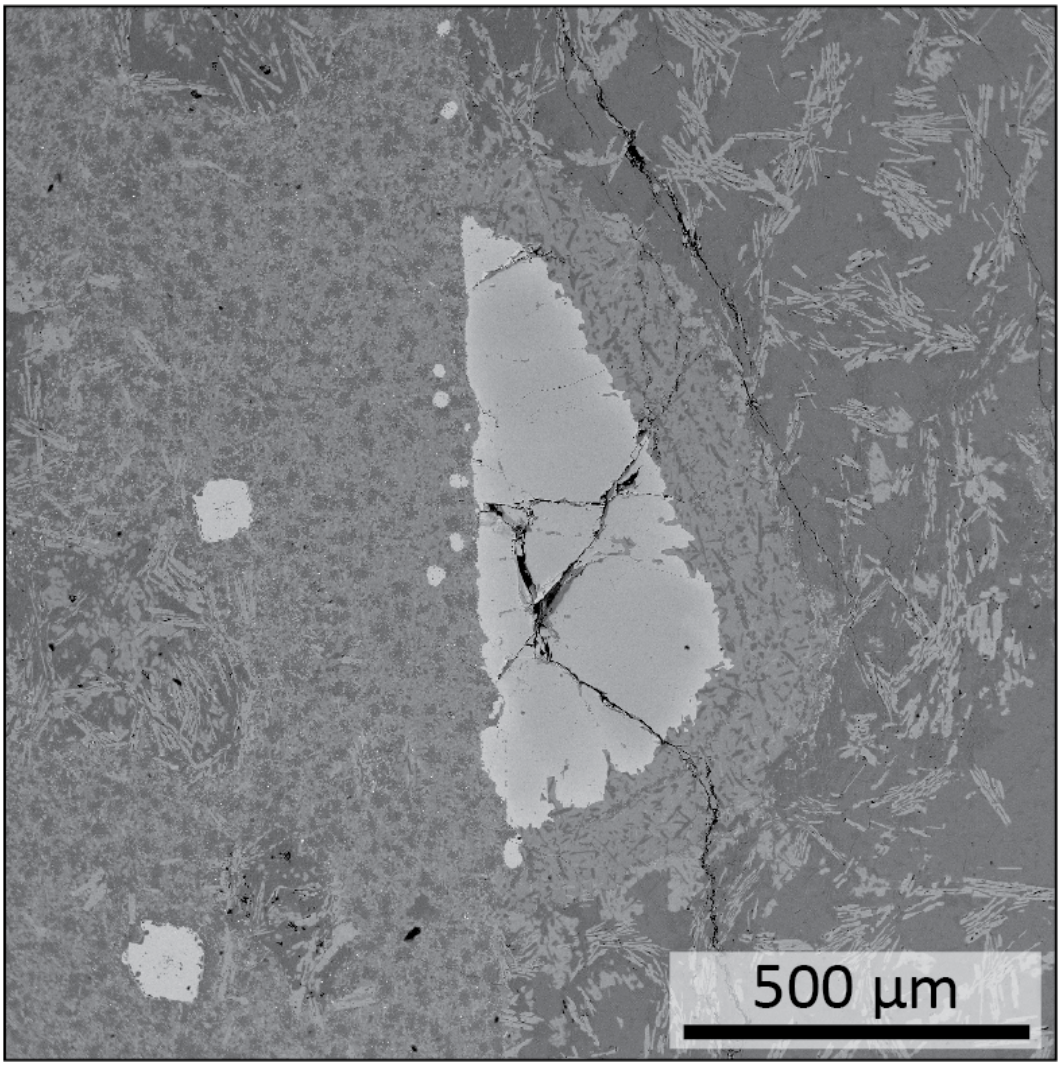

Figure 4.C2.2 BSE-SEM image of the investigated garnet grain in contact with the pseudotachylyte. Euhedral poikilitic garnets grains can be observed growing from the matrix of the pseudotachylyte.

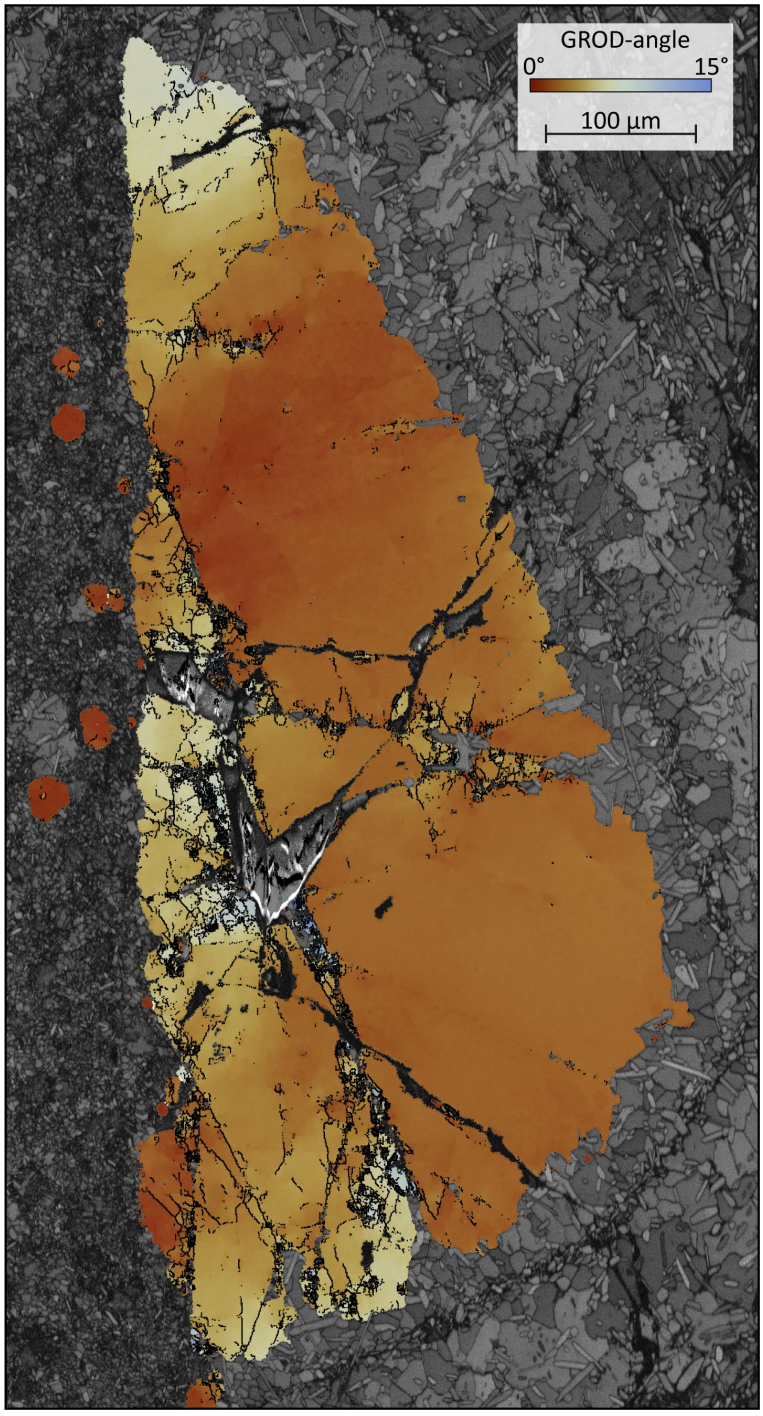

Figure 4.C2.3 EBSD Grain Reference Orientation Deviation (GROD) angle map. Each pixel is colour coded based on the deviation angle relative to the average orientation of the whole grain. Low-angle boundaries (0.5 - 10°) are plotted in black. High-angle boundaries (> 10°) are plotted in white.

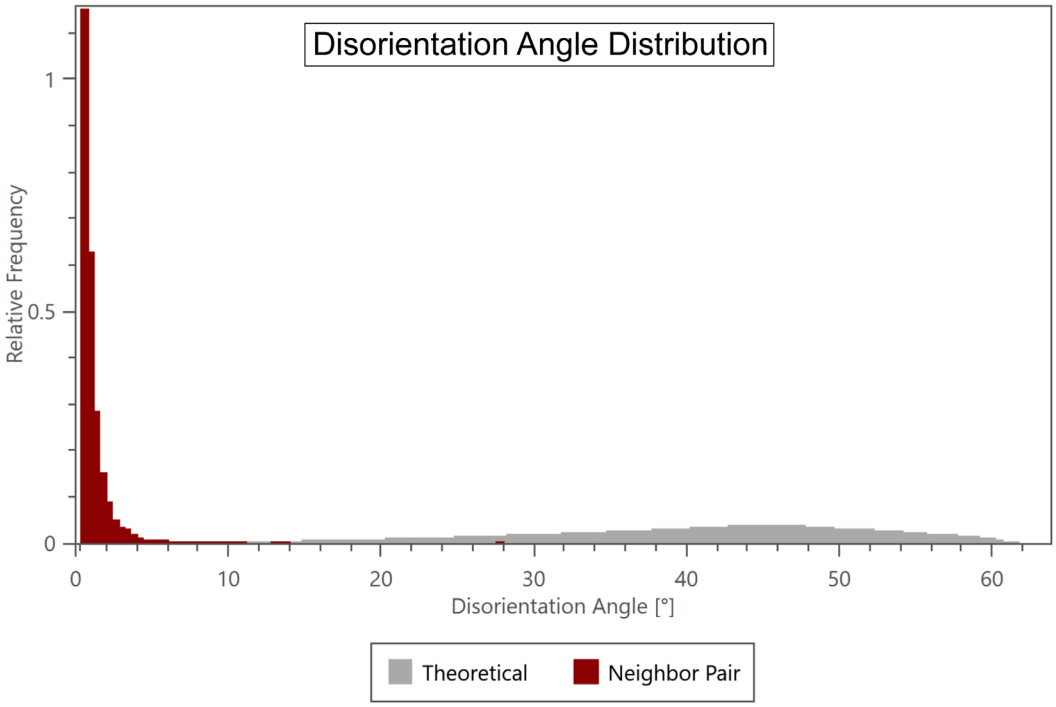

Figure 4.C2.4 Disorientation angle distribution for correlated disorientations (neighbor pair). The grey area represents the theoretical random distribution. Correlated disorientation show a peak at < 10° with the highest frequency being between 0.5 and 1.5°.

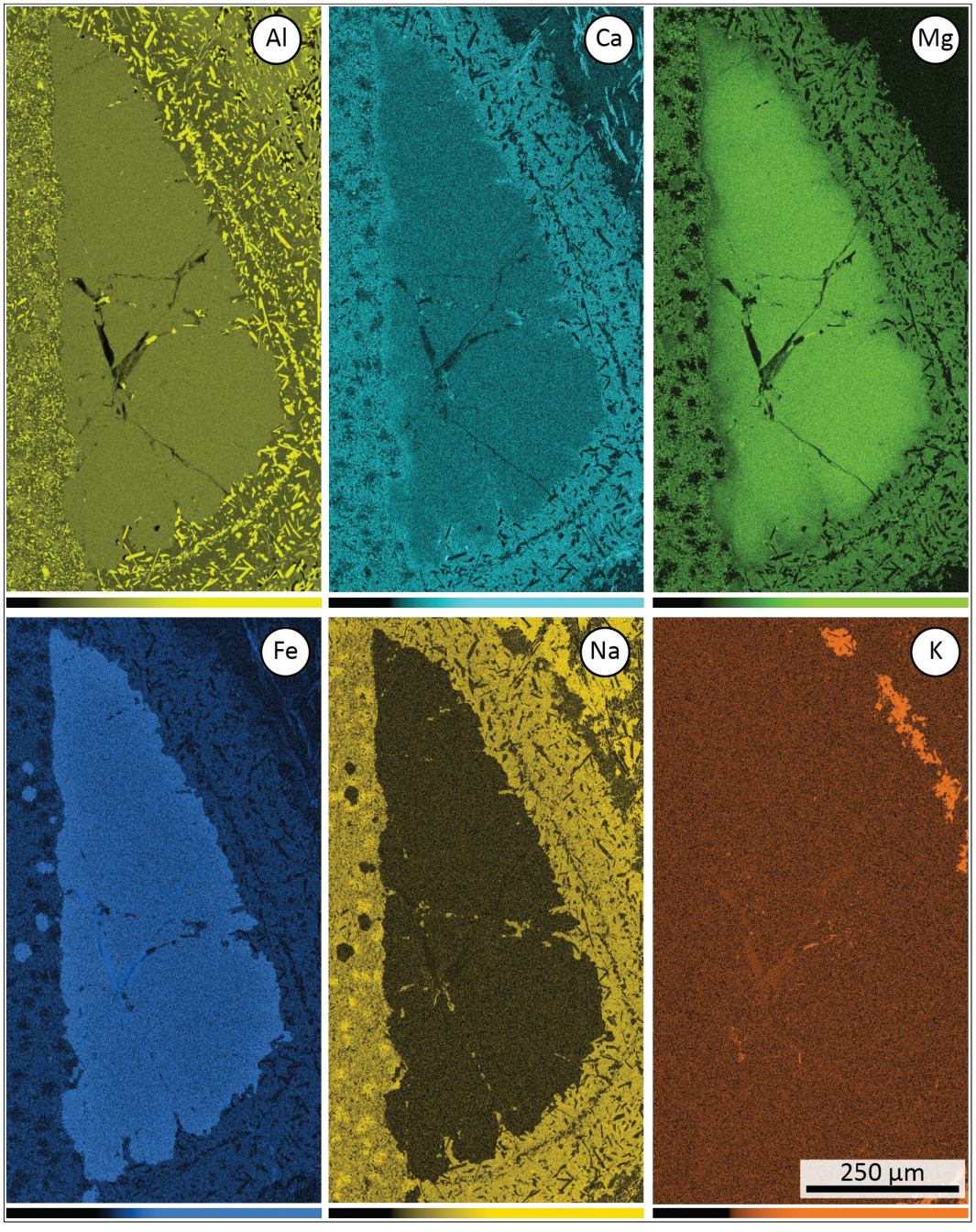

Figure 4.C2.5 EDS X-rays element distribution maps for Al, Ca, Mg, Fe, Na and K of the investigated garnet grain. Element distribution permits to identify the internal chemical zonation, mostly visible for Ca, Al and Fe.

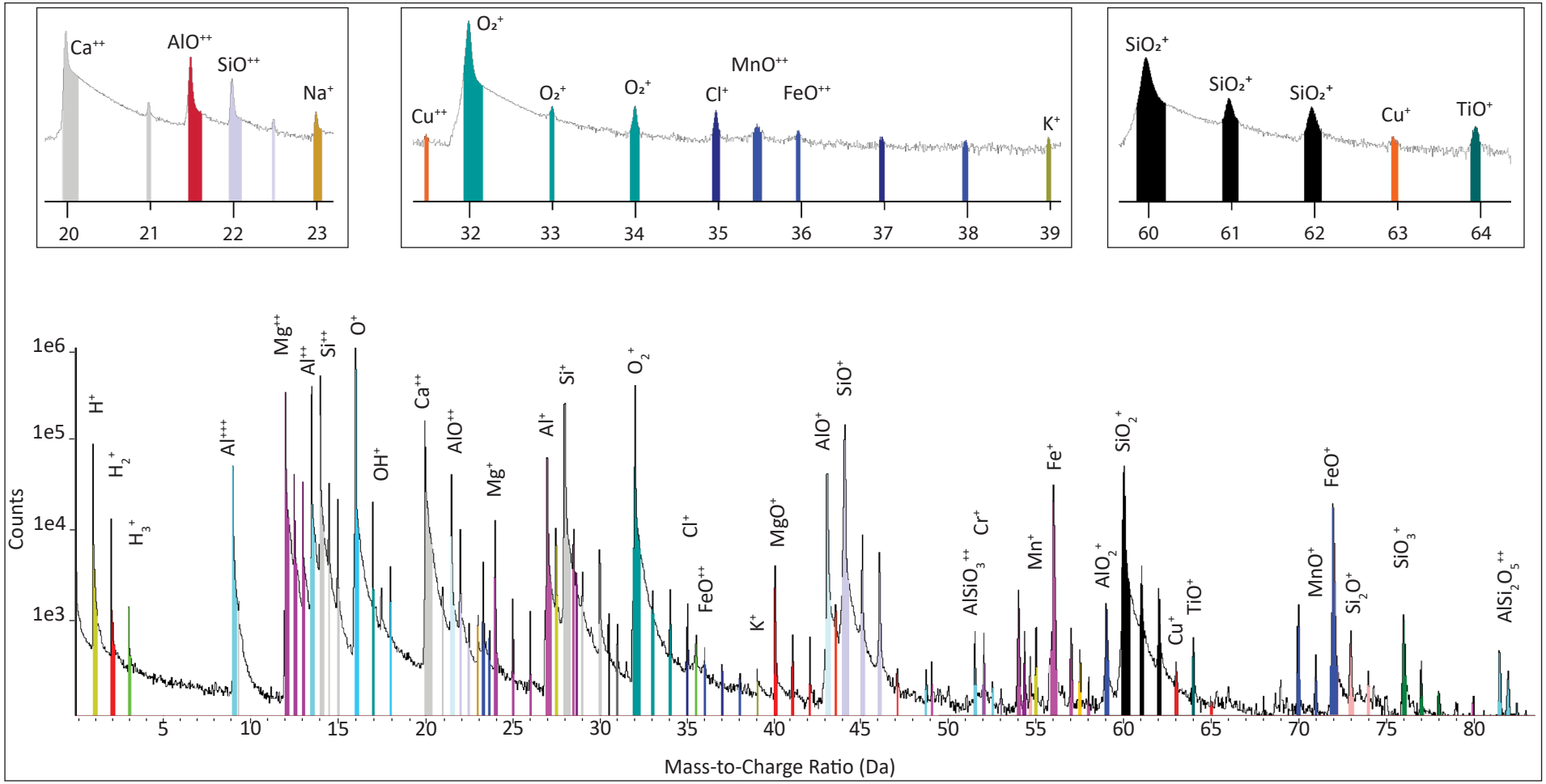

Figure 4.C2.6 Representative atom probe tomography mass spectrum of garnet from sample M6.

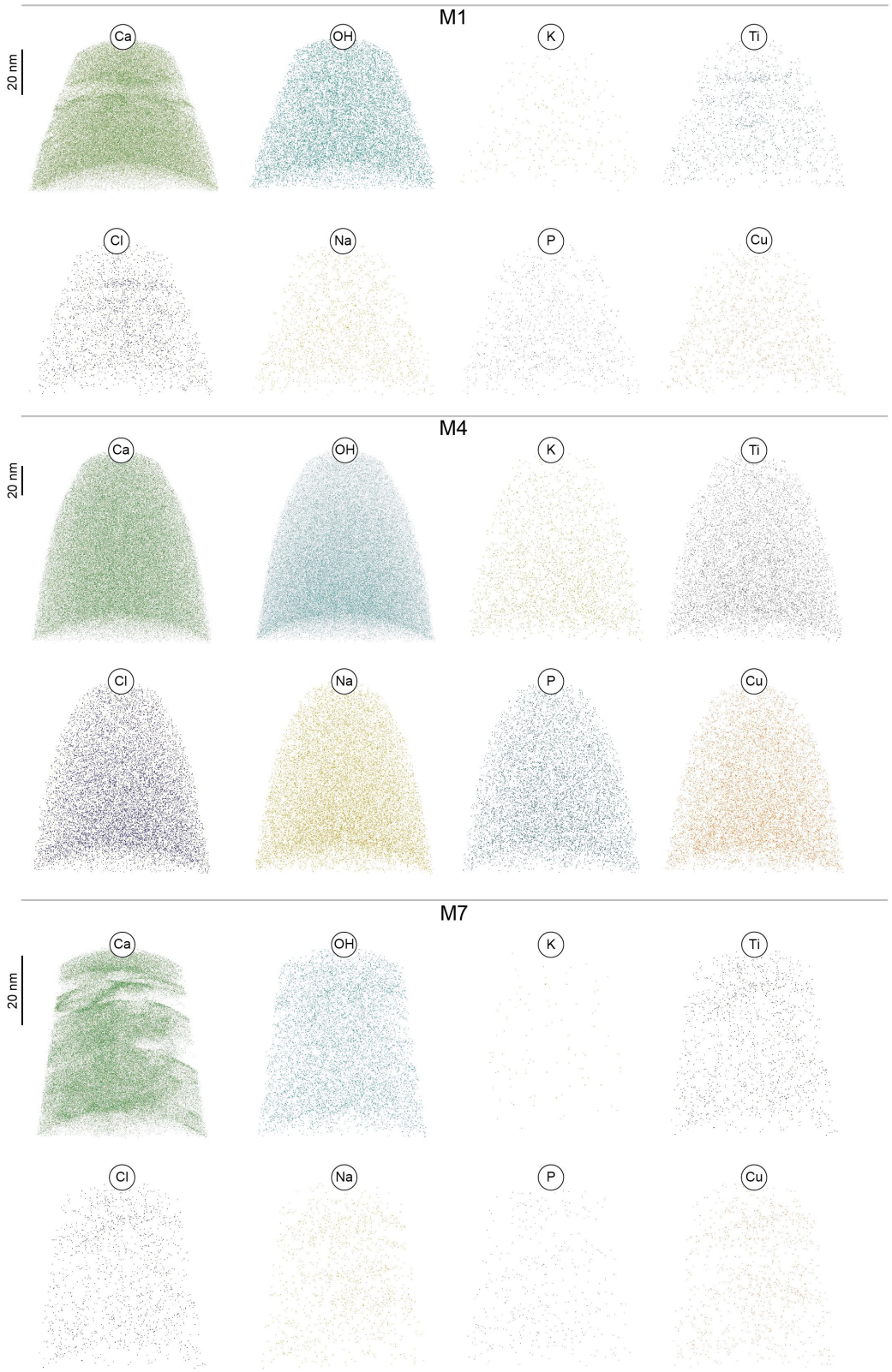

Figure 4.C2.7 Atom probe reconstructions of the remaining five analysed specimens showing the trace elements distributed along the interface in M6. The homogeneous distribution of the elements can be seen in all of the specimens. Irregularities present in specimen M1 and M7 derives from microfractures during the evaporation of the samples.

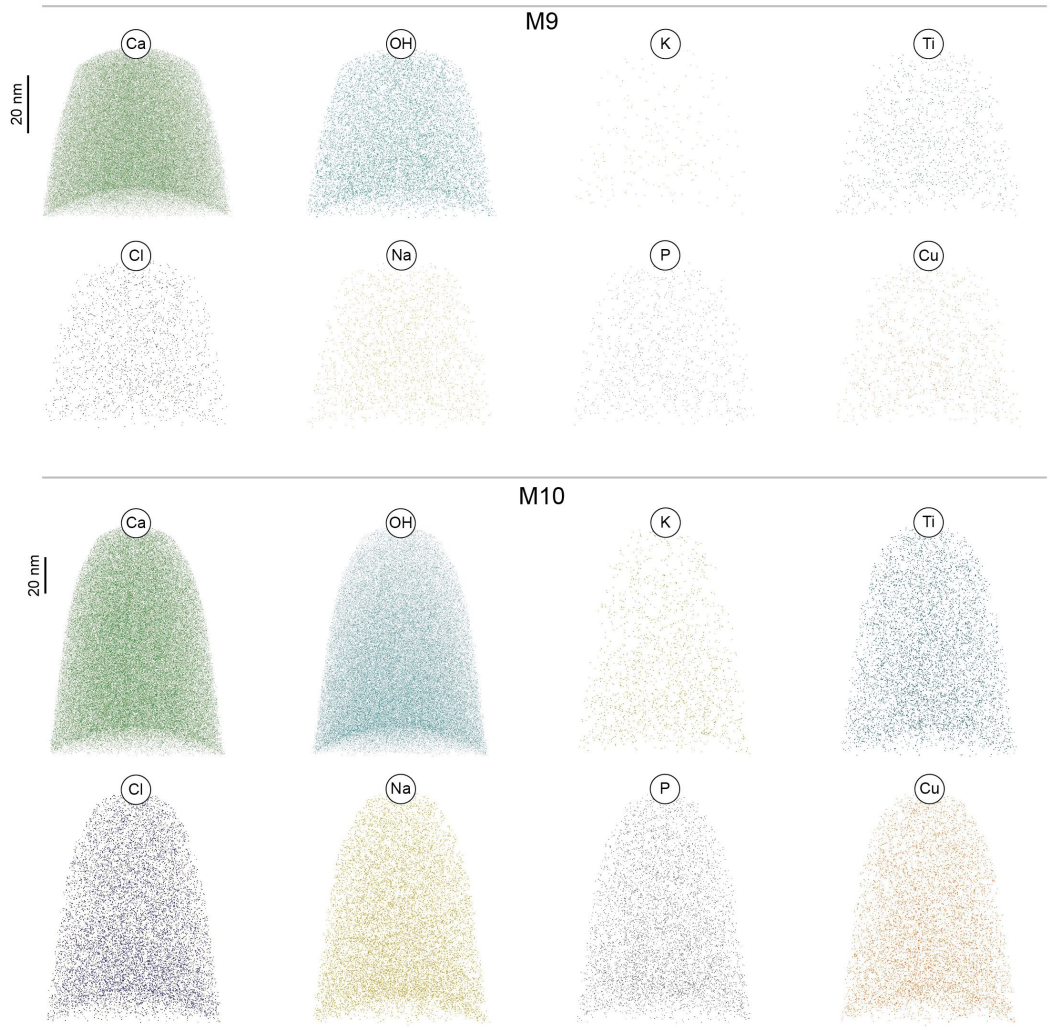

Figure 4.C2.7 Continued.

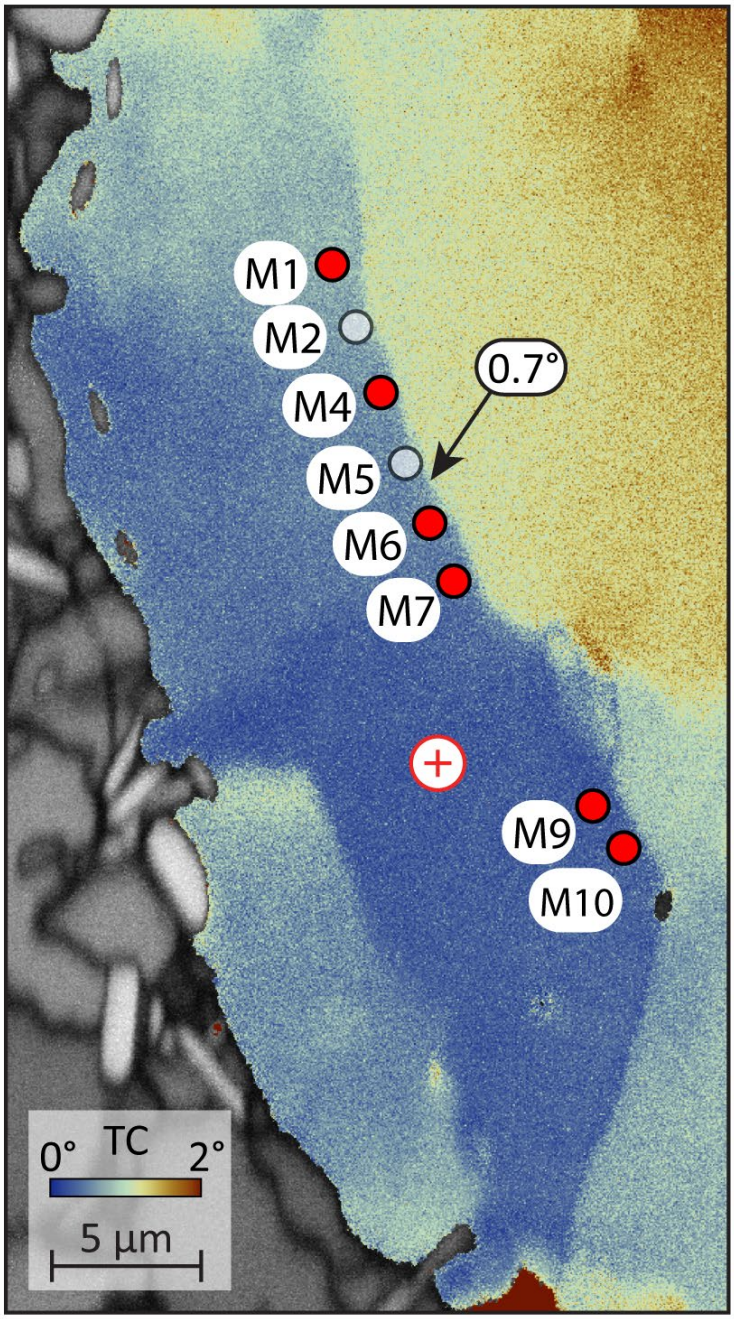

Figure 4.C2.8 EBSD Texture Component map. Each pixel is colour coded based on the deviation angle relative to the reference point indicated by a red cross in the map. The arrow indicates the low-angle boundary analysed by APT. The location of the successful APT specimens is indicated with red circles in the map.

Table 4.C2.1 Composition of the specimen M6 and the low-angle boundary obtained from APT. Concentrations are expressed in atomic %.

Element	**Si**	*σ*	**O**	*σ*	**Mg**	*σ*	**Fe**	*σ*	**Al**	*σ*	**Ca**	*σ*	**Mn**	*σ*
Garnet	21.90	*0.11*	47.20	*0.1*	6.92	*0.07*	1.67	*0.03*	12.93	*0.09*	3.75	*0.05*	0.25	*0.01*
Interface	20.70	*0.03*	47.47	*0.04*	6.35	*0.01*	1.32	*0.007*	11.44	*0.02*	4.42	*0.01*	0.23	*0.003*

	Ti	*σ*	**Cu**	*σ*	**P**	*σ*	**K**	*σ*	**Na**	*σ*	**Cl**	*σ*	**H**	*σ*
Garnet	0.01	*0.002*	0.003	*0.001*	0.009	*0.002*	0.001	*0.0005*	0.01	*0.002*	0.01	*0.003*	0.17	0.01
Interface	0.17	*0.002*	0.05	*0.0013*	0.04	*0.001*	0.05	*0.001*	0.17	*0.002*	0.16	*0.002*	1.43	*0.007*

Table 4.C2.2 Composition of the unsuccessful garnet specimens obtained from APT. Concentrations are expressed in atomic %.

Ion	**M1**	**M4**	**M7**	**M9**	**M10**
Si	23.02	23.56	22.69	23.19	23.01
O	49.39	50.28	49.98	49.83	50.36
Ti	0.01	0.01	0.02	0.01	0.01
Al	13.62	13.41	12.91	13.31	13.39
Fe	1.81	2.06	1.83	1.78	1.94
Mn	0.29	0.26	0.24	0.26	0.25
Mg	7.61	7.22	7.98	7.21	6.78
Ca	4.17	3.12	4.26	4.33	4.17
Na	0.01	0.02	0.02	0.02	0.02
K	*b.b*	*b.b*	*b.b*	*b.b*	*b.b*
Cl	0.02	0.02	0.03	0.02	0.02
P	0.01	0.01	0.01	0.01	0.01
Cu	0.004	0.01	0.02	0.005	0.005
Cr	0.01	0.01	0.01	0.02	0.01
Sr	0.02	0.02	0.01	0.02	0.02

Table 4.C2.3 APT data acquisition settings and data summary. (det. = detection; Volt. = voltage; corr. = correction; Calib. = calibration; interp. = interpolation; Lin. = linearization method; Avg. = average)

Data set/specimen		M1	M4	M6	M7	M9a	M9b	M10
Instrument model		LEAP 4000X HR	LEAP 4000X HR	LEAP 4000X HR	LEAP 4000X HR	LEAP 4000X HR	LEAP 4000X HR	LEAP 4000X HR
Instrument settings								
Laser wavelenth (nm)		355	355	355	355	355	355	355
Laser pulse energy (pJ)		350	380	380	380	380	380	380
Pulse frequency (kHz)		250	200	200	200	200	200	200
Evaporation control		dec rate	dec rate	dec rate	dec rate	dec rate	dec rate	dec rate
Targeted det. Rate (ions/pulse)		0.6	0.5	0.5	0.5	0.5	0.5	0.5
Nominal flight path (mm)		382	382	382	382	382	382	382
Set point temperature (K)		60	60	60	60	60	60	60
Sample Temperature (K)		69.2	69.2	69.2	69.2	69.2	69.2	69.2
Chamber Pressure (torr)		3.1 E-11	2.9 E-11	2.9 E-11	2.9 E-11	3.0 E-11	2.8 E-11	3.0 E-11
Data summary								
LAS Root version		15.41.342l	15.41.342l	15.41.342l	15.41.342l	15.41.342l	15.41.342l	15.41.342l
CAMECAROOT version		18.46.428	18.46.428	18.46.428	18.46.428	18.46.428	18.46.428	18.46.428
Analysis Software		IVAS 3.8.3	IVAS 3.8.3	IVAS 3.8.2	IVAS 3.8.3	IVAS 3.8.3	IVAS 3.8.3	IVAS 3.8.2
Total ions		6575691	30000530	19902574	2751946	6256246	20000868	31000821
	single	78.90%	81.30%	79.60%	78.70%	79.60%	81.40%	81.00%
	multiple	20.60%	18.30%	20.00%	20.80%	20.00%	18.30%	18.60%
	partial	0.50%	0.40%	0.40%	0.50%	0.40%	0.30%	0.40%
Volt./bowl corr. Peak (Da)		16	16	16	16	16	16	16
Mass Clib (peaks/interp)		9/Lin.	9/Lin.	9/Lin.	9/Lin.	9/Lin.	9/Lin.	9/Lin.
*(M/ΔM) for $^{12}Mg^{2+}$		991.7	1012.9	1018.1	922.6	977.9	1015.9	996.4
**($M/\Delta M_{10}$)		193.3	206.8	167.6	89.1	191.9	198.7	182
Time independent background (ppm/ns)		17.265	16.414	13.233	11.342	15.983	16.787	15.548
Reconsruction								
Final specimen state		Intact	Intact	Intact	Fractured	Intact	Intact	Intact
pre-/post analysis imaging		SEM	SEM	SEM	SEM	SEM	SEM	SEM
Radius evolution model		voltage	voltage	shank angle	voltage	voltage	voltage	voltage
Field factor(k)		3.3	3.3	3.3	3.3	3.3	3.3	3.3
Image compression factor		1.65	1.65	1.65	1.65	1.65	1.65	1.65
Assumed E-field (V/nm)		28.92	28.92	28.92	28.92	28.92	28.92	28.92
Detector efficiency		0.36	0.36	0.36	0.36	0.36	0.36	0.36
vg. Atomic volume (nm3)		0.008950	0.008950	0.008950	0.008950	0.008950	0.008950	0.008950
$V_{initial}$;V_{final} (V)		2530-5980	2620-6996	2935-6160	2140-5376	2960-5294	5300-6675	2630-6485

*ΔM is full width at half maximum

** ΔM_{10} is full width at tenth maximum

det. = detection; Volt. = voltage; corr. = correction; Calib. = calibration; interp. = interpolation; Lin. = linearization method; Avg. = average

Table 4.C2.4 Summary of detected and ranged ions within the garnet mass spectrum of specimen M6.

Ion	m/z (Da)	Ion	m/z (Da)
O^+	15.99	$Si_2O_4^+$	119.95
O_2^+	31.99	$Si_3O_5^{++}$	54.62
OH^+	17	$AlSiO_3^{++}$	51.46
Na^+	22.99	$AlSiO_3^+$	102.94
Mg^{++}	11.99	$Al_2Si_2O_5^{++}$	81.43
Mg^+	23.99	P^+	30.98
MgO^+	39.98	PO^+	46.97
Al^{+++}	8.99	Cl^+	34.97
Al^{++}	13.49	K^+	38.98
Al^+	26.98	Ca^{++}	19.98
AlO^{++}	21.48	TiO^+	63.94
AlO^+	42.98	Cr^+	51.96
Al_2O^{+++}	23.31	Mn^{++}	27.47
AlO_2^+	58.97	Mn^+	54.95
Si^{+++}	9.32	MnO^{+++}	23.64
Si^{++}	13.99	MnO^{++}	35.47
Si^+	27.97	MnO^+	70.99
SiO^{++}	21.98	Fe^{++}	28.47
SiO^+	43.97	Fe^+	55.94
SiO_2^{++}	30.48	FeO^{++}	35.96
SiO_2^+	59.97	FeO^+	71.93
SiO_3^+	75.96	$Fe_2O_3^{++}$	79.92
Si_2O^+	72.93	Cu^{++}	31.46
$Si_2O_2^+$	87.89	Cu^+	62.14
$Si_2O_3^+$	103.94	Ga^+	68.14

Appendix D

5.D Supplementary Figures and Data Tables to Chapter 5

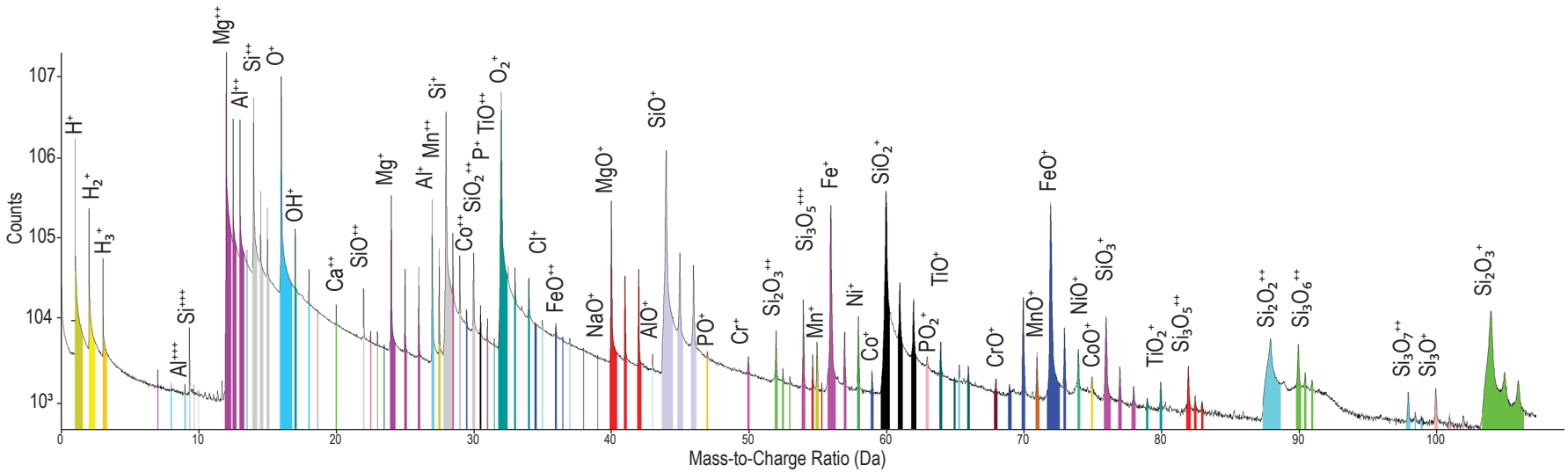

Figure 5.D.1 Representative atom probe tomography mass-to-charge ratio spectrum of olivine from sample LAB-8°.

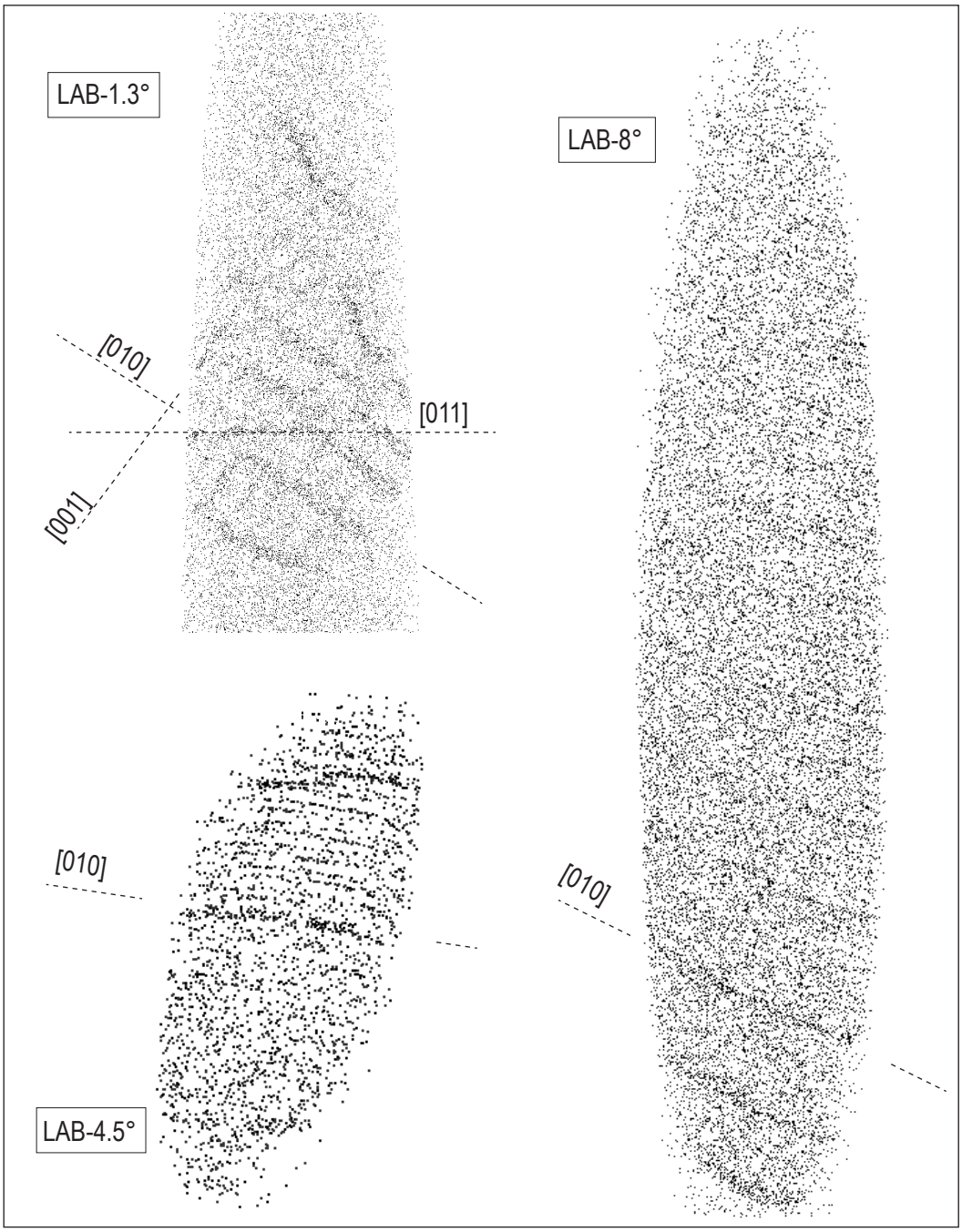

Figure 5.D.2 Atom probe reconstruction of samples LAB-1.3°, LAB-4.5° and LAB-8° showing the inferred crystallographic directions represented by decorated dislocations. Each dot represents a single detected atom of Ca.

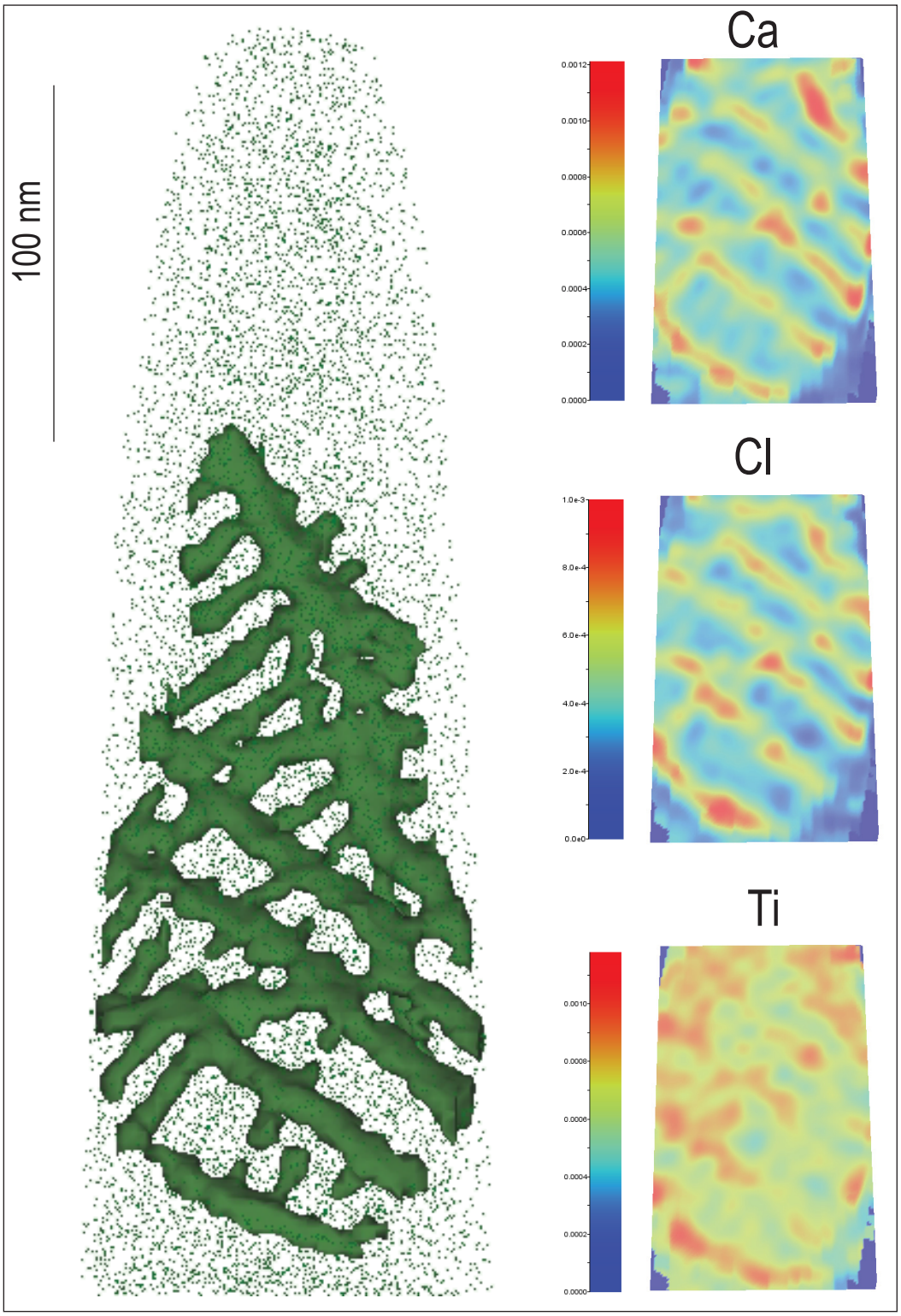

Figure 5.D.3 (left) 3D Ca-isosurface rendering of the enriched region of the investigated low-angle boundary LAB-1.3°. (right) 2D compositional profiles of the enriched region displaying atomic concentrations for Ca, Cl and Ti. Peaks of concentration are visible at the dislocation intersections.

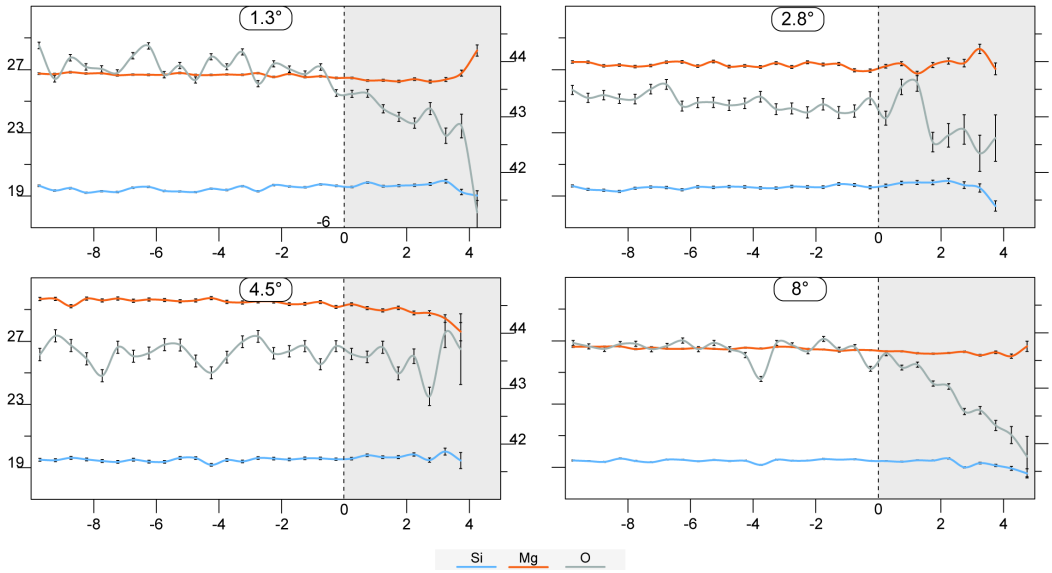

Figure 5.D.4 Proximity histogram profiles for Mg, Si and O expressed in at. % from the edge (distance 0) towards the inner side of the interfaces. Distance is expressed in nm. *Left y scale* shows concentration for Si and Mg. *Right y scale* indicates concentrations for O.

Table 5.D.1 APT data acquisition settings and data summary. (det. = detection; Volt. = voltage; corr. = correction; Calib. = calibration; interp. = interpolation; Lin. = linearization method; Avg. = average)

Data set/specimen		LAB-1.3°	LAB-2.8°	LAB-4.5°	LAB-8°
Instrument model		LEAP 4000X HR	LEAP 4000X HR	LEAP 4000X HR	LEAP 4000X HR
Instrument settings					
Laser wavelenth (nm)		355	355	355	355
Laser pulse energy (pJ)		150	150	80	120
Pulse frequency (kHz)		200	200	200	200
Evaporation control		dec rate	dec rate	dec rate	dec rate
Targeted det. Rate (ions/pulse)		0.8	0.8	0.8	0.8
Nominal flight path (mm)		382	382	382	382
Set point temperature (K)		60	60	50	50
Sample Temperature (K)		69.2	69.2	57.3	57.3
Chamber Pressure (torr)		2.9 E-11	3.4 E-11	2.6 E-11	3.0 E-11
Data summary					
LAS Root version		15.41.342l	15.41.342l	15.41.342l	15.41.342l
CAMECAROOT version		18.46.428	18.46.428	18.46.428	18.46.428
Analysis Software		IVAS 3.8.3	IVAS 3.8.2	IVAS 3.8.2	IVAS 3.8.3
Total ions		128225797	56375910	228525507	142640574
	single	77.60%	79.50%	73.70%	78.60%
	multiple	22.10%	20.20%	25.90%	21.20%
	partial	0.30%	0.30%	0.40%	0.20%
Volt./bowl corr. Peak (Da)		12	12	12	12
Mass Clib (peaks/interp)		9/Lin.	9/Lin.	5/Lin.	6/Lin.
*(M/ΔM) for $^{12}Mg^{2+}$		1095.6	1035.2	1005.8	1094.7
**(M/ΔM_{10})		177.4	36.2	65.8	136.9
Time independent background (ppm/ns)		25.091	12.07	25.205	13.344
Reconsruction					
Final specimen state		Intact	Intact	Intact	Intact
pre-/post analysis imaging		SEM	SEM	SEM	SEM
Radius evolution model		voltage	voltage	voltage	voltage
Field factor(k)		3.3	3.3	3.3	3.3
Image compression factor		1.65	1.65	1.65	1.65
Assumed E-field (V/nm)		25	25	25	25
Detector efficiency		0.36	0.36	0.36	0.36
vg. Atomic volume (nm3)		0.01095	0.01095	0.01095	0.01095
$V_{initial}$;V_{final} (V)		3111.5-8752.0	3796.9-7404.5	4113.5-6801.0	5640.4-8715.6

*ΔM is full width at half maximum

** ΔM_{10} is full width at tenth maximum

det. = detection; Volt. = voltage; corr. = correction; Calib. = calibration; interp. = interpolation; Lin. = linearization method; Avg. = average

Appendix E

6.E Supplementary Tables to Chapter 6

Table 6.E.1 Summary of acquisition parameters of all the specimens analysed in this research project.

ID	Sample	Tip	Duration (min)	Total ions	Good Hits (%)	Stopped Voltage	Temperature (K)	Laser pulse frequency (kHz)	Laser pulse energy (pJ)	Detection rate (ions/pulse)	Specimen conditions
2515	Melt/Grt	M-1	1276	45074104	89.6	7479	60	200	450	0.003	Fractured
2516	Melt/Grt	M-2	125	4830971	95.8	5464	60	200	480	0.004	Fractured
2517	Melt/Grt	M-3	165	7077336	91	6409	60	200	480	0.004	Fractured
2518	Melt/Grt	M-4	148	3155285	100	4285	60	200	480	0.004	Fractured
2519	Melt/Grt	M-5	12	110822	88.5	2578	60	200	450	0.004	Fractured
2520	Melt/Grt	M-6	107	3176873	96.5	4257	60	200	480	0.004	Fractured
2522	Melt/Grt	M-8	103	1607055	88.8	3954	60	200	480	0.004	Fractured
2522	Melt/Grt	M-8	258	5411618	85.1	2077	60	200	450	0.004	Fractured
2523	Melt/Grt	M-9	72	1460900	84.7	5245	60	200	450	0.004	Fractured
2524	Melt/Grt	M-10	240	5192261	83	5811	60	200	480	0.004	Fractured
2525	Melt/Grt	M-11	333	21462038	78.3	6974	60	200	500	0.004	Fractured
2525	Melt/Grt	M-11	109	6857985	80.9	5978	60	200	500	0.006	Fractured
2526	Melt/Grt	M-12	19	162659	96.8	5351	70	200	370	0.002	Fractured
2527	Melt/Grt	M-13	363	16640931	82.1	6164	70	200	370	0.005	Fractured
2528	Melt/Grt	M-14	59	633194	93.8	5627	70	200	370	0.005	Fractured
2529	Melt/Grt	M-15	43	503619	81.9	5702	60	200	350	0.005	Fractured
2530	Melt/Grt	M-16	23	155583	99.8	4779	70	200	370	0.002	Fractured
2533	Melt/Grt	M-19	159	6199347	93.7	8634	60	200	380	0.005	Fractured
2534	Melt/Grt	M-20	4	1449222	82.4	1583	60	200	480	0.004	Fractured
2535	Melt/Grt	M-21	573	28420181	96.8	5351	60	200	480	0.004	Good
2536	Melt/Grt	M-22	673	31212039	86.7	5485	60	200	400	0.004	Good
2729	Garnet	M-1	91	6575691	80.9	5978	60	250	350	0.006	Good
2732	Garnet	M-4	518	30000530	82	7001	60	200	380	0.006	Good
2734	Garnet	M-6	339	19902574	82.2	6207	60	200	380	0.005	Good
2735	Garnet	M-7	67	3496923	81.5	5374	60	200	380	0.005	Fractured
2737	Garnet	M-9	127	6256246	80.6	5295	60	200	380	0.005	Good
2737	Garnet	M-9	348	20000868	83.6	6686	60	200	380	0.005	Good
2738	Garnet	M-10	538	31000821	80.9	6488	60	200	380	0.005	Good
2337	Olivine	M3	2454	228525507	73.6	9534	50	200	80	0.008	Good
2338	Olivine	M4	18	121867	99.6	5523	50	250	120	0.008	Fractured
2340	Olivine	M6	1225	140949643	72.6	8485	50	200	80	0.01	Good
2341	Olivine	M-7	1449	132826969	78.7	9664	60	200	150	0.008	Good
2342	Olivine	M-8	1379	128225797	80.4	8745	60	200	150	0.008	Good
2343	Olivine	M-9	1177	106808795	81	9407	60	200	150	0.008	Good
2344	Olivine	M-10	1035	95321056	76.4	8963	60	200	150	0.008	Good
2345	Olivine	M-11	956	87028010	80.5	8610	60	200	150	0.008	Good
2346	Olivine	M-12	136	11541215	78.8	6053	60	200	120	0.008	Fractured
2347	Olivine	M-13	150	12419579	79.1	6495	60	200	150	0.005	Fractured
2348	Olivine	M-14	119	9558347	74.5	6319	60	200	120	0.008	Fractured
2349	Olivine	M-15	631	56375910	79.8	7405	60	200	150	0.008	Good
2350	Olivine	M-16	170	13651588	79.4	6307	60	200	150	0.008	Fractured
2355	Olivine	M-21	1547	142640574	79.3	8709	60	200	120	0.008	Good

F Permission statement for Chapter 2 content

SPRINGER NATURE LICENSE
TERMS AND CONDITIONS
Apr 14, 2022

This Agreement between Curtin University -- Tommaso Tacchetto ("You") and Springer Nature ("Springer Nature") consists of your license details and the terms and conditions provided by Springer Nature and Copyright Clearance Center.

License Number	5243940603537
License date	Feb 07, 2022
Licensed Content Publisher	Springer Nature
Licensed Content Publication	Contributions to Mineralogy and Petrology
Licensed Content Title	Pre-nucleation geochemical heterogeneity within glassy anatectic inclusions and the role of water in glass preservation
Licensed Content Author	Tommaso Tacchetto et al
Licensed Content Date	Aug 21, 2021
Type of Use	Thesis/Dissertation
Requestor type	academic/university or research institute
Format	print and electronic
Portion	full article/chapter
Will you be translating?	no
Circulation/distribution	200 - 499
Author of this Springer Nature content	yes
Title	Pre-nucleation geochemical heterogeneity within glassy anatectic inclusions and the role of water in glass preservation
Institution name	Curtin University
Expected presentation date	Apr 2022
Requestor Location	Curtin University Kent Street Perth, 6102 Australia Attn: Curtin University
Total	0.00 AUD

Terms and Conditions

G Permission statement for Chapter 5 content

SPRINGER NATURE LICENSE
TERMS AND CONDITIONS
Apr 14, 2022

This Agreement between Curtin University -- Tommaso Tacchetto ("You") and Springer Nature ("Springer Nature") consists of your license details and the terms and conditions provided by Springer Nature and Copyright Clearance Center.

License Number	5287941405118
License date	Apr 14, 2022
Licensed Content Publisher	Springer Nature
Licensed Content Publication	Contributions to Mineralogy and Petrology
Licensed Content Title	Disorientation control on trace element segregation in fluid-affected low-angle boundaries in olivine
Licensed Content Author	Tommaso Tacchetto et al
Licensed Content Date	Jul 12, 2021
Type of Use	Thesis/Dissertation
Requestor type	academic/university or research institute
Format	print and electronic
Portion	full article/chapter
Will you be translating?	no
Circulation/distribution	200 - 499
Author of this Springer Nature content	yes
Title	Disorientation control on trace element segregation in fluid-affected low-angle boundaries in olivine
Institution name	Curtin University
Expected presentation date	Apr 2022
Requestor Location	Curtin University Kent Street Perth, 6102 Australia Attn: Curtin University
Total	0.00 AUD

Terms and Conditions

Springer Nature Customer Service Centre GmbH
Terms and Conditions

This agreement sets out the terms and conditions of the licence (the **Licence**) between you and **Springer Nature Customer Service Centre GmbH** (the **Licensor**). By clicking 'accept' and completing the transaction for the material (**Licensed Material**), you also confirm your acceptance of these terms and conditions.

1. **Grant of License**

    1. The Licensor grants you a personal, non-exclusive, non-transferable, world-wide licence to reproduce the Licensed Material for the purpose specified in your order only. Licences are granted for the specific use requested in the order and for no other use, subject to the conditions below.

    2. The Licensor warrants that it has, to the best of its knowledge, the rights to license reuse of the Licensed Material. However, you should ensure that the material you are requesting is original to the Licensor and does not carry the copyright of another entity (as credited in the published version).

    3. If the credit line on any part of the material you have requested indicates that it was reprinted or adapted with permission from another source, then you should also seek permission from that source to reuse the material.

2. **Scope of Licence**

    1. You may only use the Licensed Content in the manner and to the extent permitted by these Ts&Cs and any applicable laws.

    2. A separate licence may be required for any additional use of the Licensed Material, e.g. where a licence has been purchased for print only use, separate permission must be obtained for electronic re-use. Similarly, a licence is only valid in the language selected and does not apply for editions in other languages unless additional translation rights have been granted separately in the licence. Any content owned by third parties are expressly excluded from the licence.

3. Similarly, rights for additional components such as custom editions and derivatives require additional permission and may be subject to an additional fee. Please apply to Journalpermissions@springernature.com/bookpermissions@springernature.com for these rights.

4. Where permission has been granted **free of charge** for material in print, permission may also be granted for any electronic version of that work, provided that the material is incidental to your work as a whole and that the electronic version is essentially equivalent to, or substitutes for, the print version.

5. An alternative scope of licence may apply to signatories of the STM Permissions Guidelines, as amended from time to time.

- **Duration of Licence**

1. A licence for is valid from the date of purchase ('Licence Date') at the end of the relevant period in the below table:

Scope of Licence	Duration of Licence
Post on a website	12 months
Presentations	12 months
Books and journals	Lifetime of the edition in the language purchased

- **Acknowledgement**

1. The Licensor's permission must be acknowledged next to the Licenced Material in print. In electronic form, this acknowledgement must be visible at the same time as the figures/tables/illustrations or abstract, and must be hyperlinked to the journal/book's homepage. Our required acknowledgement format is in the Appendix below.

- **Restrictions on use**

1. Use of the Licensed Material may be permitted for incidental promotional use and minor editing privileges e.g. minor adaptations of single figures, changes of format, colour and/or style where the adaptation is credited as set out in Appendix 1 below. Any other changes including but not limited to, cropping, adapting, omitting material that affect the meaning, intention or moral rights of the author are strictly prohibited.

2. You must not use any Licensed Material as part of any design or trademark.

3. Licensed Material may be used in Open Access Publications (OAP) before publication by Springer Nature, but any Licensed Material must be removed from OAP sites prior to final publication.

- **Ownership of Rights**

1. Licensed Material remains the property of either Licensor or the relevant third party and any rights not explicitly granted herein are expressly reserved.

- **Warranty**

IN NO EVENT SHALL LICENSOR BE LIABLE TO YOU OR ANY OTHER PARTY OR ANY OTHER PERSON OR FOR ANY SPECIAL, CONSEQUENTIAL, INCIDENTAL OR INDIRECT DAMAGES, HOWEVER CAUSED, ARISING OUT OF OR IN CONNECTION WITH THE DOWNLOADING, VIEWING OR USE OF THE MATERIALS REGARDLESS OF THE FORM OF ACTION, WHETHER FOR BREACH OF CONTRACT, BREACH OF WARRANTY, TORT, NEGLIGENCE, INFRINGEMENT OR OTHERWISE (INCLUDING, WITHOUT LIMITATION, DAMAGES BASED ON LOSS OF PROFITS, DATA, FILES, USE, BUSINESS OPPORTUNITY OR CLAIMS OF THIRD PARTIES), AND
WHETHER OR NOT THE PARTY HAS BEEN ADVISED OF THE POSSIBILITY OF SUCH DAMAGES. THIS LIMITATION SHALL APPLY NOTWITHSTANDING ANY FAILURE OF ESSENTIAL PURPOSE OF ANY LIMITED REMEDY PROVIDED HEREIN.

- **Limitations**

1. ***BOOKS ONLY:***Where **'reuse in a dissertation/thesis'** has been selected the following terms apply: Print rights of the final author's accepted manuscript (for clarity, NOT the published version) for up to 100 copies, electronic rights for use only on a personal website or institutional repository as defined by the Sherpa guideline (www.sherpa.ac.uk/romeo/).

2. For content reuse requests that qualify for permission under the STM Permissions Guidelines, which may be updated from time to time, the STM Permissions Guidelines supersede the terms and conditions contained in this licence.

- **Termination and Cancellation**

1. Licences will expire after the period shown in Clause 3 (above).

2. Licensee reserves the right to terminate the Licence in the event that payment is not received in full or if there has been a breach of this agreement by you.

Appendix 1 — Acknowledgements:

For Journal Content:
Reprinted by permission from [**the Licensor**]: [**Journal Publisher** (e.g. Nature/Springer/Palgrave)] [**JOURNAL NAME**] [**REFERENCE CITATION** (Article name, Author(s) Name), [**COPYRIGHT**] (year of publication)
For **Advance Online Publication papers:**
Reprinted by permission from [**the Licensor**]: [**Journal Publisher** (e.g. Nature/Springer/Palgrave)] [**JOURNAL NAME**] [**REFERENCE CITATION** (Article name, Author(s) Name), [**COPYRIGHT**] (year of publication), advance online publication, day month year (doi: 10.1038/sj.[JOURNAL ACRONYM].)
For Adaptations/Translations:
Adapted/Translated by permission from [**the Licensor**]: [**Journal Publisher** (e.g. Nature/Springer/Palgrave)] [**JOURNAL NAME**] [**REFERENCE CITATION** (Article name, Author(s) Name), [**COPYRIGHT**] (year of publication)
Note: For any republication from the British Journal of Cancer, the following credit line style applies:
Reprinted/adapted/translated by permission from [**the Licensor**]: on behalf of Cancer Research UK: : [**Journal Publisher** (e.g. Nature/Springer/Palgrave)] [**JOURNAL NAME**] [**REFERENCE CITATION** (Article name, Author(s) Name), [**COPYRIGHT]** (year of publication)
For **Advance Online Publication** papers:
Reprinted by permission from The [**the Licensor**]: on behalf of Cancer Research UK: [**Journal Publisher** (e.g. Nature/Springer/Palgrave)] [**JOURNAL NAME**] [**REFERENCE CITATION** (Article name, Author(s) Name), [**COPYRIGHT**] (year of publication), advance online publication, day month year (doi: 10.1038/sj.[JOURNAL ACRONYM])
For Book content:
Reprinted/adapted by permission from [**the Licensor**]: [**Book Publisher** (e.g. Palgrave Macmillan, Springer etc) [**Book Title**] by [**Book author**(s)] [**COPYRIGHT**] (year of publication)

Statement

Every reasonable effort has been made to acknowledge the owners of copyright material. I would be pleased to hear from any copyright owner who has been omitted or incorrectly acknowledged